

**DEVELOPMENT OF ULTRATHIN POLY-SIGE FILMS
AS STRUCTURAL LAYERS FOR APPLICATIONS IN
NANOELECTROMECHANICAL SYSTEMS**

BY

ASAFA, TESLEEM BABATUNDE

A Dissertation Presented to the
DEANSHIP OF GRADUATE STUDIES

KING FAHD UNIVERSITY OF PETROLEUM & MINERALS

DHAHRAN, SAUDI ARABIA

In Partial Fulfillment of the
Requirements for the Degree of

DOCTOR OF PHILOSOPHY

In

MECHANICAL ENGINEERING

MAY 2013

KING FAHD UNIVERSITY OF PETROLEUM & MINERALS

DHAHRAN- 31261, SAUDI ARABIA

DEANSHIP OF GRADUATE STUDIES

This thesis, written by **TESLEEM BABATUNDE ASAFA** under the direction of his thesis advisor and approved by his thesis committee, has been presented and accepted by the Dean of Graduate Studies, in partial fulfilment of the requirements for the degree of **DOCTOR OF PHILOSOPHY IN MECHANICAL ENGINEERING.**




Dr. Syed Said
(Advisor)



Dr. Zuhair Gasem
Department Chairman



Dr. Nouar Tabet
(Co-Advisor)



Dr. Salam A. Zummo
Dean of Graduate Studies



Dr. Ann Witvrouw
(Member)

28/5/13
Date



Dr. Tahar Laoui
(Member)



Dr. Nasser Al-Aqeeli
(Member)

© TESLEEM BABATUNDE ASAFA

2013

Dedication

To

My wife Rihanat and our kids: Mahfuz, Fareedah and Faheemah

ACKNOWLEDGMENTS

"... And be thankful to Me, and do not be ungrateful to Me." (Al-Qur'an 2:152).

Indeed, whoever is ungrateful to men will be ungrateful to God.

All praises and adorations are due to Almighty Allah for guiding me thus far. May His Blessings and Benedictions be showered upon the noble soul of Prophet Muhammad, his companions and those who follow his path till the day of judgement. The journey to the successful completion of this dissertation was very challenging and rough. However, its outcomes are fulfilling and rewarding. While the road ahead seemed blocked, the Center of Research Excellence in Nano-manufacturing Applications (CENA) was instituted by King Abdullah City of Science and Technology (KACST), Riyadh, Saudi Arabia as a joint consortium between INTEL Corporation and KACST. I was fortunate to be among the first group of scholars who were sponsored to Interuniversities Microelectronic Center (imec), Leuven, Belgium to conduct research for my Ph.D. dissertation. I am therefore highly indebted to the CENA/KACST for such a generous scholarship and immense support. Without the study leave granted by King Fahd University of Petroleum and Minerals, availing this scholarship would have been impossible. This kind gesture is immensely appreciated. Hitherto, Ladoke Akintola University of Technology, Ogbomosho granted me a study leave under which the entire Ph.D. research was conducted. My appreciation is indeed unlimited.

Several people contributed to the success of this work and thus deserved to be acknowledged. In the first instance, I thank my advisor, Prof. Syed Said for his immense contributions and supports. To Dr Ann Witvrouw who was my industrial advisor while at imec as well as a member of my dissertation committee, thank you for your training, criticism and guidance. I also appreciate your effort for traveling from Belgium to Saudi Arabia to attend my Ph.D. defence presentation. Seeing you during my defence did relax my nerves and propel me to give a good presentation as acknowledged by the attendees. I also thank my co-advisor Dr Nouar Tabet for his technical contributions and immense

assistance. To Drs Tahar Laoui and Naser Al-Aqeel who were members of my Dissertation committee, thank you for your advice and technical support. I also appreciate all the contributions, assistance, kindness and understanding from imec colleagues: George (who doubled as my mentor), Simone, Maliheh, Ashesh, Guy, Kris, Bert, Olalla, Rita, Agnes, Jeroen, Philippe, Alain, Basten, Hugo and from my CENA colleagues: Ahmad, Alaa, Moatassim, Bishoy, Qaid, and Zanaty. Let me put it on record that I enjoyed working in your company and I felt sad saying ‘good bye’ to you. If an opportunity to work with you crosses my path again, I will grasp it without hesitation.

I am equally grateful to the members of the Nigerian Community at KFUPM for encouragements, supports and advice most especially Dr Balarabe, Dr Babalola, Dr Olatunji, Ahmad, Suli, Wasuu, Fatai, Kabir, Maruf and many others. I am indebted to my colleagues at Mechanical Engineering Department of LAUTECH: Dr Durowoju, Prof Lucas, Prof Adebiyi, Dr Onawumi, Engr. Sangotayo, Engr. Ajayeoba, Engr. Adekunle, Dr Okekunle and many others for your prayers and supports. The moral supports from uncles and friends: Dr Lateef, Dr Akinboro, Dr Abdul-Hammed, Dr Rauf, Dr Oriola and Dr Ige among others are appreciated.

Finally, I am very grateful to my parents, uncles, aunts, sisters, brothers, and in-laws for their supports, prayers and encouragements. To my wife Rihanat and our kids: Mahfuz, Fareedah and Faheemah. Thank you for bearing with me thus far. You endured my long period of absence from home and several sleepless nights. You magnanimously accepted relocating you from Nigeria to Saudi Arabia and then to Belgium and later back to Saudi Arabia while my research lasted. You have proved to me that no group or individual is more supportive and encouraging than a good and enduring family. I love you dearly.

To several other people who have supported me either morally or financially, please do accept my warm acknowledgements. I appreciate all of you.

Tesleem Asafa

May 2013

TABLE OF CONTENTS

| | |
|--|-------------|
| ACKNOWLEDGMENTS | III |
| TABLE OF CONTENTS | V |
| LIST OF TABLES | IX |
| LIST OF FIGURES | X |
| LIST OF ABBREVIATIONS | XIII |
| ABSTRACT (ENGLISH) | XIV |
| ABSTRACT (ARABIC) | XVI |
| CHAPTER 1 INTRODUCTION | 1 |
| 1.1 NEMS: What and Why? | 1 |
| 1.2 Why Polycrystalline Silicon Germanium (Poly-SiGe)? | 7 |
| 1.3 Objectives of the Dissertation | 9 |
| 1.4 Outline of the Dissertation | 10 |
| CHAPTER 2 LITERATURE REVIEW | 12 |
| 2.1 Materials for M/NEMS | 12 |
| 2.1.1 Metals | 13 |
| 2.1.2 Nonmetals | 14 |
| 2.1.3 Ceramics | 15 |
| 2.1.4 Polymers | 16 |
| 2.2 Brief History of Poly-SiGe Research for MEMS Applications | 17 |

| | | |
|--|---|-----------|
| 2.3 | Resistivity and Surface Properties of Poly-SiGe Films | 21 |
| 2.4 | Thin Film Stress Models..... | 24 |
| 2.4.1 | Precoalescence Stress Models | 26 |
| 2.4.2 | Coalescence and Postcoalescence Stress Models | 28 |
| CHAPTER 3 EXPERIMENTAL METHODS | | 31 |
| 3.1 | Film Deposition by LPCVD | 32 |
| 3.2 | Thickness, Microstructure and Surface Roughness Characterization ... | 37 |
| 3.3 | Characterization of Electrical and Structural Properties | 39 |
| 3.3.1 | Film Resistivity | 39 |
| 3.3.2 | Mobility and Concentration of Carriers | 41 |
| 3.3.3 | Determination of the Crystal Structure by XRD | 43 |
| 3.4 | Characterization of Mechanical Properties | 46 |
| 3.4.1 | Stress Measurement Technique | 46 |
| 3.4.2 | Characterization of Mechanical Properties | 48 |
| 3.5 | Other Characterization Techniques | 52 |
| CHAPTER 4 MODELING STRESSES IN THIN FILMS | | 54 |
| 4.1 | Modeling..... | 54 |
| 4.1.1 | Approach, Justification and Assumptions | 55 |
| 4.1.2 | Stress Generation at Precoalescence Stage..... | 58 |
| 4.1.3 | Stress Generation at Coalescence and Postcoalescence Stages..... | 60 |

| | | |
|--|---|------------|
| 4.2 | Modeling Results, Validation and Comparison..... | 64 |
| 4.3 | Parametric Studies | 67 |
| 4.4 | Application of the Current Model to Poly-SiGe Films..... | 69 |
| 4.5 | Further Discussion of the Current Model and Experimental Results..... | 73 |
| CHAPTER 5 DEVELOPMENT OF ULTRATHIN SIGE FILMS: OPTIMIZATION AND PARAMETRIC STUDIES..... | | 76 |
| 5.1 | The Grey-Taguchi Multi-Response Optimization | 76 |
| 5.1.1 | The L32 Orthogonal Array and Grey Relational Analysis..... | 78 |
| 5.1.2 | Selection of Optimal Process Condition..... | 84 |
| 5.1.3 | Analysis of Variance (ANOVA) and Confirmation Test | 86 |
| 5.2 | Further Characterization of the Optimized and the Experimental Best Films..... | 91 |
| 5.3 | Investigation of the Influences of Germanium Fraction, Boron Concentration and Chamber Pressure on Some Films Properties | 93 |
| 5.3.1 | Germanium Fraction..... | 94 |
| 5.3.2 | Boron Concentration | 108 |
| 5.3.3 | Chamber Pressure | 113 |
| 5.3.4 | Influence of Germanium Fraction on the Elastic Moduli and Hardness..... | 115 |
| CHAPTER 6 EVOLUTION OF STRESS, RESISTIVITY AND SURFACE CHARACTERISTICS OF SIGE FILMS..... | | 121 |
| 6.1 | Stress Evolution..... | 121 |
| 6.1.1 | Stress Evolution Curves | 122 |
| 6.1.2 | Stress-Thickness Evolution and Local Stresses | 125 |

| | | |
|--|--|------------|
| 6.2 | Resistivity Evolution in Poly-SiGe Films | 129 |
| 6.2.1 | Resistivity Evolution Curve | 130 |
| 6.2.2 | Crystallinity | 134 |
| 6.3 | Evolution of Surface Properties | 135 |
| 6.3.1 | Application of Power Spectral Density Function | 135 |
| 6.3.2 | Fractal Analysis..... | 140 |
| 6.3.3 | Surface Topography and Scaling Exponents..... | 141 |
| CHAPTER 7 FABRICATION OF NANOCANTILEVERS AND STRAIN GRADIENTS EVALUATION..... | | 147 |
| 7.1 | Cantilever Fabrication..... | 148 |
| 7.1.1 | Photomask Layout..... | 148 |
| 7.1.2 | Fabrication Steps..... | 150 |
| 7.2 | Strain Gradient Evaluation | 157 |
| 7.2.1 | Strain Gradients in the ~100nm-Thick Cantilevers | 159 |
| 7.2.2 | Strain Gradients in the ~60nm Thick Cantilevers | 169 |
| 7.2.3 | Strain Gradients, Stress and Resistivity Variations..... | 173 |
| CHAPTER 8 CONCLUSIONS AND RECOMMENDATIONS..... | | 177 |
| 8.1 | Conclusions | 177 |
| 8.2 | Recommendations and Future Studies | 180 |
| REFERENCES..... | | 181 |
| VITAE..... | | 200 |

LIST OF TABLES

| | |
|---|-----|
| Table 1.1: Expected effect of scaling on sensitivity of SiGe resonator..... | 6 |
| Table 4.1: Comparison between predicted and measured compressive stress..... | 65 |
| Table 4.2: Stresses at coalescence and continuous stages for Cu (001) films | 67 |
| Table 4.3: Surface and grain boundary stresses obtained from the current model | 73 |
| Table 5.1: Experimental parameters and their levels..... | 78 |
| Table 5.2: Design layout and experimental results..... | 82 |
| Table 5.3: Normalized average values, grey relational coefficient (GRC)..... | 83 |
| Table 5.4: Response table for the grey relational grade..... | 85 |
| Table 5.5: Analysis of variance results for multi-performance characteristics | 88 |
| Table 5.6: Results of performance measures for initial and optimal deposition | 90 |
| Table 5.7: Process condition for the SiGe deposition..... | 94 |
| Table 5.8: Surface characteristics for the influences of boron concentration..... | 113 |
| Table 6.1: Deposition conditions used for evolutionary study | 122 |
| Table 6.2: AFM parameters, surface fractal dimensions (D) and fitting parameters | 140 |
| Table 7.1: Dimensions of the cantilevers..... | 150 |
| Table 7.2: Deposition conditions for poly-SiGe films and some preliminary results | 152 |
| Table 7.3: Strain gradients for wafer D (Film A - experimental best recipe)..... | 166 |
| Table 7.4: Stress gradients for wafer E (Film B - optimized recipe)..... | 167 |
| Table 7.5: Strain gradients in the 60 nm thick cantilevers..... | 171 |

LIST OF FIGURES

| | |
|--|----|
| Figure 1.1: Dimensions of MEMS and NEMS devices in perspective..... | 3 |
| Figure 1.2: A cantilever resonator fabricated on a substrate.. .. | 6 |
| Figure 2.1: Stress-structure evolution during film growth..... | 25 |
| Figure 2.2: Principle of coalescence | 28 |
| Figure 3.1: Schematic diagram of Applied Materials Centura platform. | 33 |
| Figure 3.2: Reactor chamber A of LPCVD for SiGe film deposition.. .. | 34 |
| Figure 3.3: Stages in SiGe deposition process on blanket wafer | 37 |
| Figure 3.4: (a) FEI NOVA 200 SEM, and (b) Multimode AFM tool..... | 38 |
| Figure 3.5: KLA-Tensor OmniMap RS75 four-point probe..... | 40 |
| Figure 3.6: Hall voltage V_H is generated due to the Lorenz force | 43 |
| Figure 3.7: D8 Bruker AXS X-ray diffractometer..... | 45 |
| Figure 3.8: Tencor FLX-2320 stress measurement tool | 48 |
| Figure 3.9: MTS Nano Indenter XP..... | 50 |
| Figure 3.10: A schematic view of cross-section of poly-SiGe stack sample..... | 52 |
| Figure 4.1: AFM image showing significantly isolated islands | 56 |
| Figure 4.2: (a) SEM image showing grain structure of Cu film (b) hexagonal shape..... | 61 |
| Figure 4.3: Precoalescence stress evolution..... | 68 |
| Figure 4.4: Poly-SiGe islands at the precoalescence growth stage..... | 70 |
| Figure 4.5: Stress evolution in poly-SiGe films deposited by CVD..... | 72 |
| Figure 5.1: Flow chart for the Grey-Taguchi Multi-objective Optimization process..... | 79 |
| Figure 5.2: Effects plot for grey relational grade | 86 |
| Figure 5.3: Characteristics of the optimized film compared to all experimental data..... | 90 |

| | |
|--|-----|
| Figure 5.4: Glancing incidence XRD spectra of the optimized film. | 92 |
| Figure 5.5: Example of an RBS profile for measuring germanium fraction. | 95 |
| Figure 5.6: GIXRD spectra for the films containing different germanium fractions | 96 |
| Figure 5.7: Influences of germanium fractions..... | 99 |
| Figure 5.8: TEM images for 0.84 and 0.87 of germanium fraction..... | 101 |
| Figure 5.9: Dark-field TEM images with lattice resolution..... | 102 |
| Figure 5.10: Expanded TEM image..... | 103 |
| Figure 5.11: AFM images (400 nm x 400 nm) of poly-SiGe ultrathin films..... | 104 |
| Figure 5.12: Height–height correlation function $H(r)$ | 107 |
| Figure 5.13: SIMS profiles for the measured boron concentrations. | 108 |
| Figure 5.14: GIXRD spectra for the films containing different germanium fractions | 109 |
| Figure 5.15: Dependence of Hall mobility on germanium fraction..... | 111 |
| Figure 5.16: AFM images of poly-SiGe ultrathin films | 112 |
| Figure 5.17: (a) GIXRD spectra (b) grain size and deposition. | 114 |
| Figure 5.18: AFM images of poly-SiGe ultrathin films | 115 |
| Figure 5.19: Nanoindentation curves for a 100 nm thick poly-SiGe film. | 117 |
| Figure 5.20: Hardness versus indentation curves for a 100nm thick poly-SiGe film..... | 118 |
| Figure 5.21: Elastic modulus and hardness variation with germanium fraction..... | 120 |
| Figure 6.1: Stress evolution curves for the films A and B..... | 125 |
| Figure 6.2: Stress-thickness versus thickness evolution for films A and B | 127 |
| Figure 6.3: Average local stresses in the discrete layers for the films A and B.. | 129 |
| Figure 6.4: Resistivity evolution in the films A and B, Hall mobility | 134 |
| Figure 6.5: GIXRD spectra for 3, 7, 60 and 100 nm thick poly-SiGe films..... | 135 |

| | |
|---|-----|
| Figure 6.6: Morphological evolution as revealed by the AFM images.. | 136 |
| Figure 6.7: 3 distinct features in the PSD curves | 138 |
| Figure 6.8: Cross-sectional line profiles of the surface structures | 139 |
| Figure 6.9: Root-mean-square (<i>rms</i>) roughness of the films. | 144 |
| Figure 6.10: Correlation length as a function of the deposition time. | 146 |
| Figure 7.1: The layout of imec's newly designed NEMS mask | 149 |
| Figure 7.2: Fabrication sequence of the nanomechanical cantilever. | 151 |
| Figure 7.3: SEM images (a) after oxide etch for anchor definition. | 155 |
| Figure 7.4: A simple flow chart of the operating procedure of Gemetic pad fume | 156 |
| Figure 7.5: Schematic diagram of a released upwardly bending cantilever | 159 |
| Figure 7.6: An alternative method for measuring tip deflection of a cantilever. | 161 |
| Figure 7.7: SEM images of (a) array 1 (b) array 3. | 163 |
| Figure 7.8: Deflection profiles for 3 downward bending cantilevers | 164 |
| Figure 7.9: Arrays of released cantilevers chosen from array no. (a) 1 (b) 2 (c) 3 | 165 |
| Figure 7.10: Top down view of the arrays of released cantilevers | 166 |
| Figure 7.11: Arrays of released cantilevers chosen from array no. (a) 1 (b) 2 (c) 3 | 167 |
| Figure 7.12: Comparison of the strain gradients | 168 |
| Figure 7.13: Arrays of released 60 nm thick cantilevers. | 170 |
| Figure 7.14: Comparison of strain gradients in the 100 nm - and 60 nm thick films. | 171 |
| Figure 7.15: Bow height difference along the scanned lines. | 175 |
| Figure 7.16: Resistivity variation in the optimized and experimental best films | 176 |

LIST OF ABBREVIATIONS

| | | |
|-----------|---|---|
| Poly-SiGe | : | Polycrystalline Silicon Germanium |
| MEMS | : | Micro ElectroMechanical Systems |
| NEMS | : | Nano ElectroMechanical Systems |
| CMOS | : | Complementary Metal Oxide Semiconductor |
| CVD | : | Chemical Vapor Deposition |
| HDP | : | High Density Plasma |
| LPCVD | : | Low Pressure Chemical Vapor Deposition |
| PECVD | : | Plasma Enhanced Chemical Vapor Deposition |
| RBS | : | Rutherford Backscattering |
| SIMS | : | Secondary Ion Mass Spectroscopy |
| SEM | : | Scanning Electron Microscopy |
| TEM | : | Transmission Electron Microscopy |
| VHF | : | Vapor hydrogen Fluoride |
| XRD | : | X-Ray Diffraction |
| AFM | : | Atomic Force Microscopy |
| Q-factor | : | Quality –factor |
| DNA | : | Deoxyribonucleic Acid |
| STM | : | Scanning Tunneling Microscopy |
| PSD | : | Power Spectral Density |

ABSTRACT (ENGLISH)

Full Name : Tesleem Babatunde Asafa
Thesis Title : Development of Ultrathin Polycrystalline Silicon Germanium Films as Structural Layers for Applications in Nanoelectromechanical Systems (NEMS)
Major Field : Mechanical Engineering
Date of Degree : May 2013

In recent years, lots of research efforts have been directed towards miniaturization of devices and components in order to make them portable, compact, more efficient, more sensitive and ultimately consume less power. These reasons, among others, propel the increased research interest in nanoelectromechanical system (NEMS). The impact of NEMS is projected to cut across all aspects of life from automotive systems and communication to medicine and bioengineering.

A part of this dissertation focuses on the optimization of some characteristics of ultrathin (~100 nm) polycrystalline silicon germanium (poly-SiGe) films that are suitable for applications as structural layers for NEMS devices including biosensors, nanoswitches, nanoresonators, etc. Poly-SiGe is selected because it can be deposited at a lower temperature (< 450°C) by chemical vapour deposition technique compared to many other materials. In addition, the intrinsic stresses can be favourably tuned with germanium. For the optimization process, the grey-Taguchi approach was used to deliver an optimal combination of stress (43 MPa), resistivity (1.39 mΩ-cm) and deposition rate (0.34 nm/s) at CMOS (complementary metal oxide semiconductor) compatible deposition temperature of 415°C, silane and germane flow rates of 8 sccm and 180 sccm, respectively. In addition to the optimized recipe, an ‘experimental best’ recipe selected from the Taguchi orthogonal array was further characterized. Among the additional characteristics included those of chemical (boron concentration and germanium fraction), electrical (carrier concentration, Hall mobility and resistivity), and mechanical (surface roughness, elastic modulus and hardness). By using these recipes, detailed experimental studies of evolution of stress, resistivity and surface properties were conducted to

understand how the trend of the local stresses across the film thickness is influenced. It is shown that a large variation in the local stresses is an indication of a strain gradient expected in a free-standing structure.

Based on the ‘experimental best’ and the optimized recipes, series of ~100 nm and ~60 nm thick nanocantilevers were fabricated following the established procedure for surface micromachining. The deflections at the cantilever tips were measured from scanning electron microscopy and atomic force microscopy images for a number of cantilevers of various dimensions (0.3 – 10 μm long and 0.3 – 1 μm wide). The average strain gradients are then calculated to be $-0.083 \pm 0.009 / \mu\text{m}$, $-0.02 \pm 0.004 / \mu\text{m}$ and $-0.20 \pm 0.036 / \mu\text{m}$ for the cantilevers processed with 100 nm thick optimized, 100 nm thick experimental best and 60 nm thick experimental best recipes, respectively. The strain gradient of $-0.02 \pm 0.004 / \mu\text{m}$, which implies a downward tip deflection of ~10 nm for 1 μm long, 0.84 μm wide and 0.1 μm thick cantilever, is considered to be a good structural layer for applications in nanoswitches, nanoresonators, biosensors among others. Evidence from the stress and resistivity maps, for one of the films, shows that the slight variation in the strain gradients can be attributed to the observed stress and resistivity variations.

Finally, based on the concept of surface stresses, a new intrinsic stress model is proposed. The equations that describe the stress evolution at the precoalescence, coalescence and postcoalescence stages of film growth are derived. The models are tested and are found to agree with the experimental results fairly accurately.

ABSTRACT (ARABIC)

ملخص الرسالة

الاسم الكامل : تسليم باباتوندي اسافا

عنوان الرسالة : عنوان الرسالة: تطوير افلام متعدد الكريستالات السليكون الجرمانيوم الرقيق جدا كطبقات إنشائية للتطبيقات الانظمة النانو الكهروميكانيكية (NEMS)

التخصص : الهندسة الميكانيكية

تاريخ الدرجة العلمية : مايو 2013

في السنوات الأخيرة، وجهت الكثير من الجهود البحثية نحو التصغير من الأجهزة والمكونات من أجل جعلها محمولة، مدمجة، أكثر كفاءة، وأكثر حساسية مما يجعلها تستهلك طاقة أقل. هذه الأسباب وغيرها، دفع الى الاهتمام المتزايد في بحوث نانو نظام الكهروميكانيكية (NEMS). ومن المتوقع أن تشمل جميع جوانب الحياة من أنظمة السيارات والاتصالات والطب والهندسة الحيوية.

جزء من هذه الأطروحة يركز على التحسين من بعض الخصائص الافلام الرقيقة جدا بسماكة (~ 100 نانومتر) المكونة من كريستالات السليكون الجرمانيوم (بولي SiGe) والتي يمكن استخدامها كطبقات لبناء أجهزة (NEMS)، بما في ذلك أجهزة الاستشعار، ومفاتيح نانو، نانو مرنانات، الخ. تم اختيار البولي SiGe لامكانية ترسيب في درجة حرارة أقل بالمقارنة مع العديد من المواد الأخرى (> 450°م) بواسطة تقنية ترسيب الأبخرة الكيميائية. إضافة إلى ذلك، فإن الضغوط الجوهرية يمكن ضبطها بشكل إيجابي مع الجرمانيوم. تم استخدام منهج جراي تاجوشى لايجاد المزيج الأمثل من التوتر (MPa43)، المقاومة (1.39 mΩ سم) ومعدل الترسيب (0.34 نانومتر / ثانية) في مكمل معدن أكسيد أشباه الموصلات CMOS، وفي درجة حرارة متوافقة للترسيب (415°م)، و باستخدام معدلات تدفق سيلاني و جيرمن (SCCM 8) (SCCM180)، على التوالي. بالإضافة إلى هذه الصفة الأمثل، تم اختيار أفضل وصفة تجريبية من صفيق تاجوشى لمزيد من التوصيف. من بين الخصائص المقاسة الأخرى تشمل المواد الكيميائية (تركيز البورون والجرمانيوم آسر) والكهربائية (تركيز الناقل، قاعة التنقل

والمقاومية)، والميكانيكية (خشونة السطح، ومعامل مرونة وصلابة). باستخدام هذه الوصفات، تم عمل دراسات تجريبية مفصلة لتكون التوتر، المقاومة وخصائص السطح، لفهم كيفية تأثير التوتر المحلي في كافة أنحاء سماكة الفيلم. وتبين أن الاختلاف الكبير في الضغوط المحلية في كافة أنحاء سماكة الفيلم هو مؤشر على التغير في درجة التمدد في الهيكل القائم بذاته.

استنادا إلى أفضل التجارب والوصفة الأمثل، تم تصنيع سلسلة نانو الكابولي (nano cantilever) بسماكة من $100 \sim 60$ نانومتر، و 60 نانومتر، باتباع الإجراءات المعمول بها في قطع الاسطح متناهي الصغر. تم قياس الانحناءات في اطراف نانو الكابولي باستخدام المجهر الإلكتروني والمجهر الذري القوة لعدد من الكابولي لأبعاد مختلفة من $(0,3)$ حتى 10 ميكرون طولي و $0,3-1$ ميكرون عرضي). ثم تم احتساب متوسط التدرجات في التمدد لتكون $0,083 \pm 0,009$ / ميكرون، $0,004 \pm 0,02$ / ميكرون و $0,036 \pm 0,20$ / ميكرون لالكابولي بسماكة 100 نانومتر تمت معالجتها باستخدام الوصفة الأمثل، و بسماكة 100 نانومتر و 60 نانومتر تمت معالجتها باستخدام الوصفة الأفضل تجريبيا ، على التوالي. يعتبر التدرج في التمدد $0,004 \pm 0,02$ / ميكرون، الذي يؤدي الى انحناء طرف الكابولي من الهبوط ~ 10 نانومتر ل 1 ميكرومتر طولي، و $0,84$ ميكرون عرضي وسماكة $0,1$ ميكرومتر ، ليكون طبقة هيكلية جيدة لتطبيقات مفاتيح نانو nano-switches ، و نانو مرينات nano-resonators، و أجهزة الاستشعار وغيرها. الأدلة من توزيع التوتر والمقاومة، لواحد من الأفلام، يدل على أن اختلاف طفيف في تدرجات التمدد يمكن أن يعزى إلى الاختلافات الملحوظ في الإجهاد و المقاومة.

وأخيرا، استنادا إلى مفهوم الضغوط السطحية، تم اقتراح نموذجا جديدا للإجهاد الجوهري. و تم اشتقاق المعادلات التي تصف تطور التوتر في مرحلة ما قبل التحام، والتحام بعد التحام لمراحل نمو الفيلم. كما تم اختبار النماذج ووجدت أنها تتوافق مع النتائج التجريبية بدقة إلى حد ما.

CHAPTER 1

INTRODUCTION

1.1 NEMS: What and Why?

The impacts of microelectromechanical systems (MEMS) are large and wide spanning across all aspects of life from automotive systems and communication to medicine and bioengineering. MEMS products are found in inkjet print heads, miniature mechanical switches, biosensors, data storage system, wireless electronics, fiber optics, fluidic systems, micro fuel cells, accelerometers, gyroscopes, micromirrors, microactuators, and chemical pressure sensors among others [1, 2]. In the 90s, MEMS applications were pronounced in and largely limited to automotive industries. Today, however, MEMS products are moving towards consumer applications with capacity to incorporate intelligence into the human environment [3]. MEMS are controlling our communications networks, and saving lives by inflating automobile air bags [2]. They are traveling through human body to monitor blood pressure and deliver drugs.

Recent estimation of the MEMS market by Yole Développement shows that an estimated 8 billion units of MEMS devices are manufactured globally by 2012 and that the MEMS market is expected to reach \$5.4 billion by 2017 [4]. Based on this market survey, MEMS applications in cell phones, pressure sensors, inertial sensors, RF MEMS switches, oscillators, microdisplays, microspeakers, environmental sensors,

touchscreen and joysticks are expected to significantly influence the market trend in the next few years.

Although MEMS products are expanding, the desire to miniaturize them is proportionally growing as science of micromachining advances. Products with portable and compact components having low mass and low power consumption are desirable. Sensors with high mechanical resonance frequencies (faster response to applied forces), higher quality or Q-factor, and high surface-to-volume ratio are ideal for surface-based sensing mechanisms. These reasons, among others, propel the search for miniaturized devices under the concept of nanoelectromechanical system (NEMS). Indeed, both NEMS and MEMS are electromechanical systems. They involve the combination of mechanical, electrical and sometimes optical, biological or radio frequency components [1]. While MEMS refers to microscopic devices with a characteristic length of less than 1mm but more than 100nm, NEMS devices have a characteristic length of about 100nm or less. One dimension of a typical NEMS structure is smaller than a quantum-dot transistor whereas that of MEMS can be as large as a strand of human hair. Bhushan [5] puts the dimensions of NEMS and MEMS in the right context (see Fig. 1.1). Few examples of NEMS applications include nanoresonators, nanoaccelerometer, a non-volatile NEMS memory, relay and switches with carbon nanotubes among others [6].

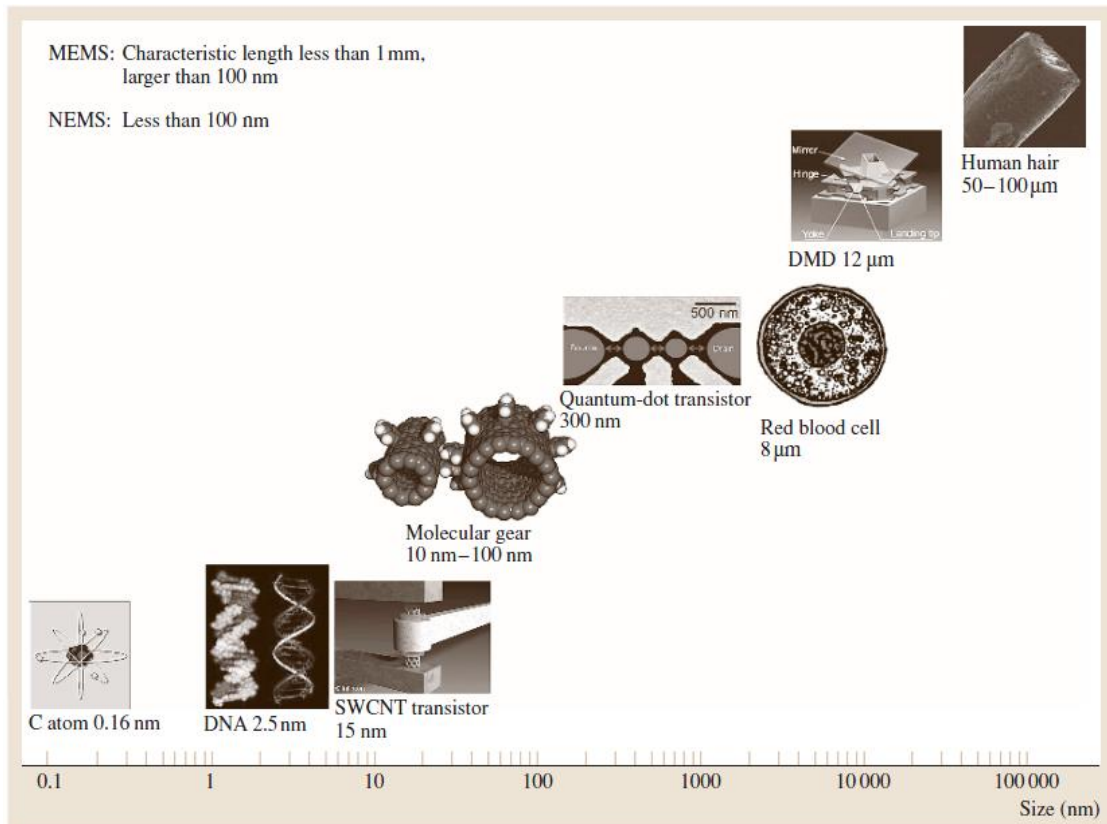


Figure 1.1: Dimensions of MEMS and NEMS devices in perspective. Examples of MEMS/NEMS structures: a vertical single walled carbon nanotube (SWCNT), transistor (5nm wide and 15nm high), a carbon-nanotube-based gear, quantum-dot transistor, and digital micromirror device (DMD). At the extreme of these devices are a carbon (C) atom of 0.16nm radius and human hair of about 50-100 μm thick [5].

NEMS devices are produced by micromachining using a top-down or a bottom-up approach [7]. The bottom-up approach may be by chemical self-assembly, chemical vapour deposition or hot plate techniques while the top-down approach may involve metallic thin films or etched semiconductor layers that are produced with the help of etching, scanning probe tools or with nanolithography methods. The spontaneous rise in the applications of NEMS is credited to the continuous improvement in the science and

technology of these fabrication techniques. This technology enables fabrication of large arrays of devices, which individually perform simple tasks, but in combination can accomplish complicated functions. NEMS are increasingly applied in biosensing, DNA molecule detection, mass measurement (mass spectroscopy) and as microcantilevers with integrated sharp nanotips for STM and AFM [6]. Out of these applications, the use of nanocantilevers or nanoresonators for chemical, biological or medical applications has been the focus of many research groups. Good review articles on nanoresonators and biosensors have been published recently [8, 9].

With a particular reference to sensing applications, several experimental and simulation studies have shown that by reducing the size of structural layers, the sensitivity of a device can be enhanced significantly [9]. Recently, Chaste et al. [10] realized a chemical sensor of 1.7 yg (1.7×10^{-24} g) sensitivity by using 150 nm long, 1.5 nm diameter carbon nanotube resonators (the best reported sensitivity for nanotube based sensor so far). Hitherto, the best mass resolution achieved in the past for carbon nanotube resonators was about 200 yg [11]. For microfabricated resonators made from poly-Si film, a measured sensitivity of 7000 yg was already achieved [12]. For non-carbon nanotube based resonators (mostly silicon based), various lengths (3 μm – 3 mm), geometries (rectangular, triangular, single layer, composite, step-discontinuity, arrays), actuator/sensing methods (active piezoelectric, electric, magnetic, active magnetoresistive, optical, impedance, thermal noise, etc), mode types (transverse, torsional) and measurement media (air, liquid, vacuum) have been explored to improve sensitivity [8].

Recently, Witvrouw [13] conducted wide range simulations on how the sensitivity of poly-SiGe resonator is influenced by scaling the resonator size. Table 1.1 shows that by scaling down SiGe resonator from a dimension of $4 \times 300 \times 10 \mu\text{m}^3$ to $1 \times 0.1 \times 0.1 \mu\text{m}^3$, as small as 112 molecules can be measured instead of 4×10^7 molecules for the bigger dimension. Mass of 112 molecules is equivalent to 3 ag (3×10^{-18} g) or 1 aM of measurable concentration. This indicates that the detection sensitivity can be enhanced significantly by miniaturizing the resonator. In addition to the short lengths of the nanoresonators, other conditions such as low noise, cryogenic temperature and an ultrahigh vacuum environment favour the detection of small masses [10]. With these conditions, the energy dissipation that usually leads to the degradation of the resonance quality factor, and thus a mass sensitivity reduction, is reduced, making it possible to detect a mass change as small as 1 zg.

For a nanocantilever shown in Fig. 1.2, the measure of energy dissipation or Q-factor is evaluated from the full width at half maximum and the central frequency of the spectrum. The central frequency f_o (so-called resonance frequency) can either be

obtained from resonance measurement or from $f_o = \frac{h}{4\pi L^2} \sqrt{\frac{E}{\rho}}$ where h, L, E and ρ are the

thickness, length, modulus and density of the resonator material, respectively. This equation indicates that the resonance frequency is significantly enhanced by reducing the length of the resonator. By estimation, the resonance frequency prior to and after the

cantilever is loaded, the detectable mass Δm can be calculated from $\Delta m = \frac{k}{4\pi} \left(\frac{1}{f_1^2} - \frac{1}{f_o^2} \right)$

where k is the cantilever stiffness and f_1 is the resonance frequency after loading.

Table 1.1: Expected effect of scaling on sensitivity of SiGe resonators [13]

| Material, size (W x L x H) | M_{eff} | Q in air | ΔM | Equivalent # molecules | Measurable concentration* |
|-------------------------------------|------------------|----------|------------|------------------------|---------------------------|
| SiGe, 4 x 300 x 10 μm^3 | 41 ng | 500 | 1 pg | 4×10^7 | 0.3 pM |
| SiGe, 3 x 100 x 2 μm^3 | 1.5 ng | 6100 | 2.4 fg | 49760 | 1 fM |
| SiGe, 1 x 1 x 0.1 μm^3 | 0.34 pg | 100 | 34 ag | 1272 | 10 aM |
| SiGe, 1 x 0.1 x 0.1 μm^3 | 0.03 pg | 100 | 3 ag | 112 | 1 aM |

* assuming 50nt, 200 μl volume, 10% binding and 1 sensor/ test volume:

NB: 1 pg = 1×10^{-12} g; 1 fg = 1×10^{-15} g; 1 zg = 1×10^{-21} g

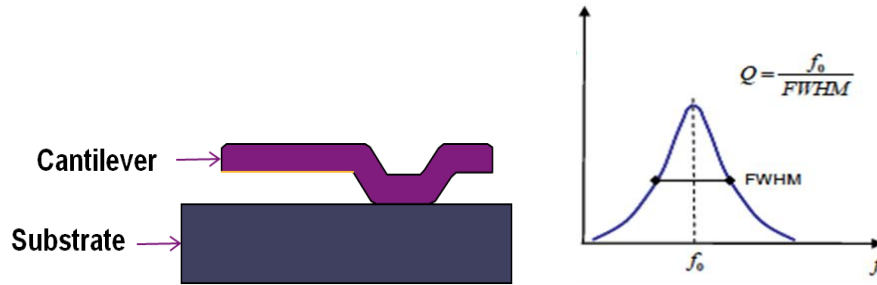


Figure 1.2: (a) A cantilever resonator fabricated on a substrate (b) calculation of quality-factor (Q-) factor. FWHM and f_0 are the full width at half maximum and the center frequency of the spectrum, respectively. The vertical axis represents the energy of the signal.

M/NEMS are driven by CMOS (complementary metal oxide semiconductor) and both components can be made separately and then connected together (hybrid system) or M/NEMS made on top of CMOS (monolithic system or the so-called MEMS-last approach). A survey of the current MEMS market shows that about half of these systems use a hybrid approach where MEMS and controlling CMOS are developed separately

[14]. Since this approach is modular, it has a shorter development time compared to the monolithic approach. In addition, CMOS and MEMS technologies can be independently optimized. However, for those systems where performance and miniaturization are of utmost importance, or when many interconnections are needed between M/NEMS and CMOS, then a monolithic integration approach becomes indispensable. In such an approach, parasitic bond pad size and length are virtually eliminated and assembly and packaging costs are lower [15]. To adopt the MEMS-last approach, it is necessary to use structural materials which can be tuned to a desired property at a temperature that will not damage the CMOS components.

1.2 Why Polycrystalline Silicon Germanium (poly-SiGe)?

Quite a large array of materials has been explored as structural layers, sacrificial layers, contacts or interconnects for M/NEMS and many other applications. The final choice of materials ultimately depends on applications, economy, availability, ease of tuning the material properties, process compatibility, and reliability [15]. Among these materials are single-crystalline silicon (Si), polycrystalline Si (poly-Si), Si_3N_4 , SiO_2 , Vanadium oxides, SiC, metals, shape memory alloy (SMA) metals, piezoelectric materials, diamond, polymers and high-temperature superconductive materials [16]. These materials possess certain unique properties that, when combined with MEMS technology, make them attractive for certain applications. However, most of them suffer a setback when considered for postprocessing in the MEMS-last approach. For examples, metal can creep during operation causing RF switch failures while poly-Si requires a high deposition temperature [17]. In addition, a high annealing temperature of 800°C or higher

is required to achieve a considerable low stress if polycrystalline silicon is to be used as a structural material for surface micromachined MEMS [18]. The requirement of high temperature annealing makes such materials unsuitable for monolithic integration with fabricated driving electronics (CMOS) in the MEMS-last approach.

In contrary, poly-SiGe can be deposited at a lower temperature compared to many other materials especially poly-Si, hence, physical phenomena like grain growth, changes in morphology with annealing, dopant activation and diffusion are expected to be less significant than in poly-Si [17]. Also, poly-SiGe alloys have a high melting temperature ($>900^{\circ}\text{C}$) [19], a high tensile strength ($\sim 1.60\text{GPa}$) and a high creep resistance. By alloying Si with germanium (Ge), the stress can be substantially reduced even at lower fabrication temperatures ($\sim 650^{\circ}\text{C}$ or lower). Improvement in the tensile stress is attributed to a higher crystallinity [20] and also the higher thermal stress associated with a higher germanium fraction (details in chapter 6). In addition, doping poly-SiGe with boron further enhances deposition at significantly lower temperature ($\sim 450^{\circ}\text{C}$) compatible with standard CMOS resulting into low as-deposited stress and low electrical resistivity [21, 22]. Poly-SiGe possesses good piezoresistive properties and can easily be tuned by changing the doping concentration and germanium content [23, 24]. Due to the aforementioned characteristics, the use of poly-SiGe films has been successfully demonstrated in various technological applications including low frequency comb drive devices [25], high frequency resonators [26], bolometers [27], gyroscopes [28], resonator based light sensors [29], data storage devices [30], microcrystalline SiGe micromirrors [31] and pressure sensors [23, 24] among others.

However, Ge content must be maintained at the optimal requirement for the formation of poly-SiGe films because a higher Ge concentration results in less reliable devices. Cases of unstable GeH and Ge oxidation [32], atmospheric corrosion and increased surface roughness have been reported [21]. It is interesting to note that poly-SiGe films can be obtained even at the subnanometer scale and that their properties can be enhanced by an optimization process. It is demonstrated in this thesis that polycrystalline SiGe films with good electrical and structural properties can be obtained at the nanometer scale.

1.3 Objectives of the Dissertation

The overall objective of this dissertation is to develop a robust ~100 nm thick poly-SiGe structural layers with optimized stress, deposition rate and resistivity for applications in nanoelectromechanical devices like biosensors, nanoswitches, resonators and so on.

The specific objectives are:

- Deposition and characterization of ~100 nm thick poly-SiGe films and optimization of the film stress, resistivity and deposition rate,
- Modeling stress evolution for the growth of poly-SiGe films,
- Studying how stress, resistivity and crystallinity evolve and understanding how these properties are influenced by deposition parameters,
- Fabrication of nanocantilevers / doubly clamped beams and calculating their strain gradients.

1.4 Outline of the Dissertation

The arrangement of the contents of this dissertation is described in the following paragraphs. Chapter 1 provides the general introduction to M/NEMS and discusses why miniaturization is not only important but also critical. It encompasses the basic motivations for this work which are about miniaturization of sensors and actuators vis-à-vis fabrication at nanometer scale. Chapter 1 also briefly addresses why poly-SiGe is selected in spite of myriads of materials that are currently available. It also includes the thesis objectives. Chapter 2 presents the reviews of the literature that are most relevant to this study. It examines the various materials that are currently available for M/NEM applications. Then, a brief history of poly-SiGe research for MEMS applications is discussed. Herein, various developments between 2010 and 2013 are given more attention and appropriate references are provided. Finally, a brief review of thin film growth models is provided.

Chapter 3 examines the detailed experimental procedure designed to achieve the stated objectives. It discusses the deposition technique, the characterization methods and the experimental design. The Applied Materials Centura LPCVD tool is briefly discussed and characterization techniques such as SEM, AFM, XRD, RBS, TEM, SIMS, stress measurement, 4-point probe, Hall measurement and nanoindentation are discussed. In chapter 4, an improved surface stress based approach toward modeling intrinsic stresses in thin films is proposed. It offers an alternative approach to other stress models currently available in the literature. The approach is based on the concept of surface stresses where dome-shaped islands and hexagonal shaped grains are used. The models results are

compared with experimental studies of stress evolution in copper and silver films. Finally, surface stresses and stresses due to grain boundary formation are obtained for poly-SiGe films.

Chapter 5 is divided into 2 parts. The first part is a report of the procedure for the simultaneous optimization of stress, resistivity and deposition rate for LPCVD deposited ultrathin (100 ± 5 nm) poly-SiGe films by using the grey-Taguchi approach. The second part discusses how germanium fraction, boron concentration and chamber pressure influence the stress, deposition rate, resistivity, grain size, Hall mobility, carrier concentration and surface properties of ultrathin poly-SiGe films. Evidences for the film behaviour are supported by TEM images. In chapter 6, studies of evolution of stress, resistivity and surface properties of poly-SiGe films are reported. The different behaviour at the postcoalescence state for 2 selected recipes is examined. The resistivity behaviour is discussed in term of the Hall mobility, carrier concentration and grain size. A one-dimensional power spectral density (PSD) analysis is used to evaluate the thickness dependent surface properties.

The fabrication procedure for nanocantilevers and the techniques for measuring the strain gradient are presented in chapter 7. The procedure is also applicable for fabricating other nanostructures such as doubly clamped beams, logic, cup and lump mass structures. Nanocantilevers of two different thicknesses (100nm and 60nm) are processed following the established surface micromachining route. The cantilevers' tip deflections are measured from SEM and AFM images from where the strain gradients are obtained. Finally chapter 8 provides the conclusions as well as the recommendations for further study.

CHAPTER 2

LITERATURE REVIEW

2.1 Materials for MEMS / NEMS

The wide range of existing M/NEMS devices is due to a huge number of materials currently available. In general, materials used for M/NEMS can be categorized into four groups: (i) metals such as Ag, Al, Au, Ni, Cr, Cu, etc., (ii) nonmetals like Si (either single-crystalline or polycrystalline), Ge, GaAs, SiGe, etc., (iii) polymers like polyimides, SU8, polydimethylsiloxane (PDMS), etc., and (iv) ceramics such as diamond, Si_3N_4 , SiO_2 , SiC, etc. [33]. All these materials possess certain unique properties that, when combined with MEMS technology, make them attractive for certain applications. Notwithstanding, the final choice of materials ultimately depends strongly on the applications, cost, availability, environments, and reliability [15]. For a material to be used as M/NEMS structural layer, it must have low stress/strain gradient or practically low tensile stress with the upper layers more tensile than the bottom ones to avoid bending towards the substrate which may result into stiction [17]. In addition, such a material must have good mechanical, electrical, magnetic, piezoresistive or piezoelectric properties depending on the applications. As an example, for MEMS resonators and gyroscopes, materials for the structural layers must have high elastic moduli, small dimensions, low resistivities and low densities to maximize the natural frequency and

quality factor. For microheaters and thermal actuators, the structural materials must have high thermal conductivity and low thermal expansion to minimize thermal distortion. However, to obtain good performances for RF-MEMS switches, low pull-in voltage, low RF-loss, and low thermal residual stress are desired. In a past study, aluminum has been shown to be the most suitable material for use as a bridge material in RF-MEMS switches because it provides the best performance based on the above requirements [34]. It is however found that the application environment may change the selection criteria [35]. For BioM/NEMS applications, materials for the structural layers must essentially be biocompatible, chemically modifiable, and easy to fabricate. The following subsections briefly review the categories of materials for M/NEMS applications.

2.1.1 Metals

Metals like Ti, Ag, Al, Au, Ni, Cr and Cu, among others, are commonly used as MEMS structural materials or interconnect for a wide variety of applications. This is often due to their high electrical conductivity, ferromagnetic properties, optical reflectivity, hardness, low electrical noise, low deposition temperature, and relatively simple deposition techniques [17]. Although, metals do not have some of the advantages displayed by silicon in terms of mechanical properties, when used within their limitations, metals can exhibit very high degrees of reliability. Metals such as Al, Cu and Au are considered as excellent materials for RF-MEMS [35]. However, Al and Cu are very sensitive to oxygen and humidity and thus can form metal oxides making them unsuitable for applications in humid environment. Au, on the other hand, is chemically inert (noble metal) and less sensitive to thermal fluctuations due to a lower thermal expansion coefficient compared to Al and Cu [36]. Titanium, platinum and gold are good

materials for BioMEMS applications because they are biocompatible and corrosion resistant [37]. Platinum has been considered as a good candidate for applications in infrared detection due to its relatively high temperature coefficient of resistance [17].

Nickel is used in MEMS applications such as gas sensors, hearing aids, microfluidic devices, and microlenses [17]. Its good optical properties enable the realization of smooth mirrors used in optical applications. In addition, its magnetic properties make it a suitable medium for magnetic recording or as magnetoresistive heads [17]. By alloying nickel with iron (nickel ferrite) or with phthalocyanine (NiPc), chlorine or nitrogen oxide gas sensors can be made [38]. Also, titanium and nickel have been combined to actuate micropumps by using the shape memory effect [39].

2.1.2 Nonmetals

Among the most useful nonmetals for M/NEMS applications are Si, Ge and III-IV compounds such as SiGe, GeAs, InP, etc. Out of these, silicon has been extensively studied and documented because it is the fundamental material for microelectronic industries [1]. Si is suitable for electronic, mechanical, thermal, and optical integration. It has tensile yield strength of 7GPa. It is hard, brittle and deforms elastically up to a temperature of 500°C. Its properties are independent of doping and can be single crystalline, polycrystalline or amorphous depending on the deposition conditions [1, 33]. Polycrystalline silicon (poly-Si) has been widely used to conduct electrical signals for actuating or sensing [17]. Indeed, poly-Si is the most commonly used structural material in surface micromachined devices. It is a suitable material for elastic suspensions as well as for resonator applications such as sensing and RF communication. Because silicon

exhibits relatively low energy dissipation, it resonates with high Q-values. It is suitable for fabricating cantilevers at micro- and nanoscales using semiconductor fabrication processes and it forms the major material for BioM/NEMS application [8]. Silicon resonators with mechanical quality factors as high as 80,000 have been reported [17]. Other widely known applications include accelerometers, actuators, microphones and pressure sensors [1]. Amorphous silicon can be used as sacrificial layer or mask layer for dry or wet etching in MEMS technology [40].

Gallium Arsenide (GaAs) is a compound semiconductor with equal number of Ga and As atoms. It is an excellent material for photoelectronics because of its high electron mobility ($0.857 \text{ m}^2/\text{Vs}$) which is 7 times more than that of silicon [41]. It can provide the best solutions for micro-optoelectronic applications with a number of material-related and technological advantages over silicon [42]. GaAs has been demonstrated as a base material for MEMS waveguide switches [43], accelerometers and tunable optoelectronic devices [44], a low-k RF MEMS capacitive switches and suspended microheater arrays among others [45]. Other III-IV compound semiconductors such as SiGe (which will be discussed in details later) and InP have been widely applied.

2.1.3 Ceramics

Ceramics are inorganic, nonmetallic solids like SiC, Si_3N_4 , SiO_2 , etc. They are used as either sacrificial or structural layer for M/NEMS applications. SiC has attractive properties such as good mechanical strength, high thermal conductivity, ability to operate at high temperatures and its extreme chemical inertness in several liquid electrolytes [46]. SiC has been demonstrated for the manufacture of low cost MEMS pressure sensors

utilizing membrane microcontact capable of operating in harsh environments with corrosive media and temperatures up to 900°C [47]. In combination with carbon, 3C silicon carbide (3C-SiC) folded-beam microelectromechanical resonator was recently fabricated and characterized [48].

Silicon nitride (Si_3N_4) has a strong resistance to oxidation in many etchants making it a superior material for masks in deep etching. Also, it possesses a high strength electric insulation making it suitable as a non-conducting structural material. Silicon oxide is often used as a sacrificial layer in micromachining processes to allow the release of moving or deforming mechanical elements [33].

2.1.4 Polymers

Polymer materials such as elastomers, plastics and fibers are made up of long chains of organic (hydrocarbon) molecules. These materials are being actively used for biomedical applications and adhesive bonding [49]. Polymer materials provide many advantages in terms of cost, mechanical properties, and ease of processing. Elastomers, for example, can sustain greater degree of deformation. For applications where the MEMS devices are in direct contact with the elements, such as smart skins for tactile and flow sensing, the use of a robust material is crucial [50]. Photoresist polymers like SU8 epoxy are used to produce masks for creating desired patterns on substrates by photolithography technique. Ferroelectric polymers can be used as the source of actuation in micro devices such as in micro pumping. Polymers with unique characteristics are used as coating substance for capillary tubes to facilitate effective electro-osmotic flow in microfluidics [50]. Thin polymer films are used as electric insulators in micro devices,

and as dielectric substance in micro capacitors. They are widely used for electromagnetic interference and radio frequency interference shielding in microsystems. Polymers are used for encapsulation of micro sensors and the packaging of other microsystems [49].

2.2 Brief History of Poly-SiGe Research for MEMS Applications

Since the first germanium point-contact transistor was invented in 1947 at the Bells Laboratory, growth of microelectronics and microdevices has been on the rise. The piezoresistive effect in Si and Ge was discovered in 1954 [51] and subsequently led to the development of pressure sensors, accelerometers and strain gauges [1]. The growth of a high quality SiGe film on a silicon substrate by molecular beam epitaxy was first successfully demonstrated in 1975 [52]. Further works aimed at improving the growth procedures as well as the film quality were the focus of the researchers at IBM and Bell Laboratory using both MBE and CVD deposition methods. While the properties of poly-SiGe are similar to those of poly-Si, the growing interest in the former is largely attributed to its low thermal budget which is compatible with MEMS-on-CMOS integration [53]. Initial work on SiGe as a MEMS material was pioneered by researchers at the University of California (Berkeley). Further development was reported by the MEMS research groups at Interuniversities Microelectronic Center (imec) Belgium, UC Berkeley and elsewhere. A detailed discussion of SiGe MEMS research for the past few decades up till 1996 was reviewed by Sedky [17] which was further extended up till 2010/2011 in the Ph.D. dissertation of Claes [54]. In both sources [17, 54], the important properties of poly-SiGe films, especially lower deposition temperature as compared to poly-Si, were emphasized as the driving force for the rapid growth in the SiGe films for

MEMS applications. An attempt is made in the following paragraphs to summarize further studies and development of SiGe based M/NEMS in the last 2 years.

After the classical work of Lin et al. [55], several studies were conducted to lower the deposition temperature of poly-SiGe films from $> 550^{\circ}\text{C}$ in order to enable MEMS-CMOS integration. However, because MEMS-CMOS integration was not the initial target (indeed MEMS first was the approach then), earlier patents on SiGe MEMS were such that the SiGe structural layers were deposited by LPCVD at much higher temperature (650°C) [56, 57]. Bhave et al. [58] were able to reduce the deposition temperature of $1\text{-}3\mu\text{m}$ thick SiGe to 425°C using LPCVD and in-situ boron doping followed by thermal annealing at 600°C . In their work [58], they developed an RF resonator and improved its Q-factor from 20 - 30 k to 40 - 44 k. A detailed study of the influence of doping concentration and germanium content on the piezoresistivity, the resistivity and the temperature coefficient of resistance for CVD SiGe films deposited at 450°C was reported in 2010 [23]. In a similar study, Guo et al. [59] were able to identify a process window that gives maximum crystallinity, minimum resistivity variation, and slightly tensile stress based on the electrode spacing and pressure. To achieve this, they used PECVD to deposit $1.6\mu\text{m}$ thick poly-SiGe on 400 nm thick CVD poly-SiGe films at a constant temperature of 450°C but varying silane and germane flow rates as well as pressure and spacing. More recently, a post deposition laser annealing technique was used to realize functional capacitive test structures and capacitive switches [60]. In that study, selective laser annealing was used to crystallize 280 nm thick PECVD amorphous silicon (a-SiGe) films deposited at 210°C . By using 40 mJ/cm^2 of laser energy density (in

air and in reduced pressure), a contact resistivity of $5.0 \times 10^{-7} \Omega \text{ cm}^2$ and strain gradient of $-1.6 \times 10^{-6} / \mu\text{m}$ was realized.

A number of areas of MEMS technology such as packaging, failure due to electrostatic discharge (ESD) and outgassing are currently receiving attention. A proper packaging technology enables device reliability and prolongs the lifetime. The Ph.D. thesis of Claes [54] is about the development of a thin-film wafer level packaging process for poly-SiGe thin films. Successful attempts were made to develop MEMS structures with a higher and robust intrinsic electrostatic discharge (ESD) protection, which can reduce breakdown mechanisms and failure due to ESD [61] for capacitive based devices. This was achieved by smart design and process variation in which the mechanical stiffness (and thus the pull-in voltage) and gap spacing as well as the thickness of the dielectric are improved, raising voltage at failure level to a point greater than 500V. Although this approach reduces failure due to ESD, it is possible that such devices experience functionality degradation due to higher pull-in voltages and lower sensitivity to small voltages due to enhanced stiffness [61]. A compromise is therefore essential.

Outgassing is one of the biggest concerns for the thin film vacuum packaging. Since some gas molecules, like hydrogen, may be incorporated inside the thin films during the deposition process and packaging materials may outgas under certain conditions [62]. When outgassing happens, the freed gas enters the thin film package and the needed vacuum is lost. Outgassing due to device and packaging materials in MEMS technology can substantially reduce the sensitivity (or Q factor) of these devices due to increased pressure as they are expected to operate under vacuum. Wang et al. [63] show, by using thermal desorption spectroscopy (TDS), that as-deposited SiGe can outgas large

quantities of hydrogen, water vapour and CO₂ and that the quantity of CO₂ outgassing correlates with the quantity of CF₄ plasma used for the interface cleaning during PECVD SiGe deposition. While several approaches, such as sputter-deposited AlCu, sub-atmospheric pressure chemical vapour deposited SiO₂ have been suggested to seal SiGe surface micromachined cavities from the external gas penetration [64], the internal outgassing can be reduced substantially by annealing.

Some efforts have been made to raise the sensitivity for sensors fabricated on CMOS. Gonzalez et al. [65] fabricated and characterized poly-SiGe-based piezoresistive pressure sensors on Cu-backend CMOS using PECVD SiGe fabricated at a maximum temperature of 455 °C. A sensitivity of ~2.5 mV/V/bar was reported and, when operated with amplifier, the sensor exhibits sensitivity which is 64 times greater than a similar stand-alone sensor. No significant deterioration of the CMOS circuit after MEMS postprocessing was reported for this sensor. Prior to this, capacitive pressure sensors fabricated from 3.2 μm thick SiGe (deposited by combined CVD and PECVD) at a maximum temperature of 455°C and characterized to have a sensitivity of up to 73 fF/bar was reported [24]. Similarly, capacitive micromachined ultrasound transducers that were able to survive a normalized transmission pressure of 580 kPa at a DC voltage of 340 V and a break down voltage above 500 V were demonstrated [66]. The structural layers were made from 1.6 μm thick PECVD SiGe while the bottom electrodes were made from 400nm thick CVD SiGe. Also, Rochus et al. [67] shows that highly sensitive MEMS-based Xylophone Bar Magnetometers can be made from poly-SiGe films. Their design strategy targets the maximization of the Q-factor in a wide temperature range for

monolithic above-CMOS integration and packaging schemes. It is clear from the above that most structural layers are fabricated from poly-SiGe films of micrometer thickness.

2.3 Resistivity and Surface Properties of Poly-SiGe Films

The performance of poly-SiGe based M/NEMS devices is influenced by the electrical (such as the resistivity, crystallinity and Hall mobility) and mechanical properties (like the stress, the strain gradient and the elastic modulus). Since these properties are intertwined, they are significantly influenced by the crystallinity and surface roughness of the films. Knowledge of the dependence of the electrical resistivity on the dimensions of SiGe thin films is necessary due to the need for miniaturization. For example, in nanoswitches a good electrical contact is necessary between the thin structural layer and the electrode. For a specific application, the mechanical and electrical properties can be modulated by appropriately tuning the deposition parameters such as substrate temperature, germane flow rate, the chamber pressure and diborane flow rate among others.

A few studies reported how deposition parameters influence the texture and crystallinity of poly-SiGe films [20, 68-69]. These studies, and many others, show that (111), (220) and (311) planes are the 3 significant diffraction planes in ultrathin poly-SiGe films [55, 68-69, 70-71]. This indicates that a SiGe film can be textured if the grains grow predominantly along a particular plane. Such a plane is favoured with a minimal total free energy (surface or strain energy) which is the main driving force for grain growth [72]. The change in the texture is largely dependent on several conditions such as

growth rate, film thickness, substrate materials and orientation, nature of precursors, doping, and surface properties [55]. It was observed that, by incorporating more germanium in poly-SiGe CVD-grown films, intensities of (111) and (311) planes are enhanced at the expense of (220) planes [55]. For films deposited by PECVD, increased Ge concentration enhances intensities of (220) and (311) peaks [59, 68]. While the intensities ratio of the diffraction peaks have been extensively used to determine the texture of SiGe films, a careful comparison of the diffraction intensities with the relative intensities of randomly oriented powder samples of SiGe shows that the large (111) peaks that usually appear in most XRD measurements might not represent the dominant orientation [73]. Therefore, appropriate approach must be used to characterize the dependence of grain orientation on deposition conditions.

Aside crystallinity, the influence of surface morphology on the behaviour of thin films is of great interest for many applications in microelectronics, optics and micromechanics. For example, the electrical conductivity of thin films depends very much on surface and interface roughness, and the reliability of a Silicon MOSFET (metal-oxide-semiconductor field effect transistor) channel depends on the roughness of the gate oxide [74]. The surface morphology depends on the microscopic growth dynamics which is strongly influenced by the deposition conditions. Precise control of the morphology and the surface structure is necessary towards production of the desired film quality for specific applications.

To characterize the film morphology, techniques such as scanning electron microscopy (SEM) and atomic force microscopy (AFM) are often used. While these tools provide an estimate of the grain/crystallite size from the surface structure, only AFM is

suitable for an accurate determination of surface roughness. Although, a few parameters such as root mean square roughness (rms) [75] and skewness (a measure of the asymmetry of the probability of roughness distribution) quantify a surface, the surface description by these parameters is often insufficient because they give information on the height variation only and not on the lateral distribution of the surface features [76]. To quantify both the height distribution (rms roughness) and the lateral distribution and also the fractal dimension, a power spectral density (PSD) analysis is a viable tool. PSD provides valuable information on spatial frequencies of the height distribution and can be related to more fundamental physical quantities (such as the correlation length, fractal dimension and rms surface roughness) that can be measured independently. The PSD is calculated from the square magnitude of the coefficients of 1-D or 2-D Fourier transform of a digitized surface profile.

In most cases, since CVD deposited films are self-affine [77, 78], their surfaces can be described by the parameter of the roughness exponent α , together with the evolutions of the root-mean-square (rms) of the surface roughness σ , the autocorrelation length ξ , the rms local slope ρ and the fractal dimension D_f [79 – 82]. A few studies reported surface properties and resistivity evolution of SiGe films [77, 78]. However, a detailed study of the influence of deposition parameters on the surface properties of poly-SiGe film as well as the resistivity and morphological roughness evolution are missing. Because the morphological roughness due to island/grain coalescence can substantially influence the electrical and optical properties of thin films, an in-depth understanding of the behaviour becomes important.

2.4 Thin Film Stress Models

One of the critical requirements for the successful application of thin films, including poly-SiGe, is the ability to control and reproduce the results of the manufacturing processes. Consequently, understanding the effects of the growth conditions and materials properties on the resulting residual stresses is necessary to fabricate low stress thin films [83]. Irrespective of the film fabrication method, the resulting structural layers usually exist under a state of internal stress [84 – 89] which might be detrimental to the functionality and structural integrity of the final devices [90, 91]. For example, the dynamic and reliability characteristics of these layers can be altered due to the changes in the structural stiffness [92, 93]. Therefore, an accurate mathematical modeling and estimation of the magnitude of induced stress has been the subject of many publications.

Thin film stresses may develop due to thermal fluctuation or originate from intrinsic or extrinsic sources or a combination thereof [85, 88, 90-91, 94]. The intrinsic stress depends on the film microstructure, which can be controlled by the growth conditions and selection of appropriate materials [93]. The intrinsic stress evolution at precoalescence and postcoalescence stages depends on whether a material exhibits type I or type II behaviour [93 – 96]. Type I behaviour is observed in metals with high atomic mobility and high surface and grain boundary diffusivities like Au, Ag, and Cu (Fig. 2.1). In these metals, stresses evolve from compressive state during precoalescence through a coalescence tensile stress state which finally decrease and eventually become compressive at postcoalescence. However, metals with low atomic mobilities and low surface and grain boundary diffusivities exhibit type II behaviour where stresses remain

tensile after coalescence. Examples of these metals are Ti, W, Cr, Ni, and Fe. At high temperatures low mobility materials behave much like the high mobility materials because of enhanced diffusivity [97].

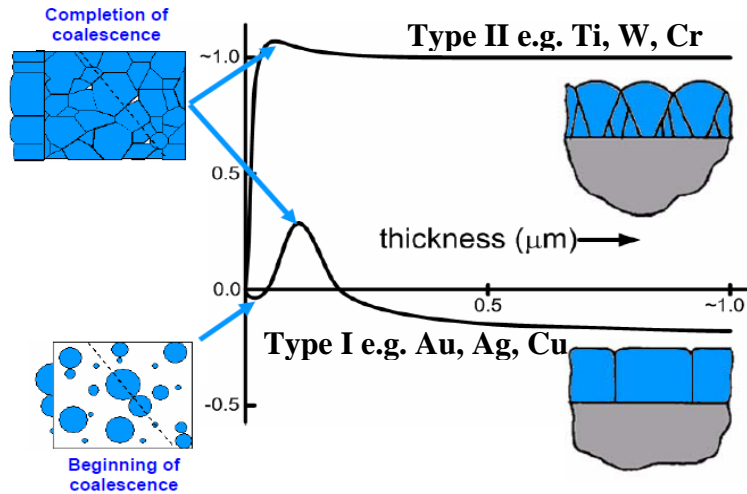


Figure 2.1: Stress-structure evolution during film growth [96]. The vertical axis is residual stress measured in GPa.

Irrespective of the stress behaviour, the resulting stress evolution is a product of dynamic competition between the mechanisms of stress generation and those of relaxation [89]. Among the mechanisms of stress build-up are island/grain growth and crystallization [98], capillary-induced growth stress, island coalescence (zipping) [99], surface stress [100], interstitial incorporation and film-substrate reaction among others. Stress relaxation mechanisms may take the form of interfacial shear, viscous flow, morphology change (rearrangement), diffusion of atoms into the grain boundary [101], dislocation emission and annihilation of excess vacancies [99]. Each stress evolution is often accompanied by relaxation though growth interruption has been found not to affect

stress behaviour because the original trend is recovered when deposition resumes as if no interruption was made [89]. In addition, a few studies are based on numerical modeling and are quite significant towards understanding the theory of stress evolution [83, 102]. Experimentally, stresses in thin films can be measured by various techniques including (synchrotron) X-ray diffraction, reflection high energy electron diffraction (RHEED), Raman spectroscopy, substrate curvature, acoustic resonance and the use of multi-beam optical stress sensors among others [93]. Curvature measurement is an alternative method commonly used to determine thin film stresses [103]. Laser deflectometry and capacitive coupling are available techniques for measuring wafer bending. Laser deflectometry allows the sample curvature to be measured when the reflected laser beam from the sample is correlated to its curvature change.

2.4.1 Precoalescence Stress Models

Many mathematical models have been developed to estimate intrinsic stresses in thin solid films based on the three stages observed for type I behaviour. The two relevant models for the precoalescence stage are those of Laugier [104] and Cammarata et al. [100]. While the approach used by the former is based on the changes in the lattice constant, that of the latter relies on surface stresses. Cammarata et al. [100] modeled a growing island as a cylinder and then used the Laplace pressure-stress relation to construct a mathematical model to estimate the induced stresses. The resulting stress σ is given by:

$$\sigma = (f_f + f_i) \left(\frac{1}{h} - \frac{1}{h_o} \right) + 2\beta f_h \left(\frac{1}{d} - \frac{1}{d_o} \right) \quad (2.1)$$

Where f_t , f_b , and f_c are the top, the bottom and the curved surface stresses of the island respectively, h_o and d_o are the critical thickness and diameter, respectively at which the island is firmly attached to the substrate and h and d are the thickness and diameter, respectively before coalescence. β is a material dependent property which is given as $\beta = (1-3\nu)/(1-\nu)$ for an elastic isotropic material where ν is the Poisson's ratio. For elastic anisotropic materials, the values of β for some materials are published in Ref.[100] .

More recently, Guisbiers et al. [105] presented a model of intrinsic residual stress (Eq. 2.9) based on the size-dependent phase transitions of e-beam evaporated thin films. They consider the stress generated due to the volume change due to a liquid-solid phase transition. However, the model is only valid for the precoalescence stage and does not take other stages into consideration. It is therefore expected not to match accurately with experimental observation.

$$\sigma_{Guisbiers\ et\ al} = \frac{E_f}{1-\nu_f} \alpha_f (T_m - T_{substrate}) \exp\left(-\frac{E_f t}{\eta_f}\right) \quad (2.2)$$

α_f is the thermal expansion coefficient of the deposited material (1/K), $T_{substrate}$ is the substrate temperature, η_f is the dynamic viscosity of the deposited material (Pa. s) and T_m is the melting temperature (K) of the nanograins constituting the film calculated from $T_m = (1-\alpha_{shape}/2L)T_{m,\infty}$, α_{shape} represents the size and shape effects on the bulk melting temperature $T_{m,\infty}$ and L is the characteristic length size of the nanograin and t is the relaxation time. Though the model overestimates the intrinsic stress, it however predicts a correct trend of intrinsic stresses.

2.4.2 Coalescence and Postcoalescence Stress Models

A few mathematical models describe the process of stress generation during the coalescence growth based on the general assumption that the driving force for islands coalescence is the reduction in the surface energy when a grain boundary is formed from neighboring islands [106 -110]. One of the earliest models was that of Hoffman [106] who theorized that neighbouring crystallites are strained in tension and spontaneously snap together to form a grain boundary when the gap between the adjacent islands reaches a critical value 'd' (see Fig. 2.2). The resulting tensile stress is

$$\sigma_{gb} = \frac{E_s}{1-\nu_s} \frac{d}{2r} \quad (2.3)$$

where r , E_s and ν_s are the radius of the grain, the elastic modulus and Poisson's ratio for the substrate, respectively.

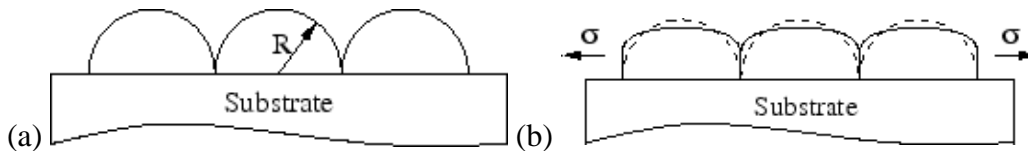


Figure 2.2: Principle of coalescence - structure of the grain island (a) before (b) after coalescence.

An obvious challenge in this model lies in the estimation of parameter d . To circumvent this challenge, Nix and Clemens [97] came up with two models using the surface energy-driven approach similar to the Griffith principle of crack propagation [108]. The first version is based on the elastic deformation of hexagonal grains which produced an upper bound stress given by:

$$\langle \sigma \rangle = \sqrt{\frac{2\gamma_s - \gamma_{gb}}{r} \frac{E}{1-\nu_s}} \quad (2.4)$$

where γ_s and γ_{gb} are free surface and grain boundary energy per unit area, respectively. In the second approach, it was assumed that elliptical arrays coalesced to form arrays of cycloidal shape. The average induced stress is given by Eq. (2.5).

$$\langle \sigma \rangle = \sqrt{\frac{(2\gamma_s - \gamma_{gb}) E(1+\nu_s)}{r(1-\nu_s)}} \quad (2.5)$$

Because the above models overestimate the induced stresses, Freund and Chason [109] used a rigorous theory of contact of elastic solids with cohesion to arrive at a modulus independent stress for a regular square array of hemispherical islands. This expression is given as:

$$\langle \sigma \rangle = \frac{2(2\gamma_s - \gamma_{gb})}{r} \quad (2.6)$$

Seel et. al. [102] considered a mechanism where islands are gradually zipped when the zipping process is energetically favourable. They obtained an upper stress limit given by Eq. (2.7).

$$\langle \sigma \rangle = \sqrt{\frac{(2\gamma_s - \gamma_{gb}) E}{r(1-\nu_s^2)}} \quad (2.7)$$

Cammarata and his coworkers explored the concept of surface energy reduction due to coalescence to model islands zipping process. The reduction in surface stress is estimated from $\frac{f_{gb}}{2} - f_h$ where f_{gb} is the interfacial stress associated with the grain boundary. By

adding the precoalescence, coalescence and postcoalescence stresses, it was shown that the final stress generated in a metallic thin film of type I behaviour can be computed from [100]:

$$\sigma = (f_f + f_i) \left(\frac{1}{h} - \frac{1}{h_o} \right) + \beta \left(\frac{f_{gb}}{d} - \frac{2f_h}{d_o} \right) \quad (2.8)$$

It should be noted that only the model of Cammarata et al. addresses both the mechanisms of precoalescence and postcoalescence stress behaviours. All other models consider only the coalescence stress generation. Even if only coalescence stress is considered, the above models generally overestimate the stresses in thin films.

CHAPTER 3

EXPERIMENTAL METHODS

This chapter presents the deposition technique, the characterization methods and the experimental designs for poly-SiGe films. All the films were deposited in a PolyGen chamber of an Applied Materials Centura low pressure chemical vapour deposition (LPCVD) tool. The films were characterized by scanning electron microscopy (SEM), atomic force microscopy (AFM), x-ray diffraction (XRD), Rutherford backscattering spectroscopy (RBS), stress measurements, 4-point probe, Hall Effect measurement, and surface profilometry among others. Because a few numbers of experiments are included in this dissertation, the experiments are divided into four major categories. The first category is about the Grey-Taguchi optimization technique. In this case, experiments were designed based on L32 orthogonal array and the analyses were made following the optimization technique of the grey relational analysis. Details are discussed in chapter 5.

The second category involved parametric studies based on the optimized recipe where some of the most influential deposition parameters were varied. This helps to understand how deposition parameters and chemical compositions influence the film properties such as stress, resistivity, crystallinity, Hall mobility, carrier concentration, grain size, elastic modulus, hardness and surface properties (such as roughness). The third category is about the studies of stress, resistivity and surface properties evolution. The evolution study was done by depositing poly-SiGe of thicknesses ranging from ~1 nm to 200 nm on separate wafers while their properties were characterized *ex-situ*. The

last category of the experimental study is that of strain gradient measurements. About 100nm and 60nm thick Poly-SiGe films were deposited on 200mm diameter Si(100) wafers, patterned with lithography, etched, vapour HF released and the strain gradients were measured from SEM and AFM images.

3.1 Film Deposition by LPCVD

An Applied Materials Centura LPCVD tool, which is a component of the imec pilot line, is used for the deposition of the poly-SiGe films. CVD is widely used for technological applications and manufacturing of industrial devices. It is also very interesting from the fundamental point of view due to its conceptual similarities with other growth techniques such as electrodeposition. LPCVD is characterized by incorporation of fewer defects due to lower pressures, good conformation or step coverage but slow growth rate and high temperature dependence. In addition, the ability to create films of varying stoichiometry makes CVD a unique method. Economically, CVD tools are affordable and its operating cost is relatively low. They are also suitable for batch and semicontinuous operations.

The Applied Materials Centura LPCVD platform is shown in Fig. 3.1. Poly-SiGe films are deposited in chamber A (or PolyGen chamber) by thermal reaction of silane and germane in hydrogen environment. The precursors are injected by a gas delivery system, which is controlled by the mass flow controller (MFC), via a shower head into the reactor (Fig. 3.2). The substrate is heated resistively by a ceramic substrate holder and the heater temperature is measured by a thermocouple integrated into the chamber. A diborane gas

is added in-situ as a p-type dopant to enhance the crystallinity and reduce the film resistivity provided the boron concentration is not higher than the equilibrium solubility concentration of boron in SiGe. If an n-type property is desired, a phosphine gas is often considered as a viable dopant. A schematic layout of the chamber A with the associated connections to the gas cylinders and exhaust system are shown in Fig. 3.2.

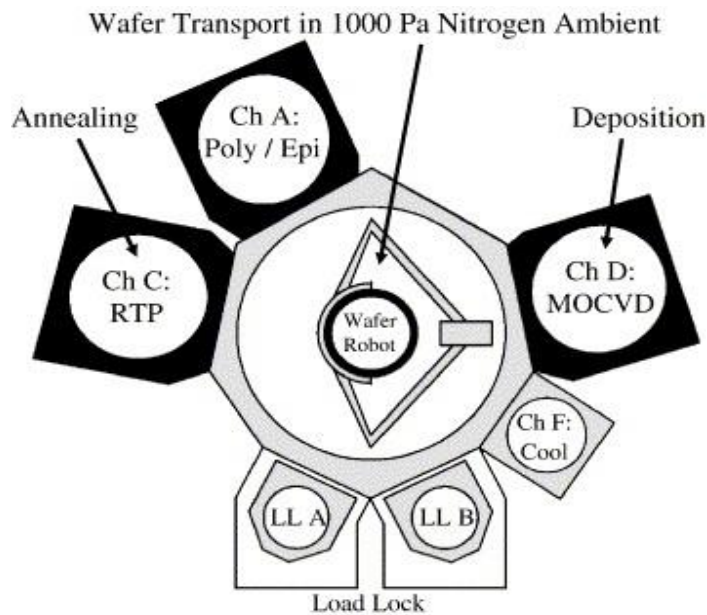


Figure 3.1: Schematic diagram of Applied Materials Centura platform: **Ch A** - Chamber A or Polygen chamber (for poly-SiGe deposition), **Ch C** - Chamber C or Rapid Thermal Process (RTP) chamber, **Ch D** - Metal oxide CVD (MOCVD) for high-k material, **Ch F** - Cooling chamber, LL A - Load lock A, LL B - Load lock B – adapted from [111]

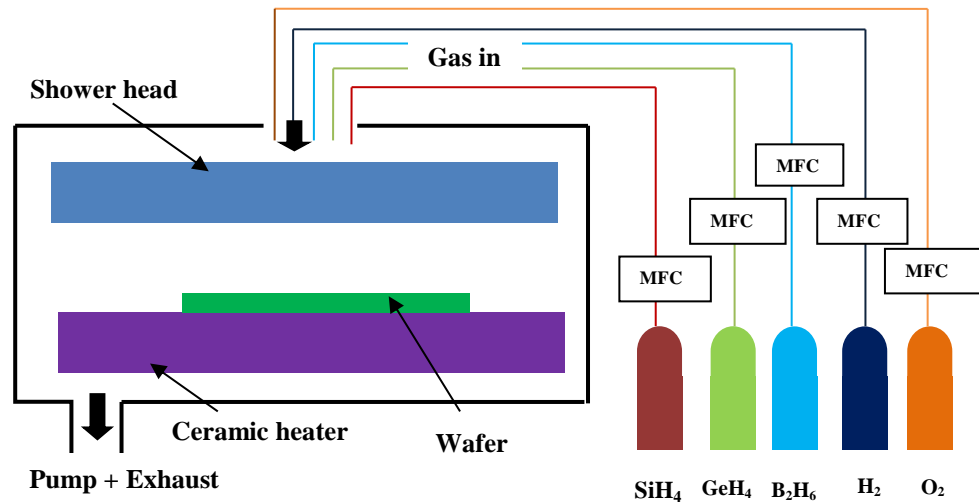
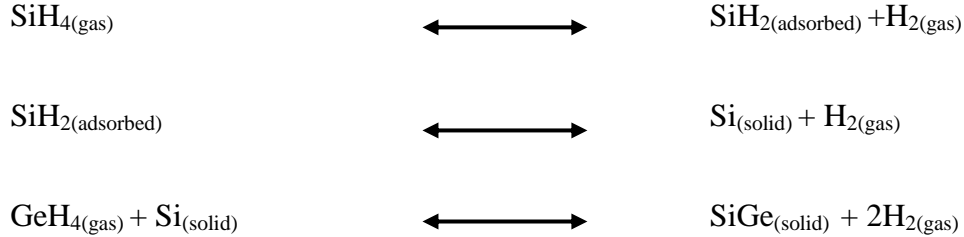


Figure 3.2: Reactor chamber A of LPCVD and its associated connections to the processing gas sources for SiGe film deposition. MFC denotes mass flow controller.

The LPCVD tool operates on the basis of ‘deposition recipe’ and ‘sequency’. A deposition recipe is an algorithm that controls the deposition variables and deposition conditions while sequency is an algorithm that defines the path that the deposition process follows. A typical deposition recipe contains a specification of deposition parameters, gas flow rates, spacing, chamber pressure, heating time, etc. After the recipe is correctly written, the deposition sequency is added to the system. Then, wafers (maximum of 25) are placed in a cassette and then transferred to the load lock. The wafers are thereafter scanned and recognized by the CVD system. The tool robot arm picks up one wafer at a time, from the wafer cassette, and transfers it to the chamber A. Prior to receiving a wafer; the chamber is purged and cleaned with N₂ gas. It should be noted that the LPCVD tool processes wafers on a one-by-one basis and not as a batch reactor.

According to Gupta et al. [112], a possible SiGe growth mechanism consists of silane pyrolysis followed by surface adsorption and finally incorporation of germanium atoms and releasing of hydrogen gas. The chemical equations are presented below.



The above reactions indicate that silicon nucleates on the oxide layer before germanium atoms are incorporated. In other words, silicon provides nucleation sites for germanium atoms, which is similar to the observation of Lin et al. [55]. It should be noted that since CVD is a thermo-chemical process, the deposition rate can be strongly dependent on the deposition temperatures through the Arrhenius relationship. Therefore, for LPCVD and many other CVD processes, the deposition is carried out under conditions where the controlling factor is either transport of the reactants to the substrate surfaces or the reaction at the surface. Because of the low deposition temperature, it is likely that the current process is reaction limited. Other deposition parameters such as chamber pressure, hydrogen flow rate and shower head-heater spacing influence the reaction rate.

A typical SiGe thin film deposition follows the steps showing in Fig. 3.3. A blanket Si (100) wafer is selected and cleaned to remove organics / particles and some metals following the procedure defined in imec's recipe (BASIC). The recipe requires that the wafer is put in a 'bath' with a mixture of NH_4OH , H_2O_2 and deionized water at 35°C with a megasonic power of 480W. It is then followed by a quick rinse in deionized water and HCl spiking at room temperature. While the first step removes organic and

metal particles, the second step removes chemical particles and prevents metal deposition. About 200 nm thick silicon nitride (SiN) is deposited at the back side. According to the imec standard procedure, this prevents contaminants from being transferred from Cu-contaminated to non-contaminated tools within the cleanroom (by removing the SiN layer before transferring the wafer to the non-contaminated tool). A silicon oxide layer (usually 1 μm or as required) is then deposited on the front side of the wafer. In most applications, the oxide layer is etched to form an anchor (where structural layers are anchored) or actuation gap. This is followed by SiGe deposition. Prior to this, the oxide layer is cleaned to remove native oxide or any contaminants that might influence the adhesion of SiGe film to the substrate. The properties and thickness of the SiGe film depend on the deposition parameters. To estimate the mass/weight of the deposited species or the stress in SiGe films, the weight of the substrate and its radius of curvature are measured prior to and after SiGe deposition using Metryx Mentor and Flexus (stress measurement tool), respectively (details in sections 3.2 and 3.3). The actual mass of the deposited species and the stress in the film are obtained from the differences in the predeposition and postdeposition values.

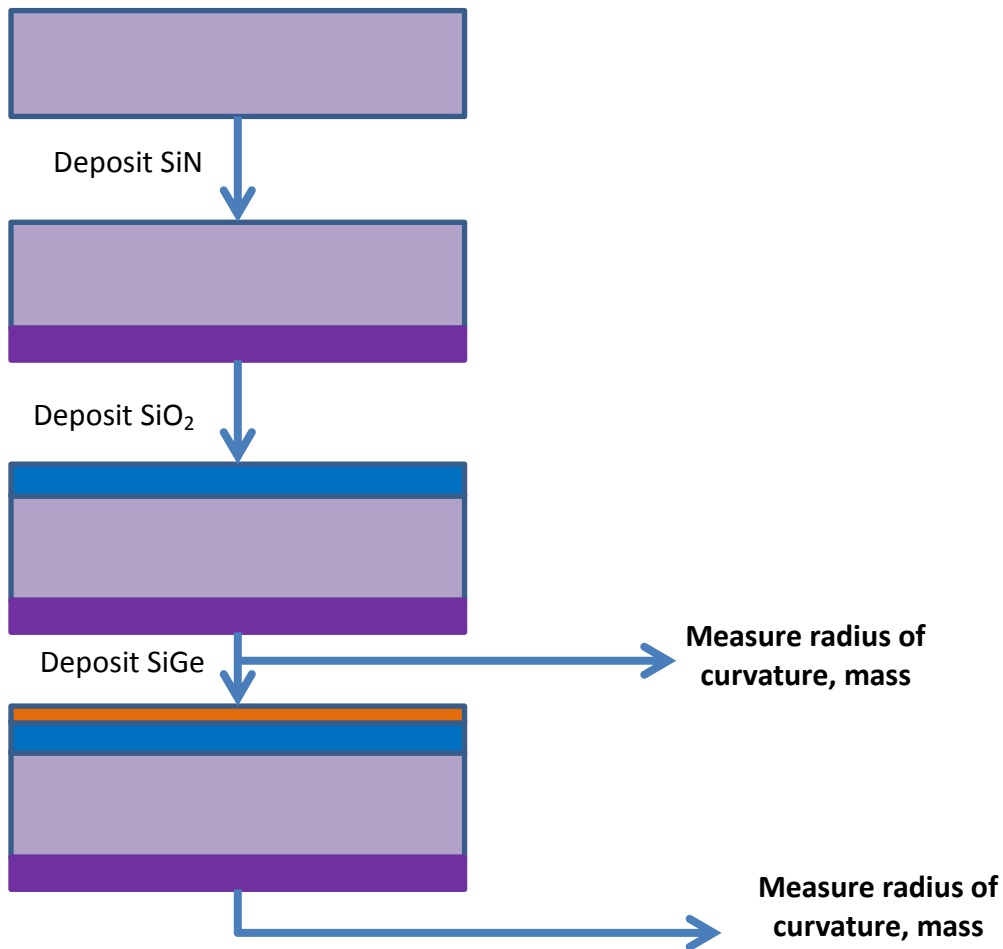


Figure 3.3: Stages in SiGe deposition process on blanket wafer

3.2 Thickness, Microstructure and Surface Roughness Characterization

As a confirmation of the weight measurement technique mentioned above, film thicknesses are also measured with FEI NOVA 200 scanning electron microscopy (SEM) by imaging the cross-section of the samples. Both the thicknesses measured by using Metryx mentor and those of the SEM do not differ more than ± 5 nm. The SEM tool is

shown in Fig. 3.4(a). In addition, surface morphologies of a few films were also acquired by using the SEM measurement.

The surface profiles of the films were obtained with a Multimode Digital Instrument atomic force microscopy (AFM) in a tapping mode (Fig. 3.4b) while the samples were exposed to the air. In this mode, the cantilever is oscillated close to its resonance frequency and its tip taps the surface only periodically, unlike in the contact mode where the tip is in contact with the sample. The surface topography is monitored through the changes in the oscillation amplitude as the tip-to-sample spacing fluctuates when a surface is scanned. The collected data consisted of height information on 512 x 512 square arrays. The lateral resolutions were 4 and 10nm for 2 μm x 2 μm and 5 μm x 5 μm area scans, respectively. The surface morphology depends on the microscopic growth dynamics, which is strongly influenced by the deposition conditions. From the AFM images, surface parameters such as roughness exponent α , root-mean-square (rms) of the surface roughness σ , the autocorrelation length ξ , the rms local slope ρ and the fractal dimension D_f [79 – 82] were extracted and analyzed.

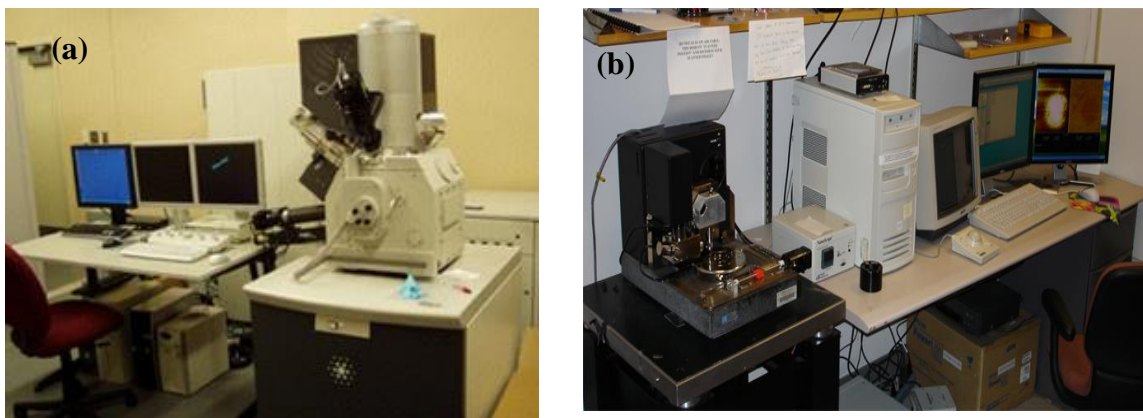


Figure 3.4: (a) FEI NOVA 200 SEM, and (b) Multimode Digital Instrument AFM tool

3.3 Characterization of Electrical and Structural Properties

3.3.1 Film Resistivity

One of the most important electrical properties of a poly-SiGe thin film is its resistivity because it determines the conductivity as well as the carrier mobility in the films. Four-point probe characterization is a standard method for studying the electrical properties of solids and thin films. However the probe spacing has to be reduced to obtain expected surface sensitivity and spatial resolution [113]. An example is a KLA-Tencor OmniMap RS75 four-point probe showing Fig. 3.5(a). A schematic view of the arrangement of the probes on a thin circular sample is shown in Fig. 3.5(b). The tool contains four thin collinearly placed tungsten carbide wires probes which are made to contact the sample under test. Each of them is supported by springs on the other end to minimize sample damage during probing. Typically, the spacing of points is around $635\mu\text{m}$ or more, and may depend on the application.

By applying current I to the outer electrodes, potential difference V can be measured with an ultrahigh impedance voltmeter between the two inner probes at different positions on the surface of the sample. The current remains constant in the circuit irrespective of the changes in the resistance in the material and the output voltage depends on the resistance changes. The depth of penetration of the current depends on the distance between the current probes and increases with increased separation. This offers a possibility of probing the film resistance at different thicknesses. In general, the depth of penetration is often limited to a half of the probe separation with the features close to the

surface having a greater impact on the current path. For a sample of semi-infinite volume, a very thin layer (thickness $t \ll s$), and equal interprobe spacing s , it can be shown that the sheet resistivity ρ is given by:

$$\rho = \frac{\pi t}{\ln 2} \left(\frac{V}{I} \right) \quad (3.1)$$

According to Eq. (3.1), it should be noted that the resistivity of a thin film is independent of the interprobe spacing s . The sheet resistance R_s is given by the following equation:

$$R_s = \frac{\rho}{t} \Rightarrow k \left(\frac{V}{I} \right) \quad (3.2)$$

where the geometric factor $k = \frac{\pi}{\ln 2}$, which is 4.53 for a semi-infinite thin sheet. This value may differ for non-ideal samples.

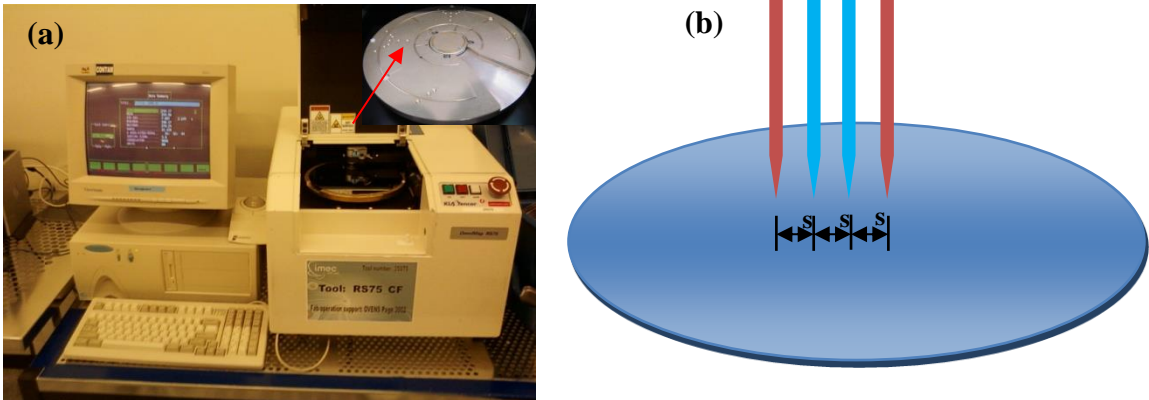


Figure 3.5: (a) KLA-Tensor OmniMap RS75 four-point probe (the inset is the measuring table), (b) an exaggerated view showing the arrangement of the four probes on 200mm diameter circular silicon wafer.

In this study, a KLA-Tencor OmniMap RS75 four-point probe was used to measure the average film resistance. The applied current $I = 2.215\text{mA}$ and the spacing $s = 1.016\text{mm}$. For each film, 49 points are measured, and the average resistance and percentage standard deviation are obtained therefrom. The percentage standard deviation is a measure of the uniformity in terms of film thickness and crystallinity. A lower value of percentage standard deviation indicates that both the film thickness and crystallinity are relatively uniform across the wafer.

3.3.2 Mobility and concentration of carriers

Aside from electrical resistance, other electronic properties such as carrier mobility as well as carrier density or concentration can be measured with Hall Effect. These properties allow an in-depth understanding of materials behaviour [114]. In theory, the Hall Effect is generated when a magnetic field of magnitude B is applied perpendicular to a moving carrier [115]. Due to the magnetic field, the moving carrier is deflected perpendicularly to both the magnetic field and the plane the carrier was traveling in (Fig. 3.6a). This deflection is produced by the Lorentz force which is given by $F = -qv \times B$, where q is the carrier charge (1.602×10^{-19} C). The Lorentz force introduces a potential difference or Hall voltage, V_H , across the sample resulting in an electric field [116]. In semiconductors, both electrons and holes deflect to the same side of the sample due to opposite charges as well as opposite velocities.

Measurement of the Hall voltage is done following the van der Pauw technique illustrated in Fig. 3.6 (b). In this technique, a constant current is forced through opposing contacts while the Hall voltage is measured across the other two. The magnitude of the

Hall voltage, V_H , is related to the current I traveling through the sample, the applied field B and the sheet density of carriers N_s by Eq. (3.3).

$$|V_H| = \frac{IB}{qN_s} \quad (3.3)$$

All measurements reported in this thesis are done by using a Lakeshore 7507 Hall Effect system at a room temperature of 20 °C. The samples are ~1cm x 1cm in dimension and 4 contacts are made with indium oxide powder and then backed in an oven at 380 °C for 1minute. Each of the samples is fixed to the Hall measurement probe, and then placed in-between two magnets. A constant current of 1.0 mA is applied across the sample while the Hall voltage is measured for the magnetic fields between -1 to +1 T. All errors of consistence are less than 0.2 %. From the Hall voltage, the carrier concentration is calculated. The carrier mobility is related to the resistivity ρ and carrier concentration N ($= N_s \cdot h$) as follows:

$$\mu = \frac{1}{qN\rho} \quad (3.4)$$

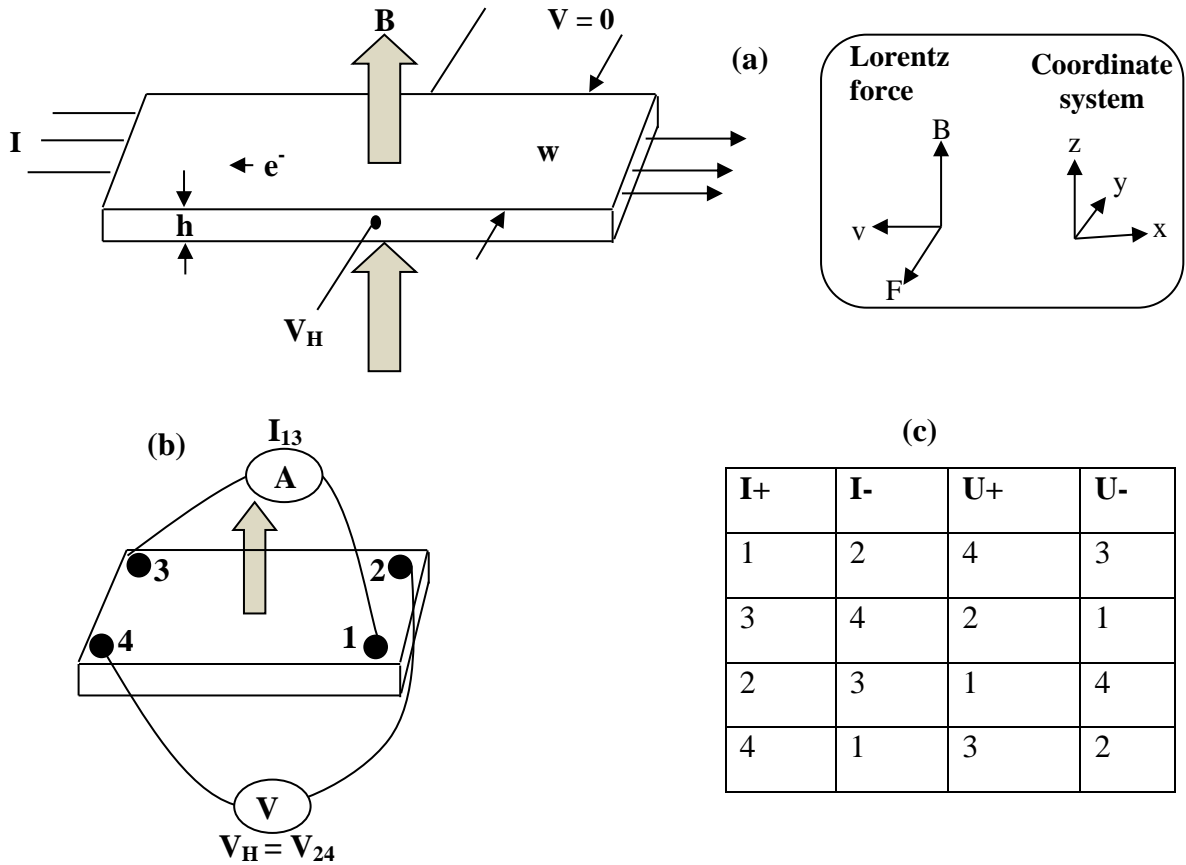


Figure 3.6: (a) Hall voltage V_H is generated due to the Lorentz force F when a magnetic field B is applied across a sample of thickness h and width w , the Lorentz force and the coordinate system are shown (b) illustration of the van der Pauw Hall Effect measurement geometry and (c) scanner configuration.

3.3.3 Determination of the crystal structure by XRD

X-rays are used to probe the chemical composition and crystal structure of a solid material. X-ray diffraction (XRD) relies on the constructive interference of X-rays scattering from a crystal lattice. The condition for the constructive interference, that can be obtained when the angle of incident beam satisfies Bragg's law, is:

$$n\lambda = 2d_{hkl} \sin \theta \quad (3.5)$$

where n is the integer number, d is the interplanar spacing and θ is the angle between incident beam and the crystal plane. From Eq. (3.5) and the diffraction spectra, the interplanar spacing d and the lattice parameter a can be obtained. In addition, the full width at half maximum (FWHM) that can be directly related to the grain size can be extracted via Scherrer equation. A PANalytical X'Pert PRO MRD X-ray diffractometer (Fig. 3.7a) is an example of a diffraction tool commonly used for thin films. The film's characteristics at near surface layers and the bulk can be obtained by changing the operating mode of the system.

Usually, two modes are possible: Bragg's Brentano (BB) and glancing incidence XRD (GIXRD) modes. In the former, both the sample and the detector move simultaneously during the measurement (Fig. 3.7b). While the sample rotates at θ , the detector moves at 2θ and the diffracted X-rays from grains oriented parallel to the surface are detected. A disadvantage of this geometry is that the effective depth probed by the incident beam changes during scan due to changes in the angle of the incident beam. Also, the spectra are often dominated by the substrate effects [117] and the peaks are hardly recognized for the case of the ultrathin films used for this study. Ideally, the BB mode is often used for thick (poly) crystalline films. Because the samples are very thin (~ 100 nm), GIXRD mode is therefore used.

In GIXRD mode, the incident X-ray beam is fixed to very a small predetermined angle of incidence (so-called glancing angle) on the sample (ω) and the detector scans 2θ diffraction from the planes not parallel to the sample's surface (Fig. 3.7c). This technique provides information from a quite thin layer and is ideally suitable for the examination of

a layer thickness on the order of 100 nm and less. Unlike in BB mode, the crystallographic plane contributing to the signal has an offset of $\theta - \omega$ compared to the film surface i.e. the planes parallel to the surface will not diffract in GIXRD (118). In this study, the diffraction profiles of the films are obtained by using GIXRD and $\text{CuK}\alpha$ ($\lambda = 0.154 \text{ nm}$) radiation operated at 45 kV and 40 mA. All the diffraction spectra were obtained in a continuous mode at a scan speed of $0.1^\circ/\text{s}$. The glancing incidence angle $\omega = 1^\circ$ was obtained by optimization and the diffraction angle was varied between $2\theta = 20^\circ$ and 65° in a step size of 0.02° .

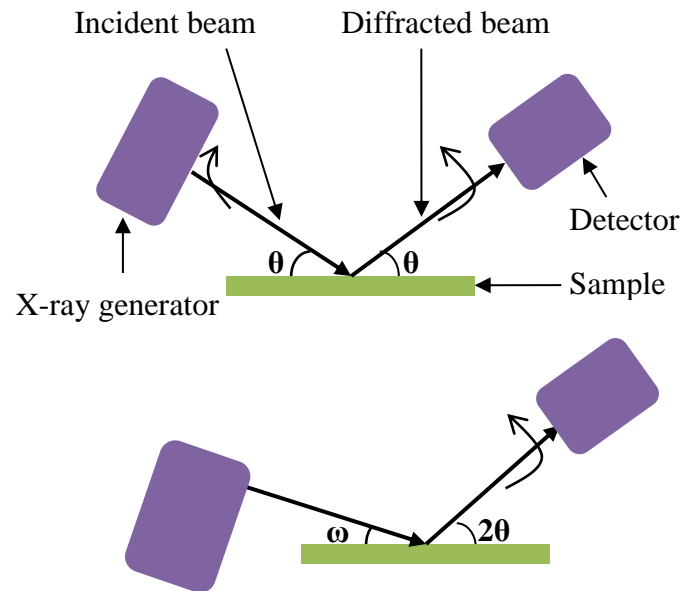


Figure 3.7: (a) D8 Bruker AXS X-ray diffractometer [www.bruker-axs.com], (b) basic geometry of Bragg-Brentano configuration and (c) GIXRD method. Note that the incident beam angle (ω) is fixed during GIXRD analysis and the detector scans 2θ degrees only.

Because the GIXRD configuration is asymmetrical (which implies having higher intensity than those obtained in BB), all the experimental spectra were converted to the symmetrical Bragg reflection using the James formula [118, 119]. The conversion factor R relates the asymmetric measured intensity I_{asym} to that of symmetric intensity I_{sym} for a given diffraction angle θ by the following equation.

$$R(2\theta) = \frac{I_{\text{asym}}}{I_{\text{sym}}} = 2 \left[1 + \frac{\sin(\omega)}{\sin(2\theta - \omega)} \right]^{-1} \quad (3.6)$$

On the basis of Eq. (3.6), about 10% reduction in intensity and in full-width-at-half-maximum (FWHM) is observed at low 2θ ($< 30^\circ$) for $\omega = 1^\circ$. The converted spectra are then fitted to the Lorentzian function [120] and the relevant peak parameters (such as height, FWHM, position and area) were obtained.

3.4 Characterization of Mechanical Properties

In addition to good electrical and structural properties, mechanical properties (like the stress, elastic modulus and strain gradient) are equally important properties especially for successful applications in poly-SiGe NEMS devices.

3.4.1 Stress Measurement Technique

A brief background about stress and its evolution in thin films is provided in section 2.4. In this study, film stresses are measured by using a Tencor FLX-2320 which uses a laser of 750 nm wavelength (Fig. 3.8a). All the measurements are performed on

the blanket silicon substrate after the silicon oxide and backside silicon nitride films are deposited right before and after the SiGe film deposition. In principle, FLX-2320 measures the changes in the radius of curvature of a substrate caused by deposition of a stressed thin film. From the curvature changes, the residual stress in the film can be calculated from the Stoney equation given by Eq. (3.7) [121].

$$\langle \sigma \rangle = \frac{M_s h_s^2}{6h_f} \left(\frac{1}{R_2} - \frac{1}{R_1} \right) \quad (3.7)$$

In Eq. (3.7), M_s is the substrate biaxial elastic modulus which is usually obtained from $M_s = E_s(1-\nu)^{-1}$ where E_s , ν_s and h_s are respectively the elastic modulus, Poisson's ratio and the thickness of the substrate and h_f is the film thickness, R_1 and R_2 are the substrate radii before and after SiGe film deposition. Appropriate application of Eq. (3.7) requires the following assumptions to be valid [122]: (i) both the film thickness h_f and substrate thickness h_s are uniform, the film and substrate have the same radius R , and $h_f \ll h_s \ll R$; (ii) the strains and rotations of the plate system are infinitesimal; (iii) both the film and substrate are homogeneous, isotropic, and linearly elastic. Assumption (i) is satisfied because the rms roughness $\ll h_f$. The other assumptions are also valid in this case.

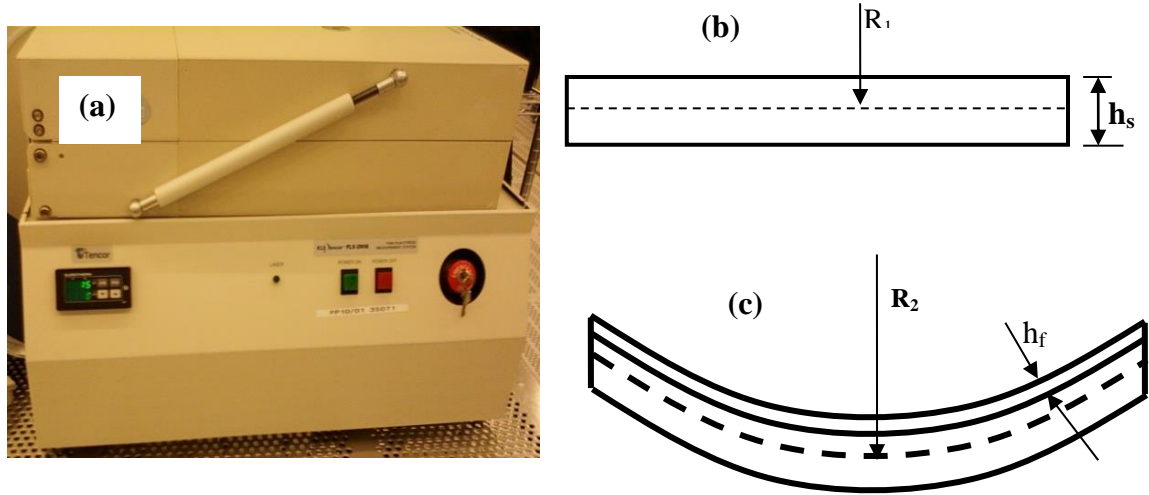


Figure 3.8:(a) Tencor FLX-2320 stress measurement tool (b) substrate without a film with a curvature radius R_1 , (c) curvature radius becomes R_2 upon film attachment to balance the influence of deposition force

3.4.2 Characterization of Mechanical Properties

One of the most popular techniques for measuring the mechanical properties of solid films is nanoindentation [123]. Other methods include an ultrasonic test, a bulge test and beam bending [124]. In this work, nanoindentation experiments are conducted to evaluate the Young's moduli and hardness of a few films by using a MTS Nano Indenter XP with a standard three sided pyramid diamond indenter tip (Berkovich indenter with tip radius <100 nm) as shown in Fig. 3.9 (a). For this method, a prescribed load is applied to an indenter (which is in contact with a specimen) and the depth of penetration is measured. At the maximum indentation depth, the load was kept constant for 10s. The area of contact at full load is determined by the depth of the impression (Fig. 3.9b) and

the known angle or radius of the indenter. The hardness H is found by dividing the maximum applied load P_{\max} by the projected contact area $A(h_c)$.

$$H = \frac{P_{\max}}{A(h_c)} \quad (3.8)$$

For an ideal tip geometry, the projected contact area is given by:

$$A(h_c) = 24.5h_c^2 \quad (3.8a)$$

Due to the blunting of the Berkovich indenter tip, the projected contact area can be estimated more accurately by using the following equation:

$$A(h_c) = 24.5h_c^2 + C_1h_c^1 + C_2h_c^{1/2} + C_3h_c^{1/4} + \dots + C_8h_c^{1/28} \quad (3.8b)$$

Where C_1 to C_8 are constants and are found by fitting A to h_c , other terms are described in Fig. 3.9.

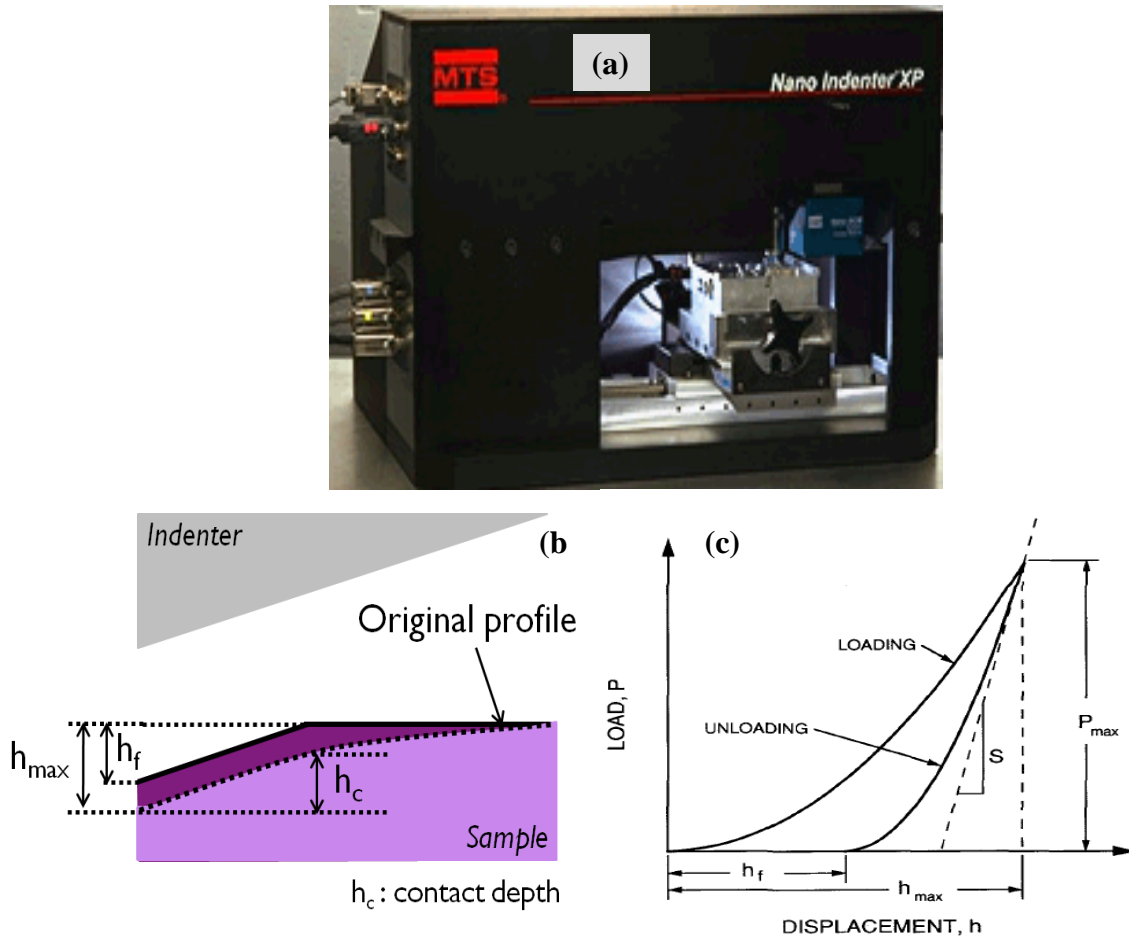


Figure 3.9: (a) MTS Nano Indenter XP, (b) schematic illustration of the unloading process showing parameters characterizing the contact geometry, (c) schematic representation of load versus indenter displacement data for an indentation experiment. P_{max} is the peak indentation load; h_{max} is the indenter displacement at peak load; h_f is the final depth of the contact impression after unloading; and S is the initial unloading stiffness [123].

The elastic modulus of each sample E_s is obtained from the shape of the unloading curve (see Fig. 3.9c) and by considering the effective modulus of the sample

E_{eff} and that of the indenter E_i as well as the Poisson ratios ν_s and ν_i for sample and indenter, respectively, based on the following equation.

$$\frac{1}{E_{\text{eff}}} = \frac{1-\nu_s^2}{E_s} + \frac{1-\nu_i^2}{E_i} \quad (3.9)$$

where $E_{\text{eff}} = \frac{\sqrt{\pi}}{2\beta} \frac{S}{A(h_c)}$, the elastic contact stiffness $S = \frac{dP}{dh}$ defines the slope of the upper

portion of the unloading curve during initial stages of unloading by using the continuous-stiffness measurement (CSM) technique, and constant $\beta = 1.034$. This was accomplished by superimposing an alternating force with known frequency, amplitude, and phase on the nominal applied force. This oscillating force then resulted in a displacement oscillation, $h(\omega) = h_0 \exp(i\omega t + \psi)$, where ω is the applied oscillation frequency, h_0 is the amplitude, and ψ is the phase angle between the force and displacement signals. The displacement response of the indenter at the excitation frequency (~75 Hz) and the phase angle between the force and displacement were then measured continuously as a function of the indentation depth.

For the estimation of the average values for the hardness and modulus, all nanoindentation experiments are performed on poly-SiGe films deposited on 1 μm thick silicon carbide (SiC) films (Fig. 3.10a). SiC is chosen because it is harder than SiGe. In such a case, less error is introduced during the measurement since it is easier to identify the point where modulus begins to rise due to the influence of the SiC substrate than when oxide layer is used. Ten measurements are made for each film (Fig. 3.10b) and the Young's moduli and hardness are evaluated. The Young's modulus is calculated at indentation depth of 30-40 nm, just before the effect of the SiC layer is felt.

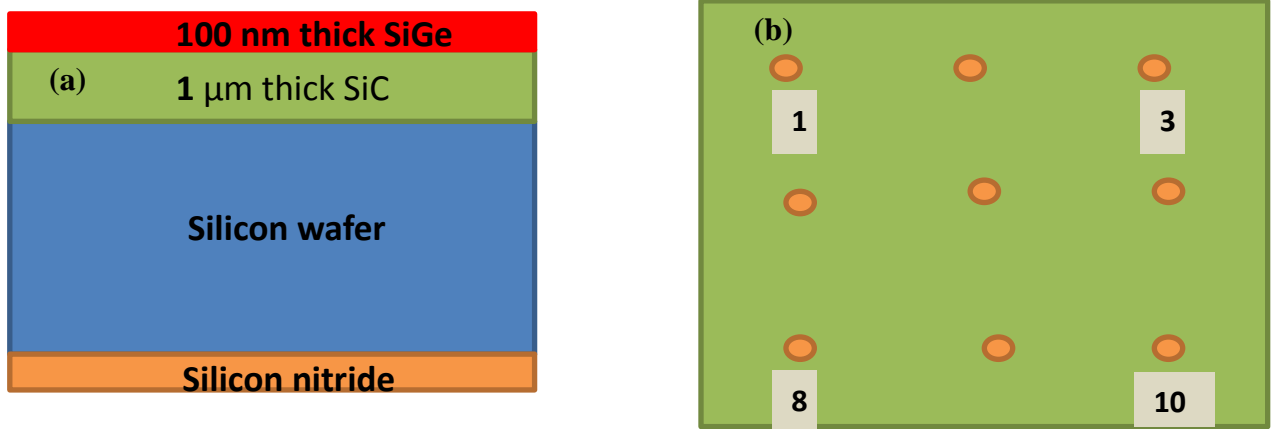


Figure 3.10: A schematic view of: (a) cross-section of poly-SiGe stack sample (b) distribution of 10 points for nanoindentation experiments.

3.5 Other Characterization Techniques

A few other characterization techniques used in this work are Rutherford backscattering spectroscopy (RBS), Raman spectroscopy, Transmission electron microscopy (TEM), Veeco surface profilometry, optical microscopy, etc.

Rutherford backscattering spectroscopy (RBS) is a technique that is used to determine the structure and composition of materials by measuring the backscattering of a beam of high energy ions impinging on a sample [125]. In this work, the RBS technique is used to determine the germanium fraction in the samples.

To quantify the relative amounts of amorphous and crystalline material in the thin poly-SiGe layers, Raman spectroscopy are used. Also, Raman mapping is an excellent way to obtain information about potential variations in crystallinity over areas of

deposited films. However, its suitability for the ultrathin samples is not guaranteed. The Raman technique relies on uniform bond angles and bond lengths in crystalline materials which results in sharp peaks. For amorphous material, there is less orderliness in its arrangement with a wider array of bond angles, bond energies and bond lengths. This non-uniformity possible states leads to a broad Raman band. It should be noted that the spectrum of SiGe is more complicated, and depends also on the composition of germanium [126].

Transmission electron microscopy (TEM) analysis is commonly used to obtain crystallographic information from specimens that are thin enough to transmit electrons [127]. While the theory and operation of TEM are fairly simple, its most significant challenge is in the sample preparation. The thickness of the specimen should be a few nanometers for the electron beam to penetrate through. A few cross-sectional TEM analyses were done to examine the crystal orientation and to calculate the grain size. Also, the interplanar spacing is visible at high magnification.

CHAPTER 4

MODELING STRESSES IN THIN FILMS

In this chapter, a new approach to model intrinsic stresses is proposed. The approach is based on the concept of surface stresses by using dome-shaped islands and hexagonal shaped grains as compared to the spherical and cylindrical shapes used for the islands and grains respectively in a few studies reported in the literature. Equations that describe the stress evolution at the precoalescence, coalescence and postcoalescence stages were derived. These models describe how stresses evolve with island / grain's height and diameter, the surface stresses, the interfacial stresses and the stress due to grain boundary formation. For Cu films deposited on silicon substrates, intrinsic stresses of -200, 140 to 230 and -260 to -80 MPa were obtained for the precoalescence, coalescence and steady state postcoalescence stages, respectively. With a few assumptions, the current models give -261, 102 and -115MPa for the three stages in that order.

4.1 Modeling

In this section, the approach to the proposed models, their underlying assumptions and the limitations are discussed.

4.1.1 Approach, Justification and Assumptions

The modeling approach is similar to that of Cammarata et al. [100] but a dome shape island is considered instead of cylindrical island for the pre-coalescence stress model. An evidence of the chosen shape is shown by the AFM image of Cu islands (Fig. 4.1) during electrodeposition of Cu films on polycrystalline ruthenium with a 2 nm thick amorphous oxide [128]. It is evidenced from Fig. 4.1 (a) that the Cu deposition is still in the pre-coalescence stage since significantly isolated islands are observed. Other thin solid films may not have exactly the same shape during the initial growth stage, it is, however, logical to assume that this will not substantially affect the resulting stress. The isolated island of Fig. 4.1(b) is then modeled as a dome (Fig. 4.1c). The curved surface stress of the island is assumed to be uniform along the entire curved surface. This is a realistic assumption prior to coalescence since the whole surface is exposed to the influence of the incoming gas flux. Once coalescence commences, some parts of the surface will be converted to the grain boundary region which will reduce the area upon which the free surface stress acts.

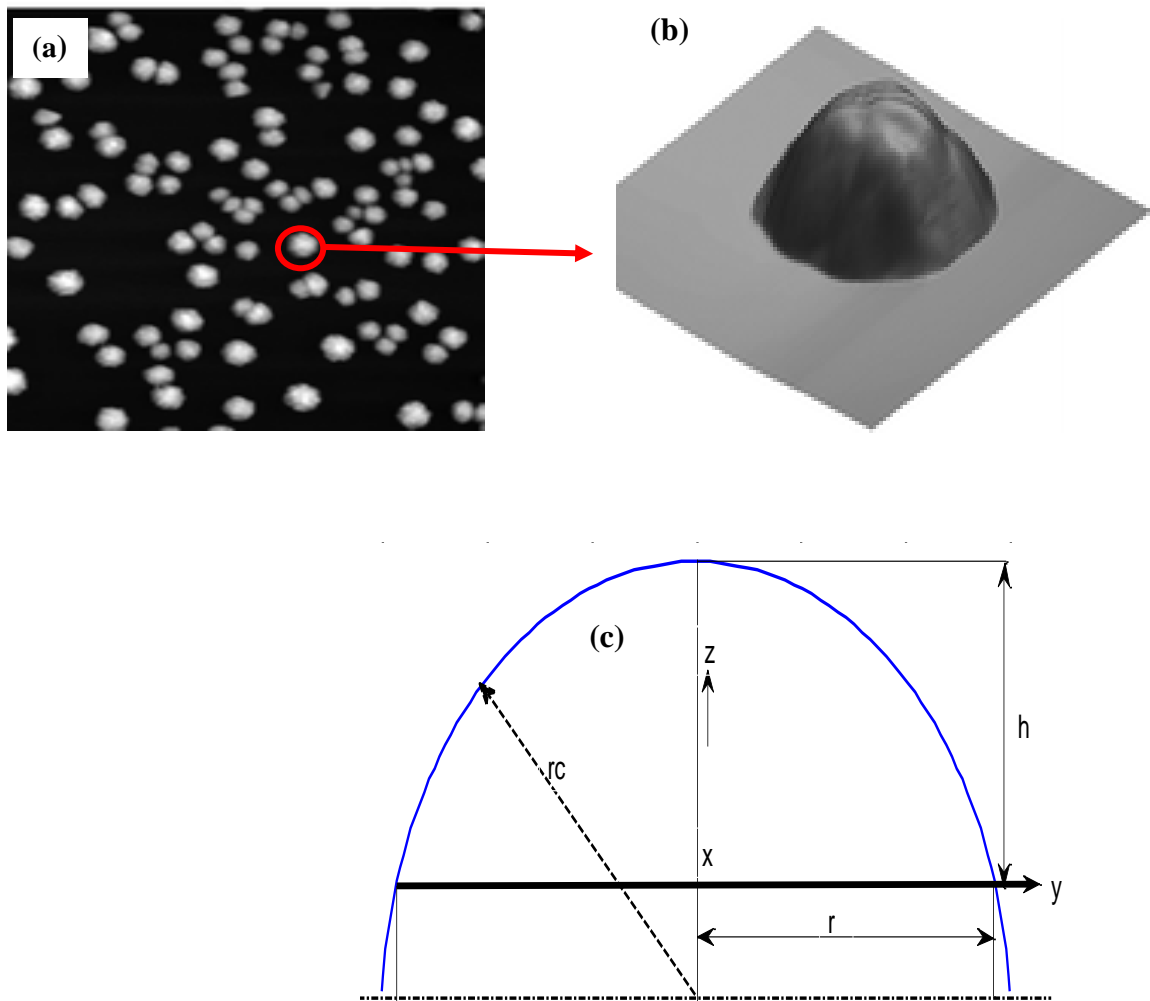


Figure 4.1: (a) AFM image showing significantly isolated islands on oxide layer, and (b) AFM image of a single Cu island [128] and, (c) spherical dome shaped model of the island. The obvious similarity between (b) and (c) is an indication of an accurate assumption. The x -component of the Cartesian co-ordinate is perpendicular to the plane of this page.

Consider the spherical dome shaped island shown in Fig. 4.1(c). The area of the convex surface having a radius of curvature r_c (radius of the sphere) and height h (height of the dome), is given by $A_z = 2\pi r_c h$. The area of the circular bottom disk (base of the dome) of radius r can be estimated from $A_{xy} = \pi r^2$ while r_c and r are geometrically related by $r_c = \frac{r^2 + h^2}{2h}$. The volume of the dome is given by $V = \frac{\pi h}{6}(3r^2 + h^2)$ and the convex surface area can therefore be written as $A_z = \pi r^2 + \pi h^2$. It is assumed that the curved surface of the island is associated with the surface stress f_c and the interface between the circular bottom disk and the substrate is associated with the interface stress f_i . The surface stress is the amount of work per unit area needed to elastically stretch a pre-existing surface, while the interfacial stress can be considered as the work needed per unit area when the film-substrate interface is elastically deformed. The in-plane Laplace pressure ΔP_r and the out-of-plane ΔP_z are assumed to be generated, due to the surface and interface stresses, along the radial and transverse directions respectively. To determine the expression for ΔP_r , a variation is conducted by changing r at constant h and vice versa for ΔP_z . Following the Laplace pressure–surface stress relation i.e.

$\Delta P = f \frac{dA}{dV}$, this gives, for an island with bottom area A_{xy} and surface area A_z :

$$\Delta P_r = f_c \left(\frac{\partial A_z}{\partial r} \right)_h \left(\frac{\partial r}{\partial V} \right)_h + f_i \left(\frac{\partial A_{xy}}{\partial r} \right)_h \left(\frac{\partial r}{\partial V} \right)_h \quad (4.1)$$

$$\Delta P_z = f_c \left(\frac{\partial A_z}{\partial h} \right)_r \left(\frac{\partial h}{\partial V} \right)_r + f_i \left(\frac{\partial A_{xy}}{\partial h} \right)_r \left(\frac{\partial h}{\partial V} \right)_r \quad (4.2)$$

By inserting the expressions for A_{xy} , A_z and V , the Laplace pressure can be written as:

$$\Delta P_r = 2(f_c + f_i) \frac{1}{h} \quad (4.3)$$

$$\Delta P_z = f_c \frac{4h}{r^2 + h^2} \quad (4.4)$$

4.1.2 Stress Generation at Precoalescence Stage

Following the island configuration shown in Fig. 4.1(c), the resulting stresses imposed by the Laplace pressure effects are $\sigma_{xx} = \sigma_{yy} = -\Delta P_r$ (assuming an in-plane isotropic stress state) and $\sigma_{zz} = -\Delta P_z$. The in-plane radial strain ε_{rr} induced during growth is related to the volumetric stresses by the Hooke's law as $\varepsilon_{rr} = s_{11}\sigma_{xx} + s_{12}\sigma_{yy} + s_{13}\sigma_{zz}$ where s_{11} , s_{12} and s_{13} are the elastic compliances of the coordinates in the x, y and z direction respectively. If the volumetric stress components are substituted into the expression for the radial strain, then the radial strain becomes:

$$\varepsilon_{rr} = -2s_{11}(f_c + f_i) \frac{1}{h} - 2s_{12}(f_c + f_i) \frac{1}{h} - 4s_{13}f_c \frac{h}{r^2 + h^2} \quad (4.5)$$

For the in-plane biaxial modulus $\frac{1}{s_{11} + s_{12}} = Y$, the in-plane radial strain is:

$$\varepsilon_{rr} = -2 \frac{(f_c + f_i)}{Yh} - 4s_{13}f_c \frac{h}{r^2 + h^2} \quad (4.6)$$

At the beginning of film growth, when island is fully attached to the substrate, the island is assumed to be strain free with an equilibrium in-plane lattice parameter $a[1 + \varepsilon_{rr}(h_o, r_o)]$

, where a is the bulk lattice parameter [129]. As the island grows, its critical lattice parameter will want to increase to $a[1 + \varepsilon_{rr}(h, r)]$. Because the film is sticking to the substrate by adhesion, the substrate prevents the lattice parameter of the deposited film from increasing to the new value. Then, the biaxial strain $\Delta\varepsilon_{rr}$ induced in the island due to the substrate constraint is $\Delta\varepsilon_{rr} = \varepsilon_{rr}(h_o, r_o) - \varepsilon_{rr}(h, r)$. The intrinsic stress σ imposed by the substrate on the island to oppose the bi-axial strain can be estimated from the stress-strain relation: $\sigma = Y\Delta\varepsilon_{rr}$. Therefore:

$$\sigma_{pre} = 2(f_c + f_i) \left[\frac{1}{h} - \frac{1}{h_o} \right] + 4s_{13} Y f_c \left[\frac{h}{r^2 + h^2} - \frac{h}{r_o^2 + h_o^2} \right] \quad (4.7)$$

If $\beta - 1 = \frac{2s_{13}}{s_{11} + s_{12}}$ is a crystallographic orientation and elastic compliance dependent parameter as proposed by Cammarata et al. [100], then the pre-coalescence stress is:

$$\sigma_{pre} = 2(f_c + f_i) \left[\frac{1}{h} - \frac{1}{h_o} \right] + 2f_c(\beta - 1) \left[\frac{h}{r^2 + h^2} - \frac{h}{r_o^2 + h_o^2} \right] \quad (4.8)$$

For an elastically isotropic material, $\beta = \frac{1-3\nu}{1-\nu}$, where ν is Poisson's ratio. If Poisson's ratio is larger or smaller than 1/3, β will be negative or positive, respectively. For an elastically anisotropic material, the sign of β will depend on the elastic constants and the crystallographic orientation. Equation (4.8) represents the induced intrinsic stress generated at the pre-coalescence stage before impingement. Comparing Eq. (4.8) to the pre-coalescence model of Cammarata and his coworkers (thereafter called the CTS model) (see Eq. 2.1), few points are worth noting. First, the thickness and diameter

dependent terms are coupled in our model unlike in the CTS model where they are separately grouped. Second, the expression in the second part of the right hand side of Eq. (4.8) presents a non-linear relation between the induced stress, the island thickness and its radius unlike in the CTS model where the relationship is inversely linearly proportional. Third, the CTS model requires three surface stresses, while two are sufficient for the current model thereby reducing the number of unknown parameters. It is instructive to say that both models give the values of the upper boundary for the stress induced at the precoalescence stage. However, results of our model are closer to the experimental values compared to the previous models as described in section 4.2.

4.1.3 Stress Generation at Coalescence and Postcoalescence Stages

As the neighbouring islands coalesce to form grain boundaries, a surface stress associated with these boundaries, f_{gb} , are formed. In this analysis, it is assumed that the dome shaped islands coalesce to form a regular hexagonal grain. In reality, it should be noted that other shapes having 3, 4, 5, or even 7 sides are also possible (Fig. 4.2a). To simplifying our analysis, we however assume only hexagonal grains. The hexagonal model of Fig. 4.2 (b) has a side length r' and height h' . The parameters are denoted with primes to differentiate them from those of the precoalescence stage. The central hexagon is considered for the subsequent analysis.

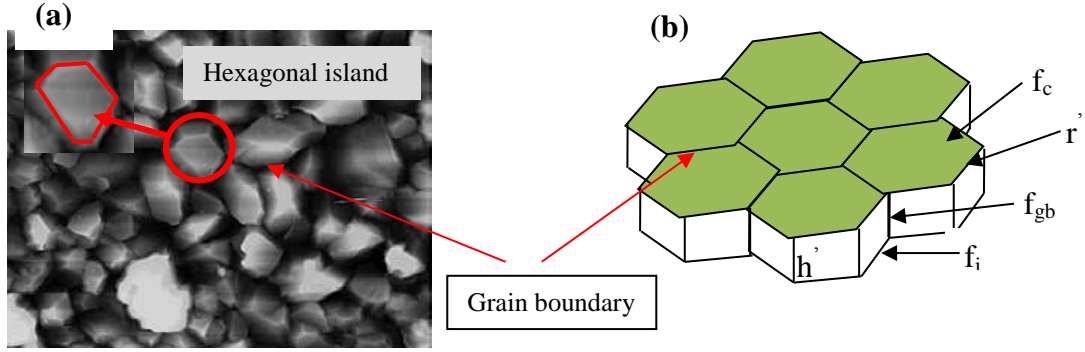


Figure 4.2: (a) SEM image showing grain structure of Cu film (inset is a single hexagonal grain) (130). Note that the grain boundaries have been etched and that other shapes are feasible, (b) hexagonal

For the hexagonal island shown in Fig. 4.2(b), the grain boundary area

$A_{gb} = 6r'h'$, the surface area $A'_{xy} = \frac{3\sqrt{3}}{2}r'^2$ and the total volume $V' = \frac{3\sqrt{3}}{2}r'^2h'$. Following

the Laplace pressure–surface stress relation described previously, i.e. $\Delta P = f \frac{dA'}{dV'}$. When

assumed in-plane isotropy, this gives:

$$\Delta P'_x = (f_c + f_i) \left(\frac{\partial A'_{xy}}{\partial r'} \right)_{h'} \left(\frac{\partial r'}{\partial V'} \right)_{h'} + \frac{f_{gb}}{2} \left(\frac{\partial A_{gb}}{\partial r'} \right)_{h'} \left(\frac{\partial r'}{\partial V'} \right)_{h'} = \Delta P'_y \quad (4.9)$$

$$\Delta P'_z = (f_c + f_i) \left(\frac{\partial A'_{xy}}{\partial h'} \right)_{r'} \left(\frac{\partial h'}{\partial V'} \right)_{r'} + \frac{f_{gb}}{2} \left(\frac{\partial A_{gb}}{\partial h'} \right)_{r'} \left(\frac{\partial h'}{\partial V'} \right)_{r'} \quad (4.10)$$

Replacing A'_{xy} , A'_z , A_{gb} and V' with their respective mathematical expressions, the

Laplace pressures become $\Delta P'_x = \Delta P'_y = (f_c + f_i) \frac{1}{h'} + \frac{f_{gb}}{\sqrt{3}} \frac{1}{r'}$ and $\Delta P'_z = \frac{2f_{gb}}{\sqrt{3}} \frac{1}{r'}$

Assuming in-plane isotropy, the resulting bi-axial strain is:

$$\varepsilon'_{xx} = -s_{11} \left[(f_c + f_i) \frac{1}{h'} + \frac{f_{gb}}{\sqrt{3}} \frac{1}{r'} \right] - s_{12} \left[(f_c + f_i) \frac{1}{h'} + \frac{f_{gb}}{\sqrt{3}} \frac{1}{r'} \right] - 2s_{13} \frac{f_{gb}}{\sqrt{3}} \frac{1}{r'} = \varepsilon'_{yy}$$

$$\varepsilon'_{xx} = -(s_{11} + s_{12}) \left[(f_c + f_i) \frac{1}{h'} + \frac{f_{gb}}{\sqrt{3}} \frac{1}{r'} \right] - 2s_{13} \frac{f_{gb}}{\sqrt{3}} \frac{1}{r'} = \varepsilon'_{yy}$$

For the in-plane biaxial modulus $Y = \frac{1}{s_{11} + s_{12}}$, the in-plane bi-axial strain is:

$$\varepsilon'_{xx} = -\frac{1}{Y} \left[(f_c + f_i) \frac{1}{h'} + \frac{f_{gb}}{\sqrt{3}} \frac{1}{r'} \right] - 2s_{13} \frac{f_{gb}}{\sqrt{3}} \frac{1}{r'} = \varepsilon'_{yy} \quad (4.11)$$

Similar to the pre-coalescence stress state, the extra biaxial strain induced in the grain due to the substrate constraint when the grain grows from its state when the grain boundary formation is just completed (h'_{imp}, r'_{imp}) to a new state (h', r') is:

$$\Delta \varepsilon'_{xx} = \varepsilon'_{xx}(h', r') - \varepsilon'_{xx}(h'_{imp}, r'_{imp})$$

The extra stress $\Delta \sigma_{,cont}$ imposed by the substrate constraint on the grain due to the film growth from (h'_{imp}, r'_{imp}) to (h', r') is:

$$\Delta \sigma_{,cont} = (f_c + f_i) \left[\frac{1}{h'} - \frac{1}{h'_{imp}} \right] + \frac{f_{gb}}{\sqrt{3}} \left[\frac{1}{r'} - \frac{1}{r'_{imp}} \right] + \frac{f_{gb}}{\sqrt{3}} (\beta - 1) \left[\frac{1}{r'} - \frac{1}{r'_{imp}} \right] \quad (4.12)$$

The change in strain due to the coalescence process (grain boundary formation) itself is the difference between Eq. (4.7) and Eq. (4.12) evaluated at the beginning and completion of coalescence process respectively.

From Eq. (4.7) we get the strain right before coalescence as:

$$\varepsilon'_{rr}(h'_{imp}, r'_{imp}) = \varepsilon_{xx}(h_{imp}, r_{imp}) = -2 \frac{(f_c + f_i)}{Y h_{imp}} - 4s_{13} f_c \frac{h_{imp}}{r_{imp}^2 + h_{imp}^2} = \varepsilon_{yy} \quad (4.13)$$

From Eq. (4.11) we get the strain right after coalescence as:

$$\varepsilon'_{xx}(h'_{imp}, r'_{imp}) = -\frac{1}{Y} \left[(f_c + f_i) \frac{1}{h'_{imp}} + \frac{f_{gb}}{\sqrt{3}} \frac{1}{r'_{imp}} \right] - 2s_{13} \frac{f_{gb}}{\sqrt{3}} \frac{1}{r'_{imp}} = \varepsilon'_{yy} \quad (4.14)$$

The change in the in-plane biaxial strain due to the impingement is given as:

$$\Delta \varepsilon_{xx,imp} = \varepsilon_{rr}(h_{imp}, r_{imp}) - \varepsilon'_{rr}(h'_{imp}, r'_{imp}) \quad (4.15)$$

$$\Delta \varepsilon_{rr,imp} = \frac{(f_c + f_i)}{Y} \left[\frac{1}{h'_{imp}} - \frac{2}{h_{imp}} \right] + 2s_{13} \left[\frac{f_{gb}}{\sqrt{3}} \frac{1}{r'_{imp}} - 2f_c \frac{h_{imp}}{r_{imp}^2 + h_{imp}^2} \right] + \frac{f_{gb}}{\sqrt{3}} \frac{1}{r'_{imp}}$$

The biaxial stress can be estimated from the stress-strain relation: $\sigma_{,imp} = Y \Delta \varepsilon_{rr,imp}$

$$\Delta \sigma_{rr,imp} = (f_c + f_i) \left[\frac{1}{h'_{imp}} - \frac{2}{h_{imp}} \right] + (\beta - 1) \left[\frac{f_{gb}}{\sqrt{3}} \frac{1}{r'_{imp}} - 2f_c \frac{h_{imp}}{r_{imp}^2 + h_{imp}^2} \right] + \frac{f_{gb}}{\sqrt{3}} \frac{1}{r'_{imp}} \quad (4.16)$$

The total stress for a continuous film can therefore be calculated from Eq. (4.7), (4.12) and (4.16):

$$\sigma_{,cont} = \sigma_{pre}(h_{imp}, r_{imp}) + \Delta \sigma_{,imp} + \Delta \sigma_{,cont} \quad (4.17)$$

$$\sigma_{,cont} = (f_c + f_i) \left[\frac{1}{h'} - \frac{2}{h_o} \right] + (\beta - 1) \left[\frac{f_{gb}}{\sqrt{3}} \frac{1}{r'} - 2f_c \frac{h_o}{r_o^2 + h_o^2} \right] + \frac{f_{gb}}{\sqrt{3}} \frac{1}{r'} \quad (4.18)$$

The stress at coalescence can be obtained from Eq. (4.18) when $(h', r') = (h'_{imp}, r'_{imp})$ and the actual stress induced by the coalescence process is given by Eq. (4.16). It should also be noted that Eq. (4.18) can be compared to only Eq. (4.8) (Cammarata et al's model for a continuous film) and not to other models. This is because both Cammarata and our approach considered the mechanism of postcoalescence stress evolution which is clearly absent from other models.

4.2 Modeling Results, Validation and Comparison

These models are validated with experimental results from literature and then compared with a few published models. For the pre-coalescence stage, we consider the stress evolution in a thin Ag(100) film deposited on a CVD oxide piezocantilever device as presented in Ref. (93). For silver with $\nu = 0.37$ [109], the values of the surface stresses are assumed to be $f_c = f_i = f_f = 0.5 \text{ N/m}$ and $f_h = 1 \text{ N/m}$ since the surface stresses for most alkaline metals are in the range of 0.2 and 1 N/m [100]. For a typical critical or lock down parameter of $h_0 = 2.5 \text{ nm}$ and an impingement parameter of $h_{imp} = 5 \text{ nm}$ and $d = 2.5 \cdot h$ for silver islands just before impingement, our pre-coalescence stress model gives about -82 MPa right before impingement while that of the CTS model gives about -119 MPa. An in-situ experimental value is in the range of -20 and +20 MPa, depending on the growth temperature. These results and those of Cu(001) deposited on an oxidized silicon substrate are presented in Table 4.1. Also for Cu (001), a good agreement between experimental results and our model is obtained. For the choice of 2.5 as a multiplier for island diameter d , the diameters and heights of a series of silicon germanium islands were

monitored (see details in section 4.3). It was found that the diameter/height ratio stabilized at ~ 2.5 prior to coalescence. Although, silicon germanium is a semiconductor material, when it is deposited at higher temperature it exhibits stress evolution similar to those of type I materials. It is therefore expected that the ratio of island diameter/height will be similar to that of Cu and Ag films which are pure metal.

Table 4.1: Comparison between predicted and measured compressive maximum stress prior to coalescence (MPa) for Ag and Cu film

| Material/ Substrate | Fitting Parameters | Ref. [100] | Eq. (4.8) | Experiment |
|--|--|------------|-----------|-------------------------|
| Ag(100)/CVD oxide piezocantilever device | $\nu = 0.37$ $f_c = f_i = f_f = 0.5$, $f_h = 1 \text{ N/m}^b$, $h_o = 1.5 \text{ nm}$, $d_o = 2.5 * h_o \text{ nm}$, $h = 5 \text{ nm}$, $d = 2.5 * h \text{ nm}$, $\beta = -0.504$ | -128.6 | -82 | -20 to +20 ^a |
| Cu(001)/oxidized silicon | $\nu = 0.34$ $f_c = f_i = f_f = 1$, $f_h =$ 1.5 N/m^b $h_o = 2 \text{ nm}$, $d_o = 2.5 *$ $h_o \text{ nm}$, $h = 5 \text{ nm}$, $d = 2.5 * h \text{ nm}$, $\beta = -0.448$ | -382 | -213 | -200 ^a |

^a [Ref [131]] ^b [Ref. [132]]

The postcoalescence stress models are validated with three experimental results from literature [131, 133, 134]. For Cu; $\gamma_{gb} = 0.715 J/m^2$ [39], $\gamma_s = 1.3135 J/m^2$ [135], $E = 127 \text{ GPa}$ and $\nu = 0.34$. We chose $h_o = 2.5 \text{ nm}$, $d_o = 2.5 * h_o$ and $f_{gb} - 2f_c = -6 \text{ N/m}$ similar to that of Cammarata and his coworkers, other parameters are similar to those in Table 4.1. Two important points are examined for comparison: (i) at the completion of coalescence and (ii) during a continuous film growth. When coalescence is completed $h_{imp} = 13 \text{ nm}$ and $h_{imp} = 2.5 * 13 \text{ nm}$ and $h = d = 60 \text{ nm}$ at a steady stress state [136]. The results for the post-coalescence stress models are presented in Table 4.2. The predictions of the current models are closer to the experimental values than any of the previous models. Both Nix-Clemens models greatly over exaggerate the induced stress. Freud-Chason and Seel models are much closer to the experimental values. The coalescence and postcoalescence models of Cammarata et al. indicate compressive stresses for both stages while the experiments indicate a tensile stress for the stress right after coalescence.

Table 4.2: Stresses at coalescence and continuous stages for Cu (001) films deposited on CVD silicon oxide

| S/N | Model/ Experiment | Source (s) | Stress after complete coalescence (MPa) | Stress in the continuous film (MPa) |
|-----|----------------------|---------------------|--|--|
| 1 | Nix-Clemens 1 | Eq. (2), Ref. [97] | 5320 | 2476 |
| 2 | Nix-Clemens 2 | Eq. (3), Ref. [97] | 6158 | 2866 |
| 3 | Freund-Chason | Eq. (4), Ref. [109] | 616 | 222 |
| 4 | Seel et al | Eq. (5), Ref. [110] | 1532 | 713 |
| 5 | Cammarata et al. | Eq. (6), Ref. [100] | -150 | -346 |
| 6 | This work | Eq. (4.18) | 102 | -115 |
| 7 | Experiment 1 | Ref. [131] | 175 | -107±33 |
| 8 | Experiment 2 | Ref. [133] | 230 | -80 |
| 9 | Experiment 3 | Ref. [134] | 140 | -260±25 |

4.3 Parametric Studies

To further explore the stress behaviour at pre-coalescence, coalescence and post-coalescence stages, a few parametric studies are carried out for Cu(001) deposited on oxidized silicon. Figure 4.3 (a) is a comparison of the pre-coalescence stress changes with island height based on the CTC and the present models (Eq. 4.8). While both models show a decreasing compressive stress with increased island height, the current model indicates a smaller compressive stress similar to what is observed in Ref. [131]. For the coalescence process, the stress that is often generated depends on both the island radius prior to the impingement as well as the thickness changes over which the coalescence process takes place (see Eq. 4.16). According to Fig. 4.3(b), the stress due to the coalescence decreases with increased thickness and increases with island diameter at

impingement. The slope of the stress-thickness is higher for smaller island at impingement compared to bigger islands.

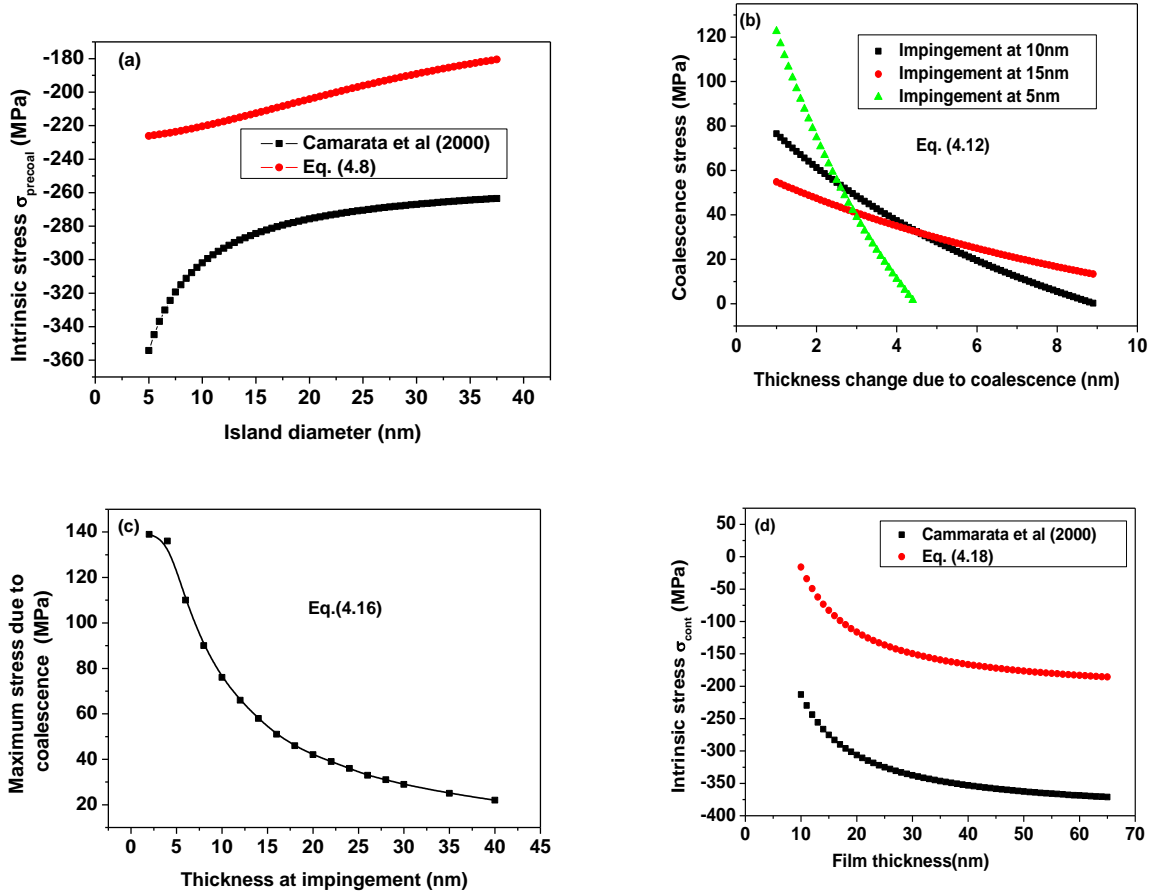


Figure 4.3: (a) Precoalescence stress evolution (b) stress changes due to the coalescence process as a function of thickness change due to impingement $h'_{imp} - h_{imp}$ (c) maximum stress variation with thickness at impingement h_{imp} (d) postcoalescence stress evolution, $f_f = f_g = 0.5\text{N/m}$, $f_h = 1.6\text{N/m}$, $d_o = 2.5\text{ nm}$.

By performing the stress computation over a few thicknesses prior to impingement, the maximum stresses generated during coalescence are shown in Fig. 4.3(c). The figure clearly shows that the maximum stress generated due to zipping decreases with island size. This finding may account for the higher compressive stress observed in films with large grains compared to those of smaller grains. Also, the intrinsic stress becomes compressive during postcoalescence evolution and tends to stabilize after a certain film thickness (Fig. 4.3d).

4.4 Application of the Current Model to Poly-SiGe Films

To apply the current model to poly-SiGe films, islands growth and coalescence processes are monitored by depositing several samples of poly-SiGe films with different thicknesses. The poly-SiGe films are grown by CVD process on top of $1\mu\text{m}$ SiO_2 layers deposited on a silicon substrate. Figure 4.4(a) and 4.4(b) are, respectively, SEM and AFM images of SiGe islands during the precoalescence growth stage. Furthermore, evolution of island diameter-to-height ratio was monitored based on both SEM and AFM images (Fig. 4.4c). An interesting observation is that this ratio decreases as the film becomes thicker and eventually stabilizes at ~ 2.5 at the outset of islands coalescence. This implies that the diameter of an island is at least 2.5 times its corresponding height at precoalescence stage.

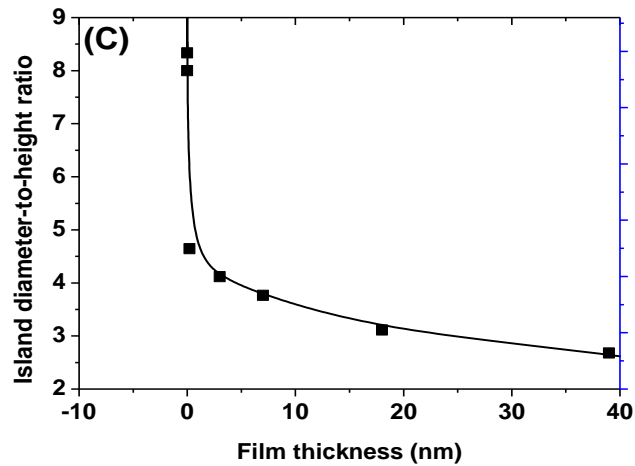
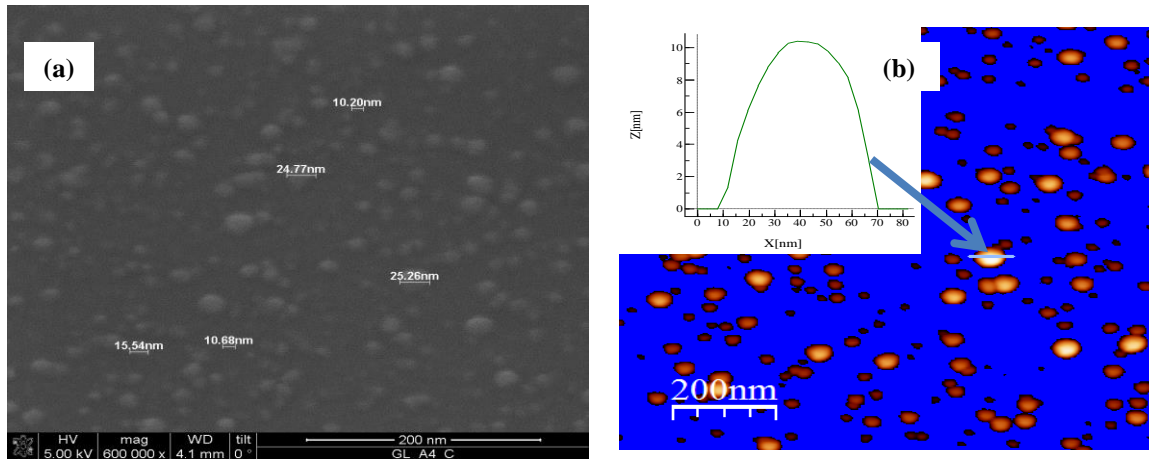


Figure 4.4: Poly-SiGe islands at the precoalescence growth stage (a) SEM image showing significantly isolated islands on SiO₂ layer obtained from FEI NOVA 200 NanoSEM operating at about 5 kV and 600,000X (b) equivalent AFM image obtained in a tapping mode and processed with WSxM software [137], the inset is a typical 2D shape of a growing island (c) ratio of island diameter to the island height as film thickens. The blue background in (b) denotes the substrate surface for a precoalescence film. The continuous line in (c) is a B-spline fitted to the experimental data to guide for the eyes.

Having shown that the pre-coalescence geometry of poly-SiGe film is similar to that of Cu, the models are then used to estimate the surface and interfacial stresses in CVD poly-SiGe. To the best of the authors' knowledge, the interfacial stresses for poly-SiGe have not been determined both experimentally and numerically. To do this we measured the residual stress for several poly-SiGe films of different thicknesses. The results obtained are shown in Fig. 4.5. The details of the experiment and the discussion of the stress evolution are presented in chapters 5 and 6. The free surface stress f_f and the interfacial stress f_i are estimated from the pre-coalescence data of Fig. 4.5. The pre-coalescence growth stage is considered to be the initial 40 nm of the film thickness. To obtain the stress values from Eq. (4.8), the value of $\beta_{\text{SiGe}(111)}$ is chosen to be 0.626 which is obtained from $\beta_{\text{SiGe}} = x\beta_{\text{Ge}} + (1 - x)\beta_{\text{Si}}$, assuming a linear relationship between Si and Ge, x being the germanium fraction in the film. The values of $\beta_{\text{Si}(111)}$ and $\beta_{\text{Ge}(111)}$ are 0.560 and 0.634 [100] respectively and $x = 0.87$ (obtained from Rutherford backscattered analysis). Other values, except the lock down values, are obtained from Fig. 4.5: $h_0 = 2.0 \text{ nm}$, $d_0 = 2.5 * h_0$, $h_1 = 3 \text{ nm}$, $d_1 = 2.5 * h_1$, $\sigma_1 = -628 \text{ MPa}$ (point I) and $h_2 = 18 \text{ nm}$, $d_2 = 2.5 * h_2$, $\sigma_2 = -259 \text{ MPa}$ (point II). By solving the two equations derived due to point I and II simultaneously, we obtained $f_c = 1.665 \text{ N/m}$ and $f_i = -0.565 \text{ N/m}$. The value of f_c is similar to the surface stress value obtained for amorphous silicon (1.28 – 2.0 N/m) by Hara et al. [138].

Following the above procedure while taking the values of $\beta_{\text{Si}(100)}$ and $\beta_{\text{Ge}(100)}$ to be 0.348 and 0.252, respectively (100), the curve surface and the interfacial stresses are calculated to be 1.637 and -0.234 N/m, respectively. The value of the grain boundary stress is estimated from Eq. (4.18) using the above values of f_f and f_i and the

experimental data from points (III) and (IV) with the assumption that the island coalescence is completed at point (III). In this case, $h_3 = 40 \text{ nm}$, $d_3 = h_3$ (point III) and $h_4 = 100 \text{ nm}$, $d_4 = h_4$ (since the grain diameter-to-height ratio tends towards 1 or lower upon coalescence), $\sigma_4 = -115 \text{ MPa}$ (point IV). The value of f_{gb} is estimated to be -3.066 N/m . No experimental or published value is available to confirm these results but they satisfy the condition for grain boundary formation: $f_c - \frac{f_{gb}}{2} > 0$. The results are summarized in Table 4.3.

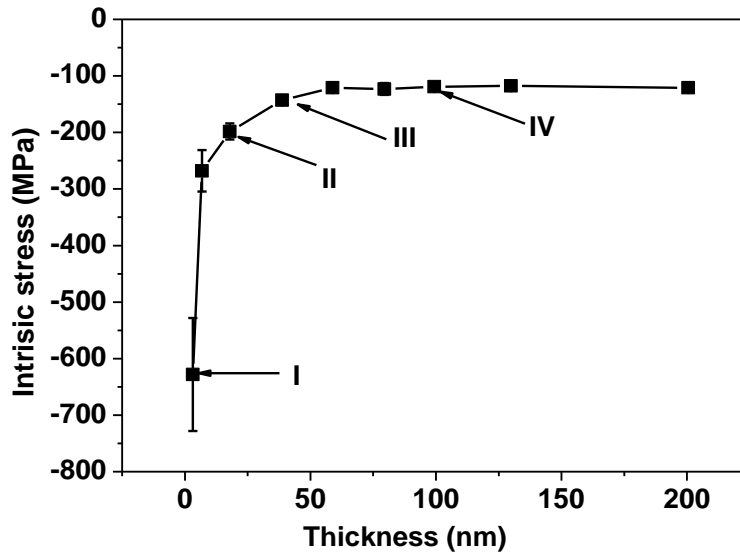


Figure 4.5: Stress evolution in poly-SiGe films deposited by CVD.

Table 4.3: Surface and grain boundary stresses (N/m) obtained from the current model

| Material | Curved surface stress, f_c | Interface stress, f_i | Grain boundary stress, f_{gb} | $f_c - \frac{f_{gb}}{2} > 0$ |
|----------------|------------------------------|-------------------------|---------------------------------|------------------------------|
| SiGe (111) | 1.865 | -0.465 | -3.066 | 3.898 |
| SiGe (100) | 1.637 | -0.2342 | -3.067 | 3.6705 |
| SiGe (average) | 1.751 | -0.3496 | -3.066 | 3.784 |
| Si(100) | *1.28 – 2.0 | - | - | - |

*Ref. [138]

4.5 Further Discussion of the Current Model and Experimental Results

In this section, we examine the differences between the results of our models and those of the experiments to find the mechanisms that might play a dominant role. At the precoalescence stage, the stresses predicted by the current model are slightly more compressive than those of the experiments (see Table 4.1). One of the possible reasons for the deviation may be due to the assumed shape of the growing islands. Indeed, dome is an approximate shape which may slightly differ from the real shape as well as from island to island. It is however interesting to note that the dome shape is more realistic than the cylindrical or spherical shape proposed in the previous studies as evidenced from the AFM image discussed earlier. Another possible reason may be associated with the inaccuracies in determining some fitting parameters especially h_0 and r_0 . Herein we have simply adopted $h_0 = 2.5$ nm similar to the choice made in Ref. [100]. A systematic experimental determination of the lock-in parameters may produce slightly different

values. We have also adopted the island diameter-to-height ratio of 2.5 as a multiplier for precoalescence island growth. This multiplier may not be an absolute value for the Cu and Ag films used for the model verification. A study of the real structural evolution in these films may be necessary for better results.

The assumption of hexagonal shaped grains and the resulting tensile stress obtained after islands coalesce are both fair when compared to the real shape of growing grains and the associated stress. However, the slightly lower tensile stress obtained from the experiment may be attributed to an incomplete island coalescence since the current model is based on a simplifying assumption of total coalescence. Because all islands do not grow at the same rate, the zipping process will not be instantaneous and its rate will differ among the growing grains. For example, it has been observed in aluminum nitride films that grain boundary zipping proceeds layer by layer when it is energetically favourable [101]. In addition, the accurate determination of the interfacial stress associated with the grain boundary f_{gb} might require an extensive experiment for each material under consideration. However, since $f_c - f_{gb}/2 > 0$ is a necessary condition for a grain boundary to form, the assumption of $f_{gb} - 2f_c = -6 \text{ N/m}$ may as well be justified. Also, the island thickness at the completion of impingement/coalescence ($h_{imp} = 13 \text{ nm}$ in the case of Cu) should be determined from SEM measurement. Such a value will be critical to the accurate evaluation of our model.

For the postcoalescence state, the stresses are slightly less compressive than most of the experimental results. This is probably because the current model is only dependent on the shape of the grain, the surface, the interfacial and the grain boundary stresses and not on the adatoms mobility and deposition rate. Various mechanisms that are responsible

for the generation of compressive stress in a postcoalescence film may explain our observation. Diffusion of atoms (atomic mobility) into and out of the grain boundary is a popular mechanism that influences stress evolution [139]. The driving force for the diffusion process is attributed to a higher surface chemical potential compared to the chemical potential in the grain boundary [101]. The rate of atomic flow into the grain boundary is proportional to the concentration of adatoms on the film surface and the atomic transition rate between the surface and the grain boundary and ceases once equilibrium is attained. The compressive stress in some thin film during the postcoalescence growth might also be due to the presence of the strain field due to the tendency of the islands to continue to expand [101].

Finally, it is assumed that the surface, interfacial and grain boundary stress/energy are dependent on the material and not the growth conditions. This may require further investigation by performing systematic and robust experiments. Generally, the current approaches are based on surface stresses and they do not include other mechanisms of stress generation and relaxation which have been the focus of previous studies [109, 133, 139 – 141]. It may be necessary to investigate a hybrid approach where the surface stress method is combined with any of the atomic-level models for more accurate results. In addition, stress relaxation mechanisms may be incorporated to lower the magnitude of the estimated stresses. More systematic and comprehensive measurements are required to obtain the stress-dependent parameters for direct comparison with the model. Though the model is very simple, it provides a useful framework for stress evolution studies in thin films and predicts experimental data well.

CHAPTER 5

DEVELOPMENT OF ULTRATHIN SIGE FILMS: OPTIMIZATION AND PARAMETRIC STUDIES

The first part of this chapter is a report a systematic procedure for simultaneous optimization of stress, resistivity and deposition rate of LPCVD deposited ultrathin ($100\pm 5\text{nm}$) poly-SiGe films by using the grey-Taguchi approach. Seven process variables were identified as important parameters for controlling the deposition process and the resulting film properties, namely the deposition temperature, the silane, germane, diborane and hydrogen flow rate, the chamber pressure and the shower head-heater spacing. By using 4 different levels for each process variable, 32 unique experiments were defined based on an L32 orthogonal array. The optimal combination of process parameters was determined by applying the grey relational analysis (GRA) for multiple performance characteristics. The second part reports the influence of germanium fraction, boron concentration and chamber pressure on the stress, deposition rate, resistivity, carrier concentration, Hall mobility, surface properties and hardness and Young modulus of ultrathin poly-SiGe films.

5.1 The Grey-Taguchi Multi-Response Optimization

One of the most widely used experimental designs for a single and multi-objective optimization is the Taguchi design of experiment [142]. This optimization technique has

been extensively applied in thin film related problems. Among them are optimization of LPCVD SiN film uniformity [143], engraving linewidth of iron oxide coated glass during lithography of photomasks [144], structure, morphology and photocatalytic performance of the rf-sputtered TiO₂ films (145). More applications are discussed elsewhere [146 – 151]. In spite of this wide range of applications, the critics' major argument against Taguchi technique is that the application of signal-to-noise ratio for data analysis lacks statistical basis and poses some computational challenges [152]. More recently, different hybrid approaches (mostly based on Taguchi technique) have been devised as alternatives to the classical Taguchi optimization technique. These include Taguchi and central composite response surface [153], CFD (computational fluid dynamics) and dynamic model of Taguchi [154], Taguchi and Fuzzy logic [155] and an integrated model of the Taguchi method, the artificial neural network (ANN), and the genetic algorithm (GA) [156, 157]. In this study, the Taguchi theory is used for the experimental design while the Grey relational analysis is then used for data analysis because of its superior performance (158).

Grey relational analysis (GRA), a subdivision of the grey relational theory, is a normalization-based evaluation technique commonly used for estimating an integrated performance index for multi-response problems [158]. It is an impact evaluation model that measures the degree of similarity or difference between two sequences based on the grade of relation [159]. Since the general grey relational theory was proposed in 1982 [160], it has been instrumental to the solutions of complex and multivariate systems. In system theory, grey systems exist between white and black systems depending on how much the relevant information is known [158]. GRA can utilize few samples and

uncertainty conditions, and can be effectively applied in optimization of multiple quality characteristics. The grey-Taguchi approach is used here to select the best deposition parameters for optimal poly-SiGe thin films characteristics, taking into account the correlation between the multiple output responses of residual stress, deposition rate and sheet resistance. The step-by-step approach for determining the optimal deposition conditions is reported in details. Finally, the optimal deposition parameters with considerations of the multiple performance characteristics are obtained and validated.

5.1.1 The L32 Orthogonal Array and Grey Relational Analysis

Having identified the seven most important deposition variables that influence the deposition process and the resulting film properties (Table 5.1), experiments based on L32 orthogonal array (O.A) were defined [142]. Subsequently, 32 films were deposited and characterized for thickness, stress, resistivity and deposition rate. Figure 5.1 is the flowchart for the experimental and grey relational analysis (GRA) as used in this study.

Table 5.1: Experimental parameters and their levels

| Process Variables | Symbol | Unit | Parameter levels | | | |
|---|--------|------------------|------------------|-----|-----|-----|
| | | | 1 | 2 | 3 | 4 |
| Deposition temp. | T | °C | 390 | 400 | 415 | 420 |
| SiH ₄ flow rate | S | *sccm | 8 | 10 | 12 | 15 |
| GeH ₄ flow rate (10% in H ₂) | G | sccm | 120 | 140 | 160 | 180 |
| Chamber pressure | P | Torr | 60 | 65 | 70 | 75 |
| B ₂ H ₆ flow rate (1% in H ₂) | B | sccm | 11 | 13 | 15 | 18 |
| Hydrogen flow rate | H | sccm | 500 | 550 | 600 | 650 |
| Shower head-heater spacing | HH | ⁺ mil | 400 | 430 | 470 | 500 |

* sccm means ‘standard cubic centimetre per minute’; ⁺1 mil = 0.0254 mm

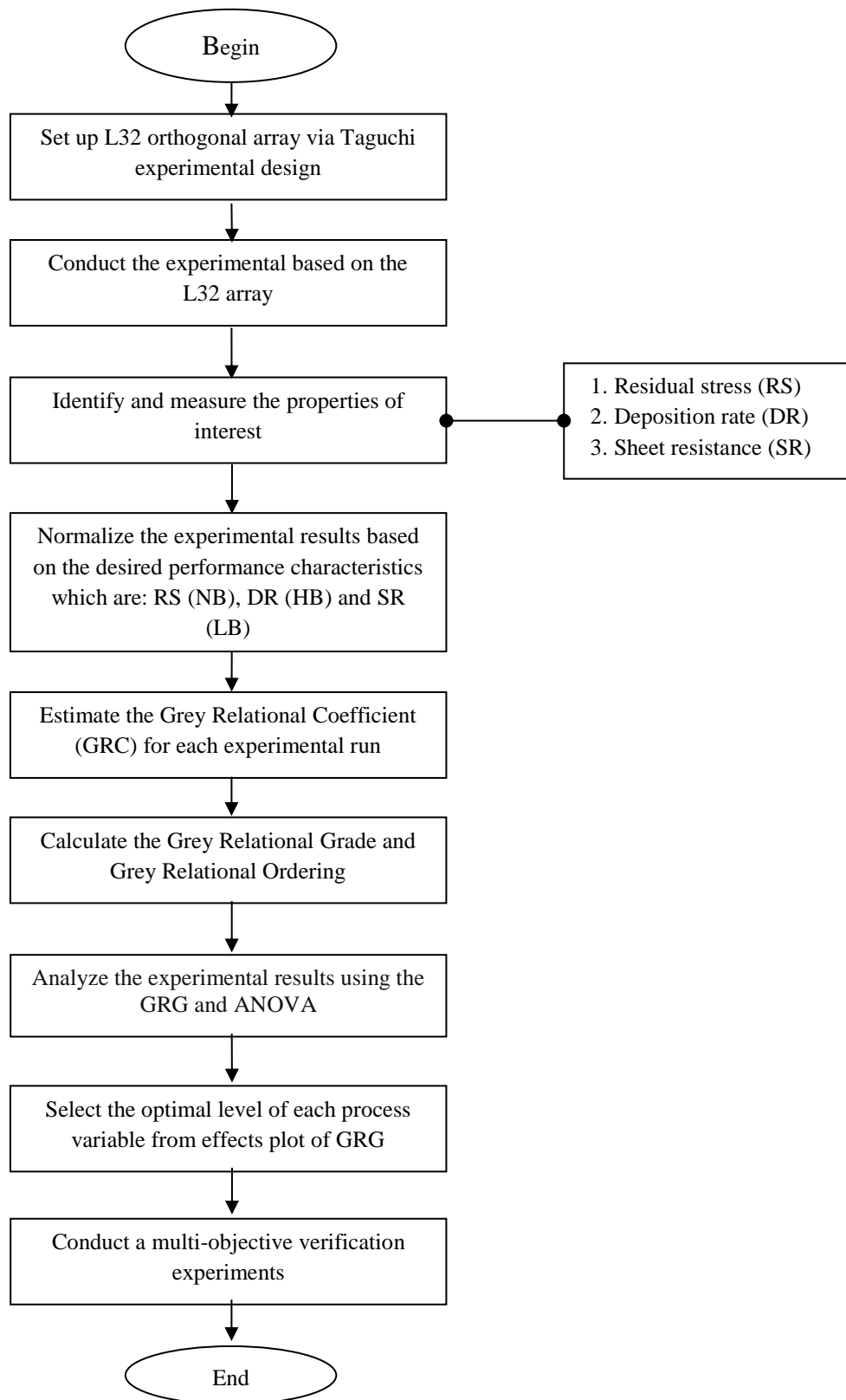


Figure 5.1. Flow chart for the Grey-Taguchi Multi-objective Optimization process

To perform GRA, the input variables were scaled such that they were comparable in terms of order of magnitude, and dimensionless on a global measurement scale [160]. The processing of each measured output depends on the optimization requirement. The residual stress was of the nominal-the-better type (NB) with the nominal value chosen as 30 MPa tensile stress, the deposition rate was of the higher-the-better type (HB) while the sheet resistance belonged to the lower-the-better type (LB). 30 MPa is chosen as the ideal residual stress as a low tensile stress is normally preferred for MEMS structural layers to get flat freestanding structures. A compressive stress can lead to buckling of doubly clamped beams which are larger than the critical length. A large tensile stress might lead to cracking or structural layer delamination. The appropriate normalization equations are given in Eqs (5.1) – (5.3) (161).

$$[Y_i(j)]_{HB} = \frac{y_i(j) - \min(y_i(j))}{\max(y_i(j)) - \min(y_i(j))} \quad (5.1)$$

$$[Y_i(j)]_{LB} = \frac{\max(y_i(j)) - y_i(j)}{\max(y_i(j)) - \min(y_i(j))} \quad (5.2)$$

$$[Y_i(j)]_{NB} = 1 - \frac{|y_i(j) - NV|}{\max\{\max(y_i(j)) - NV, NV - \min(y_i(j))\}} \quad (5.3)$$

In these equations $y_i(j)$ and $Y_i(j)$ are the experimental average and the normalized value of the j th performance characteristic for the i th experiment, and $\max(y_i(j))$ and $\min(y_i(j))$ are the maximum and minimum values of $y_i(j)$ respectively, NV is the nominal value for the residual stress. The grey relational coefficient $\beta_i(j)$ is computed using Eq. (5.4) (162):

$$\beta_i(j) = \frac{\min_i \min_j |Y_o(j) - Y_i(j)| + \lambda(j) \max_i \max_j |Y_o(j) - Y_i(j)|}{|Y_o(j) - Y_i(j)| + \lambda(j) \max_i \max_j |Y_o(j) - Y_i(j)|} \quad (5.4)$$

Where $Y_o(j)$ is the ideal normalized value of the j th performance characteristic which is chosen as 1. $\lambda(j)$ is the distinguishing coefficient for adjusting the interval of $\beta_i(j)$ and is set between 0 and 1. In this case, $\lambda(1) = 0.8$, $\lambda(2) = 0.15$, and $\lambda(3) = 0.05$ for tensile stress, sheet resistance and deposition rate respectively. These values reflected the degree of importance of the output parameters to the thin film development. Finally, by using Eq. (5.5) the grey relational grade (GRG_i) was computed as the average of the grey relational coefficient corresponding to the i th experiment for each performance characteristic.

$$GRG_i = \frac{1}{N_j} \sum_{j=1}^{N_j} \beta_i(j) \quad (5.5)$$

The GRG provides a ranking of the experimental alternatives and the closer to the ideal normalized value, the better [158].

The results of the experiments are provided in Table 5.2. The film thickness (not included), resistivity and deposition rate are fairly uniform for all the films deposited by the same recipes. The wafer-to-wafer uniformity for deposition rate is better than 3% and for those films that were deposited in the same batch, the uniformity is almost zero. This is expected because of the sophisticated LPCVD system which is used within production environments. The normalized average results, the grey relational coefficient, the grey relational grade and the ranking order for the experiments are shown in Table 5.3. Among the 32 experiments, experiment L20 has the highest GRG which implies the best multiple performance characteristics; hence, it is designated as the ‘*experimental best*’.

Table 5.2: Design layout and experimental results

| Exp No. | Experimental layout based on L32 O.A. design | Residual stress (MPa) | | | Deposition rate (nm/s) | | | Sheet resistance (Ω /sq) | | |
|---------|---|-----------------------|--------|--------|------------------------|------|------|----------------------------------|------|--------|
| | | 1 | 2 | 3 | 1 | 2 | 3 | 1 | 2 | 3 |
| L1 | T ₁ S ₁ G ₁ P ₁ B ₁ H ₁ HH ₁ | -46.2 | -42.9 | -43.5 | 0.17 | 0.17 | 0.16 | 942 | 927 | 1058 |
| L2 | T ₁ S ₁ G ₂ P ₂ B ₂ H ₂ HH ₂ | -3.9 | -10.4 | -8.9 | 0.21 | 0.21 | 0.21 | 1604 | 833 | 1701 |
| L3 | T ₁ S ₁ G ₃ P ₃ B ₃ H ₃ HH ₃ | -44.9 | -38.0 | -35.1 | 0.23 | 0.24 | 0.22 | High | 672 | * High |
| L4 | T ₁ S ₁ G ₄ P ₄ B ₄ H ₄ HH ₄ | -72.3 | -123.4 | -63.9 | 0.26 | 0.26 | 0.25 | High | High | High |
| L5 | T ₁ S ₂ G ₁ P ₁ B ₂ H ₂ HH ₃ | -161.8 | -156.4 | -157.8 | 0.13 | 0.13 | 0.13 | High | High | High |
| L6 | T ₁ S ₂ G ₂ P ₂ B ₁ H ₁ HH ₄ | -23.5 | -34.7 | -33.9 | 0.20 | 0.20 | 0.20 | 1164 | 839 | 1195 |
| L7 | T ₁ S ₂ G ₃ P ₃ B ₄ H ₄ HH ₁ | -102.0 | -108.0 | -97.7 | 0.21 | 0.21 | 0.20 | High | High | High |
| L8 | T ₁ S ₂ G ₄ P ₄ B ₃ H ₃ HH ₂ | -64.9 | -70.1 | -56.4 | 0.26 | 0.29 | 0.28 | High | High | High |
| L9 | T ₂ S ₃ G ₁ P ₂ B ₃ H ₄ HH ₁ | -179.2 | -180.8 | -179.8 | 0.15 | 0.15 | 0.15 | High | High | High |
| L10 | T ₂ S ₃ G ₂ P ₁ B ₄ H ₃ HH ₂ | -173.8 | -165.6 | -167.1 | 0.17 | 0.17 | 0.17 | High | High | High |
| L11 | T ₂ S ₃ G ₃ P ₄ B ₁ H ₂ HH ₃ | -142.0 | -140.0 | -144.3 | 0.28 | 0.27 | 0.27 | 354 | 335 | 384 |
| L12 | T ₂ S ₃ G ₄ P ₃ B ₂ H ₁ HH ₄ | -92.6 | -79.9 | -101.4 | 0.31 | 0.31 | 0.30 | 388 | 365 | 388 |
| L13 | T ₂ S ₄ G ₁ P ₂ B ₄ H ₃ HH ₃ | -268.5 | -269.6 | -267.9 | 0.16 | 0.16 | 0.15 | High | High | High |
| L14 | T ₂ S ₄ G ₂ P ₁ B ₃ H ₄ HH ₄ | -205.8 | -209.8 | -199.2 | 0.16 | 0.16 | 0.16 | High | High | High |
| L15 | T ₂ S ₄ G ₃ P ₄ B ₂ H ₁ HH ₁ | -69.9 | -63.7 | -73.3 | 0.26 | 0.26 | 0.26 | High | High | High |
| L16 | T ₂ S ₄ G ₄ P ₃ B ₁ H ₂ HH ₂ | -116.3 | -118.0 | -126.5 | 0.28 | 0.28 | 0.28 | 295 | 267 | 299 |
| L17 | T ₃ S ₁ G ₁ P ₄ B ₁ H ₄ HH ₂ | 7.8 | 19.3 | 19.0 | 0.25 | 0.24 | 0.24 | 337 | 313 | 335 |
| L18 | T ₃ S ₁ G ₂ P ₃ B ₂ H ₃ HH ₁ | -32.1 | -33.5 | -26.5 | 0.28 | 0.27 | 0.28 | 301 | 295 | 335 |
| L19 | T ₃ S ₁ G ₃ P ₂ B ₃ H ₂ HH ₄ | 8.0 | -5.1 | 12.4 | 0.32 | 0.31 | 0.31 | 300 | 259 | 314 |
| L20 | T ₃ S ₁ G ₄ P ₁ B ₄ H ₁ HH ₃ | 25.2 | 24.6 | 24.5 | 0.35 | 0.34 | 0.34 | 336 | 303 | 343 |
| L21 | T ₃ S ₂ G ₁ P ₄ B ₂ H ₃ HH ₄ | 5.6 | 3.6 | 2.9 | 0.24 | 0.23 | 0.23 | 305 | 925 | 425 |
| L22 | T ₃ S ₂ G ₁ P ₄ B ₂ H ₃ HH ₄ | -31.9 | -46.9 | -35.3 | 0.28 | 0.28 | 0.28 | 418 | 376 | 436 |
| L23 | T ₃ S ₂ G ₃ P ₂ B ₄ H ₁ HH ₂ | 2.6 | 3.2 | 5.4 | 0.30 | 0.30 | 0.30 | 967 | 821 | 976 |
| L24 | T ₃ S ₂ G ₄ P ₁ B ₃ H ₂ HH ₁ | -42.2 | -39.3 | -28.5 | 0.33 | 0.32 | 0.32 | 269 | 243 | 274 |
| L25 | T ₄ S ₃ G ₁ P ₃ B ₃ H ₁ HH ₂ | -125.5 | -125.3 | -128.8 | 0.20 | 0.20 | 0.20 | High | High | High |
| L26 | T ₄ S ₃ G ₂ P ₄ B ₄ H ₂ HH ₁ | -124.0 | -121.0 | -119.4 | 0.25 | 0.24 | 0.24 | High | High | High |
| L27 | T ₄ S ₃ G ₃ P ₁ B ₁ H ₃ HH ₄ | -43.4 | -53.4 | -49.6 | 0.27 | 0.26 | 0.27 | 197 | 213 | 216 |
| L28 | T ₄ S ₃ G ₄ P ₂ B ₂ H ₄ HH ₃ | -80.1 | -75.0 | -77.3 | 0.33 | 0.33 | 0.33 | 209 | 181 | 210 |
| L29 | T ₄ S ₄ G ₁ P ₃ B ₄ H ₂ HH ₄ | -186.0 | -179.0 | -183.2 | 0.19 | 0.19 | 0.19 | High | High | High |
| L30 | T ₄ S ₄ G ₂ P ₄ B ₃ H ₁ HH ₃ | -73.6 | -77.2 | -82.1 | 0.26 | 0.26 | 0.26 | 4223 | 393 | 5403 |
| L31 | T ₄ S ₄ G ₃ P ₁ B ₂ H ₄ HH ₂ | -29.1 | -21.4 | -24.0 | 0.26 | 0.26 | 0.26 | 432 | 428 | 438 |
| L32 | T ₄ S ₄ G ₄ P ₂ B ₁ H ₃ HH ₁ | -211.4 | -216.0 | -210.4 | 0.31 | 0.31 | 0.31 | 178 | 170 | 193 |

N.B: ‘High’ denotes the measured sheet resistance that is beyond the capability range of the 4-point probe tool. The values are replaced with 10000 during subsequent analysis.

Table 5.3: Normalized average values, grey relational coefficient (GRC), grey relational grade (GRG) and the ranking order for the experimental runs

| Exp. No. | Normalized average value Y | | | GRC | | | GRG | Ranking Order |
|----------|----------------------------|-------|-------|-------|-------|-------|-------|---------------|
| | RS | DR | SR | RS | DR | SR | | |
| L1 | 0.752 | 0.172 | 0.920 | 0.764 | 0.057 | 0.650 | 0.490 | 17 |
| L2 | 0.874 | 0.375 | 0.878 | 0.864 | 0.075 | 0.552 | 0.497 | 18 |
| L3 | 0.768 | 0.469 | 0.317 | 0.776 | 0.087 | 0.180 | 0.348 | 20 |
| L4 | 0.610 | 0.594 | 0.000 | 0.673 | 0.110 | 0.131 | 0.305 | 23 |
| L5 | 0.369 | 0.000 | 0.000 | 0.559 | 0.048 | 0.131 | 0.246 | 27 |
| L6 | 0.797 | 0.329 | 0.910 | 0.798 | 0.070 | 0.625 | 0.498 | 16 |
| L7 | 0.557 | 0.36 | 0.000 | 0.644 | 0.073 | 0.131 | 0.282 | 24 |
| L8 | 0.686 | 0.688 | 0.000 | 0.719 | 0.138 | 0.131 | 0.329 | 21 |
| L9 | 0.298 | 0.094 | 0.000 | 0.533 | 0.053 | 0.131 | 0.239 | 30 |
| L10 | 0.335 | 0.188 | 0.000 | 0.546 | 0.058 | 0.131 | 0.245 | 28 |
| L11 | 0.424 | 0.672 | 0.982 | 0.582 | 0.133 | 0.893 | 0.536 | 15 |
| L12 | 0.594 | 0.829 | 0.980 | 0.664 | 0.226 | 0.881 | 0.590 | 11 |
| L13 | 0.000 | 0.125 | 0.000 | 0.445 | 0.055 | 0.131 | 0.210 | 32 |
| L14 | 0.214 | 0.141 | 0.000 | 0.505 | 0.055 | 0.131 | 0.230 | 31 |
| L15 | 0.669 | 0.610 | 0.000 | 0.708 | 0.114 | 0.131 | 0.318 | 22 |
| L17 | 0.952 | 0.532 | 0.985 | 0.943 | 0.097 | 0.909 | 0.650 | 5 |
| L18 | 0.797 | 0.688 | 0.987 | 0.798 | 0.138 | 0.919 | 0.619 | 8 |
| L19 | 0.917 | 0.860 | 0.989 | 0.906 | 0.263 | 0.931 | 0.700 | 3 |
| L20 | 0.983 | 1.000 | 0.986 | 0.979 | 1.000 | 0.910 | 0.963 | 1 |
| L21 | 0.914 | 0.485 | 0.963 | 0.902 | 0.089 | 0.799 | 0.597 | 7 |
| L22 | 0.773 | 0.704 | 0.977 | 0.779 | 0.145 | 0.866 | 0.596 | 9 |
| L23 | 0.913 | 0.797 | 0.925 | 0.901 | 0.198 | 0.666 | 0.588 | 12 |
| L24 | 0.777 | 0.907 | 0.992 | 0.782 | 0.348 | 0.948 | 0.693 | 4 |
| L25 | 0.476 | 0.329 | 0.000 | 0.605 | 0.070 | 0.131 | 0.268 | 26 |
| L26 | 0.493 | 0.532 | 0.000 | 0.613 | 0.097 | 0.131 | 0.280 | 25 |
| L27 | 0.737 | 0.641 | 0.998 | 0.752 | 0.123 | 0.982 | 0.619 | 6 |
| L28 | 0.641 | 0.938 | 0.998 | 0.690 | 0.445 | 0.987 | 0.708 | 2 |
| L29 | 0.288 | 0.282 | 0.000 | 0.530 | 0.066 | 0.131 | 0.242 | 29 |
| L30 | 0.640 | 0.610 | 0.558 | 0.690 | 0.114 | 0.254 | 0.353 | 19 |
| L31 | 0.817 | 0.610 | 0.975 | 0.814 | 0.114 | 0.854 | 0.594 | 10 |
| L32 | 0.188 | 0.844 | 1.000 | 0.497 | 0.243 | 1.000 | 0.580 | 13 |
| Total | | | | | | | 1.124 | |

5.1.2 Selection of Optimal Process Condition

The response table (Table 5.4) [142, 163] was computed with Matlab software to determine the effect of each process parameter on these responses. This was computed from the grey relational coefficient (GRC) by taking the average of each parameter at the same parameter level. The horizontal lines of the main effects plot (Fig. 5.2) correspond to the global average of the GRG (0.471). The closer the grey relational grade is to 1, the better is the multi-performance characteristics. From Fig. 5.2 and Table 5.4, the projected optimized condition is selected to be $T_3S_1G_4P_2B_1H_1HH_4$. This is equivalent to the following deposition parameters: deposition temperature (level 3 or 415°C), silane flow rate (level 1 or 8 sccm), germane flow rate (level 4 or 180 sccm), chamber pressure (level 2 or 65Torr), diborane flow rate (level 1 or 11sccm), hydrogen flow rate (level 1 or 500 sccm) and shower head-heater spacing (level 4 or 500 mil). The differences between the maximum and the minimum values of the average GRG are calculated, tabulated and ranked. The most influential factor on the multi-objective performance of the films is the deposition temperature based on these differences. The contributions of the hydrogen and the heater-shower head spacing are insignificant to the overall performance characteristics because of their relatively small difference. Furthermore, the level of significance of other deposition parameters on the multi-performance characteristics can be seen from the ranking in Table 5.4.

Table 5.4: Response table for the grey relational grade

| | Average grey relational grade | | | | Max. - Min. | Rank |
|-----------|-------------------------------|--------------|--------------|--------------|-------------|------|
| | 1 | 2 | 3 | 4 | | |
| T | 0.374 | 0.367 | <u>0.676</u> | 0.455 | 0.310 | 1 |
| S | <u>0.565</u> | 0.479 | 0.436 | 0.386 | 0.179 | 4 |
| G | 0.393 | 0.389 | 0.498 | <u>0.591</u> | 0.203 | 2 |
| P | 0.501 | <u>0.502</u> | 0.416 | 0.396 | 0.114 | 5 |
| B | <u>0.562</u> | 0.529 | 0.395 | 0.390 | 0.173 | 3 |
| H | <u>0.509</u> | 0.470 | 0.460 | 0.430 | 0.079 | 6 |
| HH | 0.438 | 0.467 | 0.480 | <u>0.486</u> | 0.049 | 7 |

N.B: Global average of the grey relational grade based on the response table = 0.466.

Underlined values are the optimum parameter levels which result in the best performance

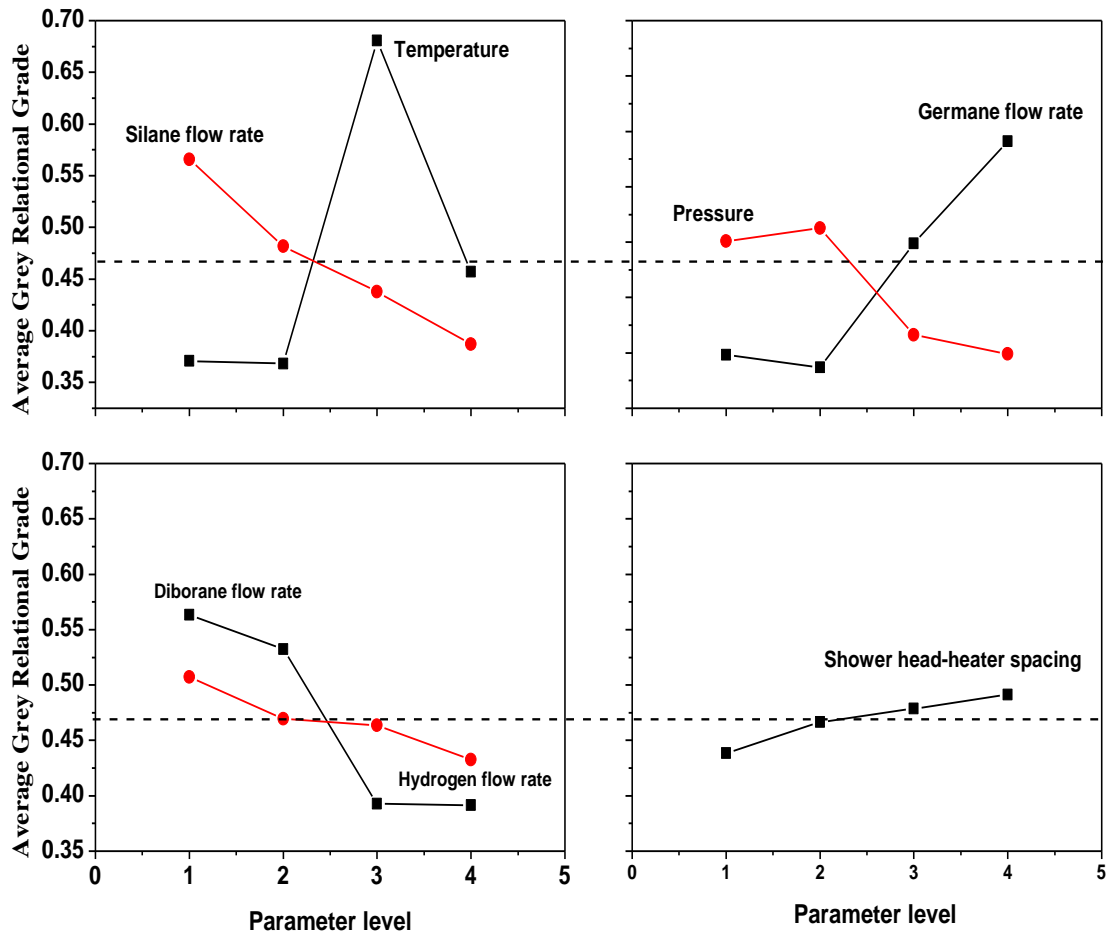


Figure 5.2: Effects plot for grey relational grade showing the influence of parameters levels on the average GRG.

5.1.3 Analysis of Variance (Anova) and Confirmation Test

The analysis of variance (ANOVA) [162, 164] was performed to investigate the level of significance of the process parameters on the variation of the quality characteristics [162]. The contribution of each of the deposition parameters on the combined characteristics of the residual stress, deposition rate and sheet resistance is

investigated. This is done by separating the total variability of the GRG, which is measured by the sum of squared deviations from the total mean of the grey relational grade, into contributions by each deposition parameter and error. The steps for ANOVA are given below.

- Degree-of-freedom for each parameter of N levels is $dof(k) = N - 1 = 4 - 1 = 3$.
- Degree-of-freedom for the treatment $dof(Tr) = \text{Total number of runs} - 1 = 32 - 1 = 31$
- The sum of square deviation due to the experimental treatment is calculated from:

$$SS(Tr) = \sum_{i=1}^{32} (GRG_i - GRG_m)^2 \text{ where } GRG_i \text{ and } GRG_m \text{ are the GRG for the } i\text{th}$$

experiment and the mean of the GRG for the 32 experiments, respectively.

- The sum of squares deviation due to each deposition parameter k is calculated from

$$SS(k) = \sum_{k=1}^7 4(GRG_k - GRG_M)^2 \text{ where } GRG_M \text{ is the global mean of all GRG from}$$

Table 5.4.

- Error due to sum of square is obtained from $SS(error) = SS(Tr) - \sum_{k=1}^7 SS(k)$
- Degree-of-freedom due to error is calculated from

$$dof(error) = dof(Tr) - \sum_{k=1}^7 dof(k)$$

- The variance of the kth parameter is given by $V(k) = \frac{SS(k)}{dof(k)}$
- Variance due to error is obtained from $V(error) = \frac{SS(error)}{dof(error)}$
- The F-value is calculated from $F(k) = \frac{V(k)}{V(error)}$

- The probability- (p-) values is obtained from [165] by using the $dof(k)$ and $dof(error)$ as a numerator and a denominator respectively.

The percentage contribution of each deposition parameter (Table 5.5) gives a clear indication of the individual contributions to the output. The deposition temperature, germane flow rate and diborane flow rate contributed about 40.6, 18 and 15.2% respectively to the change in the stress, resistivity and deposition rate and are significant at 95.0% confidence level (C.L.) going by their probability (p) values. The implication of this finding is that more attention should be focused on temperature, germane and diborane flow rate if any of the film properties is to be modulated substantially.

Table 5.5: Analysis of variance results for multi-performance characteristics

| | T | S | G | P | B | H | HH | Error | Total |
|-------------------------|-------------------|--------------------|---------------------|--------------------|---------------------|------------|-------------|--------------|--------------|
| DOF | 3 | 3 | 3 | 3 | 3 | 3 | 3 | 10 | 31 |
| Sum of Squares | 0.5 | 0.138 | 0.224 | 0.088 | 0.189 | 0.025 | 0.012 | 0.048 | 1.124 |
| Variance | 0.167 | 0.046 | 0.075 | 0.03 | 0.063 | 0.009 | 0.004 | 0.005 | - |
| Contribution (%) | 40.6 | 11.3 | 18.0 | 7.1 | 15.2 | 2.0 | 0.94 | 4.7 | 100 |
| F-value | 28.6 ^b | 8.0 ^{a,b} | 12.7 ^{a,b} | 5.0 ^{a,b} | 10.7 ^{a,b} | 1.4 | 0.7 | - | - |
| p-value | 0.00003 | 0.0051 | 0.0009 | 0.022 | 0.001 | 0.299 | 0.573 | | |

^{a,b}Significant at ^a95% and ^b90% confidence levels, DOF = degree-of-freedom

After the evaluation of the optimal parameter combination, enhancement of the process results using the optimal parametric combination were predicted and verified. A multiobjective verification experiment was conducted using the optimum deposition parameters which are: T=415°C, S=8 sccm, G=180 sccm, P=65 sccm, B=11 sccm, H=500 sccm and HH=500mil. The projected grey relational grade was computed from:

$$(GRG)_{projected} = (GRG)_m + \sum_{k=1}^{N_k} ((GRG)_{optm}(k) - (GRG)_m) \quad (5.6)$$

Where $(GRG)_{optm}(k)$ and $(GRG)_M$ are the optimum grey relational grade for deposition parameter k and the global average of GRG respectively, and $N_k = 7$ is the number of the process parameter. The confirmatory experiment shows that RS increased from -43 to 43MPa while the deposition rate increases from 0.16 to 0.34nm/s (Table 5.6). The film resistivity decreased from 10.18 to 1.39mΩ-cm. and the grey relational grade was improved by about 100% but still slightly less than the projected value. A plausible explanation for this is the inherent measurement error in the stress measurement tool. The condition for the experimental best film is also included in the table. The results of the optimized recipe in the context of others are shown in Fig. 5.3.

Table 5.6: Results of performance measures for initial and optimal deposition parameters

| | Initial parameter | Experimental Best (L20) | Optimal deposition parameter | |
|------------------------|---|---|---|---|
| | | | Predicted | Experimental |
| Combination level | T ₁ S ₁ G ₁ P ₁ B ₁ H ₁ HH ₁ | T ₃ S ₁ G ₄ P ₁ B ₄ H ₁ HH ₃ | T ₃ S ₁ G ₄ P ₂ B ₁ H ₁ HH ₄ | T ₃ S ₁ G ₄ P ₂ B ₁ H ₁ HH ₄ |
| Stress (MPa) | -43 | 24.7 | - | 43 |
| Deposition rate (nm/s) | 0.16 | 0.34 | - | 0.34 |
| Resistivity (mΩ-cm) | 10.18 | 3.47 | - | 1.39 |
| Grey relational grade | 0.49 | 0.96 | 1.09 | 1.00 |

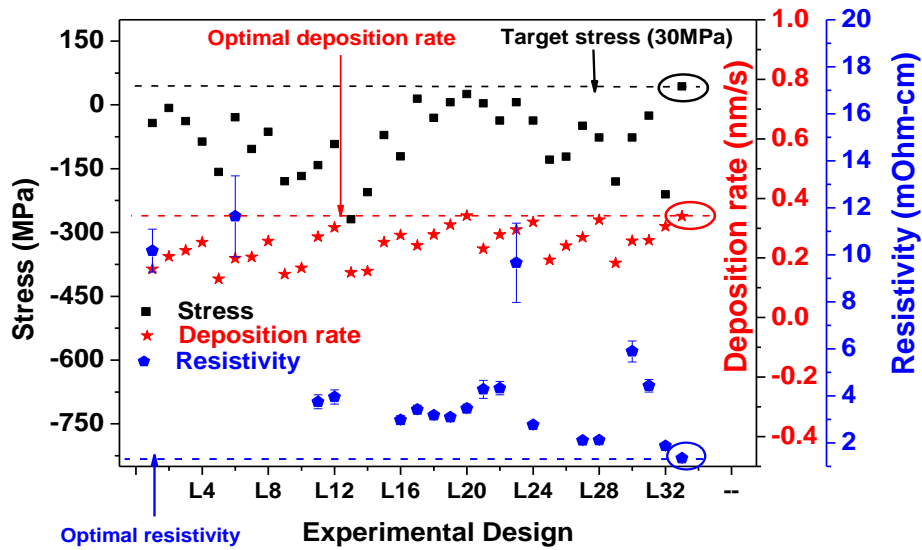


Figure 5.3: Characteristics of the optimized film (in open circle) compared to all experimental data. The horizontal dash lines indicate extension of the optimized properties.

5.2 Further Characterization of the Optimized and the Experimental Best Films

Having obtained the optimized film, further characterization of its properties is essential to be certain of its superior characteristics over other films. Based on the XRD peak parameters of Fig. 5.4 (a), the optimized film is more crystalline than the experimental best film that was obtained from the orthogonal array experimental set-up. This is because the diffraction peaks corresponding to the (111), (220), and (311) planes for the optimized film are stronger and sharper. The value of the full-width-at-half-maximum (FWHM) is 0.58° for the optimized film compared to 1.14° for the experimental best film indicating that the grain size in the former (~ 15 nm) doubles that of the latter (~ 7.5 nm) (assuming the peak width is solely a function of grain size). It should be noted that the absence of dual peaks for a particular diffraction plane indicates that the poly-SiGe alloy is homogeneous.

Also the resistivities of the two films (Table 5.6) confirm that the optimized film is more crystalline. The lower resistivity in the optimized film is justified by its higher carrier concentration ($3.57 \times 10^{21} \text{ cm}^{-3}$ compared to $0.84 \times 10^{21} \text{ cm}^{-3}$ in the experimental best) and higher Hall mobility ($3.76 \text{ cm}^2\text{V}^{-1}\text{s}^{-1}$ compared to $2.04 \text{ cm}^2\text{V}^{-1}\text{s}^{-1}$ in the experimental best). The Rutherford backscattering spectrometry (RBS) profiles indicate that the germanium concentration in the optimized film is 87% (Fig. 5.4b) compared to 89% in the experimental best film. Surprisingly, the higher value of the latter does not translate to better electrical properties as indicated. The cross-sectional SEM image of Fig. 5.4(c) indicates a precise deposition of a 100nm thick SiGe film. Both the AFM and top-down SEM images show that the optimized film exhibits a cauliflower surface morphology where smaller grains aggregate to form larger grains (Fig. 5.4 d & e). The root mean square surface roughness of the optimized film (4.2nm) is slightly lower than that of the experimental best film (4.6nm) indicating a high surface uniformity.

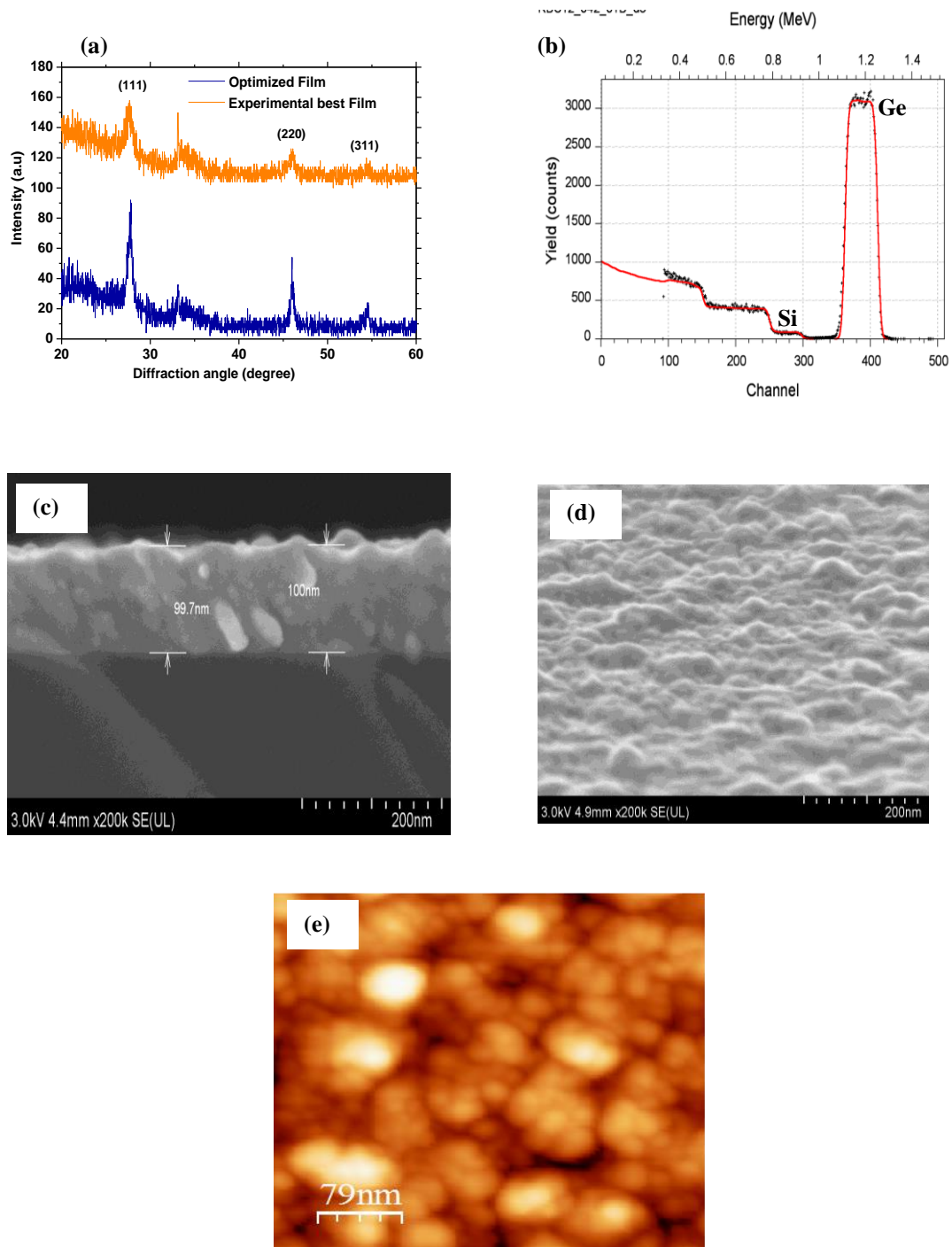


Figure 5.4: (a) Glancing incidence XRD spectra of the optimized film shows slightly sharper peaks than those of the experimental best film for (111), (220) and (311) planes, (b) RBS profile shows 87% Ge fraction in the optimized sample (c) cross-sectional SEM image (d) surface topography and (e) AFM images of the optimized film.

5.3 Investigation of the Influences of Germanium Fraction, Boron Concentration and Chamber Pressure on Some Films Properties

This section describes the parametric studies conducted to examine how the germanium fraction, boron concentration and the chamber pressures (CP) influence the film resistivity, stress, deposition rate, grain size and surface properties of ultrathin poly-SiGe films. These parameters were selected because they significantly influence the properties of the films (see section 5.1 for details). The resistivity and residual stress are among the most important characteristics of poly-SiGe thin films. The resistivity determines the electrical response when poly-SiGe is used as a structural layer for M/NEMS applications. A condition with slightly tensile stress is required for thin films if delamination or structural failure is to be prevented. Higher deposition rate will enhance fabrication of poly-SiGe based devices if the process is to be economically viable. It is therefore important to investigate how these characteristics change with some deposition parameters. Deposition temperature and other conditions were kept constant while the film thickness is kept at 100 ± 5 nm. Twelve films were deposited following the process conditions listed in Table 5.7. Experiment No. 1- 4, 5- 8 and 9 -12 were conducted to study the influence of germanium fraction, boron concentration and the chamber pressures (CP) on the above stated properties. The chemical composition and crystal structure were obtained by using SIMS and XRD in the glancing incidence mode. The carrier concentration and mobility were determined by Hall measurement. The surface structures were characterized by AFM and the mechanical properties were obtained from nanoindentation measurements.

Table 5.7: Process condition for the SiGe deposition

| Exp. No | T _{sub} (°C) | $\frac{*GeH_4}{SiH_4}$ | CP (Torr) | $\frac{\#B_2H_6}{SiH_4}$ | H ₂ (sccm) | HH (mil) | Time (s) |
|---------|-----------------------|------------------------|-----------|--------------------------|-----------------------|----------|----------|
| 1 | 415 | 100/8 | 65 | 11/8 | 500 | 500 | 550 |
| 2 | 415 | 140/8 | 65 | 11/8 | 500 | 500 | 380 |
| 3 | 415 | 180/8 | 65 | 11/8 | 500 | 500 | 295 |
| 4 | 415 | 200/8 | 65 | 11/8 | 500 | 500 | 250 |
| 5 | 415 | 180/8 | 65 | 12/8 | 500 | 500 | 290 |
| 6 | 415 | 180/8 | 65 | 15/8 | 500 | 500 | 275 |
| 7 | 415 | 180/8 | 65 | 18/8 | 500 | 500 | 295 |
| 8 | 415 | 180/8 | 65 | 20/8 | 500 | 500 | 280 |
| 9 | 415 | 180/8 | 50 | 11/8 | 500 | 500 | 415 |
| 10 | 415 | 180/8 | 60 | 11/8 | 500 | 500 | 312 |
| 11 | 415 | 180/8 | 70 | 11/8 | 500 | 500 | 280 |
| 12 | 415 | 180/8 | 80 | 11/8 | 500 | 500 | 250 |

N.B: T_{sub} = substrate temperature, *10% GeH₄ in H₂, CP=chamber pressure, #1% B₂H₆ in H₂, HH = heater-shower head spacing

5.3.1 Germanium Fraction

As previously discussed, germanium helps to reduce deposition temperature for on-CMOS applications. It can substantially reduce the residual stresses by increasing the crystalline properties of the films. Most importantly, it can be tuned to change the strain gradient in free-standing cantilevers. Fig. 5.5 (a) is one of the RBS measurements for calculating the germanium fractions in the films. The yield tails at approximately channels 150, 260, 300 and 420 correspond to Si in the silicon substrate, Si in the SiO₂ layer, Si in the SiGe film and Ge in the SiGe film, respectively.

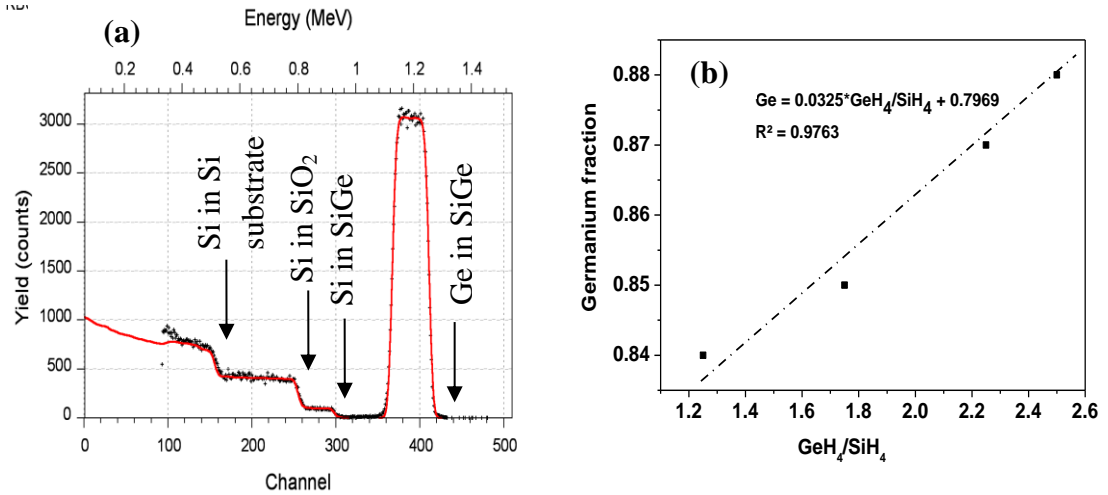


Figure 5.5: (a) Example of an RBS profile for measuring germanium fraction (b) correlation between germane/silane flow rate ratio and the germanium fraction in the films.

By calculating the Ge fractions in the other films, a good fit is obtained for GeH₄/SiH₄ ratios and the corresponding germanium fractions (Fig. 5.5b). With $R^2 = 0.98$, the fraction of germanium can be evaluated from $Ge = 0.0325 * GeH_4/SiH_4 + 0.7969$, assuming other deposition parameters are kept constant. The films are quite uniform as evidenced by the symmetry of the Ge peak.

All the films are polycrystalline as revealed by the significant peak intensity of the (111), (220) and (311) planes (Fig. 5.6) which is consistent with most published data [55, 68 – 71]. From these XRD spectra, the existence of single peaks at diffraction angles between the expected angles for Ge and Si is noted. This implies that the layers are of a homogeneous material and not built out of large clusters of Ge-rich materials embedded in silicon or vice versa. Generally, the (111) peak is slightly broader than the other peaks indicating that the grains associated with this orientation are finer than others. The peaks

intensities for all the orientations improve with increased germanium fractions accompanied with a decrease in full width at half-maximum (FWHM), suggesting that the incorporated germanium atoms significantly enhance the grain growth and thus the crystalline fraction. However, the increased germanium fractions do not influence the peak positions.

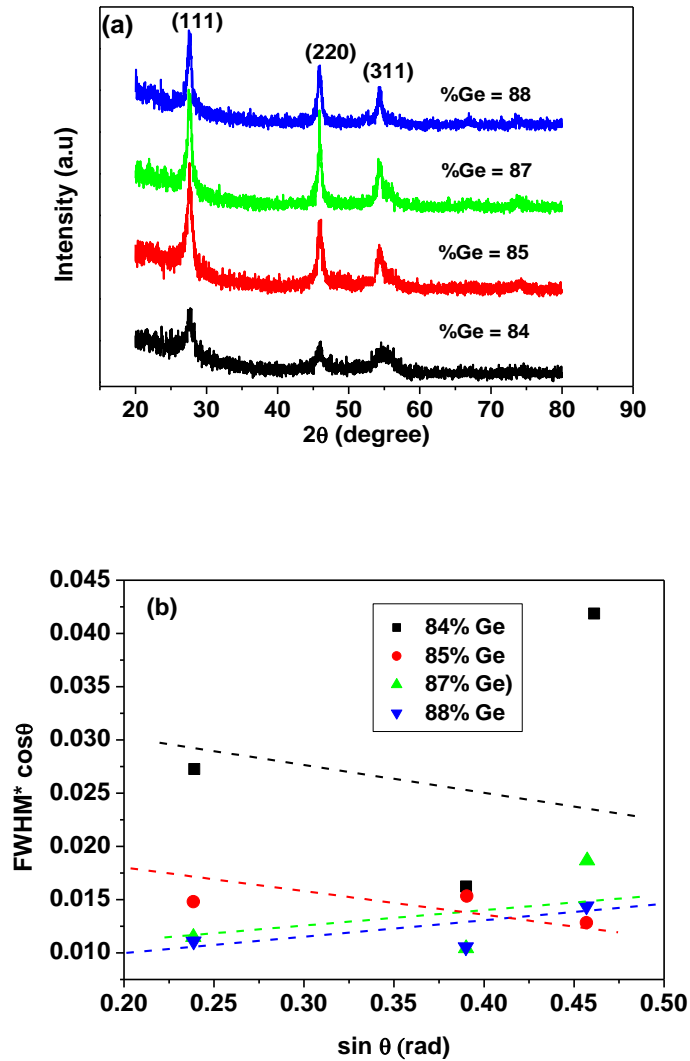


Figure 5.6: (a) GIXRD spectra for the films containing different germanium fractions (b) grain size and residual stress calculation.

The influence of the germanium fraction on the carrier concentration and carrier mobility, resistivity, stress and deposition rate are shown in Fig. 5.7. Because of the increased germanium fraction, carrier scattering is reduced which evidently raises the carrier mobility (Fig. 5.7 a). It is instructive to state that in spite of the constant boron concentration ($\sim 2.20 \times 10^{21} \text{ cm}^{-3}$), the number of the active carriers increases to a maximum value of $1.4 \times 10^{21} \text{ cm}^{-3}$ at a germanium fraction of 0.85. The carrier concentration remains relatively constant thereafter. This indicates that the amount of effective carrier in poly-SiGe films depends on the boron and germanium concentrations. While the carrier concentration remains relatively constant for $0.85 < x < 0.88$, the Hall mobility increases from ~ 2.0 to $\sim 4.2 \text{ cm}^2 \text{ V}^{-1} \text{ s}^{-1}$. This may be due to the increased grain size (Fig. 5.7 a) which leads to a reduction in the grain boundary density and possible defects at the grain boundaries. Generally, the low value of the Hall mobility observed in these samples may be attributed to the polycrystalline nature of the films and also to the low deposition temperature which significantly influences the crystalline fraction. The resistivity of the poly-SiGe film is lowered from 7.4 to 1.1 $\text{m}\Omega\text{cm}$ when germanium fraction is increased from 0.84 to 0.88.

To investigate how the changes in the germanium fractions influence the grain size and the contribution of the grain size to the measured resistivity, the full-width-at-half maximum (FWHM) was calculated from the XRD spectra of Fig. 5.6a. Two approaches were used and their results were compared. In the first approach, the grain size was estimated by assuming the microstrain (or stress) as well as the instrumental contribution to the XRD peak width are negligible. By using the Scherrer equation (166), the grain size D was calculated from: $D = 0.9\lambda/(\text{FWHM} \cdot \cos\theta)$ where λ is the X-ray

wavelength and FWHM is determined in radian. The grain size showing in Fig. 5.7(b) represents the average value based on the three peaks observed from the diffraction spectra. In the second approach, the influence of the microstrain is taken into consideration while the instrumental broadening B_o is assumed to be negligible. The grain size D and the strain ε were simultaneously obtained from the following equation [167]: $FWHM = \frac{0.94\lambda}{D\cos(\theta)} + 4\varepsilon \frac{\sin(\theta)}{\cos(\theta)} + B_o$. By plotting $FWHM * \cos(\theta)$ against $\sin(\theta)$ (Fig. 5.6 b), ε and D are obtained from the slope and the intercept, respectively. The grain size obtained thus is shown in Fig. 5. 7 (b). The results of the two approaches are quite similar except for the film with 84% Ge. Accordingly, the residual stresses do not contribute significantly to the peak broadening and thus not considered for calculation in the latter discussion. It should be noted that the residual stresses calculated from above approach are -1000, -174, -170 and 298 MPa for 84, 85, 87 and 88% Ge. These values differ from the experimental values of -178, -139, -19 and 43 MPa for the Ge fraction accordingly.

From the above results, it is clear that the grain size doubles, from ~6nm to ~12nm, which indicates a similar decrease in the grain boundary density. This consequently reduces the grain boundary defects and thus the carrier trapping and scattering at the grain boundaries [168]. As a result, the mobility improves (as discussed). Also the deposition rate doubles from 11 nm/min to 22 nm/min for the same range of germanium fraction. This may be due to the germanium enhanced desorption of hydrogen from the deposition surface [71].

For the residual stresses, it is observed that the films become more tensile, increasing from -125 MPa to 65 MPa, as the germanium fraction is increased from 0.84

to 0.88 (Fig. 5.7c). This behaviour is attributed to larger grain and also to the higher thermal stress (about 139 MPa) associated with the higher germanium fraction. Within the range of germanium fraction examined, the XRD peaks show essentially no shift, indicating that a change in lattice constant is negligible and that it does not contribute to the change in the stress.

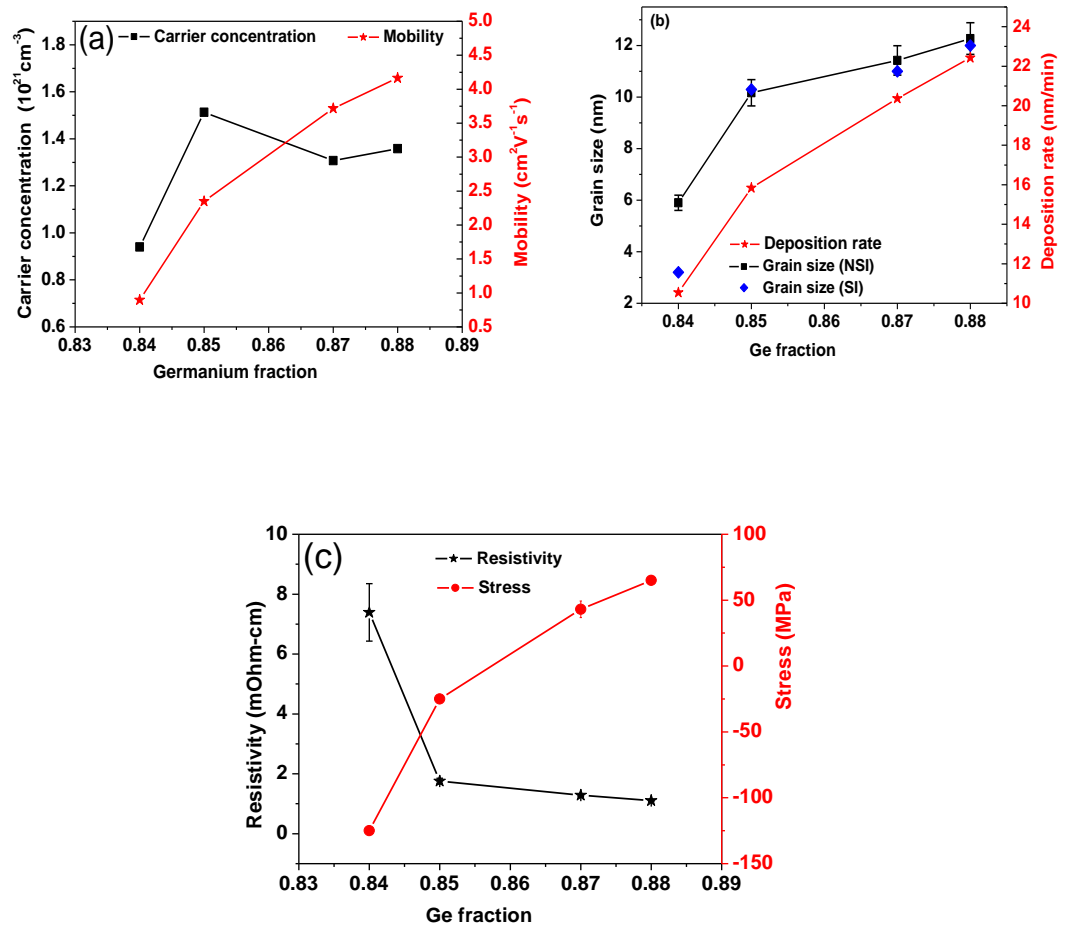


Figure 5.7: Influences of germanium fractions on (a) Hall mobility and carrier concentration (b) grain size and deposition rates; NSI indicates ‘No influence of Strain is Included’, SI means ‘influence of Strain is Included’ in the calculation (c) resistivity and stress. Boron concentration is $2.20 \times 10^{21} \text{ cm}^{-3}$

To complement the previous observations, two films with germanium fractions of 0.84 (film 1) and 0.87 (film 2) are deposited and characterized with transmission electron microscopy (TEM). The cross-section TEM images (Fig. 5.8 a, b) indicate that the films 1 and 2 are ~110nm and ~90nm thick, respectively. The top surfaces of the SiGe layers are rough (Fig 5.8 a, b). A few bright field images were taken to observe the different grains size (Fig. 5.8 c, d). The contrast variations seen in the images are due to diffraction in the grains. Because the grains are very small, they are difficult to observe with much certainty. However, the grains are smaller in the film 1 than in the film 2 (10-20nm), which complements the grain size obtained from the XRD spectra (Fig 5.7 b) for the film with 87% germanium. Also, no obvious change of grain size with depth in the layers is observed. This indicates that most of the grains show columnar structure across the layer, which is however more obvious in the film 2 than in the film 1. Such columnar structure results in a relatively high-compressive local stresses across the film thickness (as discussed in chapter 6). The stronger peaks of the XRD spectra (Fig. 5.6 a) for the film 2 imply larger grains or higher crystalline fraction and not due to its thickness.

In addition, the HR-TEM images of Fig. 5.9 and Fig. 5.10 show the lattice spacing in the films. Clearly, the films are polycrystalline but some fractions of amorphous materials are present. Distinguishing between the amorphous and the crystalline component is difficult due to projection overlap. For the expanded view of Fig. 5.10, the fully crystallized and the less crystallized regions are visible. Also, the grain orientation and crystal lattice spacing are indicated. By calculation, the lattice spacing is found to be ~0.3nm for the (111) plane while the lattice parameter is estimated to be ~0.5nm which is close to the lattice spacing for Ge (0.565nm).

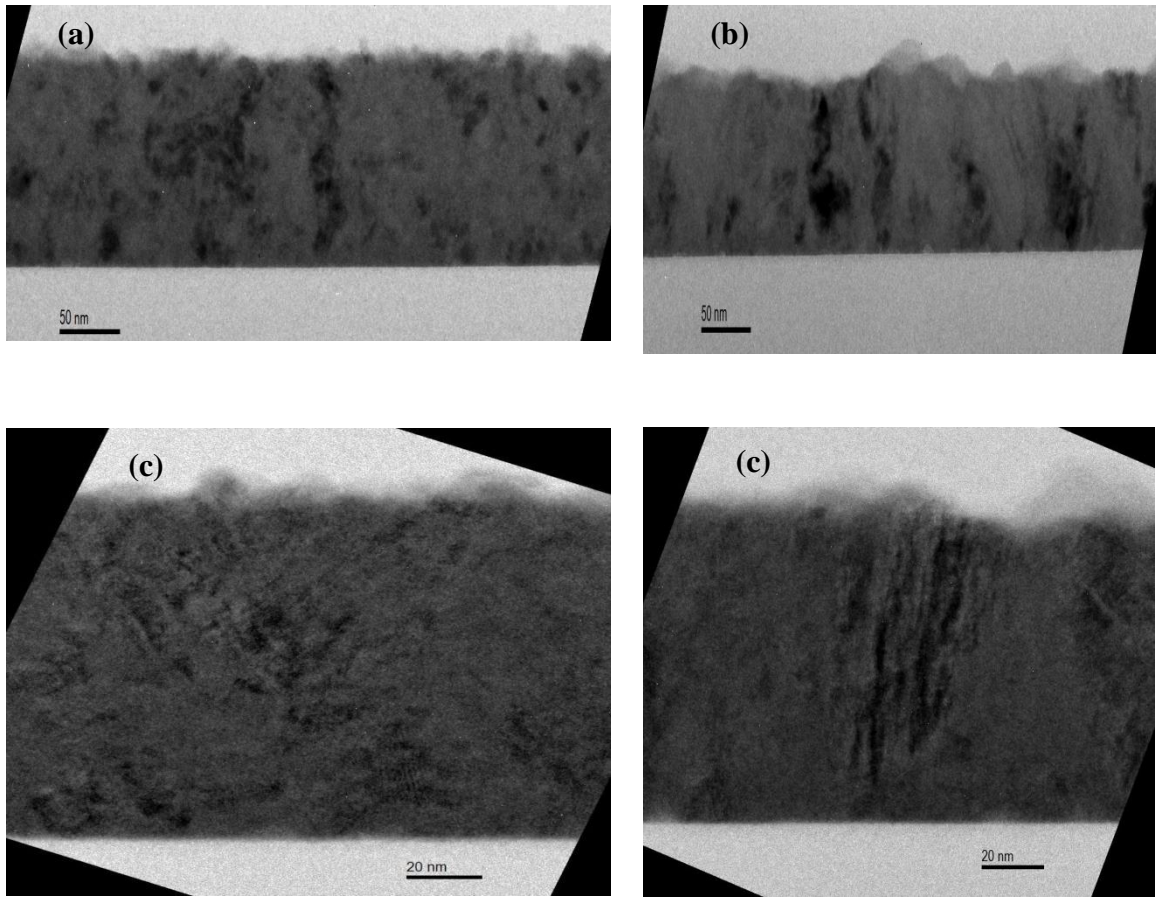


Figure 5.8: Cross-section dark field TEM images for the films containing (a, c) 0.84 (b, d) 0.87 of germanium fraction

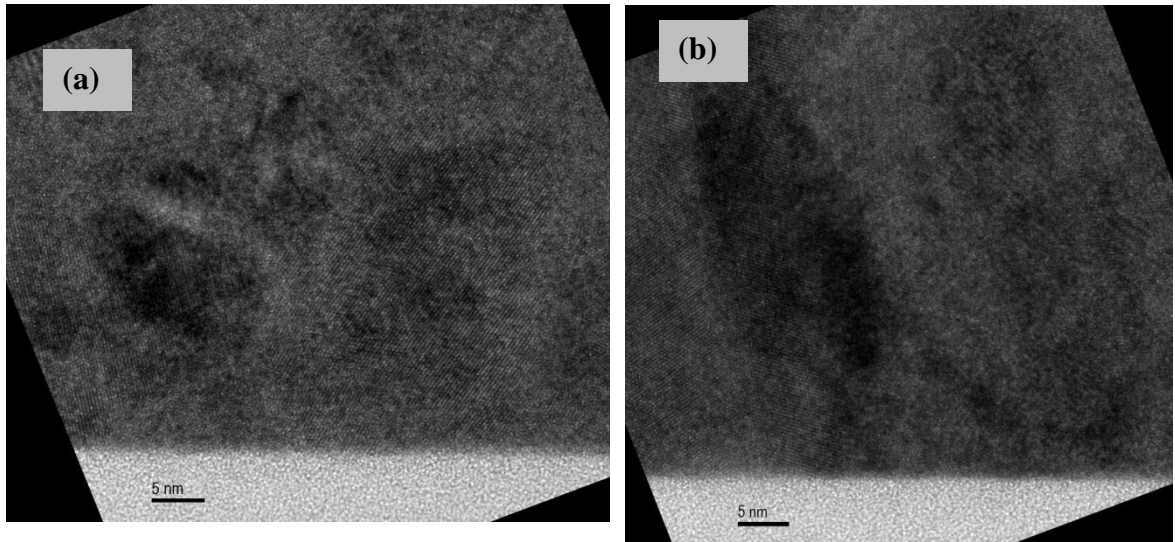


Figure 5.9: Cross-section dark field TEM images with lattice resolution showing the crystal lattice as well the crystalline and the amorphous component for the poly-SiGe film with germanium fraction of (a) 0.84 - film 1 (b) 0.87 – film 2.

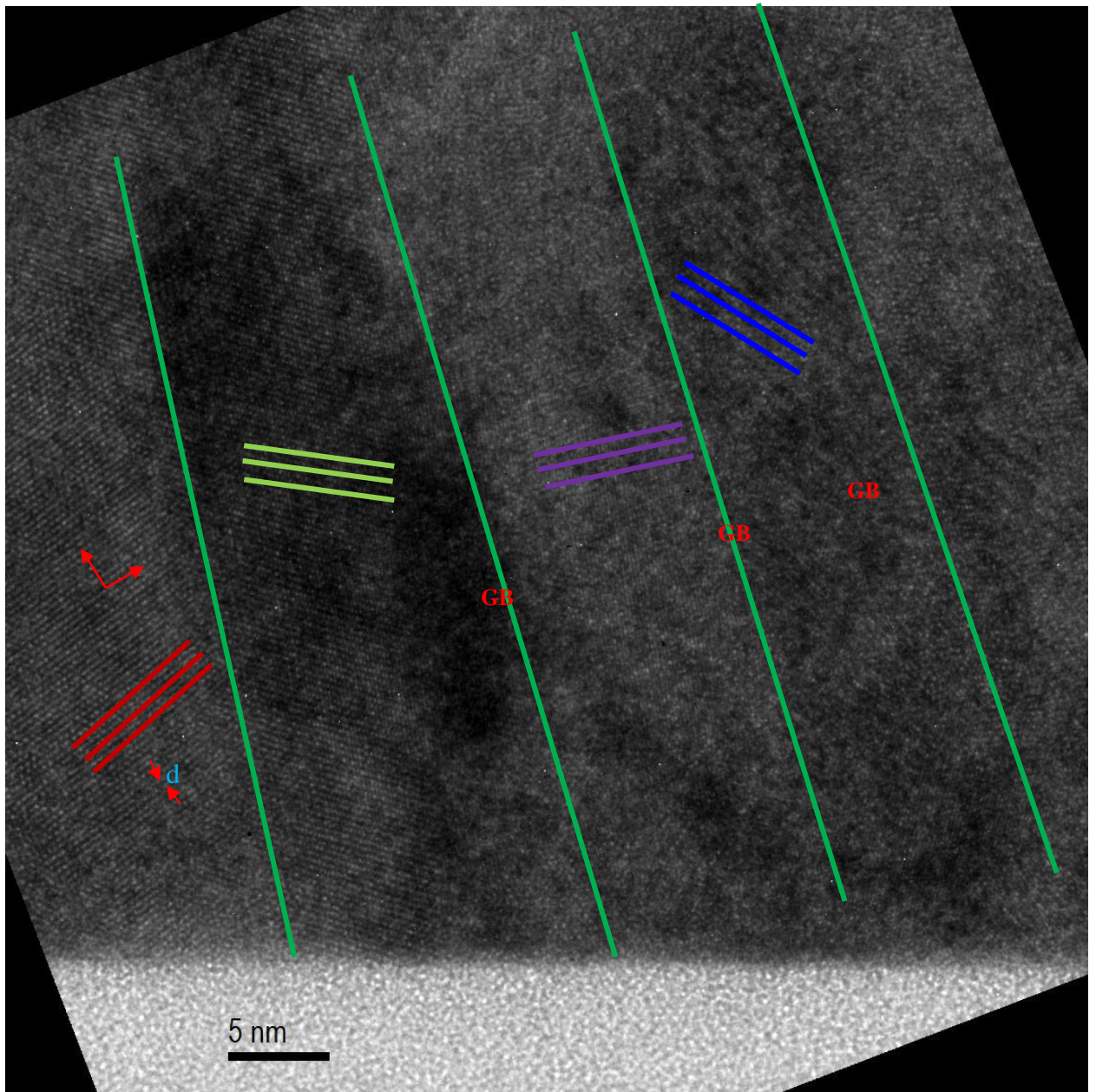


Figure 5.10: Expanded Cross-section dark field TEM images showing the crystal planes, inter-planar spacing 'd', the grain size and grain boundary (GB) for the film 2. The sample is oriented along a $\langle 110 \rangle$ zone axis of the substrate. Red arrows indicate $\{111\}$ plane.

Figure 5.11 shows 2 $\mu\text{m} \times 2 \mu\text{m}$ AFM images of the films deposited at different germanium fractions. The images show island-like morphology commonly observed in thin films deposited by LPCVD. Cauliflower morphology is observed at the surface of these films which increases in size with increased germanium fractions. The cauliflower surface morphology is also obvious from the SEM image of Fig. 5.11(e). To understand the roughening mechanism and growth behaviour of poly-SiGe films under the germanium influence, the scaling theory is applied. From the theory, the correlation functions, root mean square (rms) of the surface roughness, correlation length and scaling exponents of the growing films are evaluated by assuming that the rough surfaces exhibit self-affine and isotropic characteristics [78]. These parameters are obtained from the analysis of the height- height correlation function.

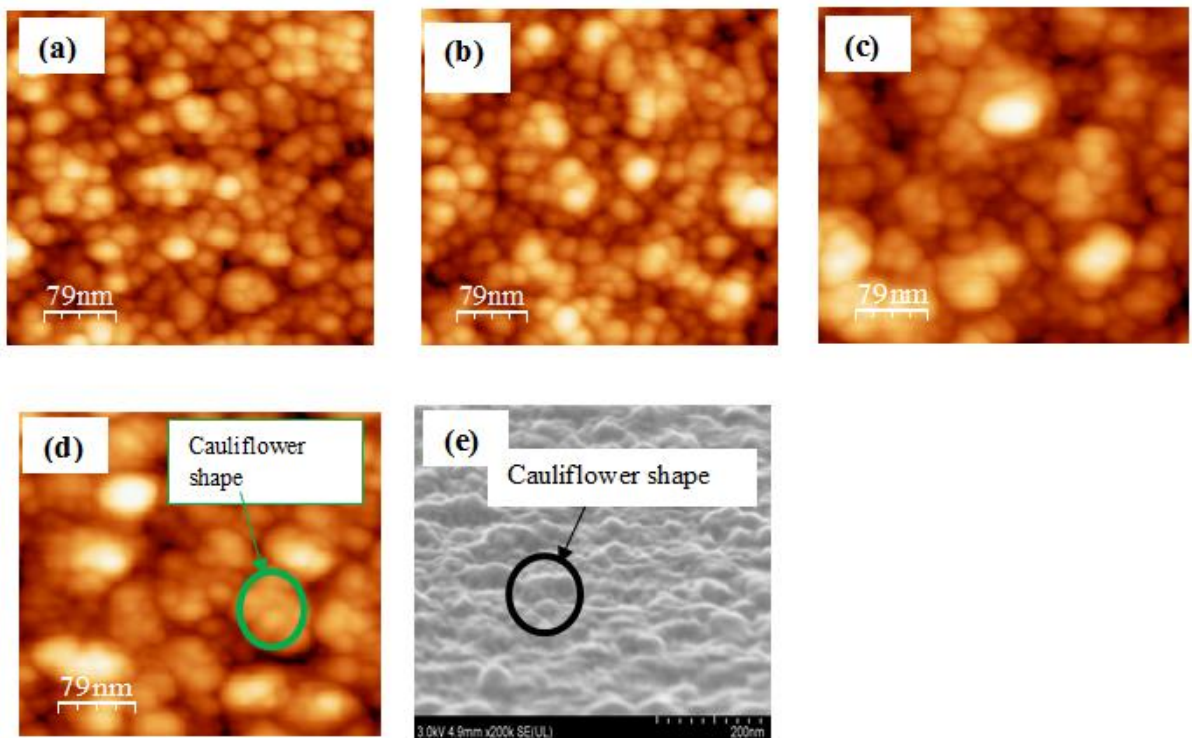


Figure 5.11: AFM images (400 nm x 400 nm) of poly-SiGe ultrathin films grown with germanium fraction of (a) 0.84, (b) 0.85, (c) 0.87, and (d) 0.88, (e) equivalent SEM image of (b).

The height - height correlation function $H(r)$ is calculated from $H(r) = \langle [Z(r) - Z(0)]^2 \rangle$ where $Z(r)$ and $Z(0)$ are the surface heights at coordinate $r [= (x, y)]$ and reference position $(0, 0)$. The brackets $\langle . . . \rangle$ indicate a statistical average. Log-log plots of $H(r)$ for the films deposited at varied germanium fractions are shown in Fig. 5.12 (a). For a surface that shows a self-affine fractal behaviour on a short length scale and that is smooth on a long length scale, $H(r)$ can be fitted to the following equation [77].

$$H(r) = 2\sigma^2 \left\{ 1 - \exp\left[-(r/\xi)^{2\alpha}\right] \right\} \quad (5.8)$$

where σ denotes the rms roughness which characterizes the vertical morphology of a surface, ξ is the lateral correlation length which is a measure of the lateral fluctuations of the surface feature which is related to the grain size [169], α is the roughness exponent which describes the local “jaggedness” of the topography. For the films with varied germanium fraction, all the corresponding $H(r)$ follow a similar trend (Fig. 5.12 a). The values of α and ρ are calculated from $H(r) \propto \rho^2 r^{2\alpha}$ at the region I where $r \ll \xi$ (79) and ρ is the average magnitude of the lateral surface slope. The parameter σ is obtained from $H(r) = 2\sigma^2$ at the region II where $r \gg \xi$. The set of roughness parameters σ, ξ, α and ρ allows a comprehensive quantitative characterization of a random rough surface. These parameters are plotted against germanium fraction in Fig. 5.12 (b and c).

From the height-height correlation function, the correlation length has a similar trend with the grain size obtained from the XRD technique. However, the grains size obtained from the AFM images are twice as large as those obtained from the XRD and TEM techniques. This difference is probably because the grain size measured from AFM is the surface-projected grain size due to the surface morphology of coalesced grains [170] while XRD and TEM provide information based on the average crystallite size

which is usually much smaller in comparison. Also, AFM tips are often not sharp enough and may distort the observed images and thus influence the calculated grain size. In addition, the possibility that all the grains are not perfectly columnar cannot be ruled out. Similar to the XRD results, exposed grain size is found to increase from 24nm to 32 nm when the germanium fraction is increased from 0.84 to 0.88.

Except for the film deposited with a germanium fraction of 0.84, it is observed that increased germanium fraction roughens the film surfaces (Fig. 5.12b). The increased rms roughness from 3.8nm to 4.8nm can be attributed to the increased grain size (see Fig. 5.7c) or increased density of cauliflower structures (Fig. 5.11). It is interesting to know that the lowest rms roughness is found when germanium fraction is 0.85 at which the film resistivity is virtually independent of the germanium fraction (Fig. 5.7) or a point of transition from a largely amorphous film to a polycrystalline films (Fig. 5.6a). This may be a good film for applications where minimum surface roughness is a dominant requirement. Also, the roughness exponent α slightly increases from 0.93 to 0.97 as germanium fraction is increased from 0.84 to 0.88 (Fig. 5.12c). From published data, higher value of α (close to 1) indicates that the surface has “smooth” hills and valleys (Fig. 5.11) (81), which is expected for a surface diffusion dominated or surface reaction limited growth process (82) like LPCVD technique. Both σ and ρ have a similar trend, indicating that the increased germanium fraction generally increases the rms roughness of the films.

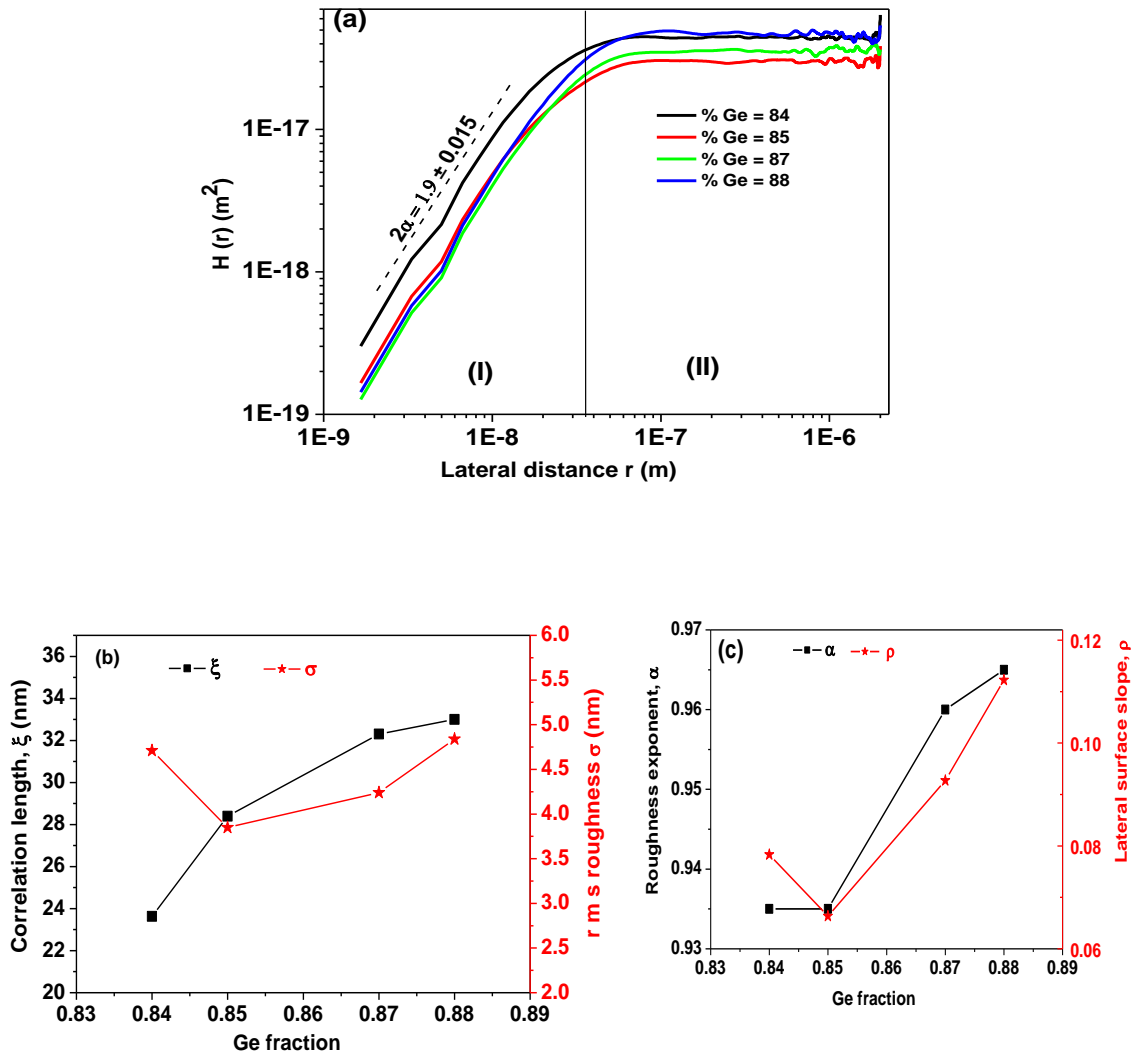


Figure 5.12: (a) Height–height correlation function $H(r)$ (b) rms roughness and correlation lateral length (c) roughness exponent and lateral surface slope for 100 nm-thick poly-SiGe films deposited under varied germanium fractions.

5.3.2 Boron Concentration

Doping poly-SiGe with boron enhances deposition at significantly lower temperature ($\sim 450^\circ\text{C}$) which is compatible with standard CMOS and often results into low as-deposited stress and low electrical resistivity [21, 22]. However care must be taken to ensure that appropriate boron concentration is added to prevent an abnormal behaviour where resistivity is increased at higher doping level [55]. Figure 5.13(a) shows a secondary-ion-mass spectroscopy (SIMS) depth analysis of the boron concentrations in the poly-SiGe films deposited at varied $\text{B}_2\text{H}_6/\text{SiH}_4$ ratios. For all the films, the germanium fraction is kept at 0.87. Figure 5.13(b) shows the boron concentration in all the films as a function of the $\text{B}_2\text{H}_6/\text{SiH}_4$ ratios. The ratio was varied from 0.015 to 0.025 which resulted in the incorporated boron concentrations ranging between $2.4 \times 10^{21} \text{cm}^{-3}$ and $4.27 \times 10^{21} \text{cm}^{-3}$. The Figure indicates that the quantity of boron atoms incorporated into the film is linearly proportional to $\text{B}_2\text{H}_6/\text{SiH}_4$ ratios. With $R^2 = 0.98$, the concentration of boron in the film can be evaluated from $B = 181.7 \times 10^{21} \text{B}_2\text{H}_6/\text{SiH}_4 - 0.38 \times 10^{21}$, provided other deposition parameters are kept constant.

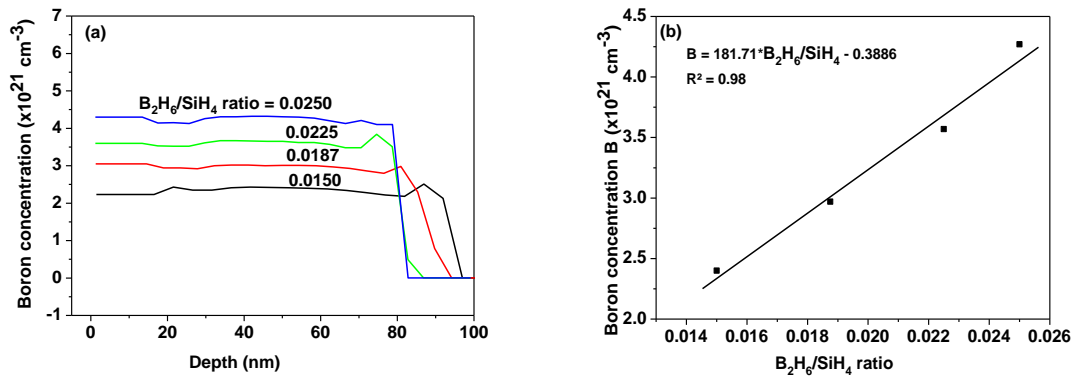


Figure 5.13: (a) SIMS profiles for the measured boron concentrations (b) correlation between $\text{B}_2\text{H}_6/\text{SiH}_4$ ratios and the boron concentrations.

Figure 5.14 shows how the boron concentration influences the crystallinity of poly-SiGe ultrathin films. The grain size decreases with an increased boron concentration which is indicated by the reduction in the peak intensities and an increase in the full-width-at-half maximum of the XRD spectra (Fig. 5.14a). The decrease in the intensity is accompanied by a reduction in the grain size and a marginal increase in the deposition rate (Fig. 5.14b). The grain size is estimated in a similar way as described in section 5.3.1. The reduction in the grain size, within the interval of the boron concentration examined, indicates that the boron atoms may impede the grain growth during deposition resulting in the shrinkage of grain [70]. This may also lead to the boron-induced degradation in the electrical characteristics such as the resistivity, carrier concentration and mobility [168] which will be discussed in the next few paragraphs.

A higher boron concentration does not enhance the growth rate although boron atoms are known to act as adsorption sites for both silicon and germanium atoms [70]. This is not important because the boron in poly-SiGe films is a dopant which influences the electronic properties and not the deposition rate.

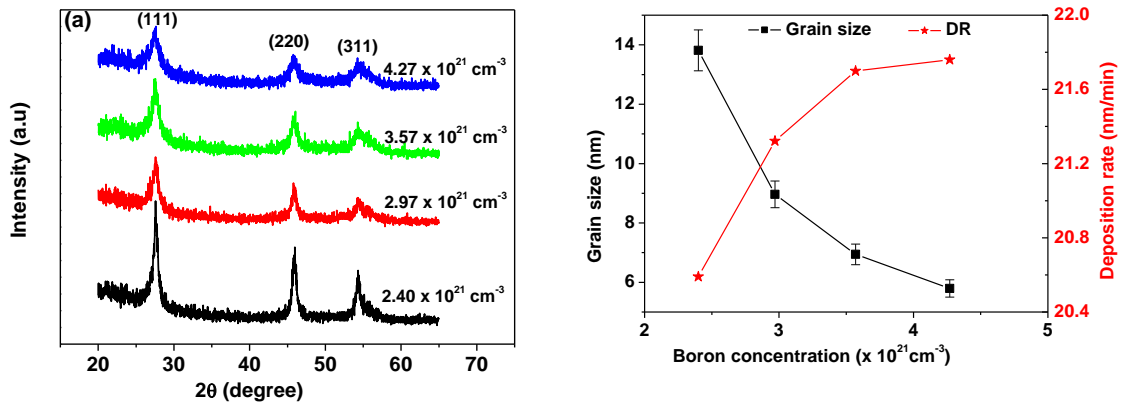


Figure 5.14(a) GIXRD spectra for the films containing different germanium fractions (b) influence of germanium fraction on the changes in the grain size and deposition rates

The amount of boron incorporated has a significant effect on electrical properties of as-deposited poly-SiGe films, which all exhibit p-type as identified by Hall Effect measurements. Figure 5.15(a) shows a significant decrease in the carrier concentration and in the Hall mobility as boron concentration increases. For all the films, the carrier concentration decreases dramatically due to the structural degradation since the boron concentration is greater than the optimum boron value of $4.0 \times 10^{19} \text{ cm}^{-3}$ (68). The excess boron atoms occupy the substitutional sites, instead of interstitial positions, inside the grains and thus obstruct electron movement across the grain boundary. Thus, the mobility is limited by ionized impurity scattering which dependent on the doping level. For *in situ* boron-doped poly-Si₁₂Ge₈₈ films deposited between 800 – 900 °C, Hellberg et al. [171] find that the boron solubility in poly-SiGe is about $4.5 \times 10^{19} \text{ cm}^{-3}$. At a lower deposition temperature used for this study (415°C), the boron solubility will be slightly lower and may be the similar to the value obtained by Sedky et al. [68]. This implies that the boron atoms in these films are not fully activated because they are more than one order of magnitude higher than the solid solubility of boron in SiGe films. This type of films is often referred to as ‘highly’ or ‘heavily doped’ films. For the highest doping level of $4.27 \times 10^{21} \text{ cm}^{-3}$, the effective carrier concentration drops to a value of $\sim 4.0 \times 10^{20} \text{ cm}^{-3}$ which is one order of magnitude lower than the incorporated boron concentration.

Depending on the film resistivity and the doping level, Hall mobility may increase or decrease with carrier concentration. For an increase in the boron concentration from 2.4×10^{21} to $4.27 \times 10^{21} \text{ cm}^{-3}$ at a constant germanium fraction of 0.87, the Hall mobility decreases from ~ 3.7 to $\sim 2.4 \text{ cm}^2 \text{ V}^{-1} \text{ s}^{-1}$. The decrease in the carrier concentration and in the Hall mobility accounts for the observed increase in the film resistivity from 1.54 to

5.56 mΩcm (Fig. 15b). The increase in resistivity may also be due to the reduction in the grain size from 14 to 6 nm (Fig. 5.14b). For a highly doped film, the increased grain boundary density/trapping states will effectively enhance capture of free carriers to form a potential barrier which ultimately degrades the electrical properties of the films.

With reference to the residual stresses, it is observed that the films become less compressive with boron concentration. The stress value goes from -100 MPa for a film with boron concentration of $2.4 \times 10^{21} \text{ cm}^{-3}$ and stabilizes at -20 MPa at a boron concentration of $2.97 \times 10^{21} \text{ cm}^{-3}$. This might be due to film densification as a result of pore annihilation.

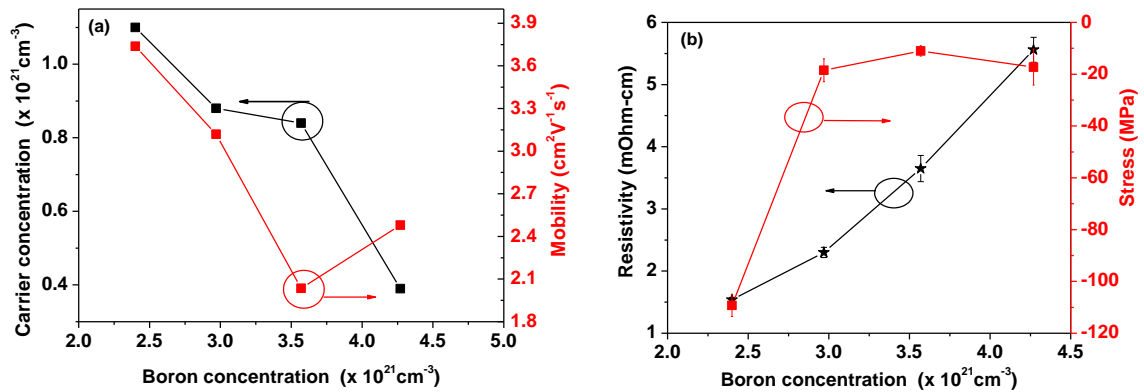


Figure 5.15(a) Dependence of Hall mobility and carrier concentration on germanium fraction (b) resistivity and stress under the influence of varied germanium fractions. Boron concentration is kept at $3.57 \times 10^{21} \text{ cm}^{-3}$.

From the AFM images (Fig. 5.16) and the standard deviation of resistance, it appears that varying boron concentrations does not significantly influence the film surface roughness. Consequently, AFM images are obtained for the films with the minimum ($2.40 \times 10^{21} \text{ cm}^{-3}$) and maximum ($4.27 \times 10^{21} \text{ cm}^{-3}$) boron concentrations as well as minimum (50 Torr) and maximum (80 Torr) chamber pressures. Following the procedure discussed in section 5.3.1, the film surface properties are analyzed and the results are summarized in Table 5.8. By increasing the boron concentration from $2.4 \times 10^{21} \text{ cm}^{-3}$ to $4.27 \times 10^{21} \text{ cm}^{-3}$, the rms roughness just slightly increases from 4.18 nm to 4.63 nm. This difference is insignificant and may lie within the measurement accuracy. The roughness exponent also shows an insignificant difference. As a result, boron concentration is not a factor to consider if the surface roughness is to be significantly modulated for any application of interest. In addition, the lateral correlation length reduces from $\sim 30 \text{ nm}$ to $\sim 28 \text{ nm}$ for the same increase in the boron concentration. This correlates well with the grain size although with lower value, as shown in Fig. 5.14.

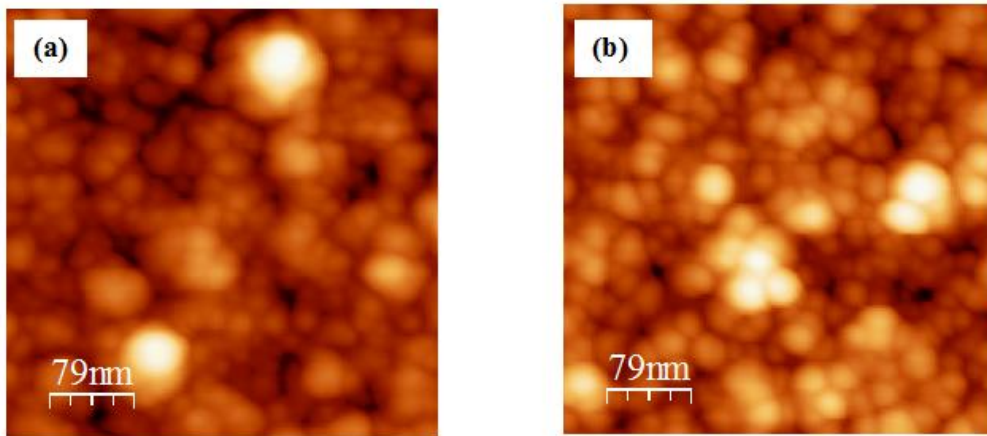


Figure 5.16: AFM images of poly-SiGe ultrathin films grown with boron concentration of (a) $1 \times 10^{21} \text{ cm}^{-3}$ (b) $4 \times 10^{21} \text{ cm}^{-3}$ at a constant germanium fraction of 0.87 and boron concentration of $3.57 \times 10^{21} \text{ cm}^{-3}$.

Table 5.8: Surface characteristics for the influences of boron concentration and chamber pressure

| Exp. Run | Condition | RMS roughness σ (nm) | Lateral correlation length ζ (nm) | Roughness exponent α |
|----------|---|-----------------------------|---|-----------------------------|
| 5 | Boron = $2.4 \times 10^{21} \text{ cm}^{-3}$ | 4.18 | 30.48 | 0.95 |
| 8 | Boron = $4.27 \times 10^{21} \text{ cm}^{-3}$ | 4.63 | 27.57 | 0.94 |
| 9 | Pressure = 50 | 4.77 | 28.53 | 0.95 |
| 12 | Pressure = 80 | 4.57 | 39.17 | 0.97 |

5.3.3 Chamber pressure

A change in the chamber pressure does not significantly influence the film crystallinity as revealed by the similar peak intensities, FWHM for all the diffraction planes (Fig. 5.17a). This implies that the grain size remains virtually unchanged within the pressure range considered (Fig. 5.17b). However, a change in the trend for the carrier concentration is observed at a pressure of 70 Torr ((Fig. 5.17d). Below 70 Torr, the carrier concentration increases and then decreases thereafter. Because the change in the resistivity with pressure is negligible (Fig. 5.17c), Hall mobility is inversely proportion to the carrier concentration. In spite of similar boron concentrations in the films, this behaviour is expected since the quantity of the effective carriers is regulated by the boron concentration, silicon and germane fractions.

A higher pressure increases the amount of the Si and Ge precursors which increases the deposition rate [172]. Therefore, the deposition rate increases as the process pressure goes up [173]. Increasing chamber pressure influences the residual stress in two folds (Fig. 5.17c). Between 50 and 60 Torr, the films become slightly tensile but more compressive thereafter. Because the resulting grains are expected to be more conical

rather than columnar in shape at low pressure [127]; the films deposited at lower pressure are less compressive.

The rms roughness is not significantly affected by increasing the chamber pressure from 50 Torr to 80 Torr (Fig. 5.18, Table 8). It changes from 4.77nm to 4.57 nm which may be due to the constant grain size (Fig. 5.14b).

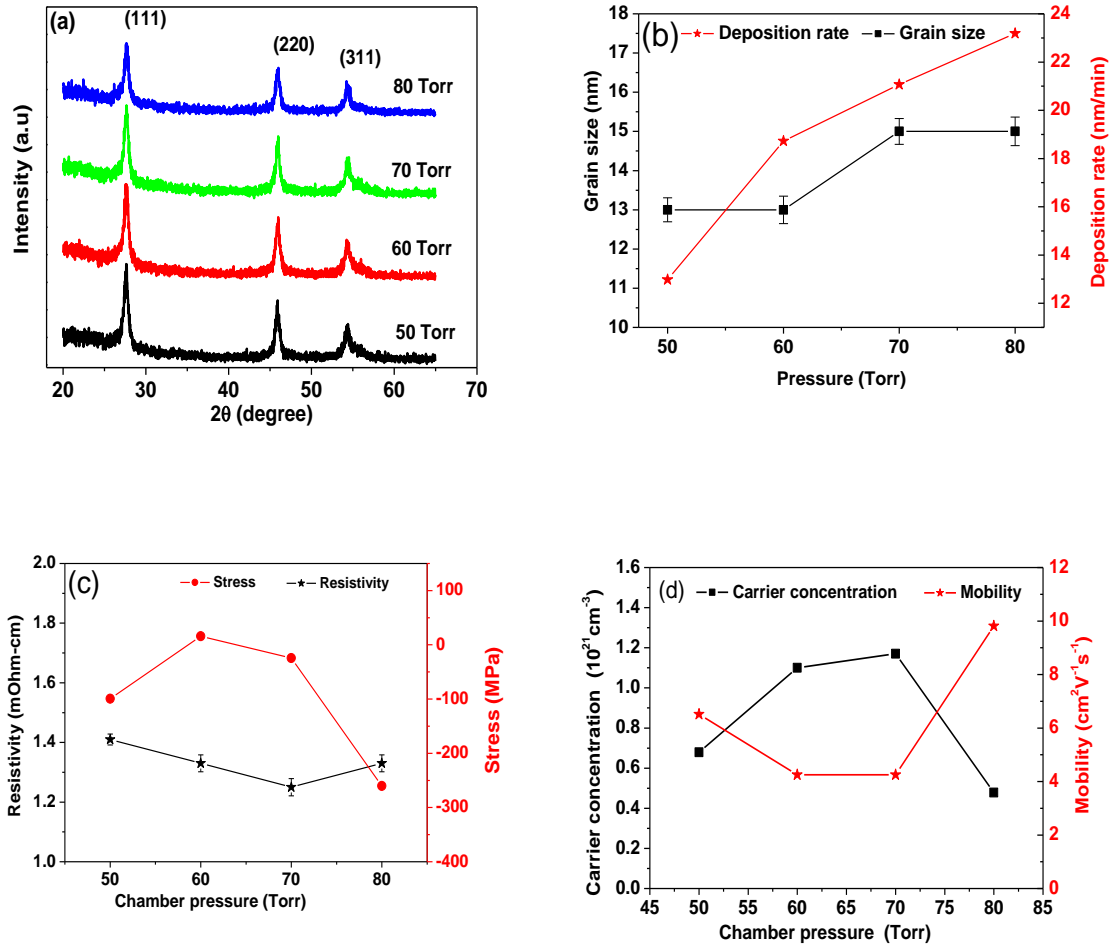


Figure 5.17: Influence of chamber pressure on (a) GIXRD spectra (b) grain size and deposition rate (c) resistivity and stress (d) carrier concentration and Hall mobility

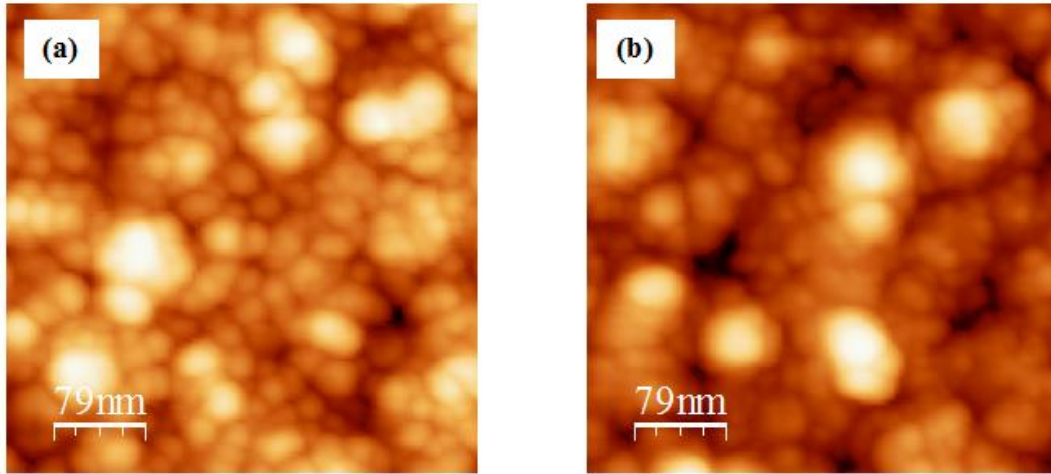


Figure 5.18: AFM images of poly-SiGe ultrathin films grown under chamber pressure of (a) 50 Torr (b) 80 Torr at a constant germanium fraction of 0.87 and boron concentration of $3.57 \times 10^{21} \text{ cm}^{-3}$

5.3.4 Influence of Germanium fraction on the Elastic Moduli and Hardness of Poly-SiGe

The influence of varying germanium fractions on the modulus and hardness of poly-SiGe films is evaluated for 100 nm thick films using the nanoindentation experiment discussed in section 3.4.2. Each point on the load-indentation depth curve (Fig. 5.19a) is an average of 10 repeated measurements. The load/depth versus depth ($P/h - h$) curve (Fig. 5.19b) and the modulus versus indentation depth ($E-h$) curve (Fig. 5.19c) are obtained from the load versus indentation depth ($P-h$) curve. For most homogeneous elastoplastic materials, the indentation loading curve obtained with self-similar indenter tips, such as Berkovich, conical, or pyramidal, are usually well described by $P = Kh^2$ [174]. From the changes in the $P/h-h$ relations, the indentation range containing the film properties without the severe effect of the substrate can be extracted. In other words, care

must be taken to ensure that the influence of the results by the substrate is significantly minimized. The selection of the critical thickness is illustrated in Fig. 5.19(b), where a linear portion of the $P/h-h$ curve is obtained for the indentation depths between 10 and 40 nm (stage II). Other regions (I, III) diverge from linearity and thus unsuitable. The critical point is extrapolated to the E-h curve where the modulus is selected between $h = \sim 35$ and $h = 43$ nm. The increased modulus with indentation depth up to ~ 10 nm (Fig. 5.19c) can be attributed to the transition between purely elastic to elastoplastic contact whereby the hardness is actually the contact pressure [175]. At the region where modulus does not substantially diverged or does not exhibit significant scattering, E is evaluated to be 101.09 ± 0.81 GPa.

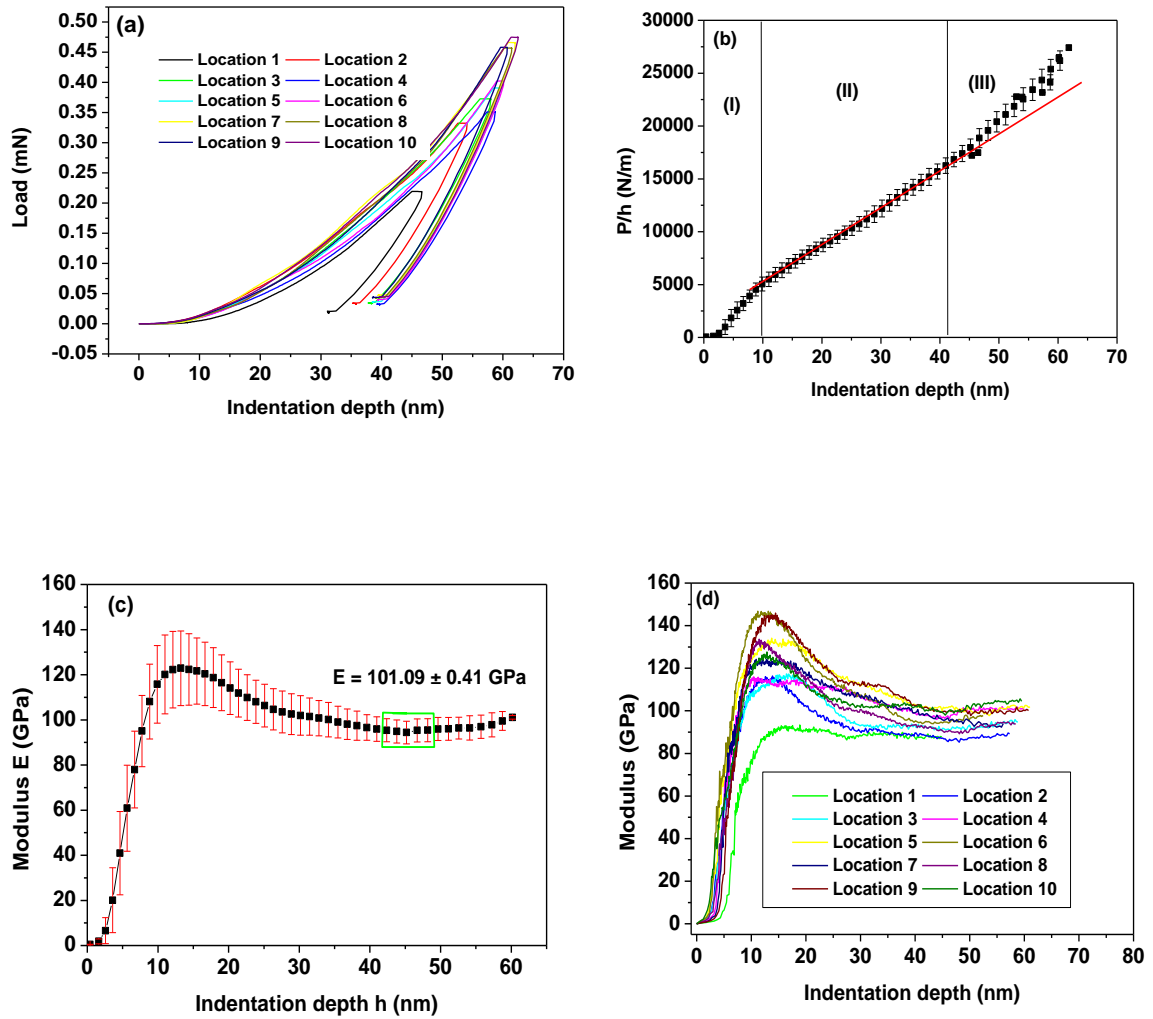


Figure 5.19: Nanoindentation curves for a 100 nm thick poly-SiGe film deposited with Germanium fraction of 0.84 (a) load versus indentation depth curve, (b) P/h versus h curve (c) modulus versus displacement curve (d) indentation curves.

A plot of hardness H as a function of the indenter depth is shown in Fig. 5.20. Similar to the observation in the $E-h$ curve, H increases with h up to $h = \sim 20$ nm. To explain this observation, Tsui et al. [176] noticed that since the force of the indenter is compressive and acts perpendicularly to the surface, compressive strain should increase

the hardness by diminishing the shear stresses beneath the indenter. The average hardness value is selected between 40 and 50 nm, where the hardness is relatively constant, to eliminate the influence of the underlying substrate. The hardness value is 8.74 ± 0.04 GPa for one of the samples.

The choice of the critical position on the P/h-h and E-h curves where modulus and hardness were evaluated (i.e. depth of about 40% of the film thickness) is in contrary to the popular Buckle's rule [177]. The rule predicts that the substrate will not significantly affect the mechanical properties of the top film if the indentation is less than 10% of the thickness of the film. This rule is, at best, a first approximation based on instruments using Vickers and Berkovich indenters. However, it seems not accurate for organic materials, metals and ceramics where indentation depth of 10-20% of film thickness is found to be appropriate and even numerical simulations put the depth at 33% [178].

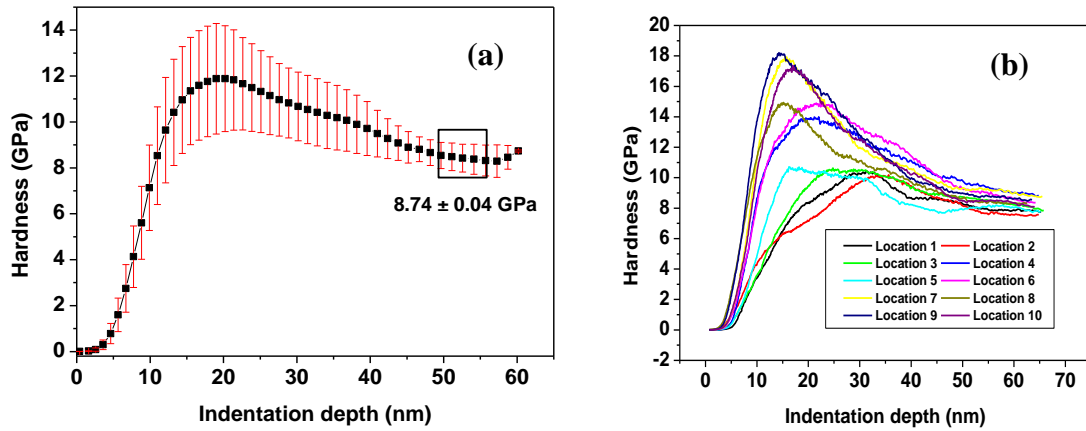


Figure 5.20: Hardness versus indentation curves for a 100nm thick poly-SiGe film deposited with germanium fraction of 0.84. Inset depicts the indentation curves for the 10 locations of Fig. 5.19(a).

Recently, Clifford and Seah [179] found that for layered systems with thicknesses below $5\ \mu\text{m}$, the 10% rule was generally invalid. They proposed that $\delta_{\text{max}} < 0.012 \cdot h^2/R$ is satisfied if the modulus is not to be influenced by the substrate. In this equation, δ_{max} is the maximum or critical indentation depth, h is the film thickness and R is the indenter radius. However, this model cannot explain our observation. For $R = 10 - 100\ \text{nm}$, the values of δ_{max} ($\sim 1.2 - 16\ \text{nm}$) is within the region where surface roughness effect is dominant (Fig. 5.20). Therefore, evaluating the modulus and hardness at this region is not appropriate. It suffices to say that the significant scattering in the E-h and H-h curves may be attributed to the relatively high rms roughness of these samples (see section 5.3.3). To rule out the influence of surface morphology, the indentation depth should be greater than the characteristic size of the surface roughness [180]. At a low indentation depth of $\sim 10 - 20\ \text{nm}$, the z-value of the rms roughness lies within the same range as the depth of indentation. This implies that the full tip radius of the indenter does not come in contact with the film surface simultaneously within this region.

Following the above evaluation procedure, the elastic moduli and hardness values were calculated for other films. The results are shown in Fig. 5.21. Based on this Figure, it is observed that either the changes in the germanium fractions do not significantly influence the hardness and elastic modulus of poly-SiGe film or that the resolution of the experimental nanoindenter is larger than the changes in the mechanical properties of the films. By considering the error bars in Fig. 5.21, it is instructive to state that the differences in the values of the moduli are within the measurement error. Theoretically, the modulus of poly-Si_{1-x}Ge_x films, x being the germanium fraction can be evaluated by using $E_{\text{Si}_{1-x}\text{Ge}_x} (\text{GPa}) = 173 - 41x$. This relationship is derived by taking moduli of poly-

Si and poly-Ge as 173 and 132GPa, respectively [181], assuming that the modulus is linearly related to the germanium fraction. For the films deposited with germanium fraction of 0.84, 0.85 and 0.87, the resulting films moduli are 139, 138 and 137GPa, respectively. Obviously, these moduli are far higher than those measured via nanoindentation. This may be because the films are very thin and their properties are still evolving. In addition, the calculated values are values for a poly-crystalline material without preferred texture. Depending on the film orientation and amorphous fraction in the film, smaller or higher values might occur.

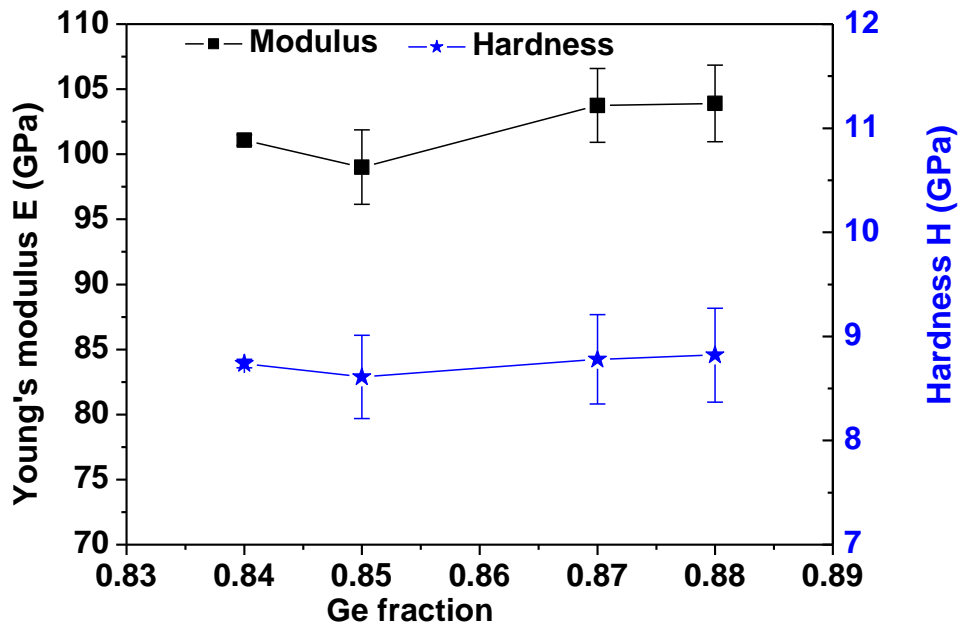


Figure 5.21: Elastic modulus and hardness variation with germanium fraction. All the films contain $2.20 \times 10^{21} \text{cm}^{-3}$ of boron. Both properties are not significantly influenced by the changes in the germanium fractions.

CHAPTER 6

EVOLUTION OF STRESS, RESISTIVITY AND SURFACE CHARACTERISTICS OF POLY-SiGe FILMS

In this chapter, detailed experimental studies of the evolution of stress, resistivity and surface properties of poly-SiGe films are presented. Various film thicknesses (~1nm – ~200 nm) are deposited by LPCVD and characterized following the techniques described in chapter 3. The experimental study shows that the intrinsic stress evolves from a pre-coalescence highly compressive stress state to coalescence less compressive state and remains constant thereafter. Also, the film's structural evolution goes through an incubation stage to a pre-coalescence stage (< 40 nm) over a transient stage (40-60 nm) and finally to a stagnation stage (> 60 nm) as evidenced by the AFM images as well as the Hall mobility. The surface properties were characterized by correlation length, root-mean-square (rms) roughness, roughness exponent, dynamic exponent and fractal dimension.

6.1 Stress Evolution

Two recipes of poly-SiGe films (A & B) were used for stress evolution study. Recipes A and B are the experimental best and optimized recipes, respectively, as reported in chapter 5. The films grown from these recipes are subsequently termed films A and B. The deposition conditions for the two films are presented in Table 6.1. For each

recipe, a few wafers were selected from the same wafers box and processed for various film thicknesses. The stress, thickness, morphology, resistivity, carrier concentration and Hall mobility were measured *ex-situ* following the procedures discussed in chapter 3.

Table 6.1: Deposition conditions used for evolutionary study

| Recipe | T _{dep} (°C) | SiH ₄ (sccm) | GeH ₄ (sccm) | CP (Torr) | B ₂ H ₆ (sccm) | H ₂ (sccm) | HH (mil) | Time (s) |
|--------|--------------------------|----------------------------|----------------------------|--------------|---|--------------------------|-------------|-------------|
| A | 415 | 8 | 180 | 60 | 18 | 500 | 470 | 5 - 565 |
| B | 415 | 8 | 180 | 65 | 11 | 500 | 500 | 5 - 565 |

T_{dep} = deposition temperature, CP = chamber pressure, HH = header-to-shower head spacing

6.1.1 Stress Evolution Curves

The stress evolution curves for films A and B are shown in Fig. 6.1. The error bars are the standard deviations based on 5 repeated measurements. All the measured stresses contain both the thermal and the intrinsic stress components. Since all the films are deposited at a temperature of 410°C ($T_{deposition}$) and characterized at the room temperature of 20°C (T_{room}), the thermal stress component σ_{th} is computed from Eq. (6.1).

$$\sigma_{th} = \frac{E_{SiGe}}{1-\nu_{SiGe}} (\alpha_{SiGe} - \alpha_{Si}) (T_{deposition} - T_{room}) \quad (6.1)$$

where E, ν and α denote the elastic modulus, Poisson's ratio and thermal expansion coefficient, respectively. For an assumed $E_{SiGe} = 100 \text{ GPa}$ (obtained from the nanoindentation experiments discussed in section 5.3), $\nu_{SiGe} = 0.22$, $\alpha_{Si} = 2.6 \times 10^{-6} \text{ K}^{-1}$, $\alpha_{SiGe} = 5.38 \times 10^{-6} \text{ K}^{-1}$ [180], the thermal stress $\sigma_{th} \sim 139 \text{ MPa}$. Since the thermal expansion coefficient of poly-SiGe is higher than that of Si, the thermal

stress generated in the film is tensile as the substrate is cooled from the deposition temperature of 410°C to room temperature of 20°C . Both the total and intrinsic stresses for the two films are shown in Fig. 6.1 (a) while the initial state of the intrinsic stress evolution is shown in Fig. 6.1 (b). At the initial growth states (precoalescence and coalescence stages), the total stress is dominated by the intrinsic stress components. However, the thermal stress component becomes significant during the continuous growth stage bringing the average stress to a tensile stress regime. Based on Fig. 6.1(a), it is observed that the intrinsic stresses in the films A & B evolve from an initial highly compressive stress regime to a less compressive stress state and stabilize thereafter. This behaviour differs from those of materials that exhibit Type I and type II behaviour (details in section 2.4). It is termed 'Modified Type I behaviour' but at the compressive stress regime. Indeed, poly-SiGe has a high melting point, low adatom mobility or a low surface and grain boundary diffusivities at low temperature. In such a case, the tendency for adatom movement into the grain boundary is insignificant making the stress to remain constant as the film thickens (182). Another explanation for the constant compressive stress can be made on the basis of the TEM images of Fig. 5.8. The columnar nature of the grains is an indication that the grain size does not vary significantly across the film thickness. This presupposes that the film is growing faster in the longitudinal direction compare to the lateral dimension.

In both films, the phenomena leading to the initial highly compressive stress state have been extensively discussed in the literature. The large stress changes observed at the onset of film growth (Fig. 6.1b) can be attributed to the island growth and coalescence of the neighbouring islands as they attempt to minimize the surface energy at the expense of

some elastic deformations [106, 183, 184]. With island growth and coalescence, the grain boundary grows and an average local tensile stress is generated within a very small interval of time. The island pre-coalescence compressive stress state can also be attributed to the capillarity effect of the island surfaces [185], the atomic peening effect [186], the island shape transition and the surface stress effect [103]. It should be noted that, unlike for materials that exhibit Type II behaviour, the tensile stress generated during coalescence process for poly-SiGe film under the current processing conditions, is not high enough to bring the average stress in the film to a tensile stress state but it significantly reduces the average compressive stress state. For the films thickness of ~40nm and greater (Fig. 6.1 b), it appears that the coalescence process is completed. Also, the relatively constant values of the post-coalescence stresses indicate that the film is in a continuous growth state. In addition, it signifies an insignificant grain grows with thickness as shown in the TEM images. In both films, further reduction in the post-coalescence compressive stress is not observed with increased thickness up to ~200nm.

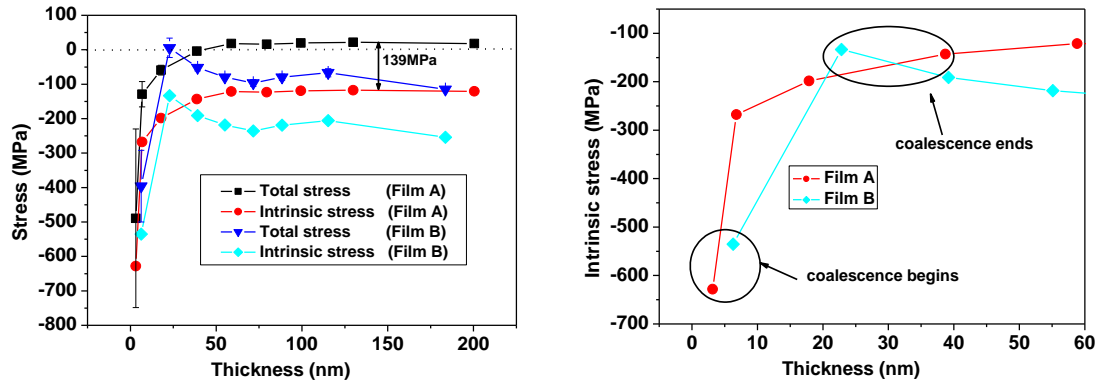


Figure 6.1: (a) Stress evolution curves for the films A and B (b) expanded view of the initial growth stage showing intrinsic stress changes during coalescence process. The continuous lines are guides to the eyes. The vertical lines are the error bars based on the standard deviation of five repeated measurements. 139 MPa indicates the offset between the total and the intrinsic stresses

6.1.2 Stress-Thickness Evolution and Local Stresses

During the film deposition, it is important to note that the measured curvature K determines the product of the average stress in the film and the film thickness ($\langle\sigma\rangle h_f$) and this can be expressed as:

$$\langle\sigma\rangle h_f \propto K \quad (6.2)$$

The change in the curvature (or the stress-thickness) of the substrate prior to and after film deposition is a measure of the applied force, due to growth stress, on the film. It thus defines the extent and direction that a released structure will bend or deflect. The stress-thickness product is sometimes called ‘force per width’ or ‘integrated stress’ in the

literature [103]. The stress-thickness versus thickness evolution curves for the two films are shown in Fig. 6.2 (a) and the initial stages of evolution are shown in Fig. 6.2 (b). It should be noted that a positive value of stress thickness implies a tensile mean stress while a negative value implies a compressive mean stress. At the onset of deposition, stress-thickness marginally increases and then decreases significantly. For most parts of the film growth process, the stress-thickness vs thickness responses are linear with the slopes of -111 and -247 MPa for films A and B, respectively. The values of the slopes denote the steady state stresses in the two films. For the range of the thickness considered, no significant stress relaxation is observed since the fitting lines do not deviate from linearity. The stress-thickness evolution curve is similar to that of poly-Ge film which exhibits a very weak tensile stress peak prior to coalescence [89]. In that paper [89], poly-Ge was deposited on oxide layer by means of electron beam evaporation technique at 750°C. The similarity between poly-SiGe and poly-Ge may be attributed to the high germanium contents in the current films.

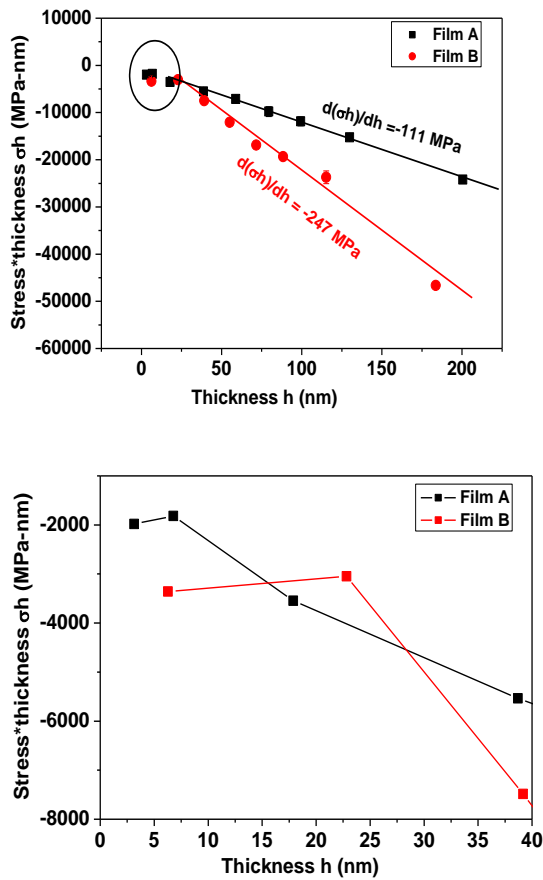


Figure 6.2: (a) Stress-thickness versus thickness evolution for films A and B (b) initial stage of stress-thickness evolution. The continuous lines in (a) are fitted to the experimented points.

To further explore the essence of the stress evolution data, the local stresses in the films are calculated. Essentially, the local stress denotes the instantaneous stress present in each discrete layer of the film during deposition. Although, the intrinsic stresses measured via an *ex-situ* approach may be less accurate than those measured *in-situ*, the former can be a good approximation by correcting for thermal stress. For simplicity, it is assumed that the stress in each layer develops independently of the others and that the

stress is confined to the direction normal to the grain boundary, which corresponds to a biaxial stress in a planar film [140]. The change in the local stress across the film thickness leads to the strain gradient that causes a released structure to bend upward or downward. The local stress $\sigma_{(h_i-h_{i-1})}$ due to an added layer $(h_i - h_{i-1})$ can be obtained from Eq. (6.3).

$$\sigma_{(h_i-h_{i-1})} = \frac{M_s h_s^2}{6} \left(\frac{1}{R_i} - \frac{1}{R_{i-1}} \right) \left\{ \frac{1}{h_i-h_{i-1}} \right\} \quad (6.3)$$

where R_i and R_{i-1} are the radii of the substrate at the film thicknesses h_i and h_{i-1} , respectively. Alternatively, for a stress evolution monitored on separate wafers, the local stresses can be estimated as follows. Given a film grown from an initial thickness h_{i-1} to a new thickness h_i with corresponding average stress σ_{i-1} and σ_i respectively, the local stress in the added layer $(h_i - h_{i-1})$ can be estimated from Eq. (6.4).

$$\sigma_{(h_i-h_{i-1})} = \frac{\sigma_i}{h_i-h_{i-1}} h_i - \frac{\sigma_{i-1}}{h_i-h_{i-1}} h_{i-1} = \frac{1}{h_i-h_{i-1}} \{ \sigma_i h_i - \sigma_{i-1} h_{i-1} \} \quad (6.4)$$

Equations (6.3) and (6.4) give the same results. However, while the former is applicable to stress evolution measurement on a single or multiple wafers, the latter is used for multiple wafers where the initial radii of the wafers may slightly differ. These equations imply that the consistency of stress-thickness of discrete layers and that of the equivalent whole stack must be satisfied. Eq. (6.4) is similar to $\sigma h_f = (h_i - h_{i-1}) \sum_{i=1}^N \sigma_{(h_i-h_{i-1})}$ as derived by Chason et al. [140] where N is the number of local layers in the stack.

Fig. 6.3 (a) shows how the local stresses change with discrete layers in both films A and B. The local stresses are generally less compressive for the film A than for the film B except for the thin slightly tensile layers indicated in Fig. 6.3 (a). These local stresses

are caused by the curvature changes as more film is deposited. As a result, the values of local stress-thickness induced by most of the discrete layers are negative. The top layer is more negative for film B than for film A, which will induce more negative strain gradient for the film B. Similarly, for a film thickness of ~ 100 nm, most of the discrete layers are under negative stress-thickness product, and obviously, this product is less compressive for the film B. It will be of interest to observe a similar difference in the strain gradients when the cantilevers in the two wafers are finally released. Details are presented in chapter 7.

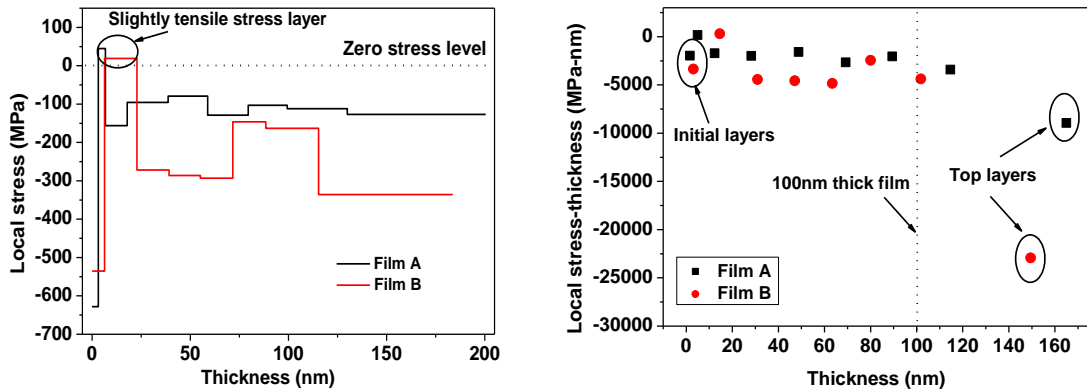


Figure 6.3: (a) Average local stresses in the discrete layers for the films A and B (b) local stress-thickness induced by each discrete layer. The local stress-thickness products induced at the top and the bottom of the films are circled.

6.2 Resistivity Evolution in Poly-SiGe Films

The knowledge of the dependence of the electrical resistivity on the dimensions of poly-SiGe thin films is necessary due to the need for miniaturization especially for

NEMS applications. For example, in nanoswitches a good electrical contact is necessary between the thin layer and the electrode. When the lateral dimensions are scaled down to a length scale (<100 nm) comparable to the electronic mean free path [187], the electrical resistivity is influenced significantly by the scattering at the grain-boundary and at the surface [19, 188 – 190]. The theory of surface scattering and its influence on resistivity have been the subject of intense studies in the past decades [187, 188, 191 – 193]. Here, the resistivity evolution in both films A and B are discussed with more emphasis on the former.

6.2.1 Resistivity Evolution Curve

Figure 6.4(a) shows how resistivity evolves for the films A and B. All measurements are based on 4-point probe measurements and further confirmed by the Hall Effect measurements. It is obvious that the resistivity evolves in a similar manner for the 2 films although the film A has higher resistivity for the range of thickness considered. The Hall mobility and the carrier concentration are shown for the film A. The results show that the carrier mobility increases for the first 40-80nm thick layer and remains constant for thicker layers. However, the carrier concentration continues to increase with thickness since mobility is inversely proportion to the product of resistivity and carrier concentration. XRD spectra for both films show higher peak intensity and a

narrower peak width for the film B as discussed in chapter 5. Details of the resistivity evolution for the film B is discussed in the next few paragraphs.

The evolution of the sheet resistance R_s , its standard deviation (STD) and the resistivity ρ for the film B is shown in Fig. 6.4 (b). The resistivity of the films shows a decreasing asymptotic trend with thickness similar to many thin films [190, 194, 195]. Three regions are identified while the film resistivity evolves. Prior to these regions (within the first 20 nm in this case), the value of the film resistivity ρ is beyond the upper measurement range limit of the 4-point probe. As shown in Fig. 6.4 (b), inset a, the film at this thickness is in the precoalescence stage and existed as individual islands or nuclei. In such a case no percolation exists in the film and consequently an electric path is not established. The Hall Effect measurements at this region do not give any results confirming the absence of percolation. Between 20 and 40 nm (regime I), initial islands coalescence occurs (Fig. 6.4 (b), inset b) and few paths are established among the clusters. The current begins to flow, and its huge increase with thickness is related to the increase in the electric paths becoming available as more islands are deposited and interconnected by percolation. This leads to a significant decrease in the average film resistivity from about 10 m Ω -cm to 4 m Ω -cm in a small thickness interval of a few nm. The sudden decrease in the resistivity can also be explained by considering the carrier concentration and the Hall mobility. For the ~37nm thick film, the carrier concentration is $\sim 1 \times 10^{21} \text{ cm}^{-3}$ and the Hall mobility rose from zero to 1.497 $\text{cm}^2 \text{V}^{-1} \text{s}^{-1}$ (Fig. 6.4a). The increase in the Hall mobility is an indication of atomic percolation and hence a decrease in the resistivity.

Regime I is followed by a transient region (regime II) where the resistivity is weakly dependent on the film thickness. The film is almost continuous as more islands coalesce to form grain boundaries leading to a slight decrease in ρ and in the STD (Fig 6.4b, inset c). It is obvious from the carrier concentration and the Hall mobility that the transient region is partly due to the increase in these properties and also due the 3D–2D transition from individual islands to a continuous film similar to the observations of Barborini et al. [187]. In this case, the transition occurs at about 40nm which may depend on the exact deposition condition. At regime III (stagnation stage), the resistivity becomes significantly stable at $\sim 3.5\text{m}\Omega\text{-cm}$. At this stage, a continuous film with hexagonal grains (or grains with 3, 4, 5 or more sides) is observed (Fig. 6.4b, inset d). The behaviour is confirmed by the Hall mobility which remains virtually unchanged at $1.53\text{ cm}^2\text{V}^{-1}\text{s}^{-1}$ although a slight increase in the carrier concentration is observed. The slight decrease in the resistivity from $4.38\text{ m}\Omega\text{-cm}$ at $\sim 40\text{ nm}$ to $3.95\text{ m}\Omega\text{-cm}$ at $d\sim 80\text{ nm}$ is justified by the slight increase in the Hall mobility from $1.49\text{ cm}^2\text{V}^{-1}\text{s}^{-1}$ to $1.53\text{ cm}^2\text{V}^{-1}\text{s}^{-1}$. While ρ and STD remain almost constant after a film thickness (h) of $\sim 60\text{ nm}$, the sheet resistance decreases further since $R_s = \rho/h$.

As will be discussed in section 6.3.3, while the grain size slightly increases, the rms roughness significantly increases with film thickness which may influence scatterings at the surface and grain boundary of the film. According to Fuchs-Sondheimer and Maydas-Shatzkes model [191], a competition between scattering at the surface and at the grain boundary contributes to the behaviour of film resistivity. Based on this model, Ke et al. [196] recently carried out an atomistic first-principles calculation of resistivity induced by atomically rough surfaces. It was shown that the resistivity increases

significantly due to surface roughness scattering. Also, it is established that increased grain size reduces resistivity due to decreased grain boundary [197]. For the insignificant changes in the resistivity for film thickness greater than $\sim 60\text{nm}$, it is posited that the increased resistivity due to increased surface roughness scattering is probably balanced by the decreased resistivity due to the reduced scattering as the grain size increases. Such an equilibrium state may be responsible for the constant Hall mobility observed. This mechanism has also been explored to explain the behaviour of the electrical resistivity as a function of thickness for continuous films [191].

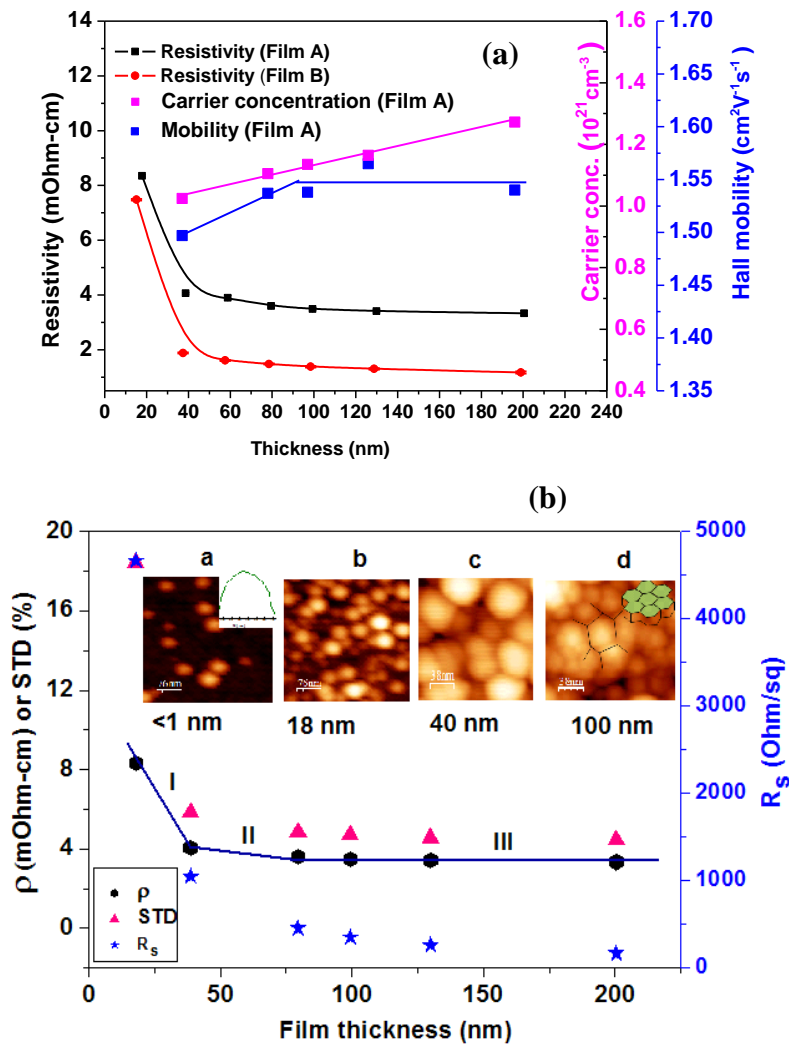


Figure 6.4: (a) Resistivity evolution in the films A and B, Hall mobility and carrier concentration in the film A (b) the evolution of the sheet resistance R_s , its standard deviation (STD) and resistivity ρ , for the film A. The AFM images (insets) associated the resistivity evolution regimes with the film growth stages: (a) pre-coalescence (b) regime I (c) transient or regime II and (d) stagnation or regime III. The 2-D dome and 3-D hexagons of insets (a) and (d) are approximate models at the respective stages of morphology evolution.

6.2.2 Crystallinity

To correlate the change in the resistivity to the film crystallinity, XRD spectra for some of the films were obtained and the results are shown in Fig. 6.5. While no diffraction peaks are observed for the films thinner than 40nm, those of 40 nm and higher are clearly polycrystalline as revealed by the significant peak intensities of (111), (220) and (311) planes. With increasing deposition time and thickness, the intensities of the diffraction peaks become stronger and sharper as the crystallinity increases. This is confirmed by the 4-point probe and the Hall Effect measurements where the resistivity of the 18 nm thick films is very high and those of the 40 nm and higher are significantly lower. The Rutherford backscattering spectrometry (RBS) profile shows that the 100 nm thick film has a germanium concentration of ~89%. This high germanium concentration enhances the crystallinity by increasing the Hall mobility at such a low deposition temperature (415°C) and small thickness.

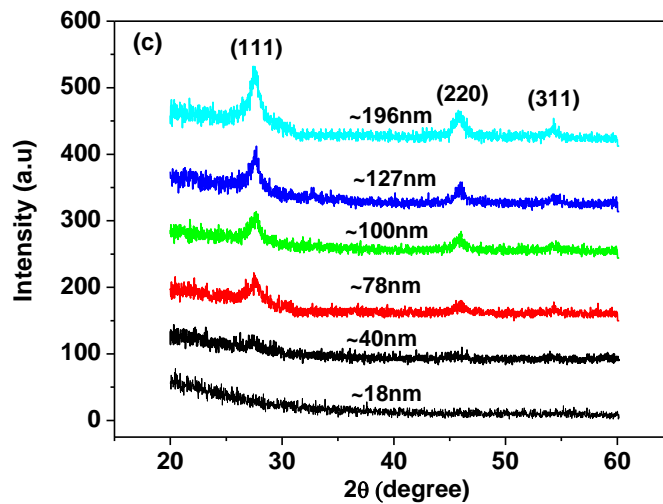


Figure 6.5: XRD spectra for 18, 40, 100nm, 126 and 200nm thick poly-SiGe films.

6.3 Evolution of Surface Properties

To gain insight into the surface structure, roughening mechanism and the growth behaviour of poly-SiGe films, a Power Spectra Density (PSD) analysis was used to extract a few important morphological and surface parameters such as correlation length, rms roughness, the fractal dimension and the scaling exponents.

6.3.1 Application of Power Spectral Density Function

Figure 6.6(a-e) shows the AFM images of 5 of the 13 samples used for both the resistivity and surface morphology evolution studies. The influence of the film thickness on the surface properties of the films is shown by the PSD curves of Fig. 6.7(a). The PSD curves show the 3 common features of most thin films. At low spatial frequencies, all the curves feature a flat region where the PSD value is independent of the spatial frequency. At the transition region between the low and high frequency regimes, the so-called ‘knee’ is

observed. After the knee, a power-law roll-off response is observed. Both the low and medium spatial frequency regions of the PSD are expected to be highly influenced by the film thickness while the high frequency region is only slightly affected by the thickness.

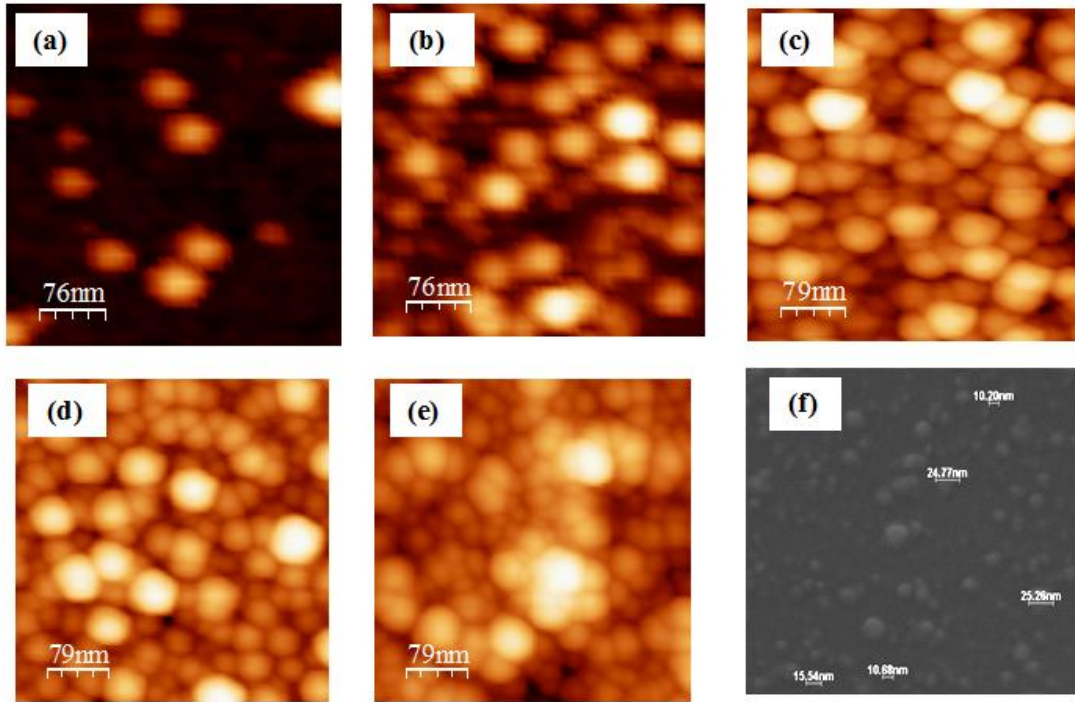


Fig. 6.6: (a) Morphological evolution of our samples as revealed by the AFM images for the film thickness of <1 (b) ~ 1 (c) 18 (d) 60 (e) 200nm, and (f) equivalent SEM image for film (b). The inset is a processed image of (b). Scan size was $2\mu\text{m} \times 2\mu\text{m}$ and the processed image size is $0.4\mu\text{m} \times 0.4\mu\text{m}$.

To fully appreciate the thickness-dependent surface properties of these films, the features of the PSD profiles are characterized with the K-correlation model (also called ABC model) [198] and some of the results are compared with those of the original AFM images. The K-correlation model allows a quantitative comparison between samples over large length scales and has been proven to be applicable to a large range of sample morphologies. For one-dimensional PSD, the K-correlation model is given as [198]:

$$PSD_{ABC} = A(1 + B^2 f^2)^{-\frac{C}{2}} \quad (6.5)$$

where A, B, and C are the adjustable model parameters and f is the spatial frequency. A is the value of the profile spectrum in the low-frequency limit at which the PSD values are frequency invariant. The quantity B determines the location of the knee and C is the exponent of the power-law fall-of at a higher frequency regime. To confirm the accuracy of the ABC model, the equivalent surface roughness σ_{ABC} and the correlation length τ_{ABC} , based on the model parameters, are computed from Eq. (6.6) [199]:

$$\sigma_{ABC}^2 = \frac{2\pi A}{B(C-1)}, \quad \tau_{ABC}^2 = \frac{(C-1)^2 B^2}{2\pi^2 C} \quad (6.6a, b)$$

Also, the surface fractal dimension D_f is determined from the relation: $D_f = (7-C)/2$ [200] and the results are compared with those obtained by using the grain's perimeter - area (P-A) relation. The P-A method is expressed by a linear relationship between $\log(P)$ and $\log(A)$ and the fractal dimension D_i is obtained from the slope of the log-log plot [199] - see Fig. 6.7(b) for an example.

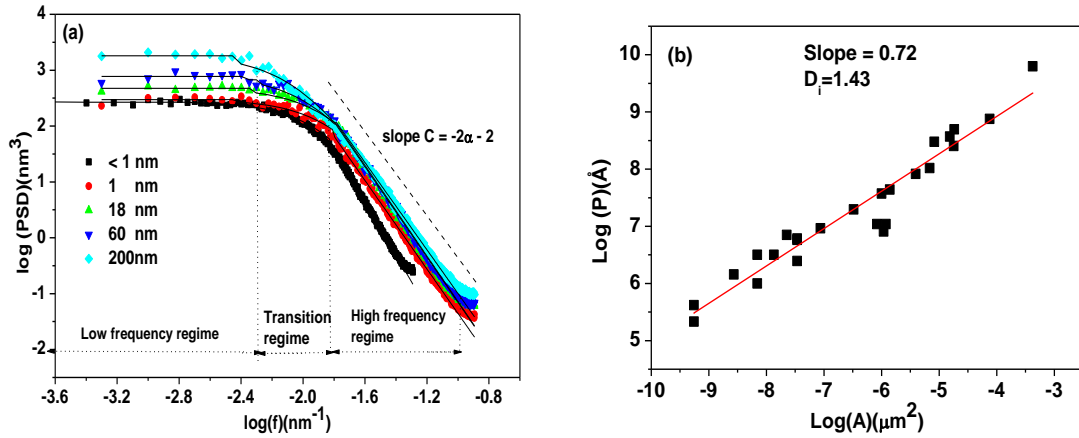


Figure 6.7: (a) 3 distinct features in the PSD curves are obtained from the AFM topographic images of Fig. 6.6(a-e). The K-correlation model (represented by the continuous lines) excellently fit the PSD data. At the high frequency regime of the curve, the slopes $C = -2\alpha - 2$ where α is the roughness exponent (to be discussed later), (b) Variation of $\log(P)$ with $\log(A)$ for 40nm-thick SiGe film which is derived from AFM image of Fig. 6.6(c).

According to the literature [169], the correlation lengths are considered to be corresponding to the grain size and are calculated from Eq. 6.4(b). They are similar to the values obtained directly from the AFM images by using the line intercept technique. For the intercept technique, the average grain size is found by dividing the total length of the lines by the total number of intersections of the grain boundaries. The longer the length of the intercept, the more representative the estimated grain size is expected to be. The island distribution, morphology and aspect ratio for Fig. 6.6 (b) are comparable to those of the SEM image of Fig. 6.6 (f) in which the ratio of island diameter to island height is in the range of 2 to 4. The correlation length of the PSD curve, for this thin film, is about 30 nm

which is at the top of the range of the grain size based on the SEM image (10 – 30 nm). The model fitting parameters, the parameters of the AFM images and the fractal dimension are shown in Table 6.1. Few points are worth noting from Table 6.1; (i) the rms roughness obtained from the AFM images (RMS) and those calculated from Eq. (6.5a) (σ_{ABC}) are very similar, (ii) the correlation lengths (τ_{ABC}) lie within the range of the grain size (D) estimated via the intercept method on the AFM images and, (iii) the fractal dimension D_f is similar to D_i obtained by using the P-A technique.

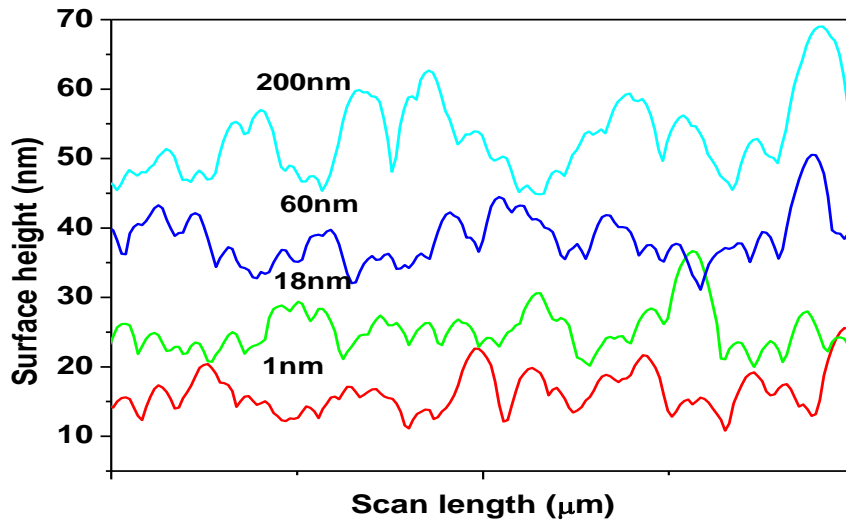


Figure 6.8: Cross-sectional line profiles of the surface structures for the AFM images of Fig. 6.6. The equivalent film thickness from which each scan line is made is shown. Note the increasing height of the structure with thickness.

Table 6.2: AFM parameters, surface fractal dimensions (D) and fitting parameters for K-correlation model

| Thickness | Deposition time | From AFM images | | | From ABC correlation model | | | | | |
|-----------|-----------------|-----------------|------|------|----------------------------|------|------|----------------|--------------|-------|
| | | GS (av.) | RMS | D | A | B | C | σ_{ABC} | τ_{ABC} | D_f |
| (nm) | (s) | (nm) | (nm) | | (nm ³) | (nm) | | (nm) | (nm) | |
| <1 | 10 | 10–40 (26) | 2.17 | 1.46 | 263 | 87 | 4.2 | 2.44 | 30.70 | 1.40 |
| ~1 | 20 | 10–45 (28) | 2.66 | 1.48 | 316 | 91 | 3.96 | 2.71 | 30.49 | 1.52 |
| ~3 | 36 | 15–65 (28) | 2.85 | 1.54 | 332 | 95 | 3.88 | 2.77 | 31.23 | 1.56 |
| 7 | 49 | 20–75 (29) | 2.94 | 1.44 | 332 | 85 | 3.90 | 2.91 | 28.09 | 1.55 |
| 18 | 77 | 20–65 (27) | 3.42 | 1.51 | 441 | 89 | 4.04 | 3.20 | 30.30 | 1.48 |
| 40 | 131 | 20–75 (30) | 3.79 | 1.43 | 826 | 100 | 3.98 | 4.17 | 33.62 | 1.51 |
| 60 | 185 | 20–75 (40) | 3.98 | 1.43 | 827 | 105 | 4.06 | 4.02 | 35.89 | 1.47 |
| 200 | 565 | 20–80 (38) | 5.28 | 1.45 | 1778 | 120 | 3.90 | 5.66 | 39.66 | 1.55 |

NB: GS (av.) = range of grain size (average grain size), D = fractal dimension based on perimeter-area evaluation, RMS = root-mean-square of surface roughness

6.3.2 Fractal Analysis

The fractal analysis helps to characterize the intrinsic variability/complexity of the surface structure [201]. A surface is fractal when the vertical roughness scales with the size of the measuring unit [77]. The complexity of the fractal surface can be quantified by its fractal dimension and its value lies between 1 and 2 for a 2D surface [202]. A fractal dimension is scale invariant and independent of the resolution of the AFM tool [203] making it an interesting surface property. The fractal dimensions of these films are obtained from both the PSD and the perimeter-area techniques as described above. From Table 6.1, the fractal dimensions for all the films are close to 1.5 and it is obvious that they do not vary significantly with the change in the film thickness. This is a clear indication that the complexity (fractal) of the surface morphology is independent of the film thickness [199, 201]. This is expected because the fractal dimension stabilizes at a thickness less than

20 monolayers (ML), independent of the type of the original surface [204]. This value is smaller than the minimum island thickness of our film assuming 1 ML of a SiGe film is equivalent to that of Si (0.27 nm) [207].

The results also show that the films exhibit self-affine fractal surfaces in which the surface roughness varies with length scales [78] as shown by the PSD curves (Fig. 6.7a). Also, the surface structures have a Gaussian distribution with $C \sim 4$ [74]. In addition, a self-affine surface has a characteristic disordered appearance with larger “large scale structures” and smaller “small scale structures” [76]. This appearance is best recognized in the AFM images of Fig. 6.6 where relatively large islands are dominant. It is also obvious from the PSD curves that about 90% of the data points are found in the medium and higher frequency regimes.

6.3.3 Surface Topography and Scaling Exponents

The $2 \mu\text{m} \times 2 \mu\text{m}$ AFM topographs of Fig. 6.6 show islands scattered randomly on the substrate for the film thickness less than 1 nm. As the film thickened, the islands coalesce and agglomerate to form densely packed grains with a slight increase in the grain size (or correlation length). The cross-sectional line profiles of Fig. 6.8 show that the islands grow, on average, in height and insignificantly along the length although a range of different island sizes is visible. The very slight increase in the grain size based on the AFM images (Table 6.1) is due to the continuous incorporation of adatoms onto the existing film, resulting in feature sizes becoming larger with increasing deposition time. The increase in the grain size is partly responsible for the observed increase (or decrease) in the film crystallinity (or resistivity) as discussed in section 6.2.

The rms roughness ($2 < \text{rms} < 6 \text{ nm}$) indicates relatively smooth surfaces. The ‘jaggedness’ (or random fluctuation) of the surface roughness at a length scale less than the correlation length, is described in term of the roughness exponent α [201]. The roughness exponent characterizes the roughness of the local surface and gives important information about the growth process which leads to the generation of such type of topography as well as the fractality of the surface. Like the fractal dimension, α can also be obtained directly from the slope C of the PSD curve (Fig. 6.7a). At a spatial frequency $f \gg 1/\tau$, Pelliccione and Lu [74] relates the PSD to f by using this expression: $PSD \propto f^{-2\alpha-2}$. By comparing $PSD \propto f^{-2\alpha-2}$ with $PSD \propto f^{-C}$ at the same frequency region, then $\alpha = (C - 2)/2$. The average value for the films is $\alpha = 0.93 \pm 0.06$ which is within the range of values (0.7 – 0.95) reported for other experimental systems [80]. From previous studies, a higher value of α (close to 1) is desirable because such a surface appears to have “smooth” hills and valleys [81] which are seen in Fig. 6.6 & 6.9. A lower value of α denotes extremely jagged or rough local surfaces. Also, the distribution of surface highs is Gaussian as rightly predicted by the value of parameter C (which is ~ 4) [74].

Furthermore, the values of α show that the films exhibit self-affine fractal surfaces and reaches saturation at a length scale beyond the lateral correlation length [78] as observed from the PSD curves of Fig. 6.7(a). In addition a self-affine surface has a characteristic disordered appearance with larger “large scale structures” and smaller “small scale structures” as previously observed [76]. This appearance is best recognized in the AFM images of Fig. 6.6 where relatively large islands are predominant. It is also obvious from the PSD curves that about 90% of the data points are found in the medium

and higher frequency regimes. Also, α close to 1 is expected for a surface diffusion dominated film growth process [82] like the CVD technique used in this work. For CVD technique it was observed that the diffusion rate of the species in the vapor phase increases with reduced pressure, which implies that surface kinetic limited control is achieved readily only at low operating pressures [205].

Also, the films can be described by the growth exponent β which characterizes the time-dependent dynamics of the roughening surface as well as the roughening rate during the film deposition. To evaluate β , the value of the rms roughness is plotted against the deposition time t which is then fitted to a power law ($rms \propto t^\beta$) [79]. Figure 6.10 is a log-log plot of these data and shows a relatively constant roughening rate. For these films, $\beta = 0.22 \pm 0.01$ using the rms roughness obtained from the AFM images and PSD analysis. This value falls between those reported (0.1 – 0.6) in the literature [74]. Another characteristic of surface morphology is the dynamic exponent ($1/z$) which is often evaluated by plotting the correlation length $\tau(t)$ as shown in Fig. 6.10. The data are fitted assuming a power law relationship $\tau \propto t^{\frac{1}{z}}$, which results in $1/z = 0.12$. These three exponents (α , β and z) characterize the behaviour of the surface and are related in a specific manner, essentially simplifying the problem of characterizing a self-affine surface to finding values for these exponents [74].

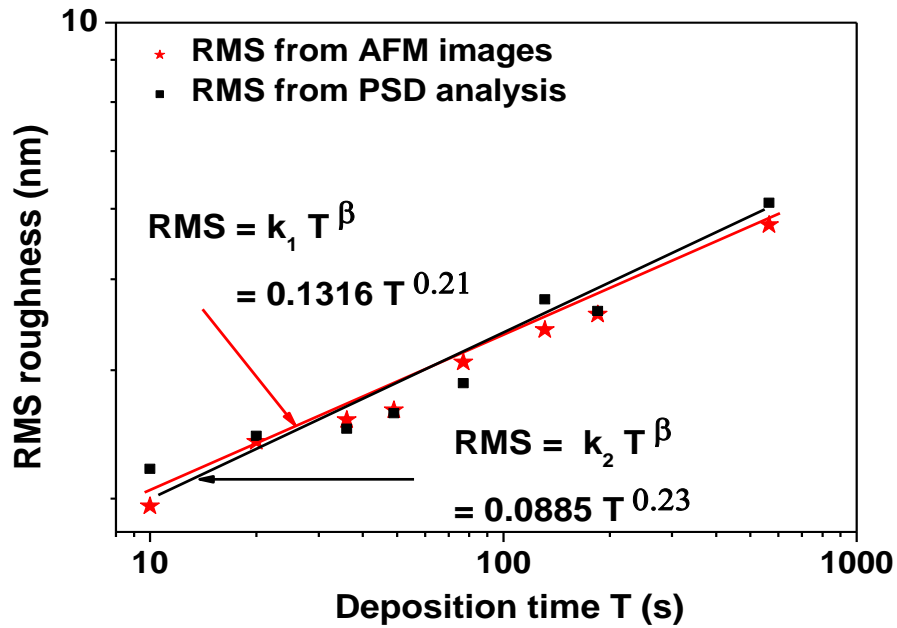


Fig. 6.9: Root-mean-square (*rms*) roughness of the films grown for set of deposition times obtained from AFM images and PSD analysis. The lines are the best fits to a log-log plot, which yields a growth exponent $\beta = 0.22 \pm 0.01$.

Although scaling exponents have not been evaluated for poly-SiGe films, these results are similar to those of amorphous silicon deposited by hot-wire CVD [79] and sputtered amorphous silicon [79]. The values of the exponents observed in this study do not agree with the Family-Vicsek scaling hypothesis [206], which requires that $\beta = \alpha/z$ is satisfied. The Family-Vicsek model describes how the rms roughness and correlation length should scale with sampling size and time. From these results, $\beta = \alpha/z = 0.11$ which is lower than $\beta = 0.20$ obtained by fitting the rms roughness to a power law (Fig. 6.9). This implies that the scaling behaviour of poly-SiGe films, at short length scales, differs significantly from the global behaviour. This discrepancy can be attributed to the

geometrical shadowing effect [79] which has been observed to cause a breakdown of dynamic scaling in many other thin films deposited by sputtering, CVD or PECVD techniques [207].

During the deposition of poly-SiGe films by LPCVD for example (74), atoms of Si and Ge do not always approach the surface in parallel; very often they arrive at the surface with a distribution of trajectories. In such a case, these molecules may bounce around the deposition chamber numerous times before they undergo a reaction at the Si substrate. Therefore, the substrate experiences a molecular flux coming from a wide range of angles and can be represented by a cosine distribution [208]. These non-normal incident fluxes can lead to a shadowing effect during growth, as some of the incident atoms will be captured at high points on a corrugated surface at the expense of lower valleys on the surface, resulting in a dramatic enhancement of the surface roughness (see Fig. 6.6 for an example). In addition, particles can be reemitted from a surface upon impact if the sticking coefficient is less than unity. The particle may then deposit on the surface at a different location, or it may bounce around the surface more before it settles, which might enhance the smoothing effect. Both shadowing and reemission effects are inherently nonlocal because an event that occurs at one place on the surface can affect the surface profile a far distance away.

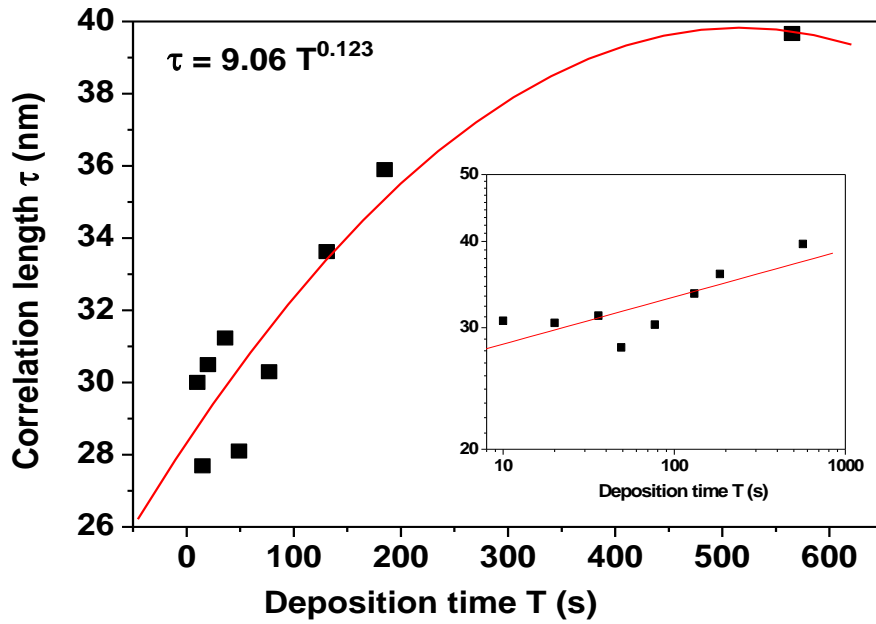


Figure 6.10: Correlation length as a function of the deposition time. The values of the correlation length were determined from the parameter B of the K-autocorrelation model calculated from Eq. 6.3(b). The data are fitted to a power law and the reciprocal of the dynamic exponent $1/z = 0.12$. The inset shows the same data plotted on a logarithmic scale.

CHAPTER 7

FABRICATION OF NANOCANTILEVERS AND STRAIN GRADIENTS EVALUATION

This chapter reports the detailed experimental procedures for the fabrication of nanocantilevers and measurement of the strain gradients. The nanocantilevers are fabricated from ~100 nm and ~60 nm thick optimized and ‘experimental best’ recipes discussed in chapter 5 following the established procedure for surface micromachining technology. The cantilevers’ tip deflections from four different arrays of cantilevers are measured and the strain gradients are calculated. The method of measuring the tip deflection was validated by using the AFM images of similar cantilevers. The average strain gradients are $-0.083 \pm 0.009 / \mu\text{m}$, $-0.02 \pm 0.004 / \mu\text{m}$ and $-0.20 \pm 0.036 / \mu\text{m}$ for the cantilevers processed with the optimized, experimental best and 60 nm thick experimental best recipes, respectively. The strain gradient of $-0.02 \pm 0.004 / \mu\text{m}$ implies a downward deflection of 10nm for a 1 μm long, 0.1 μm thick cantilever. This value is considered to be good for applications in nanoswitches, nanoresonators, and biosensors among others.

7.1 Cantilever Fabrication

7.1.1 Photomask Layout

Photomasks are generally chrome coated glass lithographic templates designed to optically transfer patterns to wafers or other substrates for device fabrication. In the current case, the pattern information is created in a graphic data system and stored in a database, reformatted and transferred to a lithography tool, and then printed onto a layer of photoresist coated onto the photomask plate. The mask is therefore a stencil used to generate a desired pattern on the resist-coated wafers by illuminating it with Deep Ultraviolet (DUV) light. DUV light are generated from excimer lasers with wavelengths of 248 and 193nm, which allow minimum feature sizes down to 50 nm. The layout of the imec's newly designed NEMS mask is shown in Fig. 7.1a. In brief, the NEMS design mask is $2 \times 1 \text{ cm}^2$ in dimension on the wafer and it is designed primarily for the fabrication of nanoswitches. It also consists of a few nanostructures for studying the mechanical properties of poly-SiGe films. Since this chapter is about fabrication and evaluation of strain gradient in the ultrathin films, the small area on the mask containing the nanocantilevers (Fig. 7.1a) is considered for the study. The expanded view and the top view of the SEM image of the arrays of the cantilevers are shown in Fig. 7. 1(b, c). The minimum length of the cantilevers is $0.3 \mu\text{m}$ while the maximum length is $10 \mu\text{m}$. the widths of the cantilevers vary from $0.2\mu\text{m}$ to $1\mu\text{m}$. A gap of 200nm separates two neighbouring cantilevers while the thickness is $\sim 100\text{nm}$. The detailed statistics of the cantilever arrays are summarized in Table 7.1. It should be noted that the cantilevers are

grouped into 5 arrays (Arrays 1, 2, 3, 4 & 5) based on the number of cantilevers, the width and the length of each cantilevers.

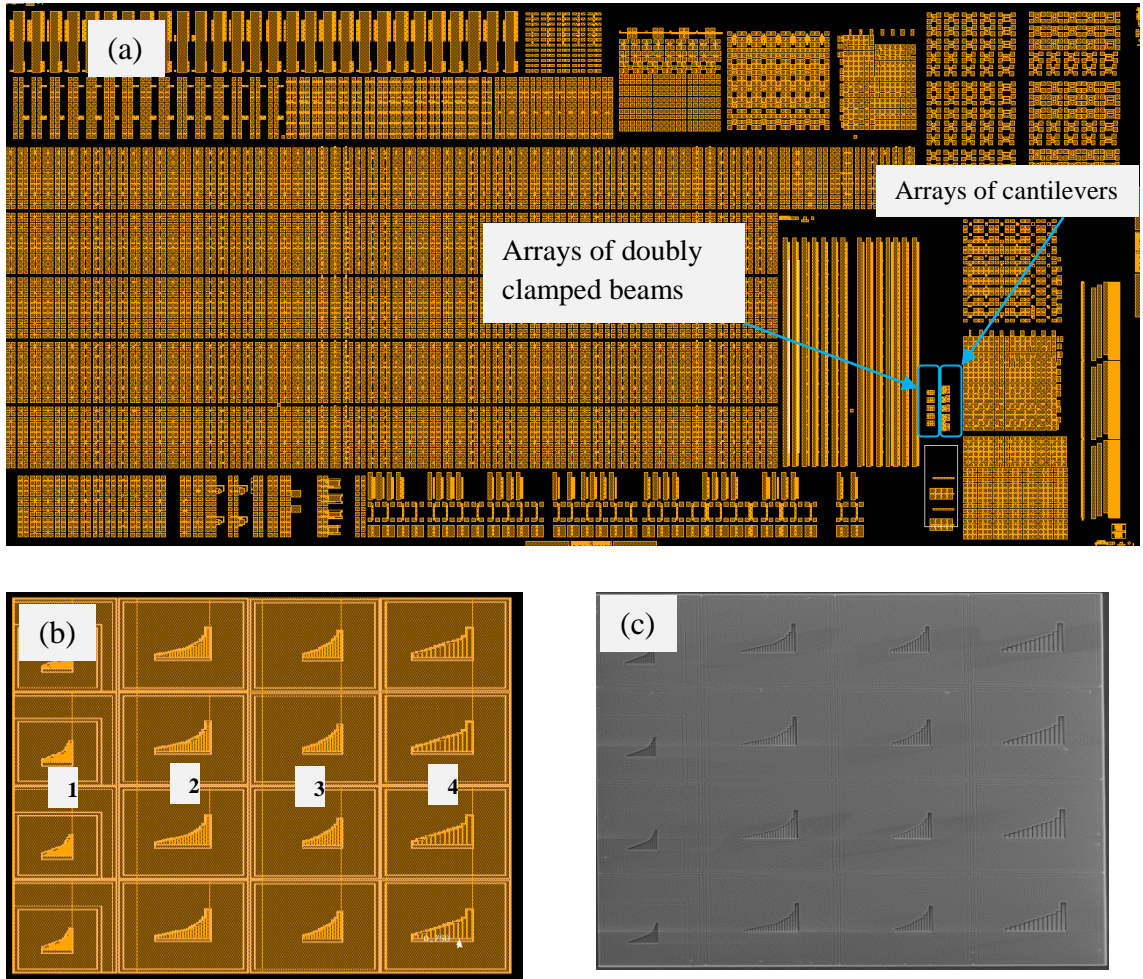


Figure 7.1: (a) The layout of imec's newly designed NEMS mask, the location of the cantilevers is indicated (b) expanded view of one of the 5 families of arrays of cantilevers (c) equivalent SEM image of (b).

Table 7.1: Dimensions of the cantilevers

| Array | No of cantilevers in the array | Length of the cantilevers (μm) | Width (nm) | Gap (nm) |
|--------------|---------------------------------------|---|-------------------|-----------------|
| 1 | 19 | 0.3 – 7 | 200 | 200 |
| 2 | 20 | 0.6 – 10 | 500 | 200 |
| 3 | 14 | 1 – 9 | 500 | 200 |
| 4 | 13 | 1 – 10 | 1000 | 200 |

7.1.2 Fabrication Steps

Figure 7.2 summarizes the surface micromachining technology employed for the fabrication of the nanocantilevers. The microfabrication employs a one-mask, two-litho process. The fabrication started with clean 200 mm diameter (100) silicon wafers. First, a 0.8 μm thick HDP (high density plasma) silicon dioxide layer is deposited (Fig. 7.2a). The SiO_2 serves as the sacrificial release layer as will be described in the following steps. To create 200nm wide anchors for the cantilevers (Fig. 7.2b), the SiO_2 layer is patterned, etched and stripped. The pattern is made via lithography using the NEMS mask described in section 7.1.1. In this process, the SiO_2 is coated with a bottom anti-reflective coating (BARC) of 59nm thick HMDS (hexamethyldisilazane) to enhance adhesion and prevent reflection. Then, a positive photoresist material of 450nm is spread uniformly on the HMDS. DUV light is used to transfer the pattern from the NEMS mask to the photoresist. The photoresist is then developed and finally dried. The layers are plasma etched in a deep dry etching system (DOM-FEOL). For the BARC etch, 85 sccm of CF_4 + 3 sccm of O_2 in 100 sccm of Ar are used and the etch time is 15s. To etch the SiO_2 layer, 7 sccm of

$C_4F_8 + 8$ sccm of O_2 in 160 sccm of Ar are used. The duration for the etch operation is 120s at the rate of $0.45\mu\text{m}/\text{min}$. This is followed by wet strip using a Mattson tool which ensured that all etched particles are removed from the anchor trenches. Fig. 7.3 (a) is a cross-section SEM image of one of the processed wafers after oxide is etched. The image indicates that the etch process is fairly uniform but the oxide layer is not completely etched (about 160nm of oxide is not etched).

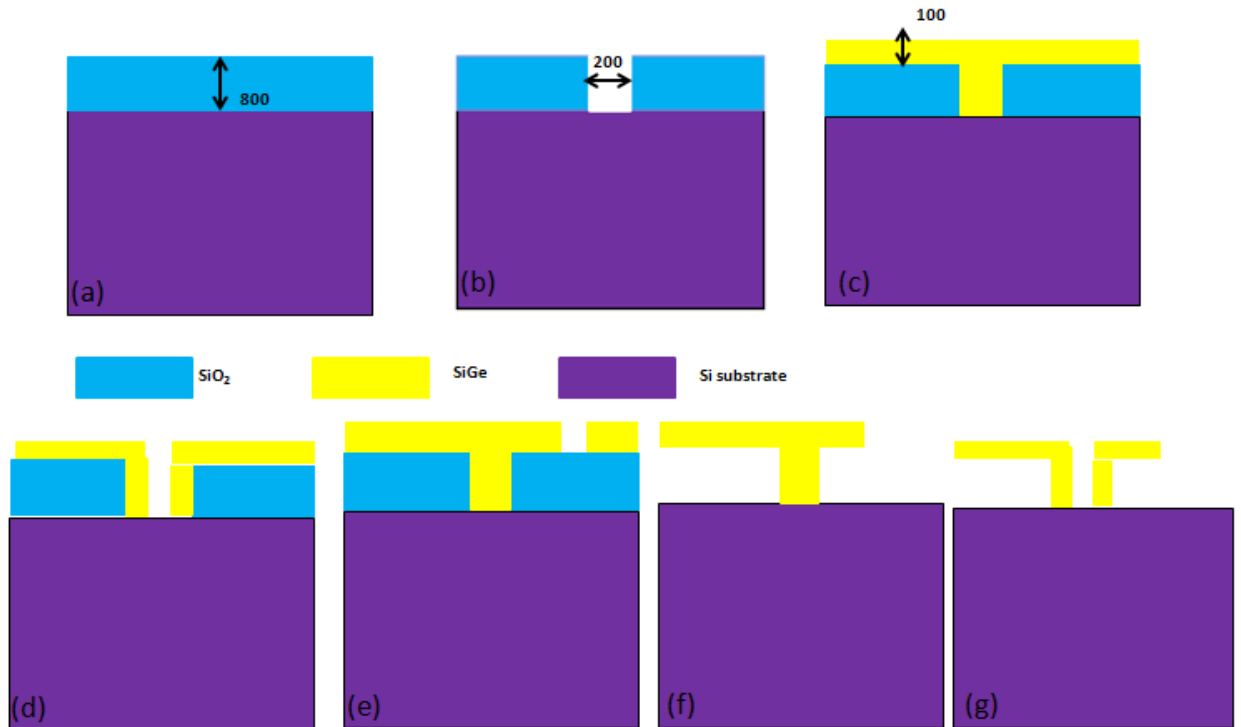


Figure 7.2: Fabrication sequence of the nanomechanical cantilever: (a) $0.8\ \mu\text{m}$ thick LPCVD SiO_2 layer (b) lithographic definition of the anchor (c) LPCVD deposition of 100nm thick poly-SiGe film (d, e) lithographic definition of the cantilever (f, g) Sacrificial SiO_2 is removed in hydrofluoric acid.

Followed the strip process is the deposition of ~100nm thick poly-SiGe film (Fig. 7.2c or d depending on whether the anchor trench is completely or partially filled) that would serve as the structural layers (i.e. the cantilevers). As described in section 3.1, poly-SiGe films are deposited using LPCVD based on the deposition recipes described in Table 7.2. For these films, the stress, resistivity and standard deviation of resistance are measured before the lithography step using the measurement techniques discussed in chapter 3. The wafers A, B, C & D are processed to evaluate the strain gradients in the ‘experimental best’ recipe while E & F are chosen for the optimized recipe. Wafer G was processed to evaluate the strain gradient in 60nm thick film deposited with the experimental best recipe. Figure 7.3(b) indicates that the poly-SiGe is deposited conformal to the underlying topography on the etched oxide, showing good step coverage, although some thinning of the film occurs on the sidewalls. The patterning of the structural layer followed the same procedure as described earlier for SiO₂ layer.

Table 7.2: Deposition conditions for poly-SiGe films and some preliminary results for fabrication of NEMS structures

| Wafer ID # | Temp (degC) | SiH ₄ (sccm) | GeH ₄ (sccm) | Press (Torr) | B ₂ H ₆ (sccm) | Hydrogen (sccm) | Spacing (mil) | Time (sec) | Stress (MPa) | Thick. (nm) | Dep rate (nm/s) | Resistivity (m-Ω/cm) | Rs % std |
|------------|-------------|-------------------------|-------------------------|--------------|--------------------------------------|-----------------|---------------|------------|--------------|-------------|-----------------|----------------------|----------|
| A | 415 | 8 | 180 | 60 | 18 | 500 | 470 | 295 | 24.1 | 114 | 0.38 | 2.64 | 17.2 |
| B | 415 | 8 | 180 | 60 | 18 | 500 | 470 | 295 | 32.8 | 114 | 0.38 | 2.66 | 18.9 |
| C | 415 | 8 | 180 | 60 | 18 | 500 | 470 | 295 | 36.1 | 114 | 0.38 | 2.62 | 19.2 |
| D | 415 | 8 | 180 | 60 | 18 | 500 | 470 | 295 | 47.0 | 115 | 0.38 | 2.66 | 15.2 |
| E | 415 | 8 | 180 | 65 | 11 | 500 | 500 | 302 | 39.1 | 115 | 0.38 | 1.43 | 9.2 |
| F | 415 | 8 | 180 | 65 | 11 | 500 | 500 | 302 | -99.0 | 115 | 0.38 | 1.47 | 4.8 |
| G | 415 | 8 | 180 | 60 | 18 | 500 | 470 | 185 | 64.6 | 60 | 0.36 | 3.08 | 11.0 |

Because of some differences in the properties of poly-SiGe films and those of SiO₂, the etch requirements differ markedly. The structural poly-SiGe layers are etched with 200 sccm HBr at a pressure of 15 mTorr, an RF power of 300 W and 150 W at the top and bottom electrodes, respectively (Fig. 7.2e). These conditions were found to etch poly-SiGe at 0.17 μm/min. The residual photoresist, poly-SiGe film and oxide particles are stripped with 200 sccm oxygen stream for 220 s. The operation is carried out at a pressure of 30 mTorr and an RF power of 1000 W. As revealed by the X-SEM image (Fig. 7.3c), the poly-SiGe layer is completely etched. After the strip operation there is a substrate decontamination process, where the wafer backside is cleaned in a mixture of 51% nitrite + 49% hydrogen fluoride solution. The cleaning operation (termed millennium clean at imec) helps to remove contaminants, usually Cu, that might have come in contact with the wafers during the previous processing steps. In this case, a little bit of the backside silicon nitride is removed during the cleaning process.

To remove moisture from the structural layer before the wafers are processed in the VHF (Vapour Hydrogen Fluoride) etch tool, a rapid thermal annealing (RTA) (by high-power tungsten-halogen lamp irradiation) is done at a temperature of 200 °C for a period of 4 minutes in 100% N₂ environment. Lastly, the oxide layer is removed in Gemetec pad fume to release the SiGe nanoresonators (Fig. 7.2 f or g). The tool uses HF vapour (49% HF) to etch isotropically the oxide layer. Because Gemetec etches aggressively, a few etching conditions are tried to obtain the best parameters for a successful release of the cantilevers. Different etching temperatures (35 and 50°C), etching times (15, 20, 25, 30, 35, 40 mins) and etching steps (single, double and triple) are tried. For each condition, the water and HF flow rates are kept constant at 1 liter/min

and the rinsing time at 10 minutes (at the etching temperature). Etching at 35°C is much faster than at 50°C (due to a higher reaction with condensed water), but the chance of the structures sticking to the substrate is equally high [209]. To minimize stiction, all etchings are done at 50°C. The detailed operation procedure for the Gemetec can be found in the operating manual [210]. The chosen Gemetec etch recipe and the experimental procedure are summarized in the following flow chart (Fig. 7.4).

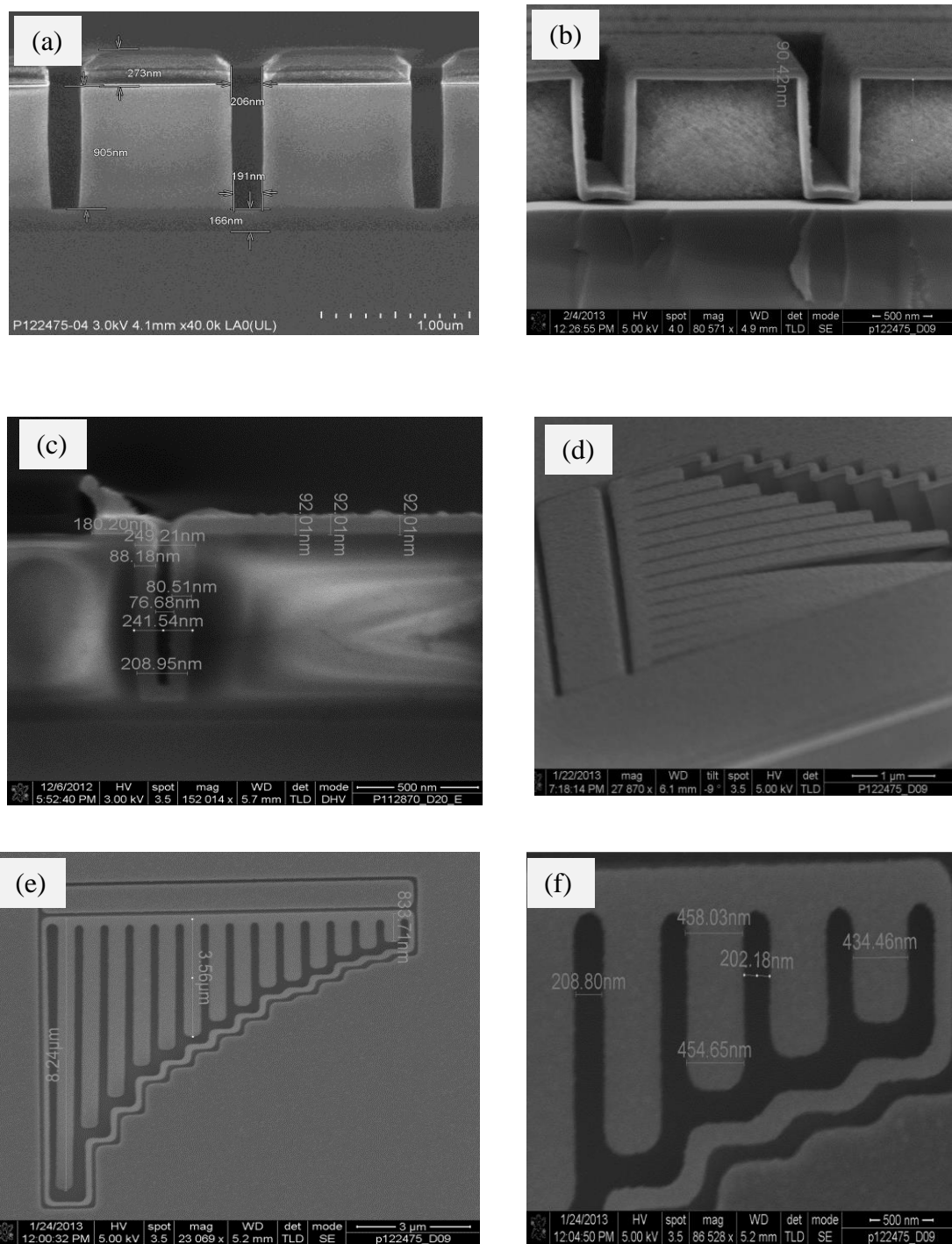


Figure 7.3: SEM images (a) after oxide etch for anchor definition (b) after poly-SiGe deposition (c) after poly-SiGe layer etch and anchor fill (d) an array of released cantilevers (e) top view of the released nanocantilevers (f) expanded top view of the released cantilevers.

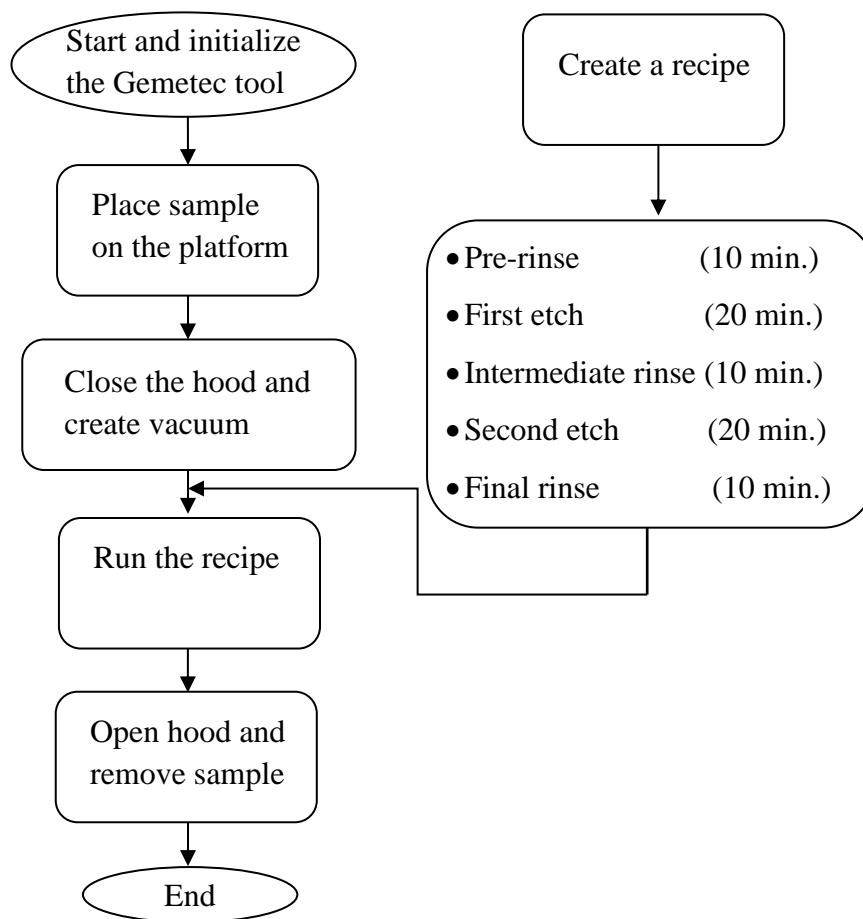


Figure 7.4: A simple flow chart of the operating procedure of Gemetic pad fume HF vapour

One of the arrays of released cantilevers in wafer E (optimized recipe) is shown in Fig. 7.3 (d) while the top and the expanded top views are shown in Fig. 3 (e) and (f), respectively. In the array, 8 of 14 cantilevers were successfully released while the other 6 cantilevers stuck to the substrate. Details are discussed in the following section.

7.2 Strain Gradient Evaluation

One of the challenges facing M/NEMS industries is to fabricate a free standing cantilever without any unwanted deflection [211]. In practice, however, thin films are not usually deposited stress free. During deposition, growth stress may emanate due to island/grain growth and crystallization [98] as well as island coalescence [99], surface stress [100], and interstitial incorporation of atoms among others. More details are discussed in section 2.4. Cantilever deflects due to the changes in the stress distribution along the growth direction causing bending moment (see section 6.1). If the stress near the film surface is less tensile compared to the stress at the bottom, the cantilevers will bend down resulting into a negative strain gradient while cantilevers with positive strain gradients bend up due to the increase of tensile strain with film thickness [211]. For an excessive deflection, cantilevers may touch the underlying substrate which might be detrimental to the dynamic and reliability characteristics of M/NEMS structures [90, 91]. Thus, the knowledge of the stress variation across thin films will help project the direction of the strain gradient. By extension, strain gradient will help estimate the maximum possible deflection during service.

For a cantilever, the strain gradient Γ is derived from Fig. 7.5 where ρ is the radius of curvature of the cantilever, θ is the angle on the circle with radius ρ between the vertical line from the point of anchor and the line connecting the middle of the circle with the end point of the cantilever, δ is the deflection at the cantilever tip, h is the thickness of the structural layer and L is the length of the cantilever. The radius ρ varies with the value of the layer thickness h . A minimum strain gradient will occur at the

bottom of the structural layer because the radius is maximum at the bottom surface. The maximum strain gradient will occur on top of the film. With the average radius ρ , the average strain gradient can be calculated from Eq. (7.1).

$$\frac{\varepsilon}{h} = \frac{1}{\rho} \quad (7.1)$$

Based on trigonometry:

$$\delta = \rho[1 - \cos(L/\rho)] \quad (7.2)$$

By using Power series expansion (and truncating higher order > 2), then:

$$\rho = \frac{L^2}{2\delta} \quad (7.3)$$

From Eqs (7.1) and (7.3), the average strain gradient can, thus, be expressed as:

$$\Gamma = \frac{\varepsilon}{h} = \frac{1}{\rho} = \frac{2\delta}{L^2} \quad (7.4)$$

All the strain gradients reported in this chapter are calculated by using Eq. (7.4). For a cantilever bending downward, the signs on δ and Γ are negative and positive for an upward bending cantilever. Since all the beams are bending downward, the strain gradients are negative.

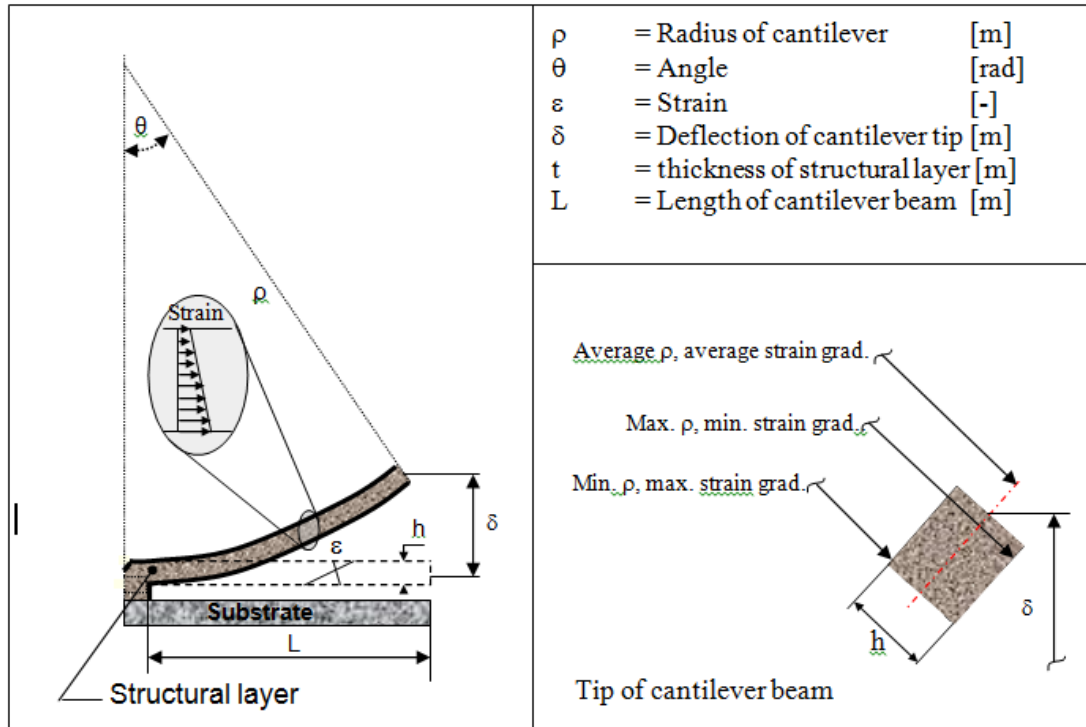


Figure 4.19 Cantilever beam

Figure 7.5: Schematic diagram of a released upward bending cantilever and its associated strain gradient variation [212]

7.2.1 Strain Gradients in the ~100nm-Thick Cantilevers

As expressed by Eq. (7.4), an accurate measurement of the cantilever deflection is essential for a reliable strain gradient result. Because of the small size of these cantilevers, it is challenging to find a suitable tool to accurately measure the tip deflection. Due to the wavelength limitation of light (400 – 700 nm) and that of the phase changes when light reflected from the top SiGe layer and the bottom oxide layer, Veeco surface profilometer, which is often used for step-height measurements, does not give an

accurate result. An alternative method is to measure the tip deflection from SEM images as demonstrated for the 4.42 μm long cantilever of Fig. 7.6 (a). In the Figure, line AB is located at the edge of the cantilever array where SiGe film is unaffected. This edge is expected to be at the same level with the top surface of the cantilever prior to HF vapour release. It is, therefore, chosen as the reference point for other measurements. The line CD is thereafter drawn parallel to the line AB at the position of the cantilever of interest. The deflection at the cantilever tip can thus be estimated as the distance between points E and F. Since the SEM image is tilted at 10° , the measured deflection is multiplied by $\cos(10^\circ)$ and then converted to the actual height based on the SEM scale of measurement. This procedure is repeated for a few images to estimate the tip deflections. As a way of verifying that the cantilevers are fully released, a few of the samples are cleaved by using the MC600i Microcleaving system. Figure 7.6 (b) indicates that the cantilevers are completely released from the underlying oxide layer. The Figure also shows that the 3.52 μm long cantilever deflects by 118 nm. The strain gradient calculated from Fig. 7.6 (b), which is 0.019 / μm - is closely related to those of Fig. 7.6 (a).

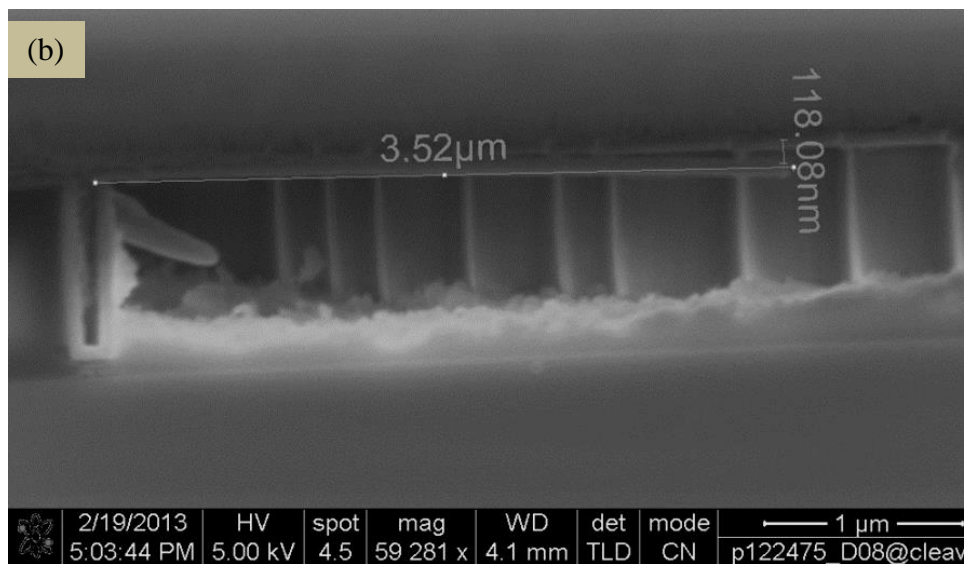
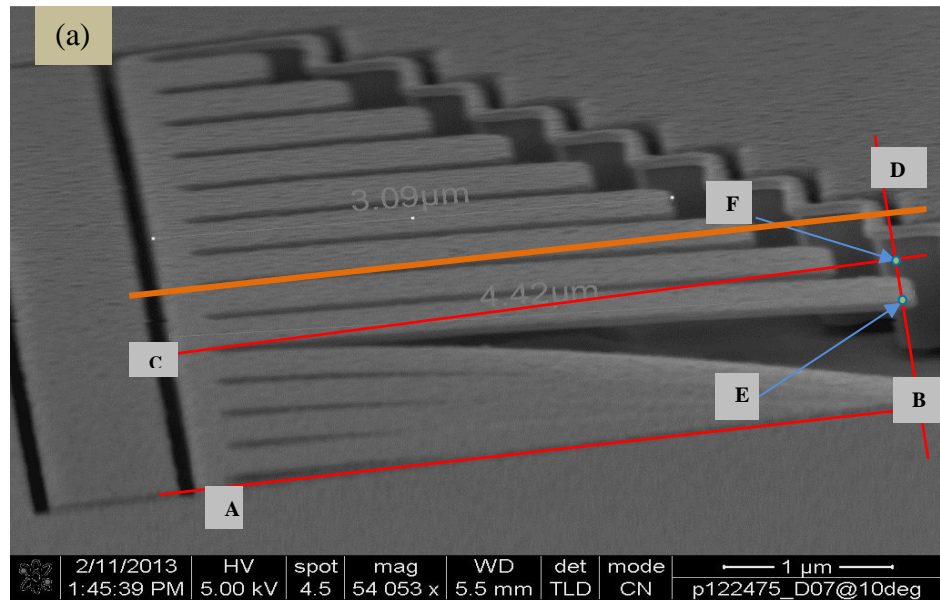


Figure 7.6: (a) A method for measuring tip deflection of a cantilever based on SEM image (the cantilever array is made from the optimized recipe). Line AB is parallel to line CD, and line EF is perpendicular to line AB (b) X-SEM image after cleaving through the orange line similar to the one showing in (a) by the MC600i Microcleaving system. The cantilever array is made from the experimental best recipe.

To confirm the accuracy of the deflection calculated from the SEM images, AFM images of two arrays are obtained at the positions similar to those of SEM images (Fig. 7.7). The measurements are carried out with Nanoscope Multimode AFM by using the tapping mode. The probe is a MicroCantilever of model OMCL-AC160TS-R3 with a spring constant of 26 N/m and a resonance frequency of 300 kHz [213]. These characteristics make the cantilever stiff and help to reveal sample surface precisely and gently. The tip is 14 μm long and has a radius of 7 nm which enhance its aspect ratio. Because the AFM cantilever is stiff coupled with the tapping mode, it is assumed that no additional deflection is induced in the nanocantilevers during imaging. The AFM images are then processed with WSxM software [137].

Figure 7.8 (a) shows the deflection profiles of the two cantilevers as obtained from the AFM images. Both curves indicate that the cantilevers deflect excessively. Based on the tip deflections, the strain gradients are calculated by using Eq. (7.4). The strain gradients for the free-standing cantilevers from the arrays number 3 are shown, together with the strain gradients calculated from the AFM images, in Fig. 7.8 (b). The strain gradients obtained from the SEM images are as accurate as those of AFM measurements; although a slight scattering is observed in the latter. It is thus worthy of note that the proposed deflection measurement method does not underestimate the strain gradients, rather it slightly overestimates them. Hence, the strain gradients from other cantilevers are obtained following the same procedure.

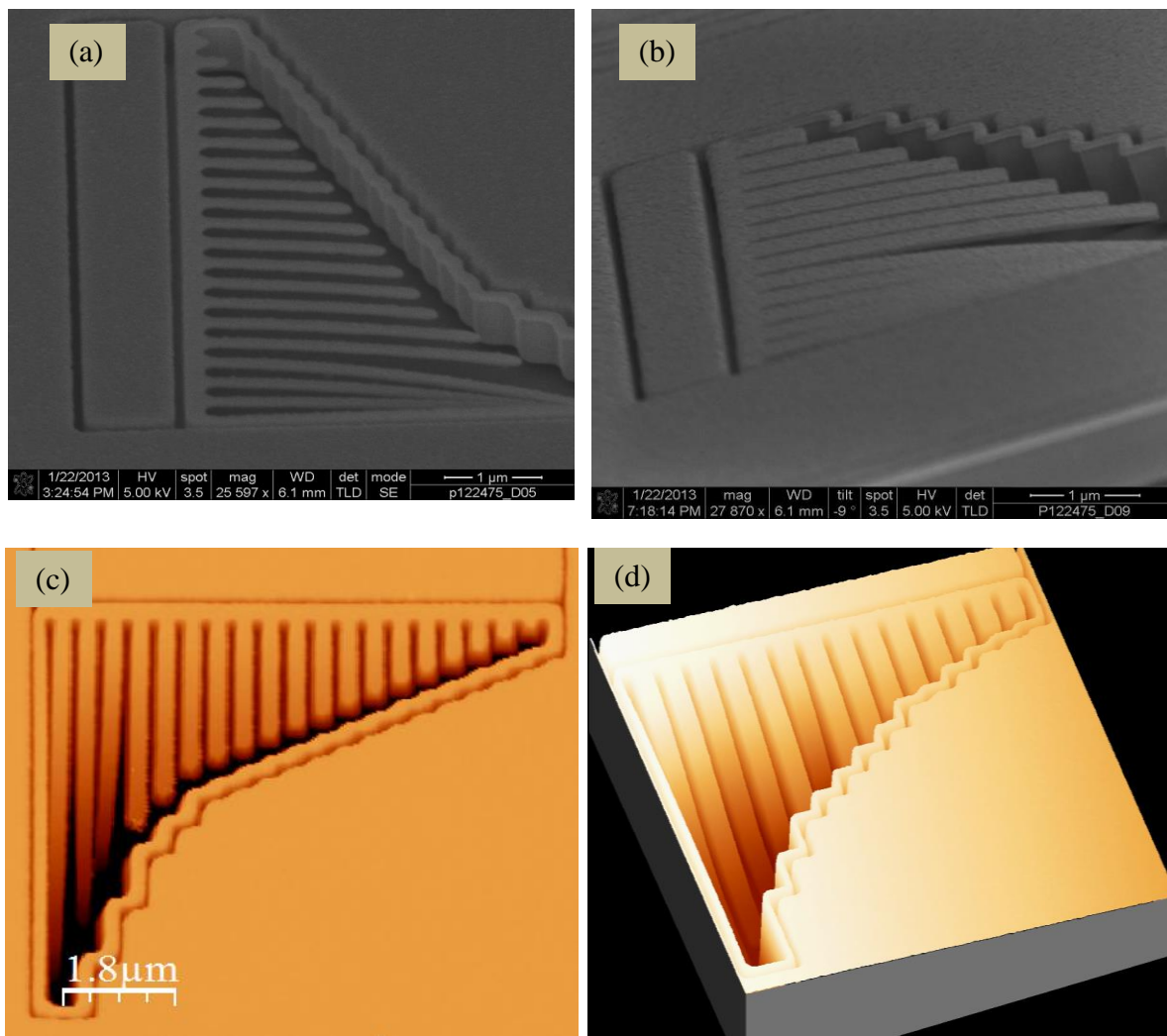


Figure 7.7: SEM images of (a) array 1 (b) array 3 and the equivalent AFM images of (c) array 1 and (d) array 3 for the optimized film

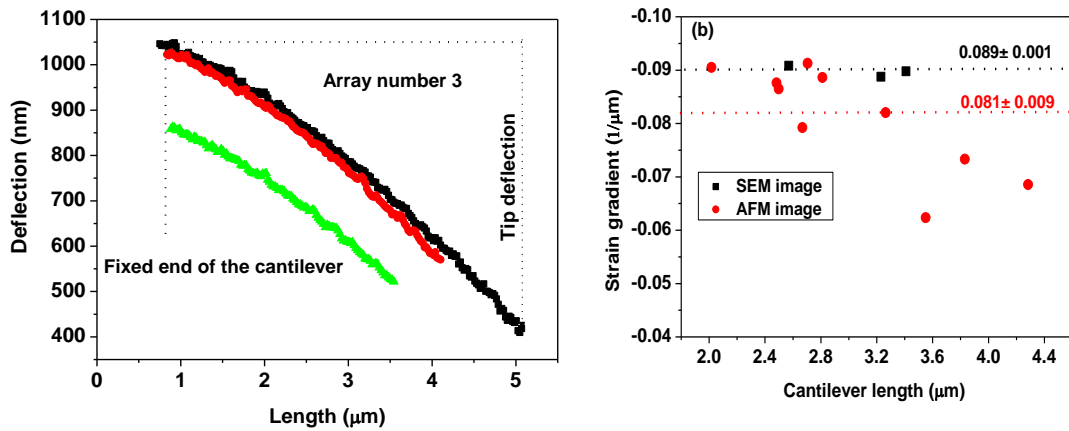


Figure 7.8: Deflection profiles for 3 downward bending cantilevers, each curve is based on one cantilever from array no.3 based on the optimized recipe (b) strain gradients computed from SEM and AFM images from array no. 3. The average values and the corresponding standard deviations of the strain gradients are indicated.

Figure 7.9 are SEM images of the cantilevers obtained from the wafer D (based on the experimental best recipe) while the top views are shown in Fig. 10. The lengths of the measured cantilevers, the tip deflections and the strain gradients are summarized in Table 7.3. By using these values, the average strain gradient is -0.02 ± 0.004 $1/\mu\text{m}$. This translates to a deflection of -10nm for $1\mu\text{m}$ long, 100nm thick cantilever. In the same way, the SEM images and strain gradients for wafer E (using the optimized recipe) are shown in Fig. 7.11 and Table 7.4, respectively. The average strain gradient is calculated to be -0.083 ± 0.009 $1/\mu\text{m}$, which imply a downward deflection of 42nm for $1\mu\text{m}$ long, 100nm thick cantilever.

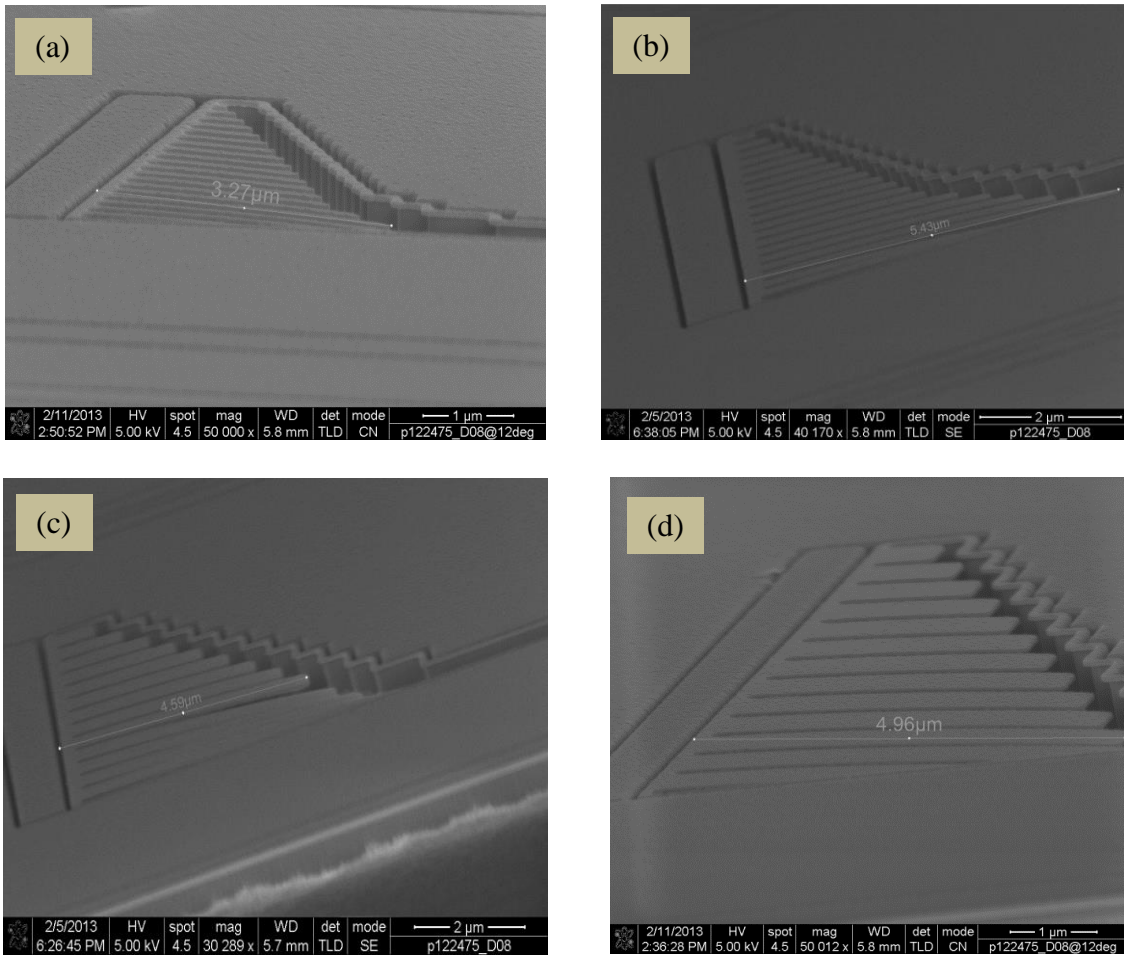


Figure 7.9: Arrays of released cantilevers chosen from array no. (a) 1 (b) 2 (c) 3 and (d) 4 for wafer D (experimental best recipe).

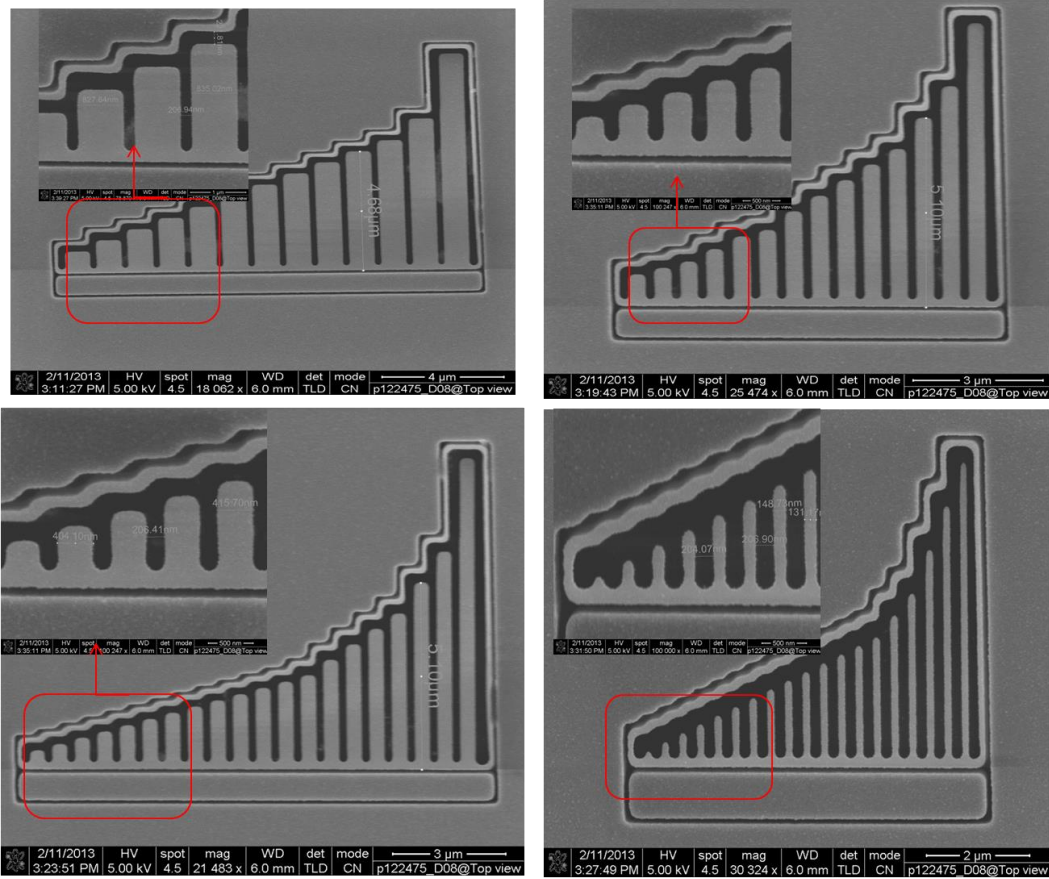


Figure 7.10: Top down view of the arrays of released cantilevers chosen from array no.

(a) 1 (b) 2 (c) 3 and (d) 4 for wafer D (experimental best recipe).

Table 7.3: Strain gradients for wafer D (Film A - experimental best recipe)

| Array No. | No. of cantilevers | Length of measured cantilever (μm) | Tip deflection (nm) | Strain gradient ($1/\mu\text{m}$) |
|-----------|--------------------|---|---------------------|-------------------------------------|
| 2 | 20 | ~5.43 | -0.19 | -0.013 |
| | | ~4.24 | -0.23 | -0.026 |
| 3 | 14 | ~4.59 | -0.19 | -0.018 |
| | | ~4.08 | -0.18 | -0.021 |
| | | ~3.63 | -0.15 | -0.022 |
| 4 | 13 | ~4.58 | -0.19 | -0.018 |
| | | ~3.90 | -0.17 | -0.022 |
| | | ~3.50 | -0.14 | -0.023 |

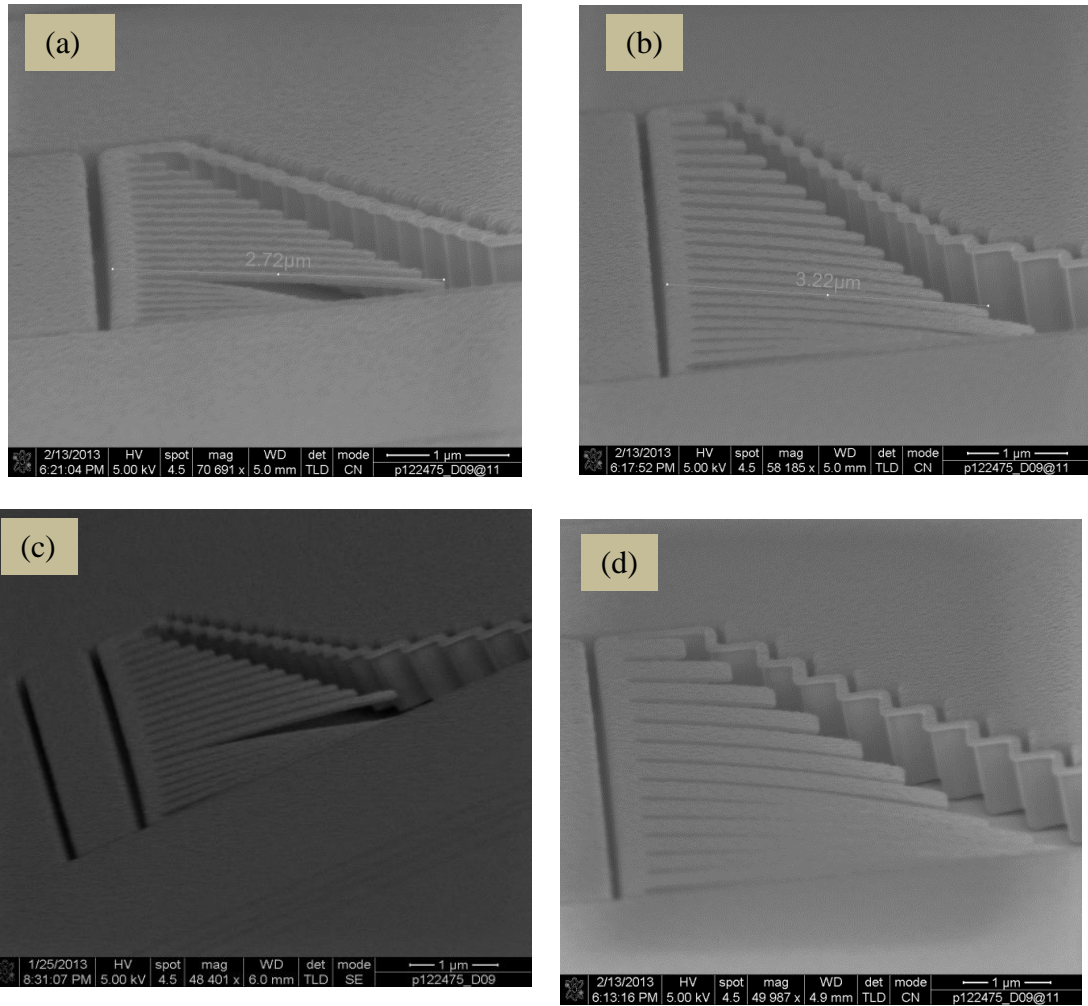


Figure 7.11: Arrays of released cantilevers chosen from array no. (a) 1 (b) 2 (c) 3 and (d) 4 for wafer D (optimized recipe).

Table 7.4: Stress gradients for wafer E (Film B - optimized recipe)

| Array No. | No. of cantilevers | Length of measured cantilever (μm) | Tip deflection (μm) | Strain gradient ($1/\mu\text{m}$) |
|-----------|--------------------|---|----------------------------------|-------------------------------------|
| 2 | 20 | 3.62 | -0.45 | -0.069 |
| | | 2.71 | -0.30 | -0.083 |
| | | 2.16 | -0.21 | -0.090 |
| 3 | 14 | 3.41 | -0.52 | -0.089 |
| | | 3.23 | -0.46 | -0.088 |
| | | 2.57 | -0.30 | -0.090 |

Fig. 7.12 compares the strain gradient in a pictorial format. Based on these results, it suffices to conclude that the strain gradient in the experimental best recipe is about 4 times lower than those of the optimized films. The discrepancy between the strain gradients is anticipated because the previous study of stress evolution based on the two recipes (section 6.1) clearly indicates that the optimized film has a higher curvature (large deflection or higher stress-thickness product) compared to the experimental best recipe. This shows a clear relationship between the stress gradient and the strain gradient across the films. With the knowledge of the stress gradient, it is possible to compare relatively the anticipated strain gradients in different released structures. Also, the difference in the germanium fractions may be responsible for the observed difference in the strain gradients.

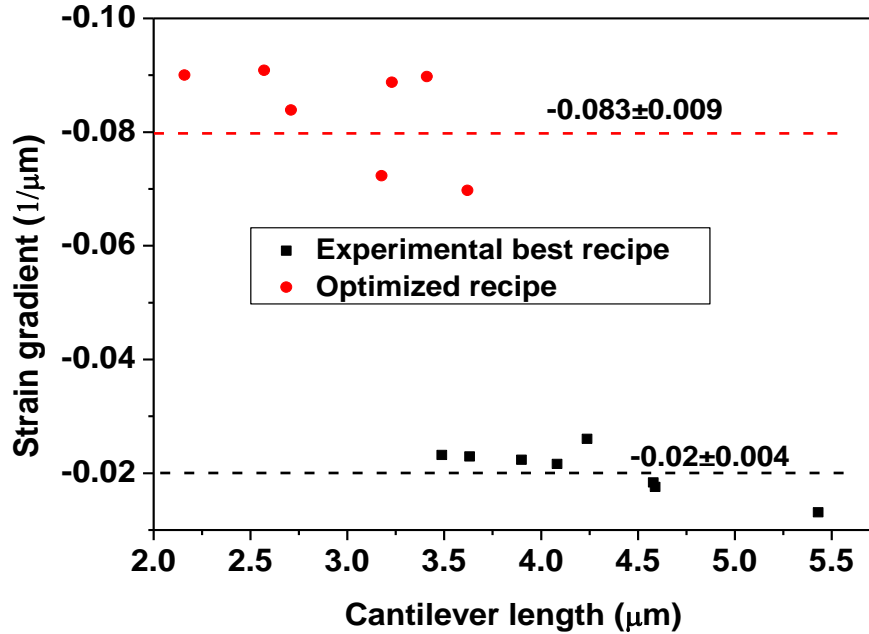


Figure 7.12: Comparison of the strain gradients between the films deposited by using the experimental best and the optimized recipes

7.2.2 Strain Gradients in the ~60nm Thick Cantilevers

The SEM images of the released 60nm-thick cantilevers are shown in Fig. 7.13. The cantilevers are processed along with the ~100nm thick cantilevers using the experimental best recipe. The strain gradients for the cantilevers are calculated based on the procedure earlier discussed. The results are summarized in Table 7.5. It is obvious that most of the cantilevers touch the substrate. Those that are free standing have an average strain gradient of $-0.20 \pm 0.036 / \mu\text{m}$ which implies a deflection of ~100nm for 1 μm long cantilever. This is obviously high for applications where the actuation gap is smaller than 100 nm. The strain gradients for the ~60 nm and ~100 nm thick films are compared in Fig. 7.14(a). The former is about one order of magnitude higher than the latter. Thus far, it is clear that the strain gradient increases significantly as the structures are scaled down (Fig. 7.14b). In the next paragraph, it is shown that the large difference in the strain gradient does not translate to a difference in the Young's modulus.

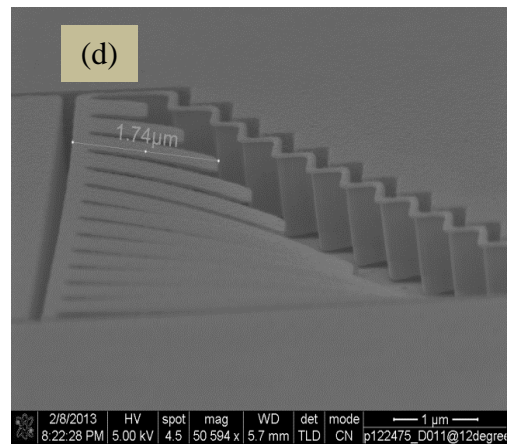
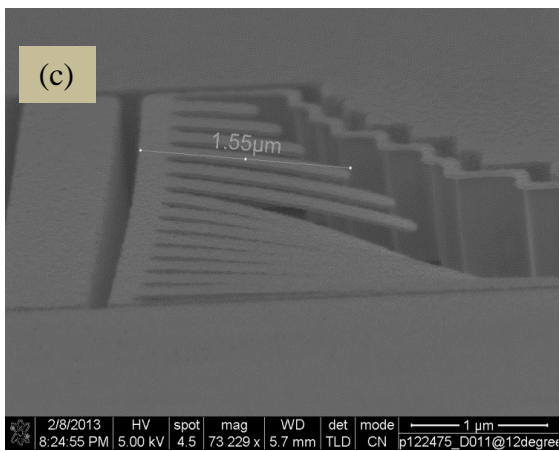
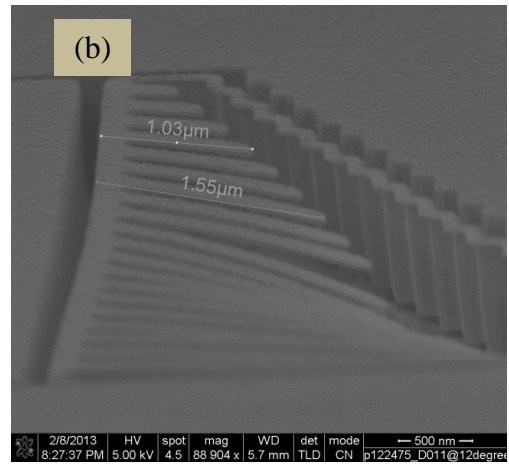
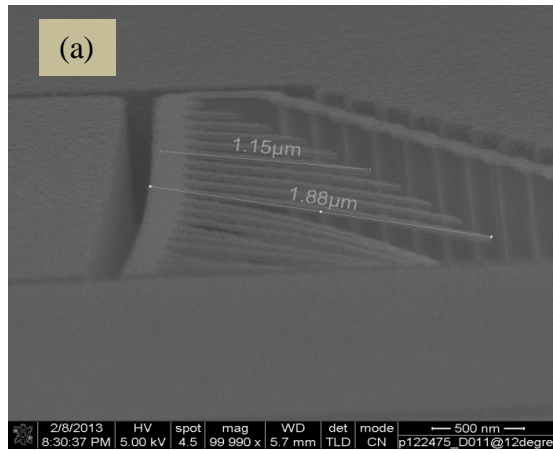


Figure 7.13: Arrays of released ~ 60 nm thick cantilevers fabricated by using the experimental best recipe. The arrays are chosen from column (a) 1 (b) 2 (c) 3 and (d) 4.

Table 7.5: Strain gradients in the ~60 nm thick cantilevers

| Array No. | No. of free-standing Cantilevers | Length of measured cantilever (μm) | Tip deflection (μm) | Strain gradient ($1/\mu\text{m}$) |
|-----------|----------------------------------|---|----------------------------------|-------------------------------------|
| 1 | 10 | 1.15 | -0.17 | -0.261 |
| | | 1.88 | -0.36 | -0.207 |
| | | 1.52 | -0.24 | -0.213 |
| 2 | 9 | 1.55 | -0.28 | -0.233 |
| | | 1.03 | -0.12 | -0.226 |
| | | 1.36 | -0.22 | -0.246 |
| 3 | 6 | 1.55 | -0.17 | -0.148 |
| | | 1.85 | -0.29 | -0.169 |
| | | 1.99 | -0.32 | -0.163 |
| 4 | 5 | 1.74 | -0.25 | -0.167 |
| | | 2.12 | -0.44 | -0.197 |
| | | 1.26 | -0.14 | -0.181 |

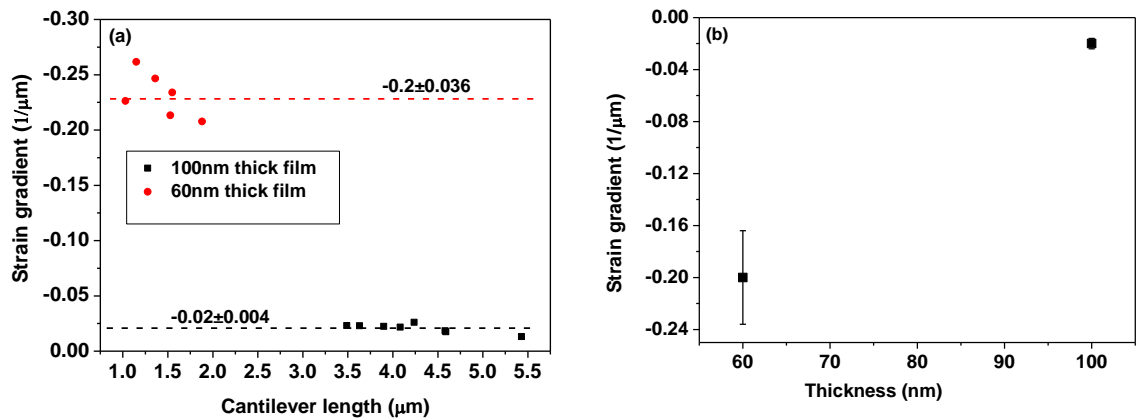


Figure 7.14: (a) Comparison of strain gradients in the 100nm and 60nm thick films deposited with experimental best recipe (b) thickness-dependent average strain gradient.

Since the residual stresses in the ~60 nm and ~100 nm thick films are similar and that the cantilevers have the same surface areas, these stresses are expected to induce thickness dependent deflections in the nanostructures as observed from their respective SEM images. From the SEM image for the 60 nm thick structure (Fig. 7.13), the deflections for 1.36, 1.55 and 1.85 μm long cantilevers are 0.22, 0.17 and 0.29 μm , respectively. In the case of 100 nm thick cantilevers, the deflections are 0.19, 0.18 and 0.15 μm for 4.59, 4.08 and 3.63 μm long cantilevers, respectively (Fig. 7.9). By using classical mechanics, the vertical deflection δ for a cantilever of a length L can be determined from $\delta = \frac{ML^2}{3EI}$ where M and E are the bending moment and the Young's modulus of the film, respectively. The area moment of inertial $I = bh^3/12$, where b and h are the width and thickness of the cantilever, respectively. The above formula implies that:

$$\delta \propto h^{-3} \tag{7.5}$$

Equation (7.5) indicates that thickness is a critical parameter due to its cubic dependence and that a slight thickness variation will lead to a large deflection. Since the residual stresses in the structures and the surface areas are the same, then the bending moment can

be considered equal. This implies that $\frac{\delta_{100}}{\delta_{58}} = \left[\frac{h_{100}}{h_{58}} \right]^{-3}$ must hold if the moduli are actually

equal. From the experimental data, $\frac{\delta_{100}}{\delta_{58}} \approx 0.14$ and $\left[\frac{h_{100}}{h_{58}} \right]^{-3} = 0.15$ which confirms that the

moduli are similar. The slight difference in the above ratios may indicate that the cantilevers are actually softer and thus deflect more than the values obtained from the

classical mechanics. It should be noted that the thicknesses used for the calculation are ~55 nm and ~98 nm which are based on the SEM images.

7.2.3 Strain Gradients, Stress and Resistivity Variations

The variation in the microstructure through the film thickness may be a reason for the observed variation in the strain gradients for the two recipes considered. A few previous studies, such as [214], have suggested that negative gradient indicates growth of columnar grain through the film thickness, while positive gradient suggests decreasing grain size through the film thickness. Based on the TEM images of Figs 5.11 - 5.14, it is shown that the microstructure of the film grown with the optimized recipe has a columnar shape. It is thus expected that the strain gradient will be negative. The TEM images also justify the constant stress observed during the continuous growth.

It is almost impossible to manufacture arrays of cantilevers with the same strain gradients across a single wafer. This is often due to the variation in the film properties during deposition and subsequent processing steps. For instance, it may be attributed to the non-uniformity in thickness or variations in the germanium fraction. It is demonstrated that these variations often lead to a significant differences in the local stress and resistivity across the film. With variations in the local stresses, it is expected that the strain gradients will vary from point to point. By using FSM stress tool operating with a 780 nm wavelength laser, 5 different scanning modes (1, 2, 4, 6 and 10 lines) were used to calculate the stress variations across the film deposited with the experimental best recipe. For each mode, the first scan passes through the wafer notch and then through $180^\circ/n$, $n (>1)$ is the number of lines to be scanned. For a 6-line scan for instance, the lines are 30° apart with the first linescan passing through the notch.

Figure 7.15 shows that a large stress variation is observed across the film and that a single scan through the notch is a good representative of the average stress in the thin layer. In Fig. 7.15 (a), large bow height changes are clearly observed at the wafer edges, with one edge more significant, for the 10-line measurement. This translates to a large change in the wafer curvature and hence higher stress variations at the edges (Fig. 7.15b). The largest variation in the curvature changes and hence the stress is found along the axis perpendicular to the notch axis. Consequently, the stress variation at the center is very minimal. The stress variations increase with the density of the scanned lines and interestingly, the average values are almost equal (Fig. 7.15c).

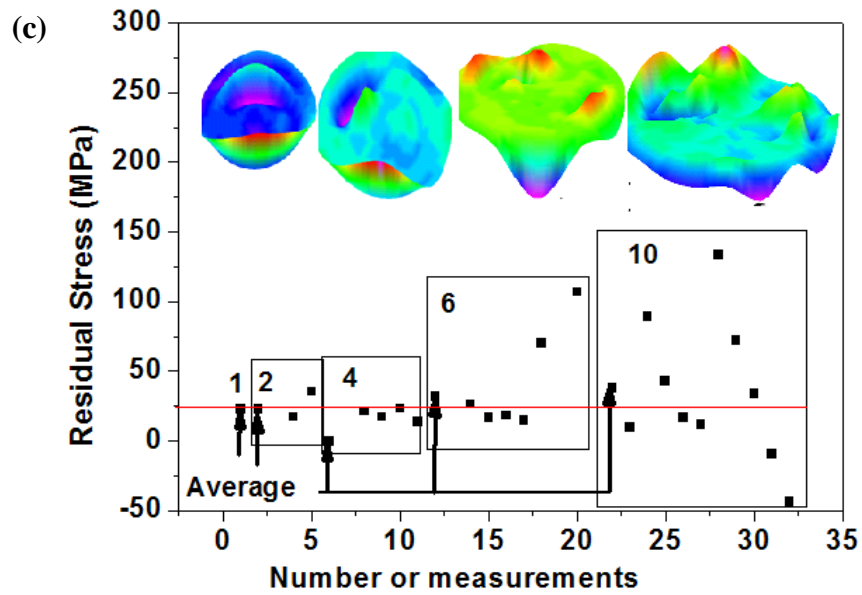
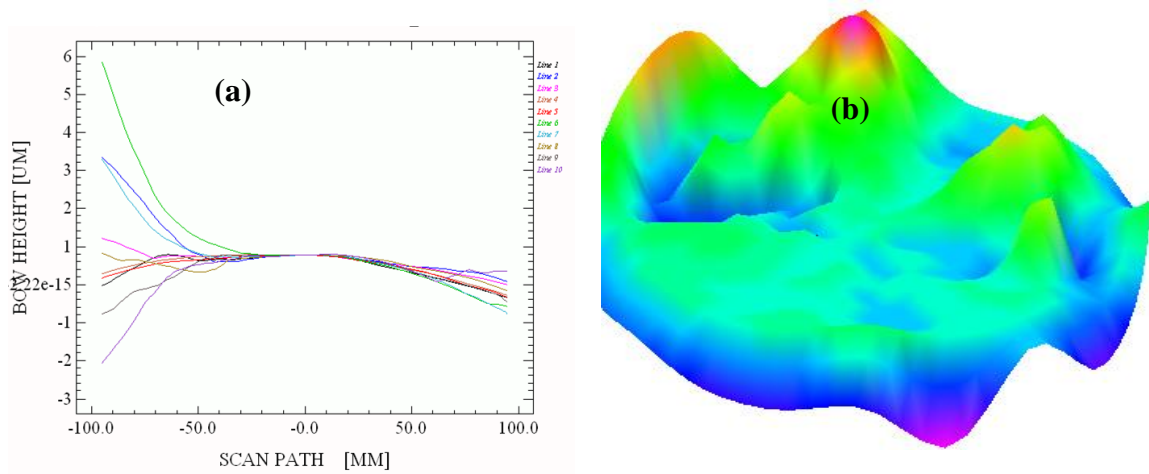


Figure 7.15: (a) Bow height difference along the scanned lines (b) stress map based on 10 lines of measurement (c) dependence of stress variation on the density of mapping. Insets are the 3D stress map images, no. 1 to 10 denote the number of lines scanned during the measurement. The horizontal red line denotes the average value for the entire measurement.

A similar resistivity variation is observed across the films (Fig.7.16). It is observed that the resistivity increases towards the center of the wafer. This may indicate that the films are thicker at the edge compared to the center. Although both films show similarity in the resistivity variation, the difference between the resistivity values is obvious. Because of this variation, the strain gradient is expected to be affected.

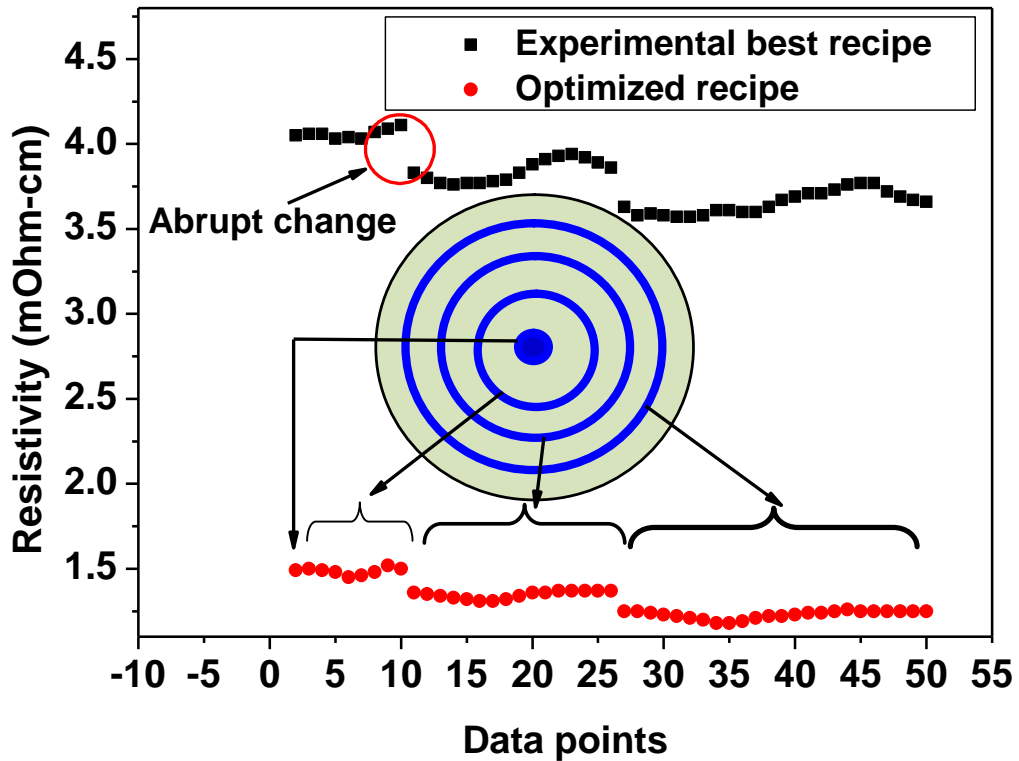


Figure 7.16: Resistivity variation in the optimized and experimental best films.

CHAPTER 8

CONCLUSIONS AND RECOMMENDATIONS

8.1 Conclusions

Polycrystalline silicon germanium films have been used to monolithically integrate Micro/Nano-ElectroMechanical Systems (M/NEMS) with its driving circuitry in the MEMS-last approach. One of the ways by which the sensitivity, efficiency and power consumption of a bioresonators, nanoswitches and many other NEMS products can be enhanced significantly is by miniaturization of the structural components. To do this, the properties of poly-SiGe films must be tailored appropriately to deliver the required characteristics for NEMS applications. Among these are low resistivity, slightly tensile stress, low strain gradient and high deposition rate at a temperature that will not damage the CMOS layer.

In this dissertation, a new approach to model intrinsic stresses is proposed. The approach is based on the concept of surface stresses by using dome-shaped islands and hexagonal shaped grains as compared to the spherical and cylindrical shapes used for the islands and grains respectively in previous studies reported in the literature. The equations that describe the stress evolution at the precoalescence, coalescence and postcoalescence stages are derived. These models describe how stresses evolve with island / grain's height and diameter, the surface stresses, the interfacial stresses and the stress due to grain boundary formation. For Cu films deposited on silicon substrates,

intrinsic stresses of -200, 140 to 230 and -260 to -80 MPa were obtained for the precoalescence, coalescence and steady state postcoalescence stages, respectively. With a few assumptions, the current models give -261, 102 and -115MPa for the three stages in that order.

Moreover, the dissertation presents a systematic procedure for the simultaneous optimization of residual stress, resistivity and deposition rate for CVD deposited ultrathin poly-SiGe films by using the grey-Taguchi optimization method. Seven process variables were identified as important parameters for controlling the deposition process and the resulting film properties, namely the deposition temperature, the silane, germane, diborane and hydrogen flow rates, the chamber pressure and the shower head-heater spacing. By using 4 different levels for each process variable, 32 unique experiments were defined based on L32 orthogonal array. The optimal combination of process parameters was determined by applying the grey relational analysis for multiple performance characteristics. The projected optimized process resulted in a ~100 nm thick poly-SiGe film with a tensile stress of 43 MPa, a very low resistivity of 1.39 m Ω -cm and a deposition rate of 0.34 nm/s. Further characterization shows that the film has a germanium concentration of 87%, a boron concentration of $2.20 \times 10^{21} \text{ cm}^{-3}$, a cauliflower surface morphology with a root-mean-square roughness of 4.2 nm, an elastic modulus of 101 GPa, a strain gradient of $-8.0 \times 10^{-2} / \mu\text{m}$, a carrier concentration of $3.57 \times 10^{21} \text{ cm}^{-3}$ and a Hall mobility of $3.76 \text{ cm}^2 \text{ V}^{-1} \text{ s}^{-1}$. The properties of the experimental best recipe, chosen from the L32 orthogonal array, are similar to those of the optimized recipe.

In addition, detailed experimental studies of evolution of stress, resistivity and surface properties of the experimental best and the optimized poly-SiGe films are presented. Various film thicknesses (~1 nm – ~200 nm) were deposited by LPCVD and characterized. The experimental study shows that the intrinsic stress evolved from a precoalescence highly compressive stress state to the coalescence less compressive state and remains constant thereafter. One of the possible reasons for the constant stress is the columnar nature of the grains as evident from the TEM images. The local stresses and local stress-thickness variations indicate that the curvatures of the films are negative. Also, the film's structural evolution goes through an incubation stage to a precoalescence stage (< 40nm) over a transient stage (40 – 60 nm) and finally to a stagnation stage (> 60 nm) as shown by the AFM images and the values of the Hall mobility. The surface properties were characterized by correlation length, root-mean-square (rms) roughness, roughness exponent, dynamic exponent and fractal dimension.

Finally, by using the optimized and the experimental best recipes, nanocantilevers were fabricated based on the established procedure for surface micromachining technology. The cantilevers were fabricated from ~100 nm and ~60 nm thick poly-SiGe films employing the new NEMS mask designed at imec, Belgium. The cantilevers' tip deflections from four different arrays were measured from SEM and AFM images and the strain gradients were calculated therefrom. The average strain gradients are $-0.083 \pm 0.009 / \mu\text{m}$, $-0.02 \pm 0.004 / \mu\text{m}$ and $-0.20 \pm 0.036 / \mu\text{m}$ for the cantilevers processed with the optimized, experimental best and 60 nm thick experimental best recipes, respectively. The strain gradient of $-0.02 \pm 0.004 / \mu\text{m}$ is considered to be good for applications in nanoswitches, nanoresonators, biosensors among others.

8.2 Recommendations for Future Studies

Having successfully fabricated nanocantilevers of a fairly acceptable strain gradient, it is necessary to optimize the process for the strain gradient specifically. Alternatively, the strain gradients in a few promising recipes can be obtained and compared to those of the optimized and the experimental best recipes. It is also important to incorporate a few processing steps to demonstrate the expected improved sensitivity for applications as bioresonators and as nanoswitches. For these applications, the addition of bottom and top electrodes will make the actuation of the structures effective. With a good response to the actuation source, it will be possible to measure a few properties like modulus, resonance frequency among others from the vibrating structures. It is also imperative to functionalize the nanocantilevers for the purpose of detection of DNA or gas molecules. With this, the minimum detectable mass of DNA or gas molecules can be determined from the shifts in the resonance frequencies of the cantilevers. It is also important to test for the reliability and life time fatigue of these structures.

For the stress evolution study, a range of film thicknesses was used with an assumption that a subsequent layer of poly-SiGe film does not densify or change the properties of the previous layer(s). This will however need further investigation. The most accurate method is to use an *in situ* stress measurement technique. In such a case, the actual stress can be obtained. On the stress model, a few deposition parameters such as the deposition rate and deposition temperature can be incorporated to account for the change in the deposition conditions.

References

- [1]. Maluf, N.; Williams, K. , An Introduction to Electromechanical Systems Engineering. Boston: Artech House, 2004.
- [2]. Lyshevski, S.E., Nano- and Microelectromechanical Systems: Fundamental of Nano- and Micro Engineering. London: CRC, 2001.
- [3]. Ryhamen, T. Impact of Silicon MEMS - 30 Year After. Edited by Tilli, M.; Lehto, A.; Motooka, T.; Lindross, V., Handbook of Silicon based MEMS Materials and Technologies . Oxford : Elsevier, 2010.
- [4]. Yole Développement, World MEMS Fab, 45 Rue Sainte Geneviève, 69006 Lyon. France, 2012.
- [5]. Bhushan, B., Introduction to Nanotechnology, Handbook of Nanotechnology. Springer, 2007.
- [6]. Li, M.; Tang, H.X.; Roukes, M.L., "Ultra-sensitive NEMS-based cantilevers for sensing, scanned probe and very high-frequency applications," Nature Nanotech., vol. 2, pp. 114-120, Jan. 2007.
- [7]. Poole, C. P; Owens, F. J., Introduction to Nanotechnology, New York : Wiley, 2003.
- [8]. Johnson, B. N.; Mutharasan, R., "Biosensing using dynamic-mode cantilever sensors: A review," Biosensors and Bioelectronics, vol. 32, no. 1, pp. 1– 18, Feb. 2012.
- [9]. Eom, K.; Park, H. S.; Yoon, D.S; Kwon, T., "Nanomechanical resonators and their applications in biological/chemical detection: Nanomechanics principles," Physics Reports, vol. 503, no. 4-5, pp. 115–163, Jun. 2011.
- [10]. Chaste, J.; Eichler, A.; Moser, J.; Ceballos, G.; Rurali, R.; Bachtold, A, "A nanomechanical mass sensor with yoctogram resolution," Nature Nanotech. vol. 7, pp. 301-304, April 2012.
- [11]. Naik, A. K.; Hanay, M. S.; Hiebert, W. K.; Feng, X. L.; Roukes, M. L., "Towards a single-molecule nanomechanical mass spectrometry," Nature Nanotech. vol. 4, pp. 445 - 450, Jun. 2009.

- [12]. Yang, Y. T.; Callegari, C.; Feng, X. L.; Ekinici, K. L.; Roukes, M. L., "Zeptogramscale scale nanomechanical mass sensing," *Nano Lett.* vol. 6, no. 4, pp. 583–586, April 2006.
- [13]. Witvrouw, A., "Scaling resonators made from poly-SiGe films," A presentation, 2011.
- [14]. Jayapal, M., "MEMS- based micromirror arrays for vision systems and display applications," *MEMS inventor Journal*, www.memsinvestorjournal.com., 2010
- [15]. Witvrouw, A.; Tilmans, H.A.C.; De Wolf, I., "Materials issues in the processing, the operation and the reliability of MEMS,". *Microelectronic Engineering*, vol.76, no. 1-4, pp. 245-257, Oct. 2004.
- [16]. Zorman, C.A.; Mehregany, M., *Materials for Microelectromechanical Systems*. Edit. Mohamed Gad-el-Hak. The MEMS Handbook. London : CRC Press, 2002.
- [17]. Sedky, S., *Post-processing techniques for integrated MEMS*. London : Aztech House, 2006.
- [18]. Zhang, X.; Zhang, T.; Wong, M., "Rapid thermal annealing of polysilicon thin films," *Journal of Microelectromechanical Systems*, vol. 9, no. 3, pp. 356 - 364, Dec. 1998.
- [19]. Bang, D.S.; Cao, M.; Wang, A.; Saraswat, K.C.; King, T., "Resistivity of boron and phosphorus doped polycrystalline SiGe films," *Applied Physics Letters*, vol. 66, no. 2, pp. 195–197, Nov. 1995.
- [20]. Bryce, G.; Severi, S.; Du Bois, B.; Willegems, M.; Claes, G.; Van Hoof, R.; Haspelslagh, L.; Decoutere, S.; Witvrouw, A., "Simultaneous Optimization of The Material Properties, Uniformity And Deposition Rate of Polycrystalline CVD And PECVD Silicon-Germanium Layers For MEMS Applications," *ECS Transactions*, vol. 16, no. 10, pp. 353-364, 2008.
- [21]. Sedky, S; Witvrouw, A.; Baert, K., "Poly SiGe, a promising material for MEMS monolithic integration with driving electronics," *Sensor and Actuator A*, vol. 97-98, pp. 503 - 511, April 2002.
- [22]. Kannan, S.; Taylor, C.; Allred, D., "PECVD growth of $\text{Si}_x\text{Ge}_{1-x}$ films for high speed devices and MEMS," *Journal of Non-Crystalline Solids*, vol. 352, pp. 1272 - 1274, Jun. 2006.
- [23]. Gonzaleza, P.; Haspelslagh, L.; Severi, S.; De Meyera, K.; Witvrouw, A., "Piezoresistivity and Electrical Properties of Poly-SiGe Deposited at CMOS-

Compatible Temperatures," Proceedings of the European Solid-State Device Research Conference (ESSDERC), pp. 476-479, 2010.

- [24]. Gonzalez, P.; Guo, B.; Rakowski, M.; De Meyer, K.; Witvrouw, A., "CMOS compatible polycrystalline silicon-germanium based pressure sensors," *Sensors and Actuators A- Physical*, vol. 188, pp 9–18, Dec. 2012.
- [25]. Franke, A.E.; Jiao, Y.; Wu, M.T.; King, T.-J.; Howe, R.T., "Post-CMOS modular integration of poly-SiGe microstructures using poly-Ge sacrificial layers," *IEEE proceeding on Solid-State Sensor and Actuator Workshop*. pp.18-21, 2000.
- [26]. Quevy, E.; Bhave, S.; Takeuchi, H.; King, T.-J.; Howe, R., "Poly-SiGe high frequency resonators based on lithographic definition of nano-gap lateral transducers," *IEEE proceeding on Solid-State Sensor, Actuator and Microsystems Workshop*, 2004
- [27]. Sedky, S; Gromova, M.; Van der Donck, T; Celis, J.P; Witrouw, A., "Characterization of KrF excimer laser annealed PECVD Si_{1-x}Ge_x for MEMS post-processing," *Sens. Actuators A- Physical*, vol. 127, pp. 316–323, March 2006.
- [28]. Witvrouw, A.; Mehta, A.; Verbist, A.; Du Bois, B.; Van Aerde, S.; Ramos-Martos, J.; Ceballos, J.; Ragel, A.; Mora, J.; Lagos, M.; Arias, A.; Hinojosa, J.; Spengler, J.; Leinenbach, C.; Fuchs, T.; Kronmuller, S., "Processing of MEMS gyroscopes on top of CMOS ICs." *IEEE International Solid-State Circuits Conference (ISSCC)*, pp. 88-89, 2005.
- [29]. Stoffels, S.; Severi, S.; Vanhoof, R.; Mertens, R.; Puers, R.; Witvrouw, A.; Tilmans, H., "Light sensitive SiGe MEM resonator for detection and frequency tuning applications," *IEEE 23rd International Conference on Micro-ElectroMechanical Systems (MEMS)*. pp. 691-694, 2010
- [30]. Heck, J.; Adams, D.; Belov, N.; Chou, T.-K.A.; Kim, B.; Kornelsen, K.; Ma, Q.; Rao, V.; Severi, S.; Spicer, D.; Tchelepi, G.; Witvrouw, A., "Ultra-highdensity MEMS probe memory device," *Microelect. Eng.*, vol. 87, no. 5-8, pp. 1198 – 1203, May-Aug. 2010.
- [31]. Haspeslagh, L.; De CostePedreira, J.O.; De Wolf, I.; Du Bois, B.; Verbist, A.; Van Hoof, R.; Willegems, M.; Locorotondo, S.; Bryce, G.; Vaes, J.; van Drienuizen, B.; Witvrouw, A., "Highly reliable CMOS-integrated 11Mpixel SiGe-based micro-mirror arrays for high-end industrial applications," *IEEE International Electron Devices Meeting*, pp. 1-4, 2008

- [32]. Wee, A; Huan, C; Thong, P; Tan, K., "A comparative study of initial oxygen and water reactions on germanium and silicon using SIMS," *Corrosion Science*, vol. 36, no. 1, pp. 9 - 22, Jan. 1994.
- [33]. Madou, M.J., *Fundamentals of Microfabrication* (2nd ed.). CRC Press, 2002.
- [34]. Sharma, A. K., Gupta, N., "Material Selection of Rf-Mems Switch Used For Reconfigurable Antenna Using Ashby's Methodology," *Progress In Electromagnetics Research Letters*, vol. 31, pp. 147-157, April 2012.
- [35]. Guisbiers, G.; Herth, E.; Legrand, B.; Rolland, N.; Lasri, T.; Buchaillet L.. "Materials selection procedure for RF-MEMS," *Microelectronic Engineering*, vol. 87, pp. 1792–1795, Nov. 2010.
- [36]. Martienssen, W.; Warlimont, H., *Springer Handbook of Condensed Matter and Materials Data.*: Springer, Berlin, 2005.
- [37]. Richards Grayson, A.C.; Shawgo, R.S.; Johnson, A.M.; Flynn, N.T.; Li, Y.; Cima, M.J.; Langer, R., " A BioMEMS Review: MEMS Technology for Physiologically Integrated Devices," *Proceeding of the IEEE*, vol. 92, pp 6-22, 2004.
- [38]. Gopal Reddy, C.V.; Manorama, S.V.; Rao V.J., "Semiconducting gas sensor for chlorine based on inverse spinel nickel ferrite," *Sensors and Actuators B: Chemical*, vol. 55, no. 1, pp. 1. 90–95, April 1999.
- [39]. Benard, W.L.; Kahn, H.; Heuer, A.H.; Huff, M.A., "A Titanium-Nickel Shape-Memory Alloy Actuated Micropump," *International Conference on Solid-State Sensors and Actuators*, Chicago, pp. 361 - 364, June 1997.
- [40]. Iliescu, C., Chen, B., "Thick and low-stress PECVD amorphous silicon for MEMS applications," *J. Micromech. Microeng.* , vol. 18 ,no. 1, pp. 015024, Jan. 2008.
- [41]. Blakemore, J. S., "Semiconducting and other major properties of gallium arsenide," *Journal of Applied Physics*, vol. 53, pp. R123-R181, May 1982.
- [42]. Hjort, K., Strucubel, K., Viktorovich, P., "Indium phosphide based micro optoelectro mechanics," *Proc. IEEE/LEOS summer topicals*, Keystone, CO, pp. 45 - 46 , Aug.1996.
- [43]. Spahn, O.B.; Sullivan, C.; Burkhart, J.; Tigges, C.; Garcia, E., "GaAs-based microelectromechanical waveguide switch," *Proc. IEEE/LEOS Int. Conf. Optical MEMS*,pp. 41 - 42, Aug. 2000.

- [44]. Chiang, Y.M.; Lau, J.; Bachman, M.; Li, G.P.; Kim, H.K.; Ra, Y.; Ketola, K., " Deep Anisotropic Etching of Gaas with Chlorine-Based Chemistries and SU-8 Mask Using Rie and High Density ICP Etching Methods." Symp. Proc.Materials Research Society: vol. 729, pp. U3.1.1–U3.1.6, 2002.
- [45]. Hotovy, I.; Rehacek, V. ; Mika, F.; Lalinsky, T.; Hascik, S.;Vanko, G.; Drzik, M., "Gallium arsenide suspended microheaterfor MEMS sensor arrays," : Microsyst Technol, vol. 14, pp. 629–635, April 2008.
- [46]. Sarro, P.M., "Silicon carbide as a new MEMS technology," Sensors and Actuators A: Physical, vol. 82, no. 1-3, pp. 210–218, May 2000.
- [47]. Behnel, N.; Fuchs, T., New SiC Pressure-Sensor-Technologies for Harsh Environments. Berlin, Germany : MikroSystemTechnik Kongress, 2009.
- [48]. Young, D. J.; Pehlivanoglu, I. E.; Zorman, C. A., "Silicon carbide MEMS-resonator-based oscillator," J. Micromech. Microeng. 19, pp. 115027, Oct. 2009.
- [49]. Liu, C., "Recent Developments in Polymer MEMS," Adv. Mater., 2007, vol. 19, pp. 3783–3790, Oct. 2007.
- [50]. Engel, J.; Chen, J.; Fan, Z.; Liu, C., "Polymer micromachined multimodal tactile sensors," Sens. Actuators A, vol. 117, pp. 50-61, July 2005.
- [51]. Smith, C.S., "Piezoresistive Effect in Germanium and Silicon," Phys. Rev., vol. 94, pp. 42-49, April 1954.
- [52]. Kasper, E.; Herzog, H.J.; Kibbel, H., "A onedimensional SiGe superlattice grown by UHV epitaxy," Applied Physics, vol. 8, pp. 199-205, Nov. 1975
- [53]. Fedder, G.K; Howe, R.T; Liu, T-J. K.; Que, E.P., "Technologies for Cofabricating MEMS and Electronics," Proceedings of the IEEE. pp. 306-322, Jan. 2008.
- [54]. Claes, G. Poly-silicon germanium thin-film package: study of structural features enabling CMOS-MEMS integration. Leuven : Katholieke Universiteit Leuven, 2011.
- [55]. Lin, H. C; Chang, C. Y.; Chen, W. H; Tsai, W. C.; Chang, T. C.; Jung, T. G.; Lin, H. Y., "Effects of SiH_4 , GeH_4 , and B_2H_6 on the Nucleation and Deposition of Polycrystalline $\text{Si}_{1-x}\text{Ge}_x$ Films," J. Electrochem. Soc., vol. 141, no. 9, pp. 2559-2563, 1994.
- [56]. Howe, R. T.; Franke, A.; King, T.-J., Polycrystalline Silicon Germanium Films for Forming Microelectromechanical Systems. 6, 210,988 USA, 3 April 2001.

- [57]. Franke, A.; Howe, R.T.; King, T.-J., Polycrystalline Polycrystalline Silicon Germanium Films for Microelectromechanical Systems Application. 6,448,622 USA, 10 Sept 2002.
- [58]. Bhave, S. A.; Bircumshaw, B. L.; Low, W. Z.; Kim, Y.-S.; Pisano, A. P.; King, T.-J.; Howe, T., "Poly-SiGe: A High-Q Structural Material For Integrated Rf MEMS,". South Carolina, Solid-State Sensor, Actuator and Microsystems Workshop, pp. 34-37, 2002.
- [59]. Guo, B.; Severi, S.; Bryce, G.; Claes, G.; Van Hoof, R.; Du Bois, B.; Haspeslagh, L.; Witvrouw, A.; Decoutere, S., "Improvement of PECVD Silicon-Germanium Crystallization for CMOS Compatible MEMS Applications,". J. Electrochem. Soc., vol. 157, pp. D103-D110, 2010.
- [60]. El-Rifai, J. ; Sedky, S.; Van Hoof, R.; Severi, S.; Lin, D.; Sangameswarana, S.; Puersa, R.; Van Hoof, C.; Witvrouw, A., "SiGe MEMS at processing temperatures below 250C,". Sensors and Actuators A: Physical, vo. 188, pp. 230–239, Dec. 2012.
- [61]. Sangameswaran, S.; Cherman, V.; De Coster, J.; Witvrouw, A.; Groeseneken, G.; De Wolf, I. "Design and fabrication of SiGe MEMS structures with high intrinsic ESD robustness," IEEE International Reliability Physics Symposium (IRPS), 2012.
- [62]. Li, Q. ; Goosen, J.F.L.; van Beek, J.T.M.; van Keulen, F.; Zhang, G.Q., "Outgassing of Materials Used for Thin Film Vacuum Packages," International Conference on Electronic Packaging Technology & High Density Packaging (ICEPT-HDP), pp. 802 - 806, 2009.
- [63]. Wang, B.; Tanaka, S.; Guo, B.; Vereecke, G.; Severi, S.; Witvrouw, A.; Wevers, M.; De Wolf, I., "Outgassing study of thin films used for poly-SiGe based vacuum packaging of MEMS," Microelectronics Reliability, vol. 51, pp. 1878–1881, Sep. - Nov. 2011.
- [64]. Gonzalez, P.; Guo, B.; Varela Pedreira, O.; Severi, S.; De Meyer, K.; Witvrouw, A., "Sealing of poly-SiGe surface micromachined cavities for MEMS-above-CMOS applications" J. Micromech. Microeng., vol. 21, pp. 115019, 2011.
- [65]. Gonzalez, P.; Rakowski, M.; San Segundo, D.; Severi, S.; de Meyer, K.; Witvrouw, A., "CMOS-Integrated Poly-SiGe Piezoresistive Pressure Sensor," IEEE Electron Device Letters, vol. 33, no. 8, August 2012.

- [66]. Helin, P.; Czarnecki, P.; Verbist, A.; Bryce, G.; Rottenberg, X.; Severi, S., "Poly-SiGe-Based Cmut Array With High Acoustical Pressure" Paris : IEEE MEMS, 2012.
- [67]. Rochus, V.; Jansen, R.; Tilmans, H. A. C.; Rottenberg, X.; Chen, C.; Ranvier, S.; Lamy, H.; Rochus, P., "Poly-SiGe-based MEMS Xylophone Bar Magnetometer," IEEE SENSORS, 2012.
- [68]. Sedky, S.; Witvrouw, A.; Saerens, A.; Van Houtte, P.; Poortmans, J.; Baert, K., "Effect of in situ boron doping on properties of silicon germanium films deposited by chemical vapor deposition at 400 °C," J. Mater. Res., vol. 16, no. 9, pp 2607-2612, Jan. 2001.
- [69]. Lin, J.L.; Lin, C.L., "The use of the orthogonal array with greyrelational analysis to optimize the electrical discharge machining process with multiple performance characteristics" Inter. J. Mach. Tools. Manuf., vol. 42, no. 2, pp. 237–244, Jan. 2002,
- [70]. Edelman, F.; Weil, R.; Werner, P.; Reiche, M.; Beye, W., "Crystallization of amorphous hydrogenated Si_{1-x}Ge_x films," Physica Status Solid, vol. 150, no.1, pp. 407-425, July 1996.
- [71]. King, T.-J.; Saraswat, K.C., "Deposition and properties of low-pressure chemical-vapor deposited polycrystalline silicon-germanium films," Journal of The Electrochemical Society, vol. 141, no. 8, pp. 2235–2241, 1994.
- [72]. Thompson, C. V., "Structure Evolution During Processing of Polycrystalline Films," Annu. Rev. Mater. Sci., vol. 30, pp. 159 - 190, Aug. 2000.
- [73]. "Powder Diffraction Data, joint Committee of Powder Diffraction Standards (JCPDS) Associateship at the National Bureau of Standards (NBS)", ed. D.K. Smith, USA,. 1976.
- [74]. Pelliccione, M.; Lu, T.-M., Evolution of Thin Film Morphology: Modeling and Simulations. New York : Springer, 2008. ISSN 0933-033X.
- [75]. Hartmann, E.; Hahn, P.O.; Behm, R.J., "Determination of nanometer structures and surface-roughness of polished Si wafers by Scanning Tunneling Microscopy" J. Appl. Phys., vol. 69, pp. 4273-4281, Dec. 2005.
- [76]. Martínez, J.F.G.; Nieto-Carvajal, I.; Abad J.; Colchero, J., " Nanoscale measurement of the power spectral density of surface roughness: how to solve a difficult experimental challenge," Nanoscale Research Letters, vol. 7, pp.174, 2012.

- [77]. Teichert, C., "Self-organization of nanostructures in semiconductor heteroepitaxy," *Physics Reports*, vol. 365, pp. 335–432, Aug. 2002.
- [78]. Palasantzas, G., "Power spectrum and surface width of self-affine fractal surfaces via the k-correlation model," *Phys. Rev. B*, Vol. 48, pp. 14472, Nov. 1993.
- [79]. Sperling, B.A.; Abelson, J.R., "Kinetic roughening of amorphous silicon during hot-wire chemical vapor deposition at low temperature," *J. Appl. Phys.*, vol. 101, pp. 02491, Jan. 2007.
- [80]. Shen, Y.G.; Liu, Z.-J.; Jiang, N.; Zhang, H.S.; Chan, K.H.; Xu, Z.K., "Effect of silicon addition on surface morphology and structural properties of titanium nitride films grown by reactive unbalanced direct current-magnetron sputtering," *J. Mater. Res.*, vol. 19, pp. 523, Oct. 2003
- [81]. Musil, J., "Hard and superhard nanocomposite coatings," *Surf. Coat. Technol.*, vol. 25, pp. 322, March 2000
- [82]. Li, B.Q.; Kojima, I.; Zuo, J.M., "Surface evolution of ultrahigh vacuum magnetron sputter deposited amorphous Si," *J. Appl. Phys.*, vol. 91, pp. 4082, April 2002.
- [83]. Tello, J.S.; Bower, A.F., "Numerical simulations of stress generation and evolution in Volmer–Weber thin films," *Journal of the Mechanics and Physics of Solids*, vol. 56, pp. no. 8, 2727–2747, Aug. 2008.
- [84]. Johlin, E.; Tabet, N.; Castro-Galnares, S.; Abdallah, A.; Bertoni, M.I.; Asafa, T.; Grossman, J.C.; Said, S.; Buonassisi, T., "Structural origins of intrinsic stress in amorphous silicon thin," *Physical Review B*, vol. 85, no. 7, pp. 075202, Feb. 2012.
- [85]. Guo, B.; Wang, B.; Wen, L.; Helin, P.; Claes, G.; De Coster, J.; Du Bois, B.; Verbist, A.; Van Hoof, R.; Vereecke, G.; Haspelslagh, L.; Tilmans, H.A.C.; Decoutere, S.; Osman, H.; Puers, R.; De Wolf, I.; Tanaka, S.; Severi, S.; Witvrouw, A., "Poly-SiGe-Based MEMS Thin-Film Encapsulation," *Journal of Microelectromechanical Systems*, vol. 21, no. 91, pp. 110 - 120, Feb. 2012.
- [86]. Mehta, A.; Gromova, M.; Rusu, C.; Baert, K.; van Hoof, C.; Witvrouw, A., "Novel high growth rate processes for depositing poly-SiGe structural layers at CMOS compatible temperatures," *Proceedings of the MEMS, Maastricht, Netherland*, pp. 721-724, 2004.
- [87]. Hüpkes, J.; Zhu, H.; Owen, J.I.; Jost, G.; Bunte, E., "Instabilities in reactive sputtering of ZnO:Al and reliable texture-etching solution for light trapping in

- silicon thinfilm solar cells," *Thin Solid Films*, vol. 520, no. 6, pp. 1913–1917, Jan. 2012.
- [88]. Xie, J.; Imanishi, N.; Zhang, T.; Hirano, A.; Takeda, Y.; Yamamoto, O., "Li-ion diffusion kinetics in LiFePO_4 thin film prepared by radio frequency magnetron sputtering," *Electrochimica Acta*, vol. 54, no. 20, pp. 4631–4637, Aug. 2009.
- [89]. Floro, J.A.; Hearne, S.J.; Hunter, J.A.; Kotula, P.; Chason, E.; Thompson, S. C.; Seel, C. V., "The dynamic competition between stress generation and relaxation mechanisms during coalescence of Volmer–Weber thin films," *Journal of Applied Physics*, vol. 89, no. 9, pp. 4886-4897, 2001.
- [90]. Wagner, L. K.; Grossman, J. C., "Light-Induced Defects in Amorphous Silicon Solar Cells," *Physical Review Letters*, vol. 101, pp. 265501, Dec. 2008.
- [91]. Pauleau, Y., "Generation and evolution of residual stresses in physical vapour-deposited thin film," *Vacuum*, vol. 61, no. 2-4, pp. 175 - 181, May 2001.
- [92]. Kim, S.Y; Park, H.S., "Utilizing Mechanical Strain to Mitigate the Intrinsic Loss Mechanisms," *Physical Review Letter*, vol. 101, no. 21, pp. 215502, Nov. 2008.
- [93]. Freund, L.B.; Suresh, S., *Thin Film Materials: Stress, Defects Formation and Surface Evolution*. Cambridge : Cambridge University Press, 2003.
- [94]. Evans, A.G.; Hutchinson, J.W., "A critical assessment of theories of strain gradient plasticity," *Acta Materialia*, vol. 57, pp. 1675-1688, Jan. 2009.
- [95]. Abermann, R., "Measurements of the intrinsic stress in thin metal films," *Vacuum*, vol. 41, no 4-6, pp. 1279-1282, Jan. 1990.
- [96]. Thompson, C. V., "Structure Evolution During Processing of Polycrystalline Films," *Annu. Rev. Mater. Sci.*, vol. 30, pp. 159 - 190, August 2000.
- [97]. Nix, W.D; Clemens, M.D., "Crystallite coalescence: A mechanism for intrinsic tensile stresses in thin films," *J. Mater. Res.*, vol. 14, no. 8, pp. 3467 - 3473, jan. 1999.
- [98]. Chaudhari, P., "Grain Growth and Stress Relief in Thin Films" *J. Vac. Sci. Techn.*, vol. 9, no. 1, pp. 520-522, 1972.
- [99]. Dorner, M. F.; Nix, W.D., "Stresses and Deformation Processes in Thin Films on Substrates," *CRC Critical Reviews in Solid State and Materials Sciences*, vol. 14, no. 3, pp. 225-267, Sept. 1988.

- [100]. Cammarata, R.C.; Trimble, T.M.; Srolovitz, D.J., "Surface stress model for intrinsic stresses in thin films," *J. Mater. Res.*, vol. 15, no. 11, pp. 2468 - 2474, Jan. 2000.
- [101]. Sheldon, B.W.; Ditekowski, A.; Beresford, R.; Chason, E.; Rankin, J., "Intrinsic Compressive Stress in Polycrystalline Films with Negligible Grain Boundary Diffusion," *J. Appl. Phys.*, vol. 94, no. 2, pp. 948-957, Jun. 2003.
- [102]. Seel, S.C.; Thompson, C.V.; Hearne, S.H.; Floro, J.A., "Tensile stress evolution during deposition of Volmer–Weber thin films," *J. Appl. Phys.*, vol. 88, no. 12, pp. 7079–7088, 2000.
- [103]. Floro, J.A.; Chason, E.; Lee, S.R.; Twisten, R.D.; Hwang, R.Q.; Freund, L.B., "Real-Time Stress Evolution During Si_xGe_x Dislocations, Islanding, and Segregation," *Journal of Electronic Materials*, vol. 26, no. 9, pp. 969-979, 1997.
- [104]. Laugier, M., "Intrinsic stress in thin films of vacuum evaporated LiF and ZnS using an improved cantilevered plate technique," *Vacuum*, volume 31, no. 3, pp. 155-157, March 1981.
- [105]. Guisbiers, G.; Van Overschelde, O.; Wautelet, M., "Nanoparticulate origin of intrinsic residual stress in thin films" *Acta Materialia*, vol. 55, no.105, pp. 3541–3546, Jun. 2007.
- [106]. Hoffman, R.W., "Stresses in thin films: the relevance of grain boundaries and impurities," *Thin Solid Films*, vol. 34 ,no. 2, pp. 185-190, 1976.
- [107]. Floro, J.A.; Chason, E.; Cammarata, R.C.; Srolovitz, D.J., " Physical origins of intrinsic stresses in Volmer-Weber thin films," *MRS Bulletin*, pp. 19-25, Jan. 2002.
- [108]. Dowling, N.E., *Mechanical Behaviour of Materials*. New Jersey : Prentice Hall, 1999.
- [109]. Freund, L. B.; Chason, E., "Model for stress generated upon contact of neighboring islands on the surface of a substrate," *J. Appl. Phys.*, vol. 89, no.9, pp. 4866 - 4873, 2001.
- [110]. Seel, .C.; Thompsona, C.V.; Hearne, S.J.; Floro, J.A., "Tensile stress evolution during deposition of Volmer–Weber thin films," *Journal of Applied Physics*, vol. 88, no.12, pp. 7079, 2000.
- [111]. Wiest, F.; Capodieci, V.; Blank, O.; Gutsche, M.; Schulze, J.; Eisele, I.; Matusche, J.; Schmidt. U.I., "Conformal aluminum oxide coating of high aspect

- ratio structures using metalorganic chemical vapor deposition," *Thin Solid Films*, vol. 496, no. 2, pp. 240 – 246, Feb. 2006.
- [112]. Gupta, R.; Yoo, W. J.; Wang, Y.; Tan, Z.; Samudra, G.; Lee, S.; Chan, D. S. H.; Loh, K. P.; Bera, L. K.; Balasubramanian, N.; Kwong, D.-L., "Formation of SiGe nanocrystals in HfO₂ using in situ chemical vapordeposition for memory applications," *Appl. Phys. Lett.*, vol. 84, no. 21, pp. 4331, 2004.
- [113]. Li, J.C.; Wang, Y.; Ba, D.C., "Characterization of semiconductor surface conductivity by using microscopic four-point probe technique," *Physics Procedia*, vol. 32, pp. 347 – 355, Jun. 2012.
- [114]. Sidan, J. Boron Activation and Diffusion in Polycrystalline Silicon with Flash-Assist Rapid Thermal Annealing. PhD Thesis, University of Florida, 2011.
- [115]. van der Pauw, L. J., "A method of measuring the resistivity and Hall coefficient on lamellae of arbitrary shape," *Philips Technical Review*, vol. 20, pp. 220-224, 1958.
- [116]. Lin, J. F.; Li, S. S.; Linares, L. C.; Teng, K. W., "Theoretical analysis of Hall factor and Hall mobility in p-type silicon," *Solid-State Electronics* vol. 24, no. 9, pp. 827–833, Sept. 1981.
- [117]. Tarey, R. D.; Rastogi, R.S.; Chopra, K.L., "Characterization of thin films by glancing incidence X-Ray diffraction," *The Rigaku Journal*, vol. 4, no. 1/1, pp. 11-15, 1987.
- [118]. Pola-Albores, F.; Paraguay-Delgado, F.; Antunez-Flores, W.; Amezaga-Madrid, P.; Rios-Valdovinos, E.; Miki-Yoshida, M., "Microstructural Study of ZnO Nanostructures by Rietveld Analysis," *Journal of Nanomaterials*, pp. 643126, 2011.
- [119]. James, R. W., *The Optical Principles of the Diffraction of X-rays*. Bell and Sons, London, UK, 413–438, 1967.
- [120]. Thompson, C.V.; Leib, J.S.; Mönig, R.; Takahashi, A., "The Origin and Control of Residual Stresses in Nanocrystalline Thin Films: The Roles of Stress Relaxation During Growth. Lecture delivered at the Dept. of Materials Science and Engineering, MIT, 2008.
- [121]. Stoney, G.G., "The Tension of Metallic Films Deposited by Electrolysis," *Proc. Roy. Soc. Lond., Ser. A*, vol. 82, pp. 172, 1909.

- [122]. Feng, X.; Huang, Y.; Rosakis, A. J., "On the Stoney Formula for a Thin Film/Substrate System With Nonuniform Substrate Thickness," *J. Appl. Mech.*, vol. 74, pp. 1276-1281, Nov. 2007.
- [123]. Oliver, W. C.; Pharr, G. M., "An improved technique for determining hardness and elastic modulus using load and displacement sensing indentation experiments" *J. Mater. Res.*, vol. 7, no. 6, pp. 1564-1583, Jan. 1992.
- [124]. Banks-Sills, L.; Shklovsky, J.; Krylov, S.; Bruck, H. A.; Fourman, V.; Eliasi, R.; Ashkenazi, D., "A Methodology for Accurately Measuring Mechanical Properties on the Micro-Scale," *Strain*, vol. 47, pp. 288–300, March 2011.
- [125]. Chu, W K. Rutherford backscattering spectrometry. *ASM Handbook.*, 1986.
- [126]. De Wolf, I.; Jian, C.; van Spengen W. M., "The investigation of microsystems using Raman spectroscopy," *Optics and Lasers in Engineering*, vol. 36, no. 2, pp. 213–223, Aug. 2001.
- [127]. Low, C.W.-Z., *Novel Processes for Modular Integration of Silicon-Germanium MEMS with CMOS Electronics*. Berkeley : PhD Dissertation of University of California, 2007.
- [128]. Guo, L.; Searson, P. C., "Influence of anion on the kinetics of copper island growth," *Nanoscale*, vol. 2, pp. 2431–2435, Nov. 2010.
- [129]. Koch, R., "The intrinsic stress of polycrystalline and epitaxial thin metal films," *J. Phys.: Condens. Matter*, vol. 6, no. 45, pp. 9519-9550, Nov. 1994.
- [130]. Ji, Y. ; Zhong, T.; Li, Z.; Wang, X.; Luo, D.; Xia, Y.; Liu, Z., "Grain structure and crystallographic orientation in Cu damascene lines," *Microelect. Eng.* 4, vol. 71, no.2, pp. 182–189, Feb. 2000.
- [131]. Seel, S C., "Stress and structure evolution during Vomer-Welber growth of thin films. PhD Thesis, MIT, Cambridge, 2002.
- [132]. Pao, C.-W.; Srolovitz, D.J.;Thompson, C.V., "Effects of surface defects on surface stress of Cu(001) and Cu(111)," *Physical Review B*, vol. 74, no. 15, pp. 5543, Oct. 2006,
- [133]. Abermann, R.; Koch, R., "The internal stress in thin silver, copper and gold films," *Thin Solid Films*, vol. 129, pp. 71 -78, July 1985.
- [134]. Shull, A.L. ,*Measurement of stress during deposition of copper and silverthin films and multilayers*. Cambridge, M.A. : Havard University, 1996.

- [135]. Murr, L.E., *Interfacial Phenomena in Metals and Alloys*. Reading, M.A. : Addison-Wesley, 1975.
- [136]. Seel, S.C., *Modified N-C*, Presentation Massachusetts Institute of Technology, 2002.
- [137]. Horcas, I.; Fernandez, R.; Gomez-Rodriguez, J.M; Colchero, J.; Gomez-Herrero, J.; Baro, A.M., "WSxM: A software for scanning probe microscopy and a tool for nanotechnology," *Rev. Sci. Instrum.*, vol. 78, no. 1, pp. 013705, 2007.
- [138]. Hara, S.; Izumi, S.; Kumagai, T.; Sakai, S., "Surface energy, stress and structure of well-relaxed amorphous silicon: A combination approach of ab initio and classical molecular dynamics," *Surface Science*, vol. 585, no. 1-2, pp.17–24, 2005.
- [139]. Chason, E.; Sheldon, B.W.; Freund, L.B., "Origins of compressive residual stress in polycrystalline thin films," *Phys. Rev. Lett.*, vol. 88, no.15, pp. 156103, March 2002.
- [140]. Chason, E.; Shin, J.W.; Hearne, S.J.; Freund, L.B., "Kinetic model for dependence of thin film stress on growth rate, temperature, and microstructure," *J. Appl. Phys.*, vol. 111, no. 8, pp. 083520, March 2012.
- [141]. Floro, J. A.; Chason, E.; Cammarata, R.C.; Srolovitz, D.J., "Physical origins of intrinsic stresses in Volmer-Weber thin films," *MRS Bulletin*, pp. 19-25, Jan. 2002.
- [142]. Taguchi, G., *Taguchi Methods - Design of Experiments*. Dearborn, MI : American Supplies Institute, 1993.
- [143]. DePinto, G.; Wilson, J., "Optimization of Lpcvd Silicon Nitride Deposition Process," *IEEE/SEMI Advanced Semiconductor Manufacturing Conference*, pp. 47 - 53, 1990.
- [144]. Chen, Y.H.; Tam, S.C.; Chen, W.L.; Zheng, H.Y., "Application of Taguchi Method in the Optimization of Laser Micro-Engraving of Photomasks" *Int. J. Mat. & Prod. Tech.*, vol. 11, no.3-4, pp. 333-344, 1996.
- [145]. Chen, D.Y.; Tsao, C.C.; Hsu, C.Y., "Photocatalytic TiO₂ thin films deposited on flexible substrates by radio frequency (RF) reactive magnetron sputtering," *Curr. App. Phy.*, vol. 12, no. 1, pp. 179-183, Jan. 2012.
- [146]. Nimitrakoolchai, O.O.; Atthi, N.; Supothina, S., "Parameter optimization by using a Taguchi's method for deposition of water-repellent film," : 3rd

International Conference on Processing Materials for Properties, pp. 1175-1180, 2009.

- [147]. Chou, W.-J.; Sun, C.-H.; Yu, G.-P.; Huang, J.-H., "Optimization of the deposition process of ZrN and TiN thin films on Si(1 0 0) using design of experiment method," *Mat. Chem. Phys.*, vol. 82, no. 1, pp. 228–236, Sept. 2003.
- [148]. Ebrahimiasla, S.; Yunus, W.M.Z.W.; Kassimb, A.; Zaina, Z., "Prediction of grain size, thickness and absorbance of nanocrystalline tin oxide thin film by Taguchi robust design," *Solid State Sciences*, vol. 12, no. 8, pp. 1323-1327, Aug. 2010.
- [149]. Ahmed, W.; Ahmed, E.; Maryan, C.; Jackson, M.J.; Ogwu, A.A.; Ali, N.; Neto, V.F.; Gracio, J., "Time-modulated CVD process optimized using the taguchi method," *J. Mat. Eng.Perf.*, vol. 15, no. 2, pp. 236-241, Dec. 2005.
- [150]. Liu, W., "Synthesis of the CuInSe₂ thin film for solar cells using the electrodeposition technique and Taguchi method," *Int. J. Min. Metall. Mat.*, vol. 16, no. 1, pp. 101 - 107, April 2009.
- [151]. Porro, S.; Musso, S.; Giorcelli, M.; Chiodoni, A.; Tagliaferro, A., " Optimization of a thermal-CVD system for carbon nanotube growth," *Physica E* vol. 37, no. 1-2, pp. 16–20, 2007.
- [152]. Maghsoodloo, S.; Ozdemir, G.; Jordan, V.; Huang, C.-H., "Strengths and limitations of Taguchi's contribution to quality, manufacturing and process engineering," *J. Manuf.Syst.*, vol. 23, no. 2, pp.73-126, 2004.
- [153]. Dubey, A.D.; Yadava, V., "Multi-objective optimisation of laser beam cutting process" *Optics & Laser Technol.*, vol. 40, no. 3, pp. 562–570, April 2008.
- [154]. Cheng, W.T.; Li, H.C.; Huang, C.N.; "Simulation and optimization of silicon thermal CVD through CFD integrating Taguchi method," *Chemical Eng. J.*, vol. 137, pp. 603–613, 2008.
- [155]. Tarng, Y.S.; Yang, W.H.; Juang, S.C., "The Use of Fuzzy Logic in the Taguchi Method for the Optimisation of the Submerged Arc Welding Process" *Int J. Adv. Manuf. Technol.*, vol. 16, no.3, pp. 688–694, April 2000.
- [156]. Wen-Hsien Ho, W.H.; Tsai, J. T.; Hsu, G.-M.; Chou, J.-H., "Process Parameters Optimization: A Design Study for TiO₂ Thin Film of Vacuum Sputtering Process," *IEEE Trans. Automation Sci.Engin.* pp. 143 - 146, 2010.
- [157]. Asafa, T.B.; Tabet, N.; Said, S.A.M., "Taguchi method–ANN integration for predictive model of intrinsic stress in hydrogenated amorphous silicon film

deposited by plasma enhanced chemical vapour deposition," *Neurocomputing*, Vol.106, pp. 86 - 94, April, 2013 .

- [158]. Singh, S., "Optimization of machining characteristics in electric discharge machining of 6061Al/Al₂O₃P/20P composites by grey relational analysis,". *Int. J. Adv. Manuf. Technol.* vol.63, pp.1191–1202, March 2012,
- [159]. Yu-Sen Yang, Y.-S.; Huang, W; Huang, W.-Y., "Mechanical and hydrophobic properties of chromium carbide films via a multi-objective optimization approach," *Thin Solid Films*, vol. 519, pp. 4899–4905, Jan. 2011.
- [160]. Deng, J.L., "Introduction to grey system theory," *J. Grey System*, vol. 1, no.1, pp. 1–24, 1989.
- [161]. Maity, K.P.; Singh, R.K., "An optimisation of micro-EDM operation for fabrication of micro-hole," *Int. J. Adv. Manuf. Technol.*, vol. 61, no. 9-12, pp 1221-1229, August 2012.
- [162]. Tsao, C.C., "Grey–Taguchi method to optimize the milling parameters of aluminum alloy, *Int. J. Adv. Manuf. Technol.*, vol. 40, pp. 41–48, no. 1-2, Jan. 2009.
- [163]. Fung, C.P., "Manufacturing process optimization for wear property of fibre-reinforced polybutylene terephthalate composites with grey relational analysis," *Wear* 254, pp. 298–306, no. 3-4, Feb. 2003.
- [164]. Hinkelmann, K.; Kempthorne, O., *Design and Analysis of Experiments*. New Jersey : John Willey and Sons, 2005.
- [165]. http://davidmlane.com/hyperstat/F_table.html. Cited: 29 Sept 2012.]
- [166]. Patterson, A.L., "The Scherrer Formula for X-Ray Particle Size Determination," *Phys. Rev.*, vol. 56, pp. 978–982, Nov. 1939.
- [167]. Popa, N.C.; Balzar, D., "An analytical approximation for a size-broadened profile given by the lognormal and gamma distribution,"*J. Appl. Cryst.*, vol. 35, pp. 338-346, Jun. 2002.
- [168]. Bouderbala, M.; Hamzaoui, S.; Amrani, B.; Reshak, A.H.; Adnane, M.; Sahraoui, T.; Zerdali, M., "Thickness dependence of structural, electrical and optical behaviour of undoped ZnO thin films," *Physica B: Condensed Matter*, vol. 403, no. 18, pp. 3326– 3330, Sept. 2008.

- [169]. Lita, A.E.; Sanchez, J. E., "Characterization of surface structure in sputtered Al films: Correlation to microstructure evolution," *J. Appl. Phys.*, Vol. 85, no.2, pp. 876, Jan. 1999.
- [170]. Fang, Z.B.; Yan, Z.I.; Tan, Y.S.; Liu, X.Q.; Wang, Y.I., "Influence of post-annealing treatment on the structure properties of ZnO films," *Appl. Surf. Sci.*, vol. 241, no. 2-3, pp. 303 - 308, March 2005.
- [171]. Hellberg, P.-E.; Gagnor, A.; Zhang, S.-L.; Petersson, C. S., "Boron-Doped Polycrystalline SiGe, Films: Dopant Activation and Solid Solubility," *J. Electrochem. Soc.*, vol. 144, no. 11, pp. 3968-3973, 1997.
- [172]. Xue, Z.Y.; Chen, D; Liu, L.J.; Jiang, H.T.; Bian, J.T.; Wei, X. "Fabrication of high quality strained SiGe on Si substrate by RPCVD," *Chinese Science Bulletin*, vol. 57, no. 1, pp. 1862-1867, 2012.
- [173]. Low, C.W.; Liu, T.-J.K.; Howe, R.T., "Study of poly-SiGe structural properties for modularly integrated MEMS" *ECS Transactions*, vol. 3, no. 7, pp. 1131–1142, 2006.
- [174]. Bolshakov A.; Pharr, G. M., "A Critical Examination of the Fundamental Relations Used in the Analysis of Nanoindentation Data," *J. Mater. Res.*, vol. 13, pp. 1049, 1998.
- [175]. He, B.-C.; Wen, H.-C.; Chinag, T.-Y.; Chang, Z.-C.; Lian, D.; Yau, W.-H.; Wu, W.-F.; Chou, C-P., "Effect of strain relaxation of oxidation-treated SiGe epitaxial thin films and its nanomechanical characteristics," *Applied Surface Science*, vol. 256, no. 10, pp. 3299–3302, March 2010.
- [176]. Tsui, T.Y.; Oliver, W.C.; Pharr, G.M.; "Influences of stress on the measurement of mechanical properties using nanoindentation: Part I. Experimental studies in an aluminum alloy," *J. Mater. Res.*, vol. 11, pp. 752–759, 1996.
- [177]. Buckle, H., "Progress in Micro-Indentation Hardness Testing," *Metallurgical Reviews*, vol. 4, no. 13, pp. 49-100, 1959.
- [178]. Cai, X.; Bangert, H., "Hardness measurements of thin films-determining the critical ratio of depth to thickness using FEM," *Thin Solid Films*, vol. 264, no. 1, pp. 59-71, Aug. 1995.
- [179]. Clifford, C.A.; Seah, M. P., "Modelling of nanomechanical nanoindentation measurements using an AFM or nanoindenter for compliant layers on stiffer substrates," *Nanotechnology*, vol. 17, pp. 5283–5292, 2006.

- [180]. Jiang, W.-G.; Su, J.-J.; Feng, X.-Q., "Effect of surface roughness on nanoindentation test of thin films," *Engineering Fracture Mechanics*, vol. 75, no. 21, pp. 4965–4972, Nov. 2008.
- [181]. Franke, A.E.; Bilic, D.; Chang, D.T.; Jones, P.T.; King, T.-J.; Howe, R.T.; Johnson, G.C., "Post-CMOS Integration of Germanium III Microstructures," *Proc. IEEE MEMS*, pp. 630-637, 1999.
- [182]. Sheldon, B.W.; Rajamani, A.; Bhandari, A.; Chason, E.; Hong, S.K.; Beresford, R., "Competition between tensile and compressive stress mechanisms during Volmer–Weber growth of aluminum nitride films," *J. Appl. Phys.*, vol. 98, no. 4, pp. 043509, 2005.
- [183]. Cammarata, R.C.; Trimble, T.M.; Srolovitz, D.J., "Surface stress model for intrinsic stresses in thin films," *J. Mater. Res.*, vol. 15, no. 11, pp. 2468 - 2474, 2000.
- [184]. Gaspar, J.; Paul, O.; Chu, V.; Conde, J.P., "Mechanical properties of thin silicon films deposited at low temperatures by PECVD," *J. Micromech. Microeng.*, vol. 20, no. 3, pp. 035022, March 2010.
- [185]. Nix, W.D.; Clement, M.D., "Crystallite coalescence: A mechanism for intrinsic tensile stresses in thin films," *J. Mater. Res.*, Vol. 14, No. 8, pp. 3467 - 3473, 1999.
- [186]. Thornton, J.A.; Hoffman, D.W., "Stress-related effects in thin films," *Thin Solid Films*, vol. 171, no. 1, pp. 5–31, April 1989.
- [187]. Barborini, E.; Corbelli, G.; Bertolini, G.; Repetto, P.; Leccardi, M.; Vinati, S.; Milani, P., "The influence of nanoscale morphology on the resistivity of cluster-assembled nanostructured metallic thin films," *New J. Phys.*, vol. 12, . 073001, July 2010.
- [188]. Reiss, G.; Hastreiter, E.; Bruckl, H.; Vancea, J., "Thickness-dependent thin-film resistivity: application of quantitative scanning-tunneling-microscopy imaging," *Physical review B*, vol. 43, no. 6, pp. 5176 - 5179, 1990.
- [189]. Gao; M.-Z.; Job, R.; Xue, D.-S.; Fahrner, W. R., "Thickness Dependence of Resistivity and Optical Reflectance of ITO Films," *Chinese Phys. Lett.*, vol. 25, pp. 1380, 2008.
- [190]. Durkan, C.; Welland, E. M., "Size effects in the electrical resistivity of polycrystalline nanowires," *Phys. Rev. B*, vol. 61, pp. 14215–14218, May 2000.

- [191]. Mayadas, A. F.; Shatzkes, M., "Electrical-resistivity model for polycrystalline films: a case of arbitrary reflection at external surfaces," *Phys. Rev. B*, vol. 1, pp. 1382–1389, Feb. 1970.
- [192]. Lucas, M. S. P., "Electrical conductivity of thin metallic films with unlike surfaces," *J. Appl. Phys.*, vol. 36, no. 5, pp. 1632, 1965.
- [193]. Namba, Y., "Electrical conduction of thin metallic films with rough surface," *J. Appl. Phys.*, vol. 39, pp.no. 13, 6117, 1968.
- [194]. Steinhögl, W.; Schindler, G.; Steinlesberger, G.; Traving, M.; Engelhardt, M., "Comprehensive study of the resistivity of copper wires with lateral dimensions of 100 nm and smaller," *J. Appl. Phys.*, vol. 97, pp. 023706, 2005.
- [195]. Lim, J.-W.; Isshiki, M., "Electrical resistivity of Cu films deposited by ion beam deposition: effects of grain size, impurities, and morphological defect," *J. Appl. Phys.*, vol. 99, pp. 094909, 2006.
- [196]. Ke, Y.; Zahid, F.; Timoshevskii, V.; Xi, K.; Gall, D.; Guo, H., "Resistivity of thin Cu films with surface roughness," *Physical Review B*, vol. 79, no. 1-6, pp. 155406, 2009.
- [197]. Liu, Y.-Y., Yang, S.-Y.; Wei, G.-X.; Song, H.-S.; Cheng, C.-F.; Xue, C.-S.; Yuan, Y.-Z., "Electrical and optical properties dependence on evolution of roughness and thickness of Ga:ZnO films on rough quartz substrates," *Surf. Coat. Technol.*, vol. 205, pp. 3530–3534, Feb. 2011.
- [198]. Church, E.L.; Takacs, P.Z., *Surface Scattering*. Optical Society Of America. *Handbook of Optics*. New York : McGraw-Hill, 2009.
- [199]. Sahoo, N.K.; Thakur, S.; Tokas, R.B., "Fractals and superstructures in gadolinia thin film morphology: Influence of process variables on their characteristic parameters," *Thin Solid Films*, vol. 503, no. 1-2, pp. 85 – 95, May 2006.
- [200]. Jakobs, S.; Duparre, A.; Truckenbrodt, H., "Interfacial roughness and related scatter in ultraviolet optical coatings: a systematic experimental approach," *Appl. Opt.*, vol. 37, no. 7, pp. 1180–1193, 1998.
- [201]. Raoufi, D.; Kiasatpour, A.; Fallah, H.R.; Rozatian, A.S.H., "Surface characterization and microstructure of ITO thin films at different annealing temperatures," *App.Surf. Sci.*, vol. 253, vol. 23, pp. 9085–9090, Sept. 2007.
- [202]. Mandelbrot, B., *Fractals and Chaos*. Berlin. : Springer, 2004. ISBN 978-0-387-20158-0.

- [203]. Jeng, Y.R.; Tsai, P.C.; Fang, T.H., "Nanomeasurement and fractal analysis of PZT ferroelectric thin films by atomic force microscopy," *Microelectron. Eng.*, vol. 65, no. 4pp. 406, April 2003.
- [204]. Shilyaev, P.A.; Pavlov, D.A.; Khokhlov, A.F., "Fractal analysis of SPM images," *Internat. Workshop on Scanning Probe Microscopy by Institute for Physics of Micro-structures, Russian Academy of Sciences, N. Novgorod*, pp. 234-235, March, 2003.
- [205]. Rees, W.S., *Introduction. CVD of Nonmetals*. New York : VCH Verlagsgesellschaft mbH, 1996.
- [206]. Family, F.; Vicsek, T., "Scaling of the active zone in the Eden process on percolation networks and the ballistic deposition model," *J. Phys. A - Mathematical and General*, vol. 18, no. 2, pp. L75-L81, 1985.
- [207]. Ramasco, J.J.; López, J. M.; Rodríguez, M. A., "Generic dynamic scaling in kinetic roughening," *Phys. Rev. Lett.*, vol. 84. pp. 2199, 2000.
- [208]. Lu, T.-M.; Zhao, Y.-P.; Drotar, J.T.; Karabacak, T.; Wang, G.-C.; *Novel mechanisms on the growth morphology of films*, edited by Bartelt, N.C.; Berbezier, I.; Hannon, J.B.; Hearne, S.J., Aziz, M.J., *Morphological and Compositional Evolution of Thin Films*, *Mat. Res. Soc. Proc.* pp. 749, 2003.
- [209]. Offenberg, M.; Elsner, B.; Laermer, F., "Vapor HF etching for sacrificial oxide removal in surface micromachining," *Proc. Electrochemical Soc. Fall Meeting*, vol. 94, no. 2, pp.1056-1057, Oct. 1994.
- [210]. Gemetec, *Operation Manual for Pad Fume of Vapour HF*.
- [211]. Gromova, M.; Mehta, A.; Baert, K.; Witvrouw, A., "Characterization and strain gradient optimization of PECVD poly-SiGe layers for MEMS applications," *Sen.Act. A*, vol. 130–131, pp. 403–410, Aug. 2006.
- [212]. Verwillegen, M.L.; van Oort, M., *Strain Diagnostics and Etch Tecnology Mask Set for Surface Micromachined Structures*. MS Thesis submitted to Hogeschool van Utrecht. 2011.
- [213]. http://probe.olympus-global.com/en/product/omcl_ac160ts_r3/. accessed on 09 Feb 2013.
- [214]. Fang, L.; Carlo C.; Jiaru, C.; Roya, M. "Residual stress characterization of polycrystalline 3C-SiC films on Si(100) deposited from methylsilane," *J. Appl. Phys.*, vol. 106,pp. 013505, 2009.

Vitae

Name : Asafa, Tesleem Babatunde

Nationality : Nigerian

Date of Birth : 3/20/1979

Email : teslimtunde@yahoo.com

Address : Mechanical Engineering, Ladoke Akintola University of
Technology, P.M.B. 4000, Ogbomosho, Oyo State, Nigeria.

Academic Background

- i. Interuniversities Micro Electronic Center, Leuven, Belgium 2011 – 2013
- ii. Katholieke Universiteit Leuven, Belgium 2011 – 2013
- iii. King Fahd University of Petroleum and Minerals, Saudi Arabia 2009 – 2013
- iv. University College London, United Kingdom 2007 – 2008
- v. University of Ibadan, Ibadan, Nigeria 2005 – 2007
- vi. Ladoke Akintola University of Technology, Nigeria 1998 – 2003